Visible and near-infrared divertor spectroscopy on the MAST and JET-ILW tokamaks

LOMANOWSKI, BARTOSZ,ALEKSANDER

Visible and Near-infrared Divertor Spectroscopy on the MAST and JET-ILW Tokamaks

Bartosz Aleksander Lomanowski

A Thesis presented for the degree of
Doctor of Philosophy

Centre for Advanced Instrumentation
Department of Physics
University of Durham
UK

August 2015

Visible and Near-infrared Divertor Spectroscopy on the MAST and JET-ILW Tokamaks

Bartosz Aleksander Lomanowski

Submitted for the degree of Doctor of Philosophy
August 2015

Abstract

Passive spectroscopy diagnostics play a key role in advancing the physics of plasma exhaust in the edge and divertor regions of tokamaks. Information obtained from spectral line intensities and profile shapes is crucial for estimating plasma parameters, particularly for studies of cold and dense detached plasmas. This work aims to characterise the visible and near-infrared spectral regions with emphasis on the Balmer and Paschen hydrogen series lines, their diagnostic applications and interpretation techniques. Whereas the Balmer series lines are measured routinely, few observations of the Paschen series lines have been carried out in the fusion plasma context. Extending observations to the near-infrared region for more detailed studies of the Paschen series is addressed through diagnostic development with the aim of providing coverage of the visible to near-infrared spectral range (350-1900 nm) along the same optical line-of-sight. An initial spectral survey on MAST using a purpose built diagnostic provides new insight into the spectral features in the near-infrared and confirmes the viability of Paschen line observations. Following the proof of concept measurements on MAST, diagnostic development on the JET ITER-like wall mirror-linked divertor spectroscopy system facilitated more refined measurements. The main outputs include first of its kind measurements of the Pa-α line and spatially resolved spectral line profile measurements of the Pa-β line. In the visible range ELM-resolved Balmer and impurity emission profile measurements at high spatial resolution were obtained using a new filtered camera system. A detailed assessment of the diagnostic scope for parameter estimation from both high-n and low-n Balmer and Paschen series lines is presented, underpinned by a parametrised line profile model which captures the relevant broadening and splitting mechanisms, including the Zeeman, Stark and Doppler processes. Interpretation of JET divertor plasma measurements, in combination with synthetic data simulation results, highlights the importance of complementary Balmer and Paschen series measurements for refining parameter estimates in divertor plasmas.

Declaration

The work in this thesis is based on research carried out at the Centre for Advanced Instrumentation, the Department of Physics, University of Durham, UK, and experiments performed at the Culham Centre for Fusion Energy, UK. No part of this thesis has been submitted elsewhere for any other degree or qualification. The work within this thesis is all that of the author, unless referenced to the contrary in the text.

Publications

Elements of this work have been published in:

Lomanowski, B. A., Meigs, A. G., Conway, N. J., Zastrow, K.-D., Sharples, R. M., Heesterman, P., Kinna, D. and JET EFDA Contributors. Enhanced visible and near-infrared capabilities of the JET mirror-linked divertor spectroscopy system. *Review of Scientific Instruments*, 85(11), 11E432, 2014.

Lomanowski, B. A., Meigs, A. G., Sharples, R. M., Stamp, M., Guillemaut, C. and JET EFDA Contributors. Inferring divertor plasma properties from hydrogen Balmer and Paschen series spectroscopy in JET-ILW. *Nuclear Fusion*, 55(12), 123028, 2015.

Acknowledgements

I would like to first thank my supervisor, Prof. Ray Sharples, for giving me the opportunity to carry out the work presented herein, his continuous guidance and support throughout the process, and for accommodating my frequent travels to Culham.

I would like to also thank Dr. Andrew Meigs at CCFE for providing access to the KT3 diagnostic at JET, his technical expertise on all things related to spectroscopy, and for a very fruitful and convivial collaboration throughout the KT3 upgrade project and 2013-2014 JET campaign. This work could not have been carried out without the financial support from the Experiments Department at JET, Dr. Klaus-Dieter Zastrow, and Dr. Neil Conway, and without subsistence support from Martin O'Brien who kindly accommodated my stay at Culham. I am grateful for the technical support from the CODAS department (Dr. Peter Heesterman, Dr. David Kinna and Colin Hogben) in helping me navigate the complexities of hardware integration, data acquisition and storage of JET diagnostics. A special thanks to Dr. Antoinette O'Grady from Princeton Instruments for facilitating the spectrometer loan. Thank you to Dr. Mike Stamp, Dr. Mathias Brix, Dr. Ephraum Delaubie and Dr. Sheena Menmuir for the enjoyable discussions during my stay at JET and to Dr. Carine Giroud for letting me salvage some much needed equipment on short notice. On the MAST side I would like to thank Dr. James Harrison for facilitating diagnostic access to the MAST divertor during the 2013 campaign, and for kindly lending me one of his spectrometers for the VIS-NIR diagnostic.

At Durham, I would like to thank Paul Clark for his methodical approach to troubleshooting electronics issues, Dr. Juergen Schmoll for his much needed assistance in polishing and assembling optical fibres and Dr. Stephen Rolt for his insights and expertise in optics.

I was very fortunate to have taken part in the training programme hosted by the University of York through the EPSRC Fusion Doctoral Training Network (now the Centre for Doctoral Training in the Science and Technology of Fusion Energy),

which facilitated a one of a kind cross-disciplinary environment at the York Plasma Institute, and provided excellent opportunities for engaging with world-leading experts in fusion-relevant disciplines. I would like to thank the many individuals that have contributed to making the CDT highly successful in training fusion scientists, and a special thanks to my contemporaries for making the first phase of the PhD experience a memorable one.

List of Acronyms

ADU Analog-to-digital unit

AFG ADAS feature generator

BES Beam emission spectroscopy

CCD Charge coupled device

CFC Carbon fibre composite

CMOS Complementary metal oxide semiconductor

CR Collisional-radiative

CT Czerny-Turner

CXRB Charge-exchange recombination spectroscopy

DN Digital number

DND Double-null divertor

DoD Degree of detachment

EFIT Equilibrium fitting

ELM Edge localised mode

EUV Extreme ultraviolet

FFM Frequency fluctuation model

FFS Framework for feature synthesis

FOV Field of view

FWHM Full width at half maximum

GCR General collisional-radiative

GDL Greenwald density limit

HFS High-field side

ILW ITER-like wall

ISP Inner strike point

JET Joint European Torus

LCFS Last closed flux surface

LFS Low-field side

LOS Line of sight

LP Langmuir probe

LSN Lower single-null

LTE Local thermodynamic equilibrium

MAR Molecular assisted recombination

MARFE Multifaceted asymmetric radiation from the edge

MAST Mega Amp Spherical Tokamak

MHD Magnetohydrodynamic

MMM Model microfield method

NEP Noise equivalent power

NIR Near-infrared

OSP Outer strike point

PFR Private flux region

PLTE Partial local thermodynamic equilibrium

PMT Photo-multiplier tube

PSI Plasma-surface interactions

QE Quantum efficiency

SCT Schmidt Czerny-Turner

SND Single-null divertor

SNR Signal to noise ratio

SOL Scrape-off layer

START Small Tight Aspect Ratio Tokamak

SXR Soft x-ray

UV Ultraviolet

VDF Velocity distribution function

VIS Visible

VUV Vacuum ultraviolet

Contents

List of Figures

List of Tables

Chapter 1

Introduction

1.1 Thermonuclear Fusion and Tokamaks

Power generation by means of nuclear reactions is fundamentally of interest due to the large energy density associated with nuclear fuels (i.e., uranium for fission reactions and deuterium for fusion reactions), which, in comparison to chemical reactions from burning fossil fuels, is greater by roughly a factor of 10^6. The large-scale base load electricity generating capacity associated with fissioning of the uranium isotope U^{235} in nuclear power plants offers an environmental advantage on the basis of reducing harmful greenhouse emissions compared to coal or gas-fired power plants. On the other hand, issues of uranium fuel reserves, the long term disposal and storage of nuclear waste, large capital and decommissioning costs and the possibility of nuclear proliferation in the reprocessing of spent fuel comprise the main arguments against the large scale adoption of nuclear power as a means of CO_2 free electricity production (Friedberg, 2007; Meneley, 2010).

Renewable energy sources such as hydroelectric, wind and solar power, although key to a mixed energy portfolio, face significant challenges in adoption primarily due to the low energy density associated with these sources and their intermittent availability compared to dispatchable generation sources (i.e., natural gas or coal power plants). Their potential deployment for large scale base load electricity generation is subject of ongoing research and debate (e.g. Resch et al., 2008; Matek and Gawell, 2015).

Thermonuclear fusion power, which involves the fusing of hydrogen isotopes, offers significant advantages that address the issues of fuel reserves, environmental impact and safety. Firstly, deuterium is abundant in ocean water and can be extracted easily and at low cost. In this sense the availability of this primary fusion

fuel is essentially infinite. Secondly, fusion power, like fission power, does not release greenhouse gases and other harmful chemicals into the atmosphere. However, unlike nuclear power from fission reactions, fusion power is inherently safe in that a radioactive meltdown is physically impossible. Moreover, the source of nuclear waste in fusion power is limited to the interaction of energetic neutrons with the containment vessel, or fusion blanket, which causes the structure to become activated. Even so, the short half-life of the activated materials is conducive to more manageable storage times once the structural components are removed, of the order of 100 years (Hamacher and Bradshaw, 2001).

Although the potential advantages of fusion power are considerable, the main challenges lie in the scientific, technological and economic complexities in achieving a viable fusion power plant. From the scientific and technological perspective, this is best illustrated by considering the conditions necessary to sustain the nuclear fusion reaction using the hydrogen isotopes deuterium (D) and tritium (T) as the fusion fuel. Figure 1.1 shows the energy dependence on the cross sections associated with the following hydrogen isotope fusion reactions (Wesson, 2004):

$$\mathrm{D}^2 + \mathrm{T}^3 \rightarrow \mathrm{He}^4 + \mathrm{n}^1 + 17.6\,\mathrm{MeV}$$
$$\mathrm{D}^2 + \mathrm{D}^2 \rightarrow \mathrm{He}^3 + \mathrm{n}^1 + 3.27\,\mathrm{MeV}$$
$$\mathrm{D}^2 + \mathrm{D}^2 \rightarrow \mathrm{T}^3 + \mathrm{H}^1 + 4.03\,\mathrm{MeV}$$
$$\mathrm{D}^2 + \mathrm{He}^3 \rightarrow \mathrm{He}^4 + \mathrm{H}^1 + 18.3\,\mathrm{MeV}$$

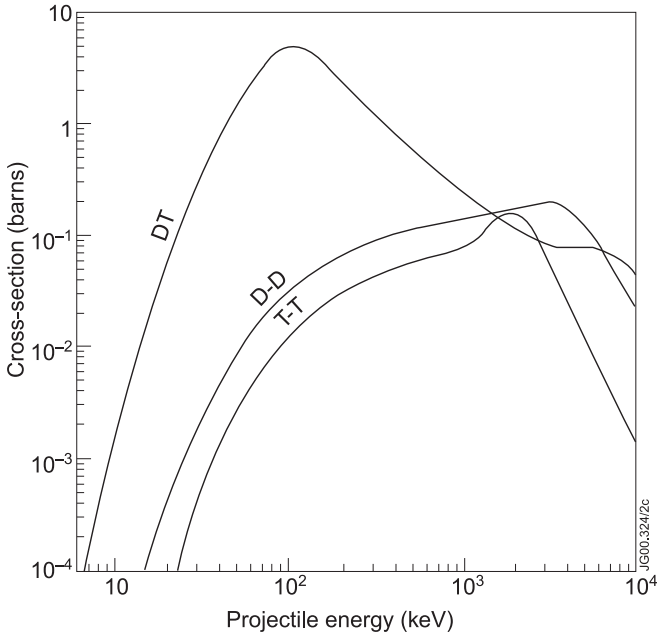

Figure 1.1: Cross-sections of hydrogen isotope fusion reactions. Courtesy of the EUROfusion image database.

Very large collision energies are thus required to overcome the Coulomb barrier in order to initiate the fusion reaction. Of these, the D-T reaction is clearly the easiest to attain as the cross-section is significant even at 10 keV. For this reason D-T fusion has been the central focus of fusion energy research, even though a supply of tritium is required to initiate the reaction. Breeding tritium using ${}_3\mathrm{Li}^6$ blankets surrounding the region of D-T fusion reactions, although a technologically challenging process, is currently the most promising approach in sustaining the reaction. Although ${}_3\mathrm{Li}^6$ comprises only 7.4% of naturally occurring lithium, known reserves are thought to be sufficiently large for thousands of years of fuel availability (Friedberg, 2007).

Above a temperature of few keV, the D-T mixture exists as a fully ionised hot plasma. The most promising approach to supplying energy to sustain the fusion reaction is to heat the D-T fuel mixture such that the hot tail of the thermal velocity distribution corresponds to energies for which the cross-section is sufficiently high. The figure of merit usually associated with fusion devices is the triple product of particle density n, energy confinement time τ_E and plasma temperature T. At values of $n\tau_E T > 5 \times 10^{21}$ m^{-3} s keV (Wesson, 2004) the burning process becomes self-sustaining (i.e., without supplementary heating) and represents the ultimate goal of *ignition*, although such a requirement is not strictly necessary to produce more energy than is supplied.

The tokamak is one approach for magnetically confining the charged particles of the hot plasma and has received the most attention over the past few decades of fusion research. The reason for its success is the tremendous progress that has been made in increasing the triple product by orders of magnitude from 10^{14} to 10^{21} m^{-3} s keV over the last 50 years (Wesson, 2004). The basic features of a tokamak device are illustrated in Figure 1.2. The plasma is magnetically confined by the combination of the toroidal magnetic field B_ϕ and the poloidal magnetic field B_θ such that the plasma pressure p (i.e., the product of the particle density and temperature) is in equilibrium with the magnetic forces. The combination of the toroidal and poloidal magnetic fields results in magnetic field lines which have a helical trajectory, the pitch angle of which is proportional to the ratio of the two magnetic field magnitude components. The toroidal field is much larger, typically by an order of magnitude, than the poloidal field, and is generated by currents in the toroidal field coils. The poloidal field is generated by a toroidal plasma current. This current is induced by transformer action using the primary solenoid circuit which drives an electric field in the plasma (the secondary circuit). The induced plasma current is also the main means of ohmically heating the plasma. The plasma

pressure increases with the strength of the magnetic field and the magnitude of the toroidal plasma current, but is limited by stability considerations and technological factors with respect to the maximum attainable toroidal field magnitude. The shaping and positioning of the plasma is achieved by additional outer poloidal field coils. Additional heating is required to raise the core temperature to few keV and is usually achieved by injecting energetic neutral particle beams (NBI heating) and by electromagnetic waves.

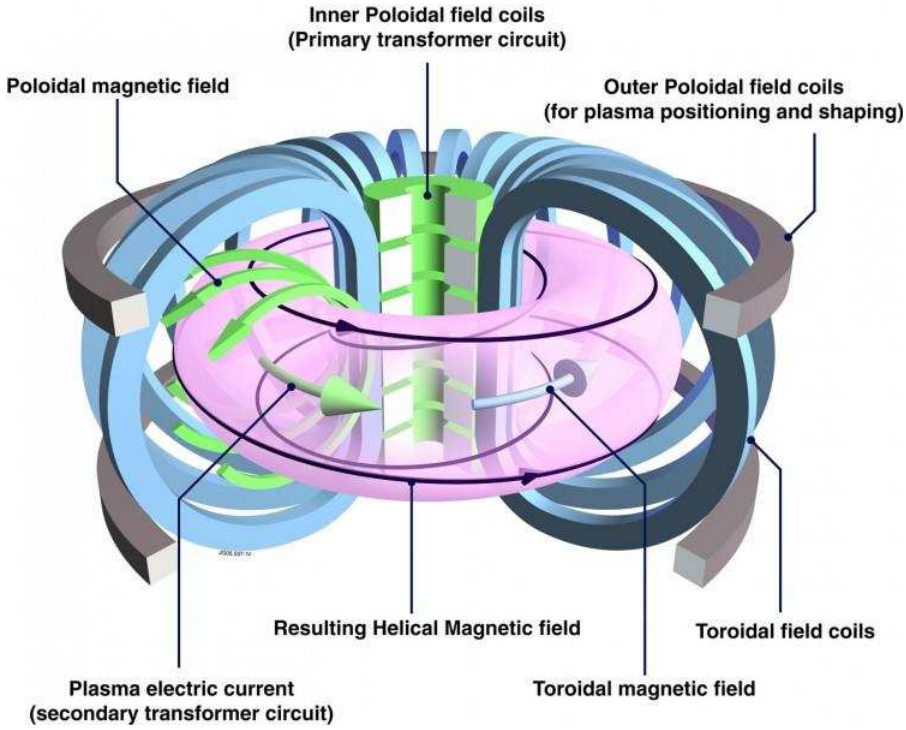

Figure 1.2: Basic features of a tokamak. Courtesy of the EUROfusion image database.

Ultimately, the energy confinement time in a tokamak reactor must be sufficiently long to sustain the thermonuclear fusion reaction. Confinement is limited by thermal convection and conduction processes, and also by radiative losses which cool the plasma. The experimentally observed transport of particles and energy out of the tokamak plasma is unfortunately much higher, up to two orders of magnitude, than the confinement time determined by Coulomb collisions alone (Wesson, 2004). This so called anomalous transport is thought to be caused by turbulence driven micro-instabilities in the plasma (Friedberg, 2007; Conner and Wilson, 1994), and consequently drives the large size of a reactor-scale device in order to compensate for the high rate of escaping particles and energy.

The inevitable outcome of the leakage of energy and particles out of the confined plasma through cross-field transport mechanisms is contact of energetic particles

with the wall and consequently the entry of impurities into the plasma. The presence of impurities has deleterious effects on the plasma as it gives rise to radiation losses and fuel dilution. The control of plasma-surface interactions (PSI) has thus been the subject of extensive study throughout the history of fusion research.

Earlier tokamak devices employed a radially outward protruding element, the limiter configuration (see Figure 1.3), thereby isolating the PSI and limiting the plasma contact with the vacuum vessel. Although this design has advantages in terms of its simplicity, it suffers from the close proximity of the limiting element in relation to the confined region, and from physical constraints on the thickness of the resulting interaction layer known as the scrape-off layer (SOL). The SOL is an open-field region outboard of the confined plasma region, dictated by the extent of the limiter geometry, and arises due to the transport of particles and energy across field lines which terminate on the limiter surface. The ability to control the influx of impurities from physical sputtering processes along a relatively thin region of PSI is therefore made difficult. The subsequent entrainment of the cold impurities can lead to an energy loss mechanism from the core plasma primarily via line radiation from collisionally excited electronic states of the impurity ions (Stangeby, 2000a).

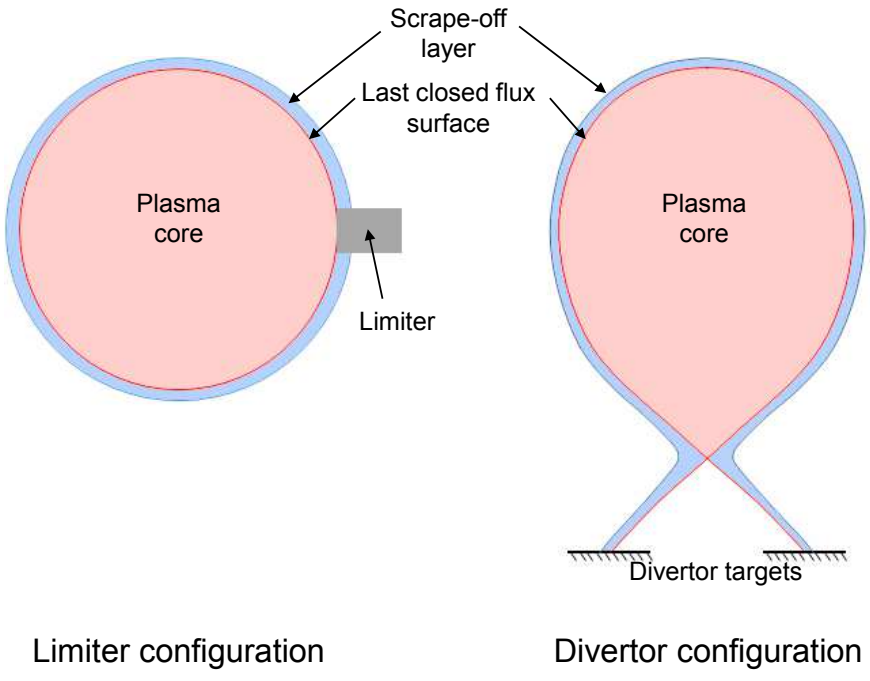

Figure 1.3: Poloidal cross-section schematic of the limiter and divertor configurations.

In an effort to provide additional control of the SOL parameters and to minimise the impact of PSI on the confined core plasma, many devices were converted to utilise

the divertor concept in the 1990s. The main features of the poloidal divertor design are shown in Figure 1.3. By introducing shaping of the magnetic topology via an additional poloidal field coil, a null in the field line geometry, known as the X-point, can be formed, thus creating a SOL dictated by the shaping parameters rather than by direct contact with the protruding limiter structure. The last closed flux surface (LCFS) separates the confined region of the plasma characterised by closed magnetic field lines, and the SOL region in which the field lines terminate on the divertor target plates. Such a configuration allows for optimisation of the target plate location and geometry. With these additional degrees of freedom, it is possible to explore the impact of various divertor geometries on the operational performance of the confined plasma and, critically, on the ability of the target plates to withstand steady-state and transient heat fluxes arising from the exhaust of energy and particles from the core.

Developing a solution to the problem of heat exhaust in tokamak divertors is considered to be the main challenge towards the realisation of magnetic confinement fusion (EFDA, 2012). Observations of plasma behaviour and measurements of plasma parameters are crucial in linking experiment with theory with the aim of predicting tokamak performance. Plasma diagnostics thus play a key role in advancing the understanding of exhaust physics processes. The work presented in this thesis focuses on the application of passive spectroscopy diagnostics for divertor plasma studies. The experimental investigations into passive spectroscopy in the visible and near-infrared spectral regions were carried out on two tokamaks at the Culham Centre for Fusion Energy. The following sections provide a brief description of their main features and engineering parameters.

1.1.1 The Mega Amp Spherical Tokamak

The Mega Amp Spherical Tokamak (Cox, 1999) is a small aspect ratio (the ratio of the major to minor radii, R/a) tokamak characterised by a plasma shape which is more spherical than the more conventional larger aspect ratio devices. Spherical tokamaks are capable of operating at higher confinement efficiencies, quantified by the normalised plasma pressure, β, defined as:

$$\beta = \frac{p}{B^2/2\mu_0} \,, \tag{1.1}$$

which is the ratio of the plasma pressure to magnetic pressure. High confinement

efficiency is desirable in a fusion reactor as it is effectively linked to the unit power cost of electricity production (Friedberg, 2007).

For a given magnetic field magnitude, the maximum plasma pressure is limited by magnetohydrodynamic (MHD) instabilities. Since the maximum β value has been shown to scale with the inverse aspect ratio (Sykes et al., 1999), spherical tokamaks are therefore more resilient against MHD instabilities providing access to high β operation. For example, a world record of $\beta \approx 40\%$ has been achieved experimentally in MAST's predecessor, START (Small Tight Aspect Ratio Tokamak) (Gryaznevich et al., 1998).

Figure 1.4 (left) shows a cutaway CAD model of the MAST machine, including the main chamber and internal structure consisting of poloidal field coils for plasma shaping and positioning, as well as the upper and lower horizontal divertor target plates. The design of the MAST vessel and open divertor geometry also provides excellent diagnostic access. This is demonstrated in Figure 1.4 (right) which shows a composite image in the visible range of a double-null MAST plasma obtained by a camera positioned at a mid-plane port. The main parameters of the MAST tokamak are summarised in Table 1.1.

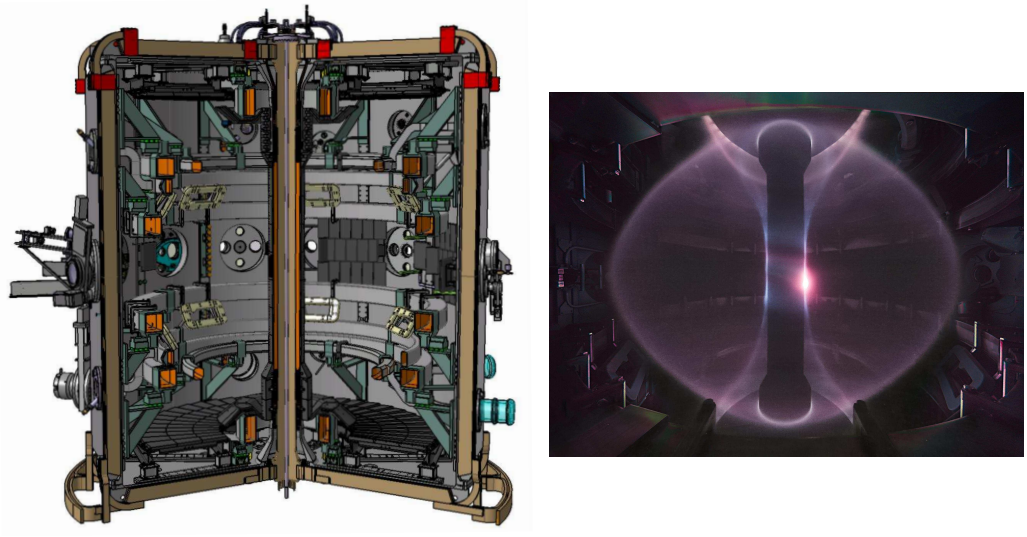

Figure 1.4: Cutaway CAD model of the MAST tokamak (left, courtesy of the CCFE design office). Composite image of a double-null (top and bottom divertor configuration) MAST plasma from visible light emission (right, courtesy of Scott Silburn (CCFE), Alex Meakins (CCFE) and James Harrison (CCFE)).

Table 1.1: Main parameters of the MAST tokamak.

Major radius (m)	0.7
Minor radius (m)	0.5
Aspect ratio	≥ 1.3
Plasma current (MA)	≤ 2
Toroidal field (T)	≤ 0.63 (R = 1 m)
NBI heating power (MW)	5
Pulse length (s)	≤ 1
Plasma volume (m^3)	8
Plasma facing components	Carbon fibre composite (CFC)

1.1.2 The Joint European Torus Tokamak

The Joint European Torus (JET) is currently the world's largest operational tokamak. It was designed for D-T operation, long pulse length and high heating power, with the principal goals of investigating heating and confinement in reactor relevant plasma conditions. In 1992-1993 JET was upgraded with a pumped divertor configuration in order to facilitate experiments with a focus on exhaust power mitigation and impurity control. During the 1997 D-T experimental campaign, the highest fusion power of 16 MW to date was achieved with a total input heating power of 24 MW and a 50-50 D-T fuel mix, thus reaching an instantaneous Q of 0.65, where the fusion gain factor Q is defined as the ratio of the produced fusion power to the total input heating power. Figure 1.5 shows an internal view of JET with a superimposed image of the plasma in the visible range. The main parameters of the JET tokamak are given in Table 1.2.

The most notable feature of the current JET configuration is the ITER-like wall (ILW) (Matthews et al., 2011) which was installed between 2009-2011 as a test-bed for the material combination selected for the next generation reactor-scale ITER tokamak (Ikeda, 2007) currently being built in Cadarache, France. Carbon has been the primary material choice for plasma facing components in fusion experiments due to its excellent heat and erosion resistance and low atomic number allowing for relatively high carbon concentrations in the plasma without deleterious effects. However, carbon is not suitable as a first wall material in tokamak reactors due due to its propensity to trap tritium, thereby limiting the lifetime of the first wall due to high levels of radioactivity. The material choices for ITER and JET-ILW are a combination of beryllium (Be) in the main chamber and tungsten (W) in the

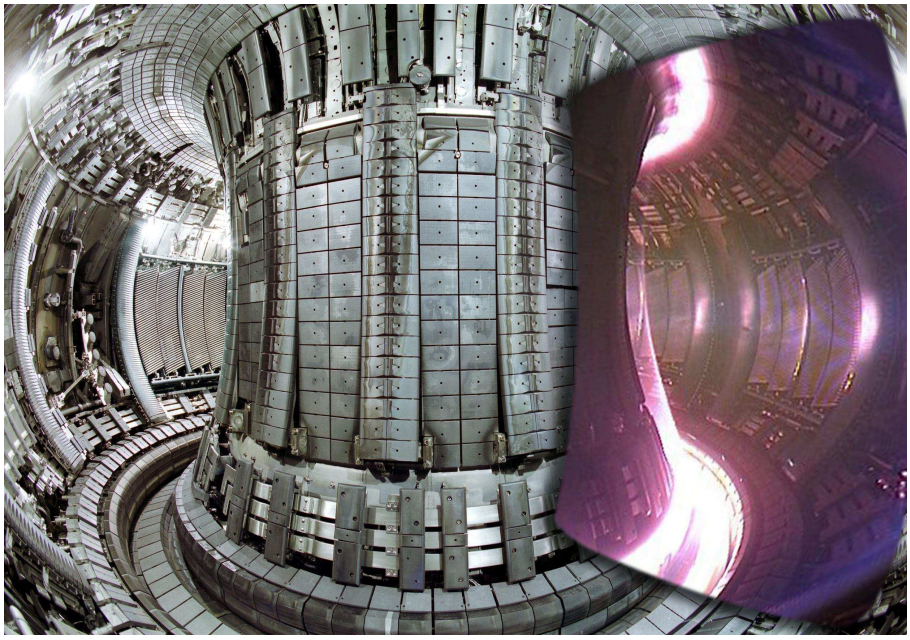

Figure 1.5: Internal view of JET with a superimposed image of the plasma taken by a camera in the visible range of the spectrum. Courtesy of the EUROfusion image database (ref. number CP05j-438-01).

divertor. Be is a light metal with high heat resistance (melting point of 1287°C) which, like carbon, has the least impact on plasma performance. W has been chosen as the divertor material due to its very high melting point of 3422°C in order to withstand the high heat fluxes at the target plates which are in direct contact with the plasma. Its high atomic number, $Z = 74$, also offers excellent erosion resistance, but its presence in the main plasma must be kept to a minimum as it can rapidly cool and dilute the core plasma.

In operation since 2011, ILW experimental campaigns have provided valuable insight and physics understanding into the impact of operating with the new mix of first wall materials. Key observations include a reduction in the long-term fuel retention compared to the JET carbon machine (JET-C) and a low effective charge ($Z_{eff} = 1.2$ in JET-ILW vs. $Z_{eff} = 2.5$ in JET-C) of the plasma as a result of the reduction in the primary beryllium source compared to the carbon source in JET-C (Brezinsek, 2015). However, operation with the Be/W wall has had an impact on the degradation of plasma confinement relative to the carbon wall due to W accumulation in the plasma core (e.g. Angioni et al., 2014) . Ongoing effort is thus targeted at improving the understanding and control of W accumulation in order improve energy confinement and develop high performance plasma scenarios in anticipation of the next D-T experimental campaign.

Table 1.2: Main parameters of the JET-ILW tokamak.

Major radius (m)	2.96
Minor radius (m)	0.96
Aspect ratio	≈ 3
Plasma current (MA)	≤ 6
Toroidal field (T)	≤ 4 (magnetic axis)
NBI heating power (MW)	≤ 24
Ion cyclotron resonance heating (ICRH) power (MW)	≤ 15
Pulse length (s)	20-60
Plasma volume (m^3)	≈ 90
Plasma facing components	Limiters: beryllium Divertor: tungsten coated CFC and bulk tungsten

1.2 Spectroscopy Diagnostics in Tokamaks

The presence of impurities in the tokamak plasma due to plasma-wall interactions, which can lead to enhanced radiative losses and fuel dilution, makes spectroscopy an indispensable tool in studying the impact of impurities on plasma performance. Line and continuum radiation emitted by impurity and working plasma species is also used for measuring plasma properties such as density, electron and ion temperature, velocity, transport coefficients and particle influx rates. Plasma spectroscopy is a broad and diverse field of research with measurement techniques spanning a wide spectral range from the near-infrared (NIR), visible (VIS), ultraviolet (UV), vacuum ultraviolet (VUV), extreme ultraviolet (EUV) to soft x-ray (SXR) regions thus covering photon energies in the range of 0.5 eV to $\approx 10^4$ eV ($\approx$0.1-2000 nm in wavelength). The fusion spectroscopist necessarily relies on a large body of knowledge concerning fundamental and derived atomic databases as well as theoretical and computational models which are routinely applied to confront spectral line intensity and spectral line profile measurements. Spectroscopic techniques are typically classed as either *active* or *passive*. Active spectroscopy concerns techniques which rely on injected particle beams as signal enhancers and localisers (e.g., neutral beam emission spectroscopy (BES), charge-exchange recombination spectroscopy (CXRB)) whereas passive spectroscopy refers to measurements of radiation emitted

by the plasma due to thermal collisional-radiative processes.

The applicability of a particular spectroscopic technique and relevant wavelength range of observation depends on the plasma properties and measurement aims. SXR, EUV and VUV spectroscopy is most suitable for line emission measurements of partially ionised medium and heavy elements (e.g., W, Fe) in the hot core region whereas UV, VIS and NIR are better suited towards line emission measurements of light impurity (e.g., C, Be, O, He, B, N, Ne, Ar) and hydrogenic species (H, D, T) in the cooler edge and divertor plasma regions. The design complexity of the signal relay elements, dispersive elements, selection and availability of detectors is largely driven by the spectral range and sensitivity requirements of the spectroscopic diagnostics. At wavelengths below 200 nm (VUV, EUV and SXR) the sharp decrease in the transmission through air, window and lens materials and the low efficiency of reflective mirror coatings necessitates vacuum instruments which can increase cost and complexity significantly and reduce measurement flexibility. At wavelengths above 200 nm (UV, VIS, NIR) measurements can be performed in the ambient environment taking advantage of more conventional optical components with high transmission/reflection efficiency and commercially available spectrometer packages. Nevertheless, spectroscopic tokamak diagnostics based on both vacuum and non-vacuum configurations have been successfully deployed on numerous tokamaks. Review articles by Stratton et al. (2008), Peacock (1996), and Fantz (2006) provide an overview of the measurement principles and application of spectroscopic diagnostics to magnetically confined fusion plasmas.

1.2.1 Passive Spectroscopy in the Visible and Near-Infrared

The flexibility of working above the 200 nm vacuum cut-off has led to wide-scale deployment of spectroscopy diagnostics in the UV-VIS-NIR spectral region, with particular emphasis on the 300-1000 nm wavelength region corresponding to the sensitivity range of charge coupled devices (CCDs). The large uptake of scientific grade CCD linear and 2D detectors in imaging and spectroscopy applications, featuring high quantum efficiency (QE) and low electronic noise, has facilitated a wide range of relatively inexpensive solutions for plasma spectroscopy diagnostics.

The most common spectrograph configuration is the Czerny-Turner design (e.g. Shafer et al., 1964) which employs two reflective elements and high efficiency plane gratings (ruled or holographic) to disperse the light and image the input slit onto a sensor. The frame transfer CCD camera is a popular choice due to high QE and

shutterless operation. CMOS (complementary metal oxide semiconductor) cameras are also gaining in popularity for filtered imaging spectroscopy applications (e.g., the Coherence Imaging diagnostic on MAST (Silburn et al., 2014)) and for high-speed imaging (> 100 kHz frame rate) of transient plasma phenomena (e.g., observations of filamentary structures in the edge and divertor on MAST (Harrison, 2014)) due to distinct speed advantages over the relatively slower sensor readout CCD options.

Spectroscopic measurements in the VIS spectral region are of particular importance for divertor plasma emission studies (e.g. Huber et al., 2013; Isler et al., 1997; Hollmann et al., 2006) with a focus on characterisation and code benchmarking of exhaust physics phenomena. Such investigations are crucial for developing exhaust power mitigation strategies (e.g. Loarte et al., 2007). The aim of such strategies is to control and limit the large heat fluxes associated with the leakage of particles and energy from the core plasma, channelled along the thin SOL to the sacrificial divertor targets. Passive spectroscopy is therefore an important tool in providing measurements of plasma parameters from the working plasma species emission (most often deuterium) and linking these observations to atomic physics. It is also commonly employed to characterise the influx and transport of intrinsic impurity species (C, Be) and extrinsic seeding gases (N_2, Ne, Ar) used to promote radiative power dissipation upstream of the divertor targets.

Spectroscopic observations of the hydrogen Balmer series lines (360-656 nm) are perhaps the most common in studies of divertor plasma emission and estimation of plasma parameters such as density and electron temperature. Observations of the Lyman series lines (90-122 nm) requires vacuum instruments and is therefore less common. Observations of the Paschen series lines (824-1875 nm) have been limited (e.g. Brezinsek et al., 2009; Soukhanovskii, 2008; Soukhanovskii et al., 2014) as their measurement is outside of the sensitivity range of CCDs, save for the higher transitions in the 824-1000 nm region. Measurement of the Paschen series lines, however, offers some potential advantages, including broader spectral line profiles which can be exploited for plasma density estimates (e.g. Soukhanovskii et al., 2006) as well as potential advantages in reduced degradation of optical components in the NIR subjected to the harsh burning plasma environment of reactor-scale fusion devices such as ITER (e.g. Soukhanovskii, 2008). This includes increased resilience to: erosion and deposition of plasma facing mirrors (e.g. Widdowson, 2011; Litnovsky et al., 2007a,b; Rudakov et al., 2006); accumulated damage and permanent transmission loss in windows, lenses and optical fibres due to radiation-induced absorption and dynamic losses in windows, lenses and optical fibres due to radiation-induced lumi-

nescence and Cherenkov radiation (e.g. Brichard et al., 2004). Of these, the optical performance degradation of the plasma facing mirrors has received significant attention. Recently, substantial progress has been made in advancing *in situ* mirror cleaning techniques using a radio frequency plasma generated around the mirror (e.g. Moser et al., 2015) for mitigation of first mirror degradation on ITER.

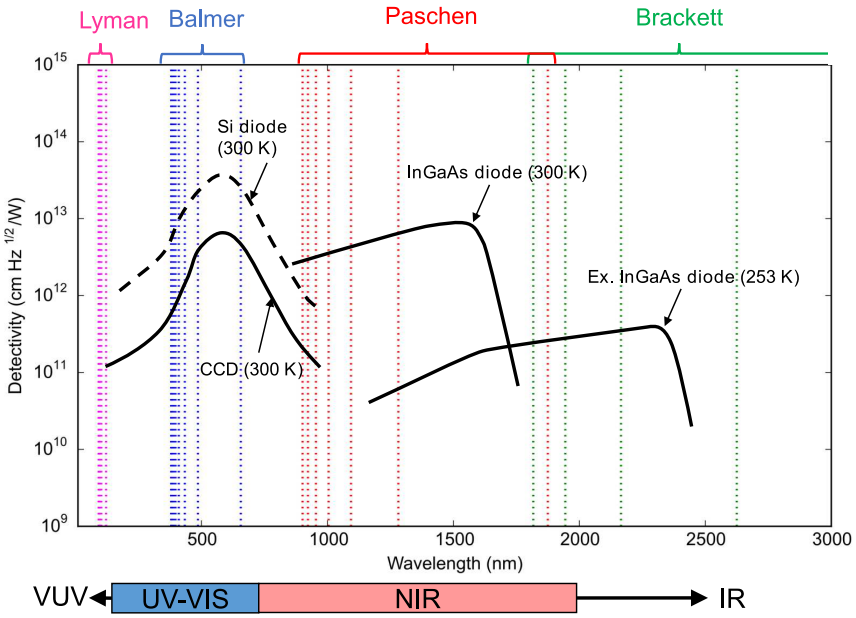

Figure 1.6: Approximate detectivity of common VIS and NIR detectors with overlaid central wavelength positions of the hydrogen Lyman, Balmer, Paschen and Brackett series lines. Data taken from (Hamamatsu Technical Information, 2011).

Figure 1.6 shows the spectral detectivity of the most common visible and near-infrared detectors in the context of the hydrogen Lyman, Balmer, Paschen and Brackett series spectral lines. Observational access to the Paschen series lines above the CCD sensitivity cut-off near 1000 nm is facilitated by the Indium Gallium Arsenide (InGaAs) photodiode which offers similar sensitivity (or detectivity) relative to CCDs and is commercially available in both linear and 2D sensor formats. The spectral sensitivity range can be shifted above 2000 nm with the extended InGaAs photodiode, although detectivity suffers as a result of an increased contribution of the internal generation of electron-hole pairs in the semiconductor depletion layer due to thermal transitions. This can be remedied to a large extent by cooling the detector.

At the time of writing, the range of commercially available NIR detector options is certainly smaller than that of scientific grade CCD and CMOS cameras. The spectral transmission curves of commonly used window and lens materials (e.g.,

BaF_2, BK7, SiO_2 (crystal quartz or fused silica), Al_2O_3 (Sapphire), CaF_2, and MgF_2) span both the VIS and NIR spectral range which allows for flexibility in VIS-NIR beam-splitter optical configurations viewing the plasma through the same line-of-sight. Thus both VIS and NIR spectroscopy share, to a large extent, commonalities in signal extraction techniques. To bring NIR spectroscopy to the level of maturity of VIS spectroscopy, more detailed investigation of the NIR spectral features in tokamak plasma observations is needed.

1.3 Thesis Outline

The main objective of the research presented in this thesis is the experimental characterisation of the VIS-NIR spectral region and evaluation of VIS-NIR spectroscopic diagnostics in the context of the measurement needs associated with tokamak exhaust physics, with particular emphasis on the hydrogen isotope Balmer and Paschen series measurements. A secondary objective concerns the identification of spectral features in the NIR region (900-1700 nm) for which, thus far, very few measurements have been obtained in magnetic confinement fusion experiments. Over the four year duration of the research project, the strategy for meeting the outlined objectives has largely conformed to the experimental campaign time lines and opportunities for diagnostic access to the MAST and JET tokamaks at the Culham Centre for Fusion Energy facilities. The work is a combination of instrument development and data interpretation underpinned by theoretical concepts in plasma spectroscopy and divertor physics.

Chapter 2 provides an overview of the fundamental theoretical aspects of plasma spectroscopy in order to motivate the interpretation of divertor plasma radiation. Key physics processes concerning plasma-wall interactions and divertor operating regimes are also discussed, followed by illustrative examples of continuum and hydrogen series line emission synthetic spectra under representative divertor plasma conditions.

Chapter 3 describes the VIS-NIR spectroscopic survey work carried out on the MAST tokamak. For this phase of the project a dedicated spectroscopy diagnostic was designed and implemented on MAST facilitating the accumulation of spectroscopic data during the M9 experimental campaign. The main features of the optical design and measurement capabilities of the VIS and NIR spectrometers are discussed along with the identification of features from observed spectra in the 350-800 nm and 900-1700 nm spectral regions. A more detailed investigation is presented on the

estimation of electron temperature using both the Balmer and Paschen series line intensities. These measurements are used in combination with a filtered imaging spectroscopy diagnostic to gain insight into the spatial distribution of temperature in the outer and inner divertor during a density ramp discharge.

Chapter 4 describes the enhanced capabilities of the JET mirror-linked divertor spectroscopy diagnostic resulting from an upgrade project in preparation for the 2013-2014 experimental campaign. The new system capabilities include the extension of the spectral range to the NIR to facilitate measurements of the Paschen series lines as well as two filtered imaging cameras with capabilities for resolving the transient edge-localised modes (ELMs) in the high-confinement (H-mode) operating regime. A critical assessment of a new VIS imaging spectrometer is also discussed with emphasis on its imaging quality improvements over the tradition Czerny-Turner design. The new system capabilities are evaluated using plasma measurements.

In Chapter 5 the properties of the Balmer and Paschen series spectral line profiles are investigated using a line profile model developed with emphasis on computation efficiency for batch least-squares fitting of experimental spectroscopic data. The model is used for estimating spatially resolved plasma density profiles across the inner and outer sections of the JET-ILW divertor. The results are compared with localised Langmuir probe measurements in order to highlight the importance of passive spectroscopy in providing estimates of plasma parameters in the detached divertor regime, in which Langmuir probe results are considered less reliable. Capabilities for estimating electron temperature in detached plasmas are also evaluated based on measurements from the mirror-linked divertor spectroscopy system. Finally, a computational model is used for a quantitative assessment of plasma parameter recovery from synthesised Balmer and Paschen spectral line profiles, the results of which highlight opportunities for future work in complementary VIS and NIR spectroscopic measurements.

Chapter 6 summarises the main findings and results and provides recommendations for future work.

Chapter 2

Characteristics of Divertor Plasma Radiation

In this chapter the principal theoretical concepts in plasma spectroscopy are reviewed. This is followed by establishing the relationships between the physical processes occurring in the divertor and the radiation emitted by the plasma species, thus leading to opportunities for inferring plasma properties using spectroscopic diagnostic techniques. The topics presented constitute the theoretical framework that will be used in subsequent chapters as the basis for the interpretation of measurements obtained from divertor spectroscopy diagnostics on the MAST and JET tokamaks.

2.1 Key Concepts in Plasma Spectroscopy

2.1.1 Measured Quantities

Laboratory plasmas are volumetric emitters. The local spectral emissivity ϵ_λ is usually given in units of W m^{-3} nm^{-1}, or by converting to ph s^{-1} m^{-3} nm^{-1} units using the photon energy $E = hc/\lambda$. Assuming the emissivity is isotropic in all directions, the emissivity per steradian is $\epsilon_\lambda/4\pi$. In plasma spectroscopy applications, photons emitted by the plasma are most often collected by means of a collimated or pseudo-collimated line-of-sight (LOS) which results in approximately uniform light collection efficiency along the LOS. If the plasma is optically thin (i.e., photons escape the plasma without being reabsorbed) the spectral radiance (often referred to as intensity in practice) corresponding to the integrated LOS measurement is

$$I_{\lambda}^{LOS} = \frac{1}{4\pi} \int_{LOS} \epsilon_{\lambda} dl \tag{2.1}$$

in units of W m^{-2} sr^{-1} nm^{-1} or ph s^{-1} m^{-2} sr^{-1} nm^{-1}. The spectral irradiance (ph s^{-1} m^{-2} nm^{-1}) at the detector plane can then be related to the spectral radiance of plasma emission by placing a source of known radiance in the path of the LOS, thus taking into account any losses along the optical train.

2.1.2 Atomic Processes in Plasmas

The population structure of atoms, ions and molecules depends on the interplay between collisional and radiative processes. It is important for the experimentalist to have an understanding of these processes in order to judiciously, and with some degree of confidence, employ atomic data for interpretation of experimental spectroscopic data.

Radiative Processes

All plasmas, including the astrophysical and laboratory varieties, emit radiation across the electromagnetic spectrum due to three main contributions:

- Bound-bound transitions: line radiation due to electronic transitions in atoms, ions and molecules.
- Free-free transitions: continuum emission due to Coulomb collisions of electrons with ions.
- Free-bound transitions: recombination continuum with edges due to recombining free electrons into bound atomic states.

In an optically thin plasma, radiation over most of the spectrum escapes the plasma volume, only approaching the black-body limit at long wavelengths. A brief summary of each process is given below:

- **Radiative transitions in ions and atoms**

  In bound-bound transitions, the probability of an electron to spontaneously radiatively decay from upper level p with energy $E(p)$ to a lower level q with energy $E(q)$ (with photon energy $h\nu = E(p) - E(q)$) is given by the Einstein A

coefficient (units s^{-1}). The local emissivity, or the rate of spontaneous decay for an excited population density $n_z(p)$ associated with a particular atom or ion, is then

$$\epsilon(p \to q) = A(p \to q) n_z(p) \tag{2.2}$$

in units of ph s^{-1} m^{-3}. Thus the excited level population densities are the observed quantities from spectral line intensity measurements, provided the local emissivity can be recovered from the line integrated spectra. The A coefficients are characteristic atomic constants typically given in terms of the absorption oscillator strength $f_{p,q}$, which is a measure of the probability for an atom to absorb a photon and make the transition $q + h\nu \to p$.

The types of radiative transitions include electric dipole, magnetic dipole and electric quadrupole transitions. The optically *allowed*, or observable, transitions are of the electric dipole type, and are characterised by large transition probabilities. For hydrogen-like ions, the allowed transition probabilities decrease with increasing principal quantum number; in other words, the lifetime of the higher excited levels increases. The magnetic dipole and electric quadrupole transitions are called *forbidden* transitions whose oscillator strengths are usually much weaker than the allowed transitions. The forbidden transitions can be neglected for light ions for which the LS-coupling scheme provides a good description of the atomic structure (Kunze, 2009, p. 91). For high-Z atoms and highly ionised atoms for which the spin-orbit interaction leads to a breakdown of LS-coupling, the probabilities of forbidden transitions can increase rapidly with nuclear charge. In the context of edge and divertor hydrogenic plasmas containing light intrinsic and extrinsic impurities, the contribution of the forbidden transitions to statistical populations of excited levels can generally be neglected. If no other radiative channel is possible, the upper excited level in a forbidden transition becomes *metastable* (Kunze, 2009, p. 97).

- **Radiative recombination**

  In the radiative recombination (free-bound) process, an electron with energy E_{kin} is captured into an excited state q of an ion resulting in the emission of a photon with energy $h\nu = E_{kin} + [E(\infty) - E(q)]$, where $E(\infty)$ is the ionisation limit energy of the recombined ion. The symbolic representation is given by

$$A^{(z+1)+}(g) + e^- \rightleftharpoons A^{z+}(q) + h\nu \tag{2.3}$$

where g denotes the ground state. The process results in continuum emission due to the continuous energy distribution of the free electrons but with discrete discontinuities attributed to the atomic structure of the bound states of the ion (see Figure 2.7). At equilibrium, the rate of the inverse process of photoionisation will be equal to the rate of radiative recombination according to the principle of detailed balance. Taking advantage of this, the standard approach for determining the radiative recombination cross-sections relies on calculations of photoionisation cross-sections instead. Based on initial work by Kramers (1923), Karzas and Latter (1961), for free electrons with a Maxwellian energy distribution, Kunze (2009, p. 100) gives the free-bound spectral emission coefficient for recombination of bare nuclei into hydrogen-like ions as

$$\begin{aligned}\epsilon_\lambda^{\mathrm{fb}}(\lambda) = \frac{64\sqrt{\pi}c(\alpha a_0)^3 E_R}{3\sqrt{3}} \times n_Z n_e Z^4 \left(\frac{E_R}{k_B T_e}\right)^{3/2} \frac{1}{\lambda^2} \exp\left(-\frac{hc}{\lambda k_B T_e}\right) \\ \times \sum_{n_q \geq n_{qmin}} \frac{1}{n_q^3} \exp\left(\frac{Z^2 E_R}{n_q^2 k_B T_e}\right) G_{n_q}^{\mathrm{bf}}(\lambda)\end{aligned} \tag{2.4}$$

where E_R is the Rydberg energy (i.e., the ionisation energy for hydrogen atom with infinite nuclear mass), a_0 is the Bohr radius, α is the fine structure constant, $G_{n_q}^{\mathrm{bf}}(\lambda)$ is the bound-free Gaunt factor associated with the principal quantum number n_q.

Although using E_R for the ionisation energy is typically sufficient, additional physical effects must be considered at high plasma densities; namely, the reduction in ionisation energy (or continuum lowering) due to the presence of Coulomb fields from other ions and electrons within the Debye radius, and a downshift of the photoionisation threshold due to the merging of Stark broadened spectral lines (Griem, 1997, p. 147). The net effect is a lowering in energy (increase in wavelength) and a smearing of the *ideal* distinct edges in the recombination continuum at the series limit corresponding to the capture of a zero-energy electron into each lower quantum level n_{qmin}.

- **Bremsstrahlung**

Bremmstrahlung (free-free) radiation corresponds quantum mechanically to transitions of free electrons in continuum states due to their deflections from Coulomb collisions with ions, resulting in a continuous spectrum. Extending the considerations in deriving the cross-sections from free electrons to bound states of an atom, and integrating only across levels above the ionisation limit of an atom or ion, Kunze (2009, p. 106) gives the free-free spectral emission coefficient as

$$\epsilon_{\lambda}^{\mathrm{ff}}(\lambda) = \frac{32\sqrt{\pi}c(\alpha a_0)^3 E_R}{3\sqrt{3}} \times n_e^2 Z_{\mathrm{eff}} \left(\frac{E_R}{k_B T_e}\right)^{1/2} \frac{1}{\lambda^2} \exp\left(-\frac{hc}{\lambda k_B T_e}\right) \overline{\xi}^{\mathrm{ff}}(\lambda) \quad (2.5)$$

following the procedure in Griem (1997, Chap. 5) and Cooper (1966), where $Z_{eff} = \frac{1}{n_e}\sum_{i,z} z_i^2 n_z^i$ is the effective charge due to the presence of hydrogenic ion species and concentrations of impurity species n_z in different ionisation stages (i). For a pure hydrogenic plasma $Z_{eff} = 1$. The values of the averaged free-free Bieberman (Gaunt) factor $\overline{\xi}^{\mathrm{ff}}(\lambda)$ are usually close to unity, and given for completeness if higher accuracy is desired.

Collisional Processes

In optically thin plasmas in which radiative transport is considered negligible, the bound excited levels of atoms, ions and molecules are populated by collisions with the surrounding charged and/or neutral particles. The strength of each process is characterised by the cross section σ, in units of m^2, such that the rate of a process involving two species with densities n_1 and n_2 for a particular transition from $q \rightarrow p$ is

$$\left.\frac{dn_1(p)}{dt}\right|_{q\rightarrow p} = n_1 n_2 \int_{\boldsymbol{v_1},\boldsymbol{v_2}} \sigma(v) v f_1(v_1) f_2(v_2)\ \mathrm{d}^3\boldsymbol{v_1}\mathrm{d}^3\boldsymbol{v_2} \quad (2.6)$$

where the integral over the velocity distribution functions $f(v_1)$ and $f(v_2)$ is called the rate coefficient, $<\sigma v>$ in units of $\mathrm{m}^3\mathrm{s}^{-1}$ for binary collisions. In electron collisions, which constitute the dominant processes in controlling the spectroscopic properties of atoms and ions in a plasma, the target species can be considered stationary due to the relatively high electron velocities. The collision strength Ω, often preferred in theoretical calculations, is a convenient dimensionless form of the cross-section which has the advantage of being symmetrical with respect to the forward

and inverse processes. An overview of the theoretical methods and approximations associated with collisional processes is given in introductory plasma spectroscopy texts (e.g. Griem, 1997; Fujimoto, 2004; Kunze, 2009). A brief summary of the main collisional processes and their importance in the tokamak plasma context is provided below:

- **Electron impact collisional excitation and deexcitation**

  $e^- + A^{z+}(q) \rightleftharpoons A^{z+}(p) + e^-$

  This is the most important of the collisional processes, in which the energy of the incident electron must be higher than the excitation threshold for a particular bound-bound transition $q \rightarrow p$ of the target species. In the reverse collisional deexcitation process, the scattered electron gains the equivalent transition energy. In thermodynamic equilibrium the forward and reverse rates are equal according to the principle of detailed balance. Of importance to plasma spectroscopy is the cross-section functional dependence on electron energy which tends to exhibit a particular energy dependence for certain transitions. The calculations are also more difficult than radiative transition probabilities since the Coulomb interaction between the free and bound electron must be considered. Experimental determination of rate coefficients is also possible using spectral line emission measurements in well diagnosed plasmas with known temperatures and a well established excitation channel. Of particular importance for interpretation of spectroscopic measurements are cross-sections for redistribution between neighbouring excited levels by electron collisions which influence the statistical populations. In collisions with molecules, the most common process is that of *collisional dissociative excitation* which plays a role in tokamak edge and divertor plasmas in breaking up cold H_2 molecules into ground-state and possibly excited neutrals, depending on the fragmentation channel.

- **Electron impact ionisation and three body recombination**

  $e^- + A^{z+}(q) \rightleftharpoons A^{(z+1)+}(g) + e^- + e^-$

  Atoms, ions and molecules are directly ionised through electron impact from the ground state and also from excited states to the ground state of the next ionisation stage, liberating a bound electron in the process. The forward process of ionisation can be regarded as the smooth transition of the excitation cross-section attributed to bound states with negative energies to ionisation

cross-sections resulting in an ejected continuum electron with positive kinetic energy. Ionisation cross sections increase strongly with the principle quantum number of the target species. The reverse process is *three-body recombination* for which cross-section calculations are more complicated as the reaction involves two electrons. In thermodynamic equilibrium, according to the principle of detailed balance, the ionisation and three-body recombination rates must be equal:

$$S(p)n_{z-1}(p)n_e = \alpha(p)n_z(1)n_e^2 \tag{2.7}$$

where $S(p)$ and $\alpha(p)$ are the ionisation and three-body recombination rate coefficients, respectively, for a bound electron in an excited level p. In tokamak edge and divertor plasmas the three-body recombination process plays an important role as a volumetric ion sink in high density and low temperature plasma due to the n_e^2 dependence. In contrast to radiative recombination in which ions recombine primarily into the ground state, three-body recombination is preferential to the excited states.

- **Dielectronic recombination and autoionisation**

  $e^- + A^{(z+1)+}(q) \rightleftharpoons A^{z+}(p^*) \rightarrow A^{z+}(p) + h\nu$

  Dielectronic recombination occurs when an electron is resonantly captured (i.e., only electrons with a specific kinetic energy are captured) by the $A^{(z+1)+}(q)$ ion and excites a second electron in the process resulting in a double excited state $A^{z+}(p^*)$ ion. The ion in this doubly excited state will then either autoionise (also called Auger breakup) or will radiatively decay to a lower singly excited level of the recombined ion $A^{z+}(p)$ producing a satellite line whose energy is slightly lower than the energy associated with the normal transition. Dielectronic capture and autoionisation rates are again equal at thermal equilibrium. The rate coefficients of these processes can significantly influence the statistical populations of excited levels, particularly for ions with more than two electron (e.g., lithium-like, beryllium-like) (Fujimoto, 2004, p. 68).

- **Charge exchange**

  $A + B^{z+} \rightarrow A^{z+} + B^{(z-1)+}$

  In charge exchange processes, a target ion captures an electron from a collision with an atom. The captured electron may not be in the ground state and the

process is considered to be resonant such that charge exchange into one particular level has a high cross-section relative to neighbouring levels. In tokamaks this process is important in the charge transfer from energetic neutral heating beams to plasma impurity atoms and forms the basis of charge exchange and beam emission spectroscopy. In edge and divertor plasmas, resonant charge exchange between thermal hydrogenic ions and atoms ($H^+ + H \rightarrow H + H^+$) plays an important role in wall erosion by fast charge exchange neutrals as well as the momentum balance in the divertor especially at low plasma temperatures. In the approximate picture the ionisation energy of the recombined hydrogenic ion should be equal to the ionisation energy of the colliding hydrogenic atom (i.e., the recombined hydrogenic ions will be in the ground state for the $H^+ + H \rightarrow H + H^+$ reaction) (Kunze, 2009, p. 132) .

- **Ion and atom collisions**

  The large mass difference between electrons and ions (ion being $10^3 - 10^4$ times heavier) requires ion energies to be larger by roughly the same factor in order for ion impact collisions to have a similar effect as an electron impact collision. Therefore ion impact cross-sections are comparable to electron impact cross-sections when ion temperatures are three orders of magnitude or so higher than the corresponding electron temperatures. However, at low temperatures consistent with the conditions in edge and divertor tokamak plasmas, ion collisions can be effective for transitions between closely lying levels, for instance, in redistributing the excited level populations between different l levels with the same principle quantum number n.

- **Molecular assisted recombination**

  The presence of molecular hydrogen in tokamak divertor plasmas can influence the ionisation/recombination balance through a process known as molecular assisted recombination (MAR). One possible channel is through the production of negative ions from electron impact with vibrationally excited H_2 molecules and subsequent charge exchange with plasma ions resulting in ground state and excited state ($n = 3, 4$) neutrals (Post, 1995):

  $H_2(v \geq 0) + e^- \rightarrow H^- + H$, $H^- + H^+ \rightarrow H + H(n = 3)$

  Although the MAR mechanism is thought to be important in addition to the conventional radiative and three-body recombination channels, direct experimental evidence has not been widely observed (e.g Lumma et al., 1997;

Krasheninnikov et al., 1997). In one study (Kubo et al., 2005) on the JT-60U tokamak the influence of MAR on the total recombination rate of plasma ions was estimated to be as important as the $H^+ + e^-$ recombination pathway.

2.1.3 Population Kinetics

Interpretation of quantitative spectroscopic measurements relies on establishing relationships between the recorded spectra and the atomic processes that govern the intensity distribution and spectral profiles of discrete and continuum features.

In the case of line radiation, the energy levels of electronic transitions are not infinitely sharp, but are modified by an energy (or wavelength) distribution function resulting from broadening and splitting mechanisms. Furthermore, the problem of intensity distribution across different line series reduces to that of the population densities of atoms and ions and their excited states, including the ground and metastable states which constitute the dominant driving populations. This problem is made simpler by making the assumption that the plasma is optically thin. This assumption is certainly valid over most of the spectrum in the temperature range of few eV to tens of keV and density range $10^{18} - 10^{21}$ m^{-3} in magnetically confined plasmas. However, the optical depth of Ly-α (H 2→1) and Ly-β (H 3→1) can be significant in some divertor plasmas (e.g. Maggi et al., 1999; Reiter et al., 2003), notably in the formation of the MARFE phenomenon (see Section 2.2.2), and is anticipated to play an important role in the ITER divertor (Stratton et al., 2008).

The local population of an atomic state p of ions of charge z is given by the coupled rate equation

$$\frac{\mathrm{d}n_z(p)}{\mathrm{d}t} = -R_z(p \rightarrow) + R_z(\rightarrow p) + \Gamma_z(p) \tag{2.8}$$

where $R_z(p \rightarrow)$ and $R_z(\rightarrow p)$ represent the sums of all collisional and radiative rates out of and into the level p, respectively, and $\Gamma_z(p)$ is the flux of $n_z(p)$ ions due to convective and diffusive transport. A general solution to this rate equation is not possible due to the large number of transitions and insufficient knowledge of the corresponding rate coefficients. A common practical approach involves reducing the total number of transitions, and therefore rate equations, and only considering the dominant processes occurring at time scales relevant to the problem.

The following section provides a brief overview of the thermodynamic relations, collisional and radiative processes and population models necessary to relate the line

radiation to the relevant atomic processes that drive the excited state populations in the context of tokamak plasmas, with emphasis on the conditions relevant to divertor plasmas. More detailed discussion is provided in plasma spectroscopy texts (e.g. Griem, 1997; Fujimoto, 2004).

Thermodynamic Equilibrium Relations

It is conceptually instructive to first consider a plasma and its radiation field in thermodynamic equilibrium before modifying the equilibrium assumptions to reflect the nature of the tokamak plasma radiation field in which emitted photons usually readily escape the plasma.

The physical state of a plasma enclosed by a fictitious box with walls at temperature T will be completely determined by T with the energy (velocity) distribution of each particle species given by the Maxwell-Boltzmann distribution, neglecting quantum effects at very high electron densities. The population densities of ions with upper level p and lower level q are then given by the rate equation

$$\frac{\mathrm{d}n(p)}{\mathrm{d}t} = n(q)B(q \to p)I_\nu - n(p)[A(p \to q) + B(p \to q)I_\nu] \tag{2.9}$$

where I_ν [$\mathrm{W\,m^{-2}\,sr^{-1}\,s}$] is the spectral radiance of the radiation field at the transition frequency $\nu = E(q \to p)/h$ and is considered to be isotropic. The rates of pairs of inverse processes $A(p \to q)$, $B(p \to q)$ are Einstein's A and B coefficients which represent deexcitation by spontaneous radiative decay and radiative decay by induced emission, respectively, and are related by

$$g(p)B(p \to q) = g(q)B(q \to p) \tag{2.10}$$

$$A(p \to q) = \frac{2h\nu^3}{c^2}B(p \to q) \tag{2.11}$$

according to the principle of detailed balance, where g denotes the statistical weight of each level. Under steady-state conditions the rate equation reduces to

$$I_\nu = \frac{n(p)A(p \to q)}{n(q)B(q \to p) - n(p)B(p \to q)}. \tag{2.12}$$

For a system in thermodynamic equilibrium the excited state populations for a given ion are described by the Boltzmann distribution and the ratios of the upper and lower populations is therefore

$$\begin{aligned}\frac{n(p)}{n(q)} &= \frac{g(p)}{g(q)}\exp\left(-\frac{E(p\rightarrow q)}{k_BT}\right)\\ &= \frac{g(p)}{g(q)}\exp\left(-\frac{h\nu}{k_BT}\right).\end{aligned} \tag{2.13}$$

Substituting equations 2.13 and

$$I_\nu d\nu = \frac{2h\nu^3}{c^2}\frac{1}{\exp(h\nu/k_BT)-1}d\nu \text{ [W m}^{-2}\text{ sr}^{-1}\text{]} \tag{2.14}$$

which is called Planck's distribution, or the black-body radiation. This distribution can be integrated over the entire spectral range to obtain the total radiance over all transition frequencies.

Complete thermodynamic equilibrium can never be reached in tokamak plasmas due to escaping photons out of the plasma leading to a radiation field in the plasma volume that is significantly below the black-body radiation distribution. However, at sufficiently high densities electron collisional processes can predominate over radiative processes to the extent that the distribution of steady-state population densities can be described according to the Boltzmann distribution (eqn. 2.13). By extending the Boltzmann distribution to continuum states of free electrons and integrating across all electron energies (see Fujimoto, 2004, p. 23), the population density of an excited level q of an ion of charge z can be connected to the ground state density of the next ionisation state, yielding the Saha equation (also referred to as the Saha-Boltzmann distribution)

$$\frac{n_{z+1}(g)n_e}{n_z(q)} = 2\frac{g_{z+1}(g)}{g_z(q)}\left(\frac{m_ek_BT}{2\pi\hbar^2}\right)^{3/2}\exp\left(-\frac{E_{z,q\infty}}{k_BT}\right) \tag{2.15}$$

where $E_{z,q\infty}$ is the ionisation energy of level q.

The conditions for which the Boltzmann and Saha relations describe the population densities and ionisation balance represent *local thermodynamic equilibrium* (LTE), for which a Maxwellian energy distribution of the electrons is a prerequisite (Kunze, 2009, p. 140). It should be noted that the Saha equation is density dependent (i.e., density links ion abundances), but excited state populations within the

same ionisation stage are density independent via the Boltzmann relation. For LTE conditions to apply to transient and spatially inhomogeneous plasmas, time scales for reaching steady state must be considered as well as the diffusion rate compared to the characteristic scale lengths of plasma parameter variations.

In general only a subset of excited levels can be considered to be in LTE. These are typically the higher levels, separated by smaller energy gaps, which remain coupled by collisions even as lower levels start to deviate from the Saha-Boltzmann distribution with decreasing density. Griem (1997, p. 215) defined a threshold level with principle quantum number n_{th}, known as the thermal limit, for which the collisional rate is ten times the radiative decay rate and thus all levels above this limit are considered to be in LTE. Since the excited level structure of the higher levels resembles that of one electron systems, the concept of the thermal limit can be applied more generally to non hydrogen-like systems and is called *partial local thermodynamic equilibrium*, or PLTE. Detailed investigations of hydrogen-like ions by Fujimoto and McWhirter (1990) with nuclear charge $Z = z + 1$ yielded an expression for the thermal limit as

$$n_{th} \approx 590(z+1)^{0.73} n_e^{-0.133} \left(k_B T_e\right)^{0.1} \tag{2.16}$$

with n_e and $k_B T_e$ in units of m^{-3} and eV, respectively.

At very low electron densities (e.g., $n_e \lesssim 10^{17}\,\mathrm{m}^{-3}$ for hydrogen levels $p \lesssim 5$), the excited state population structure can be estimated using the *coronal equilibrium* approximation. In this low density regime, collisional processes become very weak compared with radiative processes. The dominant populating mechanism is by electron collisional excitation from the ground state since the population densities of all excited levels are very low in comparison to the ground state of an ion. Collisional cross-coupling of levels is negligible due to relatively few electron-impact events, and thus the excited states are de-populated via spontaneous radiative decay back to the ground state, either directly or indirectly. If collisional excitation from metastable level populations can be ignored, the population density $n(p)$, in steady-state with the ground state ion population $n(g)$, can be written as

$$\frac{n_z(p)}{n_z(g)} = \frac{n_e C_z(g \to p)}{A_z(p \to)} \ll 1 \tag{2.17}$$

where $A_z(p \to) = \sum_{q<p} A(p \to q)$ is the sum of radiative transition probabilities from level p to all lower levels and $C_z(g \to p)$ is the electron collisional excitation rate coefficient from the ground state.

The excited state populations (within an ionisation stage) in the LTE regime are linked to electron temperature according by the Boltzmann relation and are independent of the electron density. In contrast, in the coronal regime the excited state populations depend on density through the frequency of electron collisions with ground state ions. Since the spontaneous radiative transition probabilities are constants, the line emissivity is then given by

$$\epsilon_z(p \rightarrow q) = \frac{A_z(p \rightarrow q)}{A_z(p \rightarrow)} n_e C_z(g \rightarrow p) n_z(g) \quad [\mathrm{ph\,s^{-1}\,m^{-3}}] \tag{2.18}$$

and is thus only linked to temperature through the collisional excitation rate coefficient. Additional populating mechanisms, including the radiative cascade contribution and collisional excitation from metastable populations, can modify the estimated emission rate depending on their magnitude relative to the strict coronal equilibrium assumptions.

The validity of the coronal approximation does not hold for higher levels for which collisional cross-coupling competes with radiative decay. The density range for which all levels up to $n = 6$ can be considered to be in coronal equilibrium is obtained by McWhirter (1965) for hydrogen-like ions as

$$n_e \leq 6 \times 10^{16} (z+1)^6 k_B T_e \exp\left(\frac{0.1(z+1)^2}{k_B T_e}\right) \quad [\mathrm{m^{-3}}] \tag{2.19}$$

For example, for a temperature range $10 \leq T_e \leq 100$ eV, the populations of the first six principle quantum number states of hydrogen can be estimated using the coronal approximations for densities in the range $3 \times 10^{17} \leq n_e \leq 6 \times 10^{18}$ $\mathrm{m^{-3}}$. Since tokamak divertor plasma densities can be significantly higher, the coronal assumptions are therefore not satisfied, although for heavier hydrogen-like ions they may be valid as a consequence of the $(z+1)^6$ scaling.

Collisional-Radiative Regime

The population structures and charge state distributions of the majority hydrogenic species and impurity ion content at density and temperature conditions typical of tokamak plasmas often fall between the LTE and coronal regimes. Under such conditions, it is necessary to consider the cross-coupling between levels due to collisional processes, in addition to excitation from the ground state, recombination from the

parent ion and direct and cascading radiative decay. This region in density and temperature space where cross-coupling becomes important is known as the *collisional-radiative* (CR) regime. Quantitative analysis of plasma spectroscopy measurements is underpinned by models which are capable of describing the population structure in the CR regime with sufficient accuracy commensurate with observational and plasma parameter variation time scales. Such models, in turn, rely on available collections of fundamental and derived atomic data capturing the relevant collisional and radiative processes.

The basis for collisional-radiative theory was first outlined by Bates et al. (1962) and extended by many others, notably by McWhirter and Summers (1984) in the development of the *generalised collisional radiative* (GCR) theory, which formed the basis of the practical implementation of GCR as part of the ADAS Project (Summers, 2004). This section provides a brief overview of the general approach to collisional-radiative modelling as a basis for defining the diagnostically useful deliverables used in this thesis for the analysis of hydrogenic line series and light impurity line spectra. The formulation follows that of the calculation methods used within the ADAS Project, and is described in more detail in the ADAS Manual (Summers, 2004) and related publications (e.g. Summers et al., 2002, 2006; O'Mullane et al., 2006).

The challenge of collisional-radiative modelling rests on the evaluation of the excited state populations of the atomic and ionic plasma constituents as well as the densities, or fractional abundances, of the different ion charge states. This task is complicated by the nature of tokamak plasmas, namely: steep temperature and density gradients across the core plasma to the edge, SOL and divertor regions; transient events due to ELMs and other MHD instabilities; and the variety of intrinsic and extrinsic atoms, ions and molecules that participate in collisional and radiative processes. The modelling approach can be somewhat simplified, however, by consideration of the relaxation times of the various states of plasma species in relation to the plasma development time scales and characteristic scale lengths associated with particle transport. The excited states of an atom or ion can be classified as either ordinary excited states, ground states and metastable excited states. Since the radiative decay from metastables states only occurs via forbidden transitions and thus much longer lifetimes compared to ordinary excited states, it is appropriate to group the ground and metastable levels together. In the CR regime, the redistribution of the ordinary excited states occurs through the competition of collisional and radiative processes. Relaxation times of ordinary excited states through radiative

decay are of the order of the radiative transition probabilibites, $\tau_o \leq A^{-1}$, while the relaxation times associated with redistribution of ordinary levels via electron (an to a lesser degree ion) collisions rely on the thermalisation time constant of the free electrons, τ_{e-e}, generally considered to be short such that $\tau_{e-e} < \tau_o$. The redistribution of the ground and metastable states occurs via ionisation and recombination processes, with typical lifetimes in magnetically confined plasmas of the order of the plasma diffusion rates (Summers et al., 2006). Thus, the relaxation times of the ground state ions and metastables, τ_g and τ_m, respectively, are comparable to that of τ_{plasma}, which encompasses characteristic diffusion rates and time scales of transient plasma processes. In the overall picture, the relaxation times are then ordered as

$$\tau_{plasma} \sim \tau_g \sim \tau_m \gg \tau_o \gg \tau_{e-e} \tag{2.20}$$

These considerations lead to a decoupling in the treatment of (i) the dominant ground and metastable density redistribution driven by transport, and (ii) that of the ordinary excited state population structure which is considered to be in *quasi-equilibrium* (also referred to as the *quasi-static approximation*) with the ground and metastable populations. The practical implications for the plasma spectroscopist are that the excited level populations, which describe the observed spectral line intensities, depend only on the local conditions of the plasma electron and ion densities and temperatures if radiation transport can be ignored (i.e., assuming an optically thin plasma).

The rate equation for a particular excited level p balances the relevant populating and depopulating collisional-radiative mechanisms such that the rate of change of $n(p)$ is given by

$$\begin{aligned}\frac{\mathrm{d}}{\mathrm{d}t}n(p) = &\sum_{q<p} C(q \rightarrow p) n_e n(q) \\ &- \left[\left\{ \sum_{q<p} F(p \rightarrow q) + \sum_{q>p} C(p \rightarrow q) + S(p) \right\} n_e + \sum_{q<p} A(q \rightarrow p) \right] n(p) \\ &+ \sum_{q>p} \left[F(q \rightarrow p) n_e + A(q \rightarrow p) \right] n(q) \\ &+ \left[\alpha^D(p) + \alpha^R(p) + \alpha^T(p) n_e + \frac{n_H}{n_e} \alpha^{CX}(p) \right] n_e n_{z+1}\end{aligned} \tag{2.21}$$

where the summations over $q < p$ and $q > p$ refer to the excited levels that are energetically below and above the excited level p under consideration, respectively. In

the above equation only the electron impact collisional processes are considered for clarity, where $C(p \rightarrow q)$ and $F(p \rightarrow q)$ are the collisional excitation and deexcitation rate coefficients, respectively, and $S(p)$ is the collisional ionisation rate coefficient. The first line represents the excitation flux (units of $\mathrm{m}^{-3}\ \mathrm{s}^{-1}$) into level p from lower lying levels, the second line is the depopulating flux out of level p, the third line is the populating flux from levels lying above p and the fourth line is the direct recombination contributions with α^D, α^R, α^T, and α^{CX} denoting the rate coefficients for dielectronic, radiative, three-body and charge exchange recombination, respectively.

In quasi-equilibrium, the population density $n(p)$ can be approximated as constant ($\mathrm{d}n(p)/\mathrm{d}t = 0$) for a given set of plasma conditions. Thus the set of differential rate equations for the ordinary excited states reduces to a set of coupled linear equations which can be solved using matrix methods. Practical considerations with respect to handling large numbers of balance equations (i.e., level structure resolution) must be addressed. One convenient approach consists of grouping the excited levels into: (i) the set of low-lying levels described at high resolution (e.g., the level structure of the atom/ion detailed at the LS or LSJ resolution) which includes the most relevant transitions for spectroscopic applications; and (ii) the set of highly excited levels (bundle-n levels in the GCR scheme) which account for cascading and redistributing processes as well as step-wise ionisation and recombination (Maggi, 1997). Details on the practical implementation of such classifications in the ADAS set of codes, as well as a description of the formulation of the matrix coefficients, can be found in the ADAS manual (Summers, 2004) and the overview of the GCR model for light elements in (Summers et al., 2006).

Diagnostically Useful Derived Atomic Data

Fundamental to the interpretation of spectral line emission measurements is the use of derived atomic data which relates the line intensity to the excited state population densities. For a given set of plasma density and temperature conditions, it is possible to express the emissivity (in units ph s^{-1} m^{-3}) for a given transition $p \rightarrow q$ in terms of the photon emissivity coefficients (PEC) that result from rearranging of the terms in eqn. 2.21, such that

$$\begin{aligned}\epsilon(p \rightarrow q) = &\sum_{\sigma} PEC^{(exc)}(p \rightarrow q, \sigma) n_e n_\sigma^{z+} + \sum_{\rho} PEC^{(rec)}(p \rightarrow q, \rho) n_e n_\rho^{z+1} + \\ &\sum_{\rho} PEC^{(CX)}(p \rightarrow q, \rho) n_e n_\rho^{z+1},\end{aligned} \tag{2.22}$$

where PEC^{exc}, PEC^{rec} and PEC^{CX} are the separate effective emissivity contributions attributed to collisional excitation, recombination and charge exchange processes for each metastable level denoted by σ for the ion itself and ρ for the parent ion. The scope of the included processes depends on the underlying data set. For example, in the ADAS ADF15 class which holds collections of PEC data for various iso-electronic sequences, the ADF04 specific ion fundamental data sets serve as input, the scope of which can vary depending on the available data for a particular species.

In practice the densities of the colliding species may be estimated by transport equations in order to determine the contributions from each term in eqn. 2.22, but it is often the case that one contribution predominates over the other such that the PEC data can be used directly in the interpretation of relative line intensities. For instance, for hydrogenic species the excitation component is typically much larger than recombination at high electron temperatures, whereas recombination predominates at $T_e < 1.5$ eV for most levels (see Section 2.3.1). $PECs$ are also useful in comparing spectroscopic data to spatially resolved outputs from transport models which yield the local densities of the relevant colliding species in addition to local plasma conditions.

The dominant driving populations in the GCR picture are the ground state and metastable levels which are assumed to be significantly populated with respect to the ordinary excited level populations. The ionisation balance of hydrogenic and impurity species in a plasma can be described with effective ionisation, S_{CD}, and recombination, α_{CD}, derived rate coefficients which are functions of electron temperature and density. The CD (collisional-dielectronic) subscript refers to the combination of direct and step-wise (cascade) collisional and ionisation/recombination and dielectronic recombination processes included in the calculation. Although these derived quantities are of primary interest in describing the source and sink terms in dynamic transport models, the coefficients can also be applied directly to spectroscopic line emission observations in fusion diagnostic applications. For instance, the *ionisations per photon* ratio (SXB) relates the $PEC^{(exc)}$ and S_{CD} coefficients to yield the number of ionisation events from a particular parent ion to the number of emitted photons for a particular transition $p \rightarrow q$. Assuming that the ground states are the dominant driving populations (i.e., neglecting metastable levels) the SXB is defined as

$$SXB(p \rightarrow q) = \frac{S_{CD}}{PEC^{(exc)}(p \rightarrow q)}, \tag{2.23}$$

and is given for a specific spectral line of an ion. The inverse of the SXB coefficient is known as the *photon efficiency*. These quantities are useful for relating the line integrated spectral line intensity $I^{LOS}(p \rightarrow q)$ (ph s^{-1} m^{-2} sr^{-1}) to the influx Γ (m^{-2} s^{-1}) of an ion species into the plasma from a surface as the element "burns through" to the next ionisation stage along the spectroscopic line of sight, such that

$$\Gamma = 4\pi I^{LOS}(p \rightarrow q)\ SXB(p \rightarrow q), \tag{2.24}$$

with the assumption that the population of excited level p is due mainly to excitation processes. The formulation and application of the SXB is described in detail in (Behringer et al., 1989), and additional applications in (e.g Stamp et al., 1987; Sugie et al., 1999). The ADAS class ADF13 contains collections of SXB data sets which are closely related, according to eqn. 2.23, to the ADF15 class which contains collections of PEC data sets, and to the ADF11 class which contains, among other derived quantities, collections of the S_{CD} coefficients (Summers, 2004). SXB coefficients are employed in Section 2.3.1 for calculating the hydrogen Balmer and Paschen series line spectrum and in estimating the hydrogen spectral line radiance in the JET-ILW divertor in Chapter 4.

2.1.4 Line Broadening Mechanisms

Atomic energy levels and the radiative transitions between them are not infinitely sharp and therefore must be described by an appropriate energy (wavelength) distribution. At the very least the spectral line is naturally broadened due to the uncertainty associated with the lifetime of an excited state, which connects the resulting uncertainty in the energy through the Heisenberg uncertainty principle. This effect, however, is typically negligible in comparison to broadening from temperature and density effects in laboratory plasma conditions. In addition, the presence of a magnetic field used to confine charged particles in a tokamak results in lifting of the degeneracy in the magnetic quantum number and thus the splitting of energy levels of atomic systems. Standard plasma spectroscopy textbooks give an overview of the line broadening theory (e.g. Griem, 1997, 1974; Sobelman et al., 1981), including a useful summary to the experimental spectroscopist by Kunze (2009). This

section outlines the main considerations associated with the physical broadening mechanisms which will be employed in the interpretation of spectral line shapes in Chapter 5. It should be noted that, in the practical sense, an observed spectral line profile is the result of the convolution of the intrinsic line shape with the instrumental transfer function of the spectrometer. The spectral width of the instrumental broadening component thus places a limitation on the feature resolution of the line profile.

Temperature Broadening

The thermal motion of an ensemble of atomic or ionic emitters results in a Doppler shift in the frequency of the emitted photons due to their projected velocity components in the direction of the observational line-of-sight. In the case of a Maxwellian energy distribution associated with a temperature T_i of the emitting species the monochromatic spectral line is broadened with the line shape given by a Gaussian with a full width half maximum (FWHM)

$$\frac{\Delta\lambda^{\mathrm{G}}_{1/2}}{\lambda_{p\rightarrow q}} = \sqrt{8\ln 2\frac{k_B T_i}{m_i c^2}} \tag{2.25}$$

where m_i is the mass of the emitter. In the case of a non-Maxwellian velocity distribution, the profile will mirror the velocity distribution in the line-of-sight direction.

Density Broadening

Energy levels of an emitter are influenced by the presence of surrounding atoms, molecules, ions and electrons resulting in the broadening and shifting of spectral lines. The broadening effect is proportional to the particle densities and can therefore be used as a measure of those densities, provided a suitable relationship between density and the broadened profile can be derived. Perturbations by neutral atoms and molecules are generally negligible compared to perturbations by collisions with charged particles, resulting in a shift in energies through the Stark effect. Given the large number of particles within the plasma and their long range Coulomb interactions with the emitter, the broadening process is complicated and a general solution to the time-dependent Schrodinger equation is impossible. However, due to the large difference in ion and electron velocities, a separate treatment of the fast and slow moving particles and their effect on the emitter is considered. In the *impact approximation* (Lorentz, 1906), collisions of the emitter with relatively

fast moving electrons (perturbers) can be treated as statistically independent and each one accounted for individually. If the collisions are random the profile will be Lorentzian. At the other extreme with very slow moving ion perturbers, the dynamic effects can be avoided altogether and the electric field at the radiator location can be considered constant over the lifetime of the emission process. This is known as the *quasi-static approximation*. Since the field is characterised by a distribution, the splitting of each perturbed Stark component is smeared and gives a continuous line profile. The probability distribution of the ion microfield is denoted as $H(\beta)$ where $\beta = F/F_0$ is the reduced field strength and F_0 is the normal field strength. The first calculation was carried out by Holtsmark (1919) in the ideal gas limit with the distribution derived as

$$H(\beta) = \frac{2}{\pi}\beta \int_0^\infty \mathrm{d}x \, \sin(\beta x) \exp(-x^{3/2}) \tag{2.26}$$

and the normal field strength

$$F_0 \approx 2.603 \, \frac{ze}{4\pi\epsilon_0} n_z^{2/3} \tag{2.27}$$

The microfield distribution $H(\beta)$ represents the probability that the emitter will experience a certain electric microfield F due to the presence of the surrounding ions. Hooper (1968) improved the field strength distribution by considering ion-ion correlations and Debye shielding by the electrons.

For hydrogen atoms the degenerate energy levels are subjected to the linear Stark effect. The resulting energy shifts of the Stark components by the ion microfields are usually much larger than the inverse of a typical ion-atom collision time. Modelling the ion influence using the quasi-static approximation is therefore often appropriate. The typical approach in obtaining the line profile usually proceeds by calculating the set of Stark components due to a constant electric field set up by the stationary ions. These components are then broadened by a Lorentzian profile due to electron collisions within the impact approximation. The electron broadened set of lines is then convolved with the appropriate ion microfield distribution function within the quasi-static approximation, yielding the total smeared profile. Following this procedure, approximate line widths of hydrogen atoms and hydrogen-like ions can be obtained. Kunze (2009, p. 164) gives the FWHM of a line from a transition $p \to q$ using the Holtsmark microfield distribution as

$$\frac{\Delta_{1/2}}{\lambda_{p\to q}} \approx 8.4 \times 10^{-22} \lambda_{p\to q}(n_p^2 - n_q^2)\frac{z}{Z}{n_z}^{2/3} \tag{2.28}$$

where n_p and n_q are the principal quantum numbers associated with the transition $p \to q$, Z is the nuclear charge of the emitting atom and z is the charge of the perturbing ions, $\lambda_{p\to q}$ is in units of nm and n_z in units of m^{-3}. This expression is particularly useful for fitting the line profiles of high-n lines in the hydrogen series where electron broadening can predominate and the profile can be approximated by a Lorentzian. In the lower-n lines (e.g., Ba/Pa-α, β, γ) the influence of ion microfield broadening becomes important and the assumption of static ions can underestimate the extent of broadening near the line center (Stehlé and Hutcheon, 1999). An improvement on the quasi-static approximation is made in the Model Microfield Method (Brissaud and Frisch, 1971) by introducing ion dynamics where the resultant microfield fluctuations are treated as a statistical process following Poisson statistics and employing Hooper's microfield distribution functions. A widely used set of extended tabulations for hydrogen Lyman, Balmer, Paschen and Brackett series lines for a pure hydrogen plamsa is based on the work by Stehlé and Hutcheon (1999) following the MMM formalism. Since the ions are considered dynamic, the tabulations include a temperature dependence and span an electron density and temperature range of $10^{16} < n_e < 10^{25}$ m^{-3} and $0.22 < T_e < 112$ eV, respectively. The total profile from the line center to the line wings is thus provided, from which the line FWHM can be obtained and compared to observed line profiles, provided the pure Stark broadened contribution can be isolated in measured spectra. In Section 5.1.1, a parametrisation of the Stehlé and Hutcheon (1999) MMM tabulations is described, which facilitates efficient implementation of the dataset into least-squares Stark broadening fitting routines used for inferring plasma electron density from observed spectra.

Magnetic Field Effects

The magnetic field used to confine charged particles in tokamak plasmas causes Zeeman splitting of spectral lines due to the interaction of the magnetic moment $\boldsymbol{\mu}$ associated with the emitting atom or ion with magnetic field $\mathbf{B}$ and an interaction energy given by

$$\begin{aligned} E^{mag} &= \boldsymbol{\mu} \cdot \mathbf{B} \\ &= (\boldsymbol{\mu}_L + \boldsymbol{\mu}_S) \cdot \mathbf{B} \end{aligned} \tag{2.29}$$

where $\boldsymbol{\mu}_L = -(e/2m_e)\mathbf{L}$ and $\boldsymbol{\mu}_S = -g_e(e/2m_e)\mathbf{S}$ are the magnetic moments due to the electron orbital angular momentum $\mathbf{L}$ and intrinsic electron spin angular momentum $\mathbf{S}$, respectively, and g_e is the electronic g-factor.

For weak magnetic fields where the magnetic interaction is smaller than the spin-orbit interaction, each level with total angular momentum quantum number J splits into $(2J+1)$ states due to space quantisation by the magnetic quantum number M. Dipole transitions between two such states obey the selection rules $\Delta M = 0, \pm 1$ which results in π ($\Delta M = 0$) and σ ($\Delta M \pm 1$) polarisation components. π-components are linearly polarised parallel to the magnetic field lines when viewed perpendicular to the field and do not emit in the field line direction. σ-components are circularly polarised in the direction of the field and linearly polarised perpendicular to the field direction. When observed perpendicular to the field, the plane of polarisation of the σ-components is perpendicular to the field line direction.

The shift in energy due to space quantisation by magnetic quantum number M is given by

$$\Delta E = M g_L \mu_B B \tag{2.30}$$

where g_L is the Landé factor, $\mu_B = e\hbar/2m_e$ is the Bohr magneton and B is the magnetic field magnitude. In the LS-coupling scheme the Landé factor is given by

$$g_L = 1 + \frac{J(J+1) - L(L+1) + S(S+1)}{2J(J+1)} \tag{2.31}$$

such that the energy shift for the Zeeman components away from the unshifted (non-field) transition energy between levels $p \to q$ is, in wavelength units,

$$\Delta\lambda_{p\to q}[\text{nm}] = 4.669 \times 10^{-8}[M_q g_{L,q} - M_p g_{L,p}]\lambda^2_{p\to q} B \tag{2.32}$$

where B is in units of Tesla and $\lambda_{p\to q}$ is the unshifted wavelength. The resulting multiplet structure is known as the anomalous Zeeman effect.

With increasing field strength, the Paschen-Back regime is reached where the independent magnetic interactions with the orbital angular momentum **L** and spin angular momentum **S** become larger than the spin-orbit coupling. Each state in the multiplet structure is now given in terms of the quantum numbers SM_SLM_L with selection rules $\Delta M_S = 0$ and $\Delta M_L = 0, \pm 1$, resulting in a triplet with a central unshifted π-component and two symmetrically shifted σ-components with the shift in the triplets given by

$$\Delta\lambda_{p\to q}[\mathrm{nm}] = 4.669 \times 10^{-8} \Delta M_L \lambda^2_{p\to q} B \tag{2.33}$$

Since each components in the Zeeman/Paschen-Back multiplet is either linearly or circularly polarised according to whether $\Delta M = 0$ or $\Delta M \pm 1$, the emissivity per steradian of a particular component is dependent on the observation angle θ between the line of sight and the magnetic field direction, such that

$$\Delta M = 0 : \frac{1}{4\pi}\sin^2\theta A(p \to q, L, S, J, M) n(p, L, S, J, M) \tag{2.34}$$

$$\Delta M \pm 1 : \frac{1}{8\pi}(1 + \cos^2\theta) A(p \to q, L, S, J, M) n(p, L, S, J, M) \tag{2.35}$$

where $A(p \to q, L, S, J, M)$ is the spontaneous emission rate for the given transition and $n(p, L, S, J, M)$ is the upper state population. If the distribution of populations of the same term and the magnetic sub-states for each of the terms can be assumed to be statistical, then

$$n(p, L, S, J, M) = \frac{1}{(2J+1)(2L+1)(2S+1)} n(p, L, S) \tag{2.36}$$

and the relative intensities of the Zeeman/Paschen-Back multiplet components are independent of the upper state population. This allows for analysis of the magnetic perturbations to the profile of a spectral line without prior knowledge of the excited state populations.

The basis for quantifying the magnetic effects on the profile of a spectral line in this thesis is the `ADAS603` code (Summers, 2004), which provides the Zeeman / Paschen-Back component relative intensities and wavelength shifts for hydrogenic species and several impurity transitions as a function of the magnetic field strength,

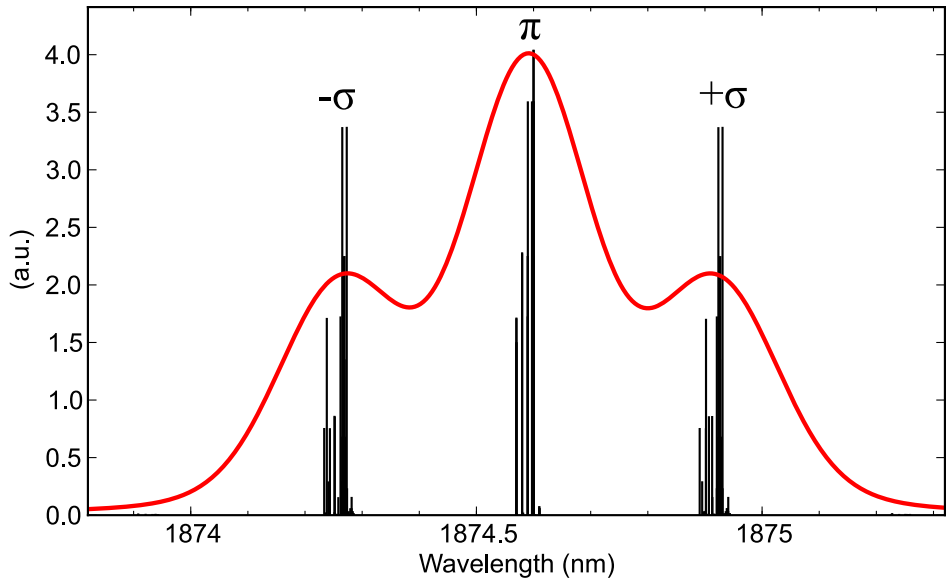

Figure 2.1: H 4→3 Zeeman/Paschen-Back σ and π polarisation components (black) calculated using the ADAS603 code for $B = 2$ T, $\theta = 90°$ and the total Stark-Doppler broadened line profile (red, scaled) for $n_e = 5 \times 10^{19}$ m^{-3} and $T = 5$ eV.

observation angle and polarisation state. As an example, Figure 2.1 shows the Zeeman / Paschen-Back multiplet components for the Pa-α (H 4→3) line, with the parameters $B = 2$ Tesla and observation angle $\theta = 90°$. An estimate of the line profile is obtained by introducing a common broadener for each component as a result of the convolution of the Doppler and Stark broadening (obtained using the MMM tabulations) for plasma parameters $n_e = 5 \times 10^{19}$ m^{-3} and $T = 5$ eV. The components are then summed to yield the total profile. This approach treats the influence of the Zeeman and Stark effects as statistically independent processes (see Section 5.1).

2.2 Divertor Physics

The operational goals of the tokamak divertor are (i) to mitigate the interaction between the plasma and the physical structures of the tokamak while maintaining the performance of the core confined region needed to sustain the fusion power source, and (ii) to provide efficient active pumping (removal) of helium ash and hydrogenic fuel. The main design strength of the divertor concept lies in its ability to localise the plasma-wall interactions away from the core, thus limiting the accumulation of impurities and fuel dilution which are detrimental to the core plasma performance

(Stangeby, 2000a).

2.2.1 Plasma-Surface Interactions

The character of the radiation emitted by divertor plasmas depends fundamentally on the physical processes occurring in the divertor due to the co-existence of plasma and solid surfaces. Consider, for example, cross-field transport of energetic charged particles crossing the confined region into the SOL. These particles move rapidly along the SOL field lines (parallel transport) to the divertor targets, which intersect the open field lines and thus limit particle diffusion in the cross-field direction (radial transport). This results in a finite thickness of the SOL which is largely dependent on the degree of cross-field diffusion and the connection length from point of entry into the SOL to the target (Stangeby, 2000a) (see Figure 2.3). The region associated with the strongest PSI processes is therefore localised to the thin strip of SOL plasma at the point of contact with the divertor targets.

Figure 2.2 illustrates the main PSI processes at the tokamak main chamber wall and divertor targets. The interface layer which mediates the flow, energy and momentum of charged particles from the quasi-neutral plasma to the solid surface is the electrostatic sheath. A net space-charge rapidly develops at the electrostatic sheath due to the higher thermal velocity of the electrons compared to the ions (Stangeby, 2000b). An *ambipolar electric field* thus forms due to the build-up of negative charge and retards further electron flow while at the same time accelerating ions towards the surface and equalising the fluxes of electrons and ions to the surface. This balance prevents the build up of charge in the plasma and thus maintains quasi-neutrality. An important theoretical result is known as the Bohm criterion (Bohm, 1949), which states that the ion velocity at the sheath edge must be greater than or equal to the ion sound speed in order for the sheath to form at the solid surface. The derivation of this result also leads to an estimate of the thickness of the sheath layer, which, for the simple case of stationary plasma ions (i.e., $T_i = 0$) turns out to be approximately equal to the Debye length (Stangeby, 2000a, p. 73). For example, for typical plasma edge conditions with $T_e = 20$ eV and $n_e = n_i = 10^{19}$ m^{-3} the sheath thickness is ~ 10 µm, and is thus an extremely thin interface between the plasma and surface. An important consequence of the ion (plasma or impurity species) acceleration in the sheath is the impact energy of the ions, $E_0 \approx 2k_BT_i + 3Zk_BT_e$, which substantially exceeds the energy attributed to a Maxwellian ion inflow of $2k_BT_i$, and thus can lead to increased sputtering (Stangeby, 2000b).

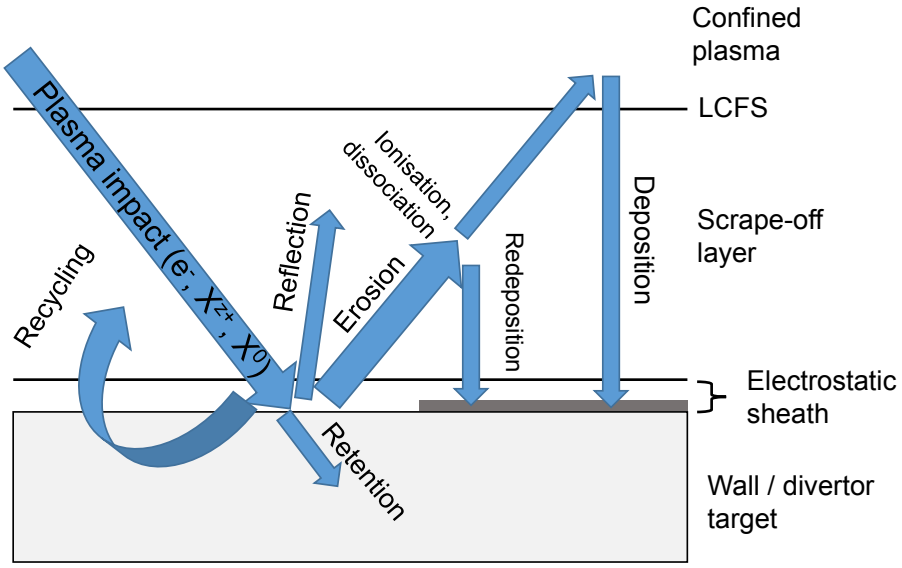

Figure 2.2: Schematic of the main plasma-wall interaction processes in a tokamak.

At the point of contact with the solid surface, some fraction of the charged particles are adsorbed and recombine to form neutrals, while some may be reflected back into the plasma. The resulting neutral is weakly bound to the surface and desorbs (is *recycled*) back into the plasma where it eventually re-ionises. The mean free path for ionisation depends on the plasma conditions as well as the energy of the desorbed neutral, its mass and ionisation energy. For the majority hydrogenic plasma species, this recycling process is sufficient to fuel the plasma if the plasma is not actively pumped. At sufficiently high energies, the impinging plasma ions can erode the solid surface through physical or chemical sputtering, thus introducing impurities into the plasma which are subsequently ionised and carried away from the erosion source. The impurity ions can also erode material through a self-sputtering process. In the JET ITER-like wall configuration, the main wall and limiters are composed of beryllium coated tiles, whereas the entire divertor consists of solid tungsten and tungsten coated tiles. Be line radiation is present, however, in the divertor plasma and can be attributed to the transport of Be ions from the main chamber walls (Be source) via the SOL down to the divertor targets (e.g. Krieger et al., 2013). The erosion of the main wall Be tiles occurs mainly due to residual plasma ions and energetic neutrals impinging on the walls via charge-exchange reactions through which relatively high temperature charged particles in the SOL plasma exchange electrons with low energy recycled neutrals from the walls. This process can lead to Be self sputtering, which has been observed to be the dominant erosion mechanism at high

impact energies (Brezinsek et al., 2014). Energetic Be ions impinging on divertor targets, being more massive than the hydrogenic species, can exceed the W sputtering threshold energy and lead to W erosion, particularly during the intra-ELM phase in high confinement mode plasmas (e.g. van Rooij et al., 2013).

The distribution of hydrogen isotope and impurity species and their ionisation stages in the divertor plasma is driven by the combination of localised erosion and recycling sources, SOL transport, temperature and pressure gradients in the cross-field and parallel direction, and drifts imposed by the magnetic configuration. Radiation emitted by the neutral and partially ionised species is then a consequence of the local densities of excited state populations and the relevant collisional and radiative processes.

2.2.2 Divertor Operating Regimes

The typical magnitude of the parallel heat flux, $q_{\parallel}$, along the open magnetic field lines of the outer SOL in large tokamaks is in the range $10^7 - 10^9$ W m^{-2} (Stangeby, 2000b) and scales according to

$$q_{\parallel} \sim \frac{P_{SOL}/2}{2\pi R \lambda_q} \frac{B}{B_\theta}, \tag{2.37}$$

where P_{SOL} is the total power entering the SOL from the core plasma, R is the major radius, B and B_θ are the total and poloidal magnetic field magnitudes, respectively, and λ_q is the characteristic power width (or heat flux decay length). For ITER, for example, P_{SOL} is in the range of 100 MW (Ikeda, 2007) and predictions of λ_q are of order few mm (e.g Eich et al., 2013) such that $q_{\parallel} \sim 2$ GW m^{-2}. Such high exhaust power densities pose a serious challenge to the successful operation of reactor-scale devices, for which the lifetime of plasma-facing components can be unacceptably short if the steady-state and transient power deposition onto the target materials exceeds physical limits (~ 10 MW m^{-2}). Optimisation of the target plate geometry in order to minimise the field line incidence angles can reduce the heat flux to the target by a factor of ~ 20 or so, but geometry optimisation alone is not sufficient for reducing the heat loads below engineering limits. The most promising approach for achieving acceptable levels of power and particle control relies on the dissipation of energy and momentum upstream of the divertor target plates by means of volumetric atomic processes. The features of divertor plasmas which exhibit such characteristics are summarised in the following brief overview of the divertor operating regimes in

order to motivate the discussion of passive spectroscopy measurements in subsequent chapters.

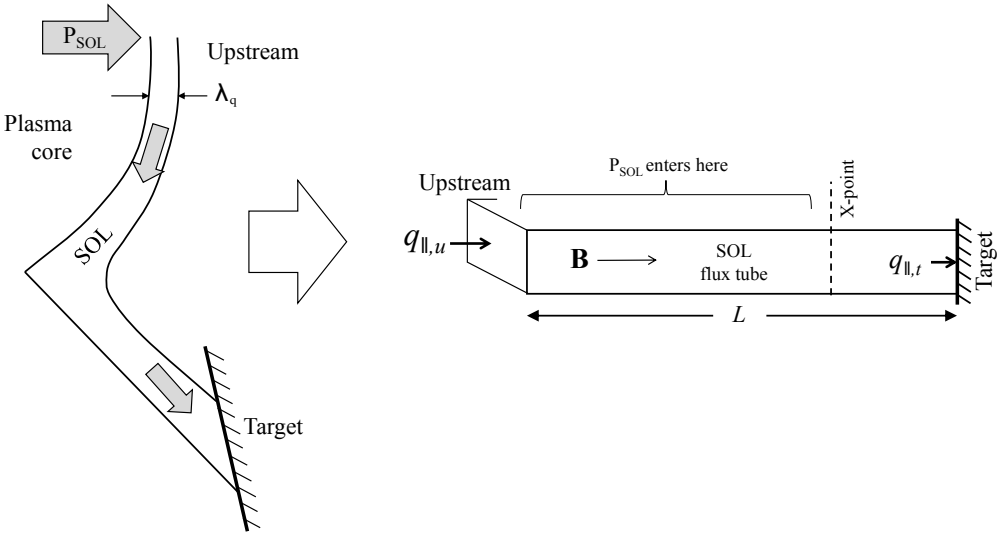

Figure 2.3: Schematic of the straightened out SOL flux tube.

A common conceptual aid used in describing tokamak divertor operating regimes is to straighten-out the open field lines in the SOL, as shown in Figure 2.3, with the upstream conditions (denoted with subscript u) on one end and the conditions at the target plate (denoted with subsript t) at the other end. L is the connection length defined as the shortest distance from the upstream position to the target surface measured along the field line. In the simplest case, the heat flux which enters the SOL upstream is carried to the target entirely by parallel convection such that the temperature along the SOL is constant (i.e., $\nabla_{\parallel} T \approx 0$, or $T_u = T_t$). This scenario is observed at moderate upstream densities and results in moderate recycling of the impinging plasma ions at the target, such that ion-neutral interactions near the plate can be neglected. In the absence of parallel temperature gradients, the electrostatic sheath represents the dominant heat sink, and is undesirable for tokamak operations due to large plasma temperatures at the targets and thus increased sputtering yields. This scenario is termed the *sheath limited regime* (commonly referred to as the attached divertor) and represents the first case in Figure 2.4.

With increasing upstream density, a higher particle flux at the target increases the rate of ionisation of recycled neutrals near the target surface, and thus diminishes the flows in the SOL which would otherwise be unencumbered in the sheath limited regime. A direct result of the reduction in the SOL flows is a decrease in convective transport, leaving conduction as the main heat transport mechanism. This leads to

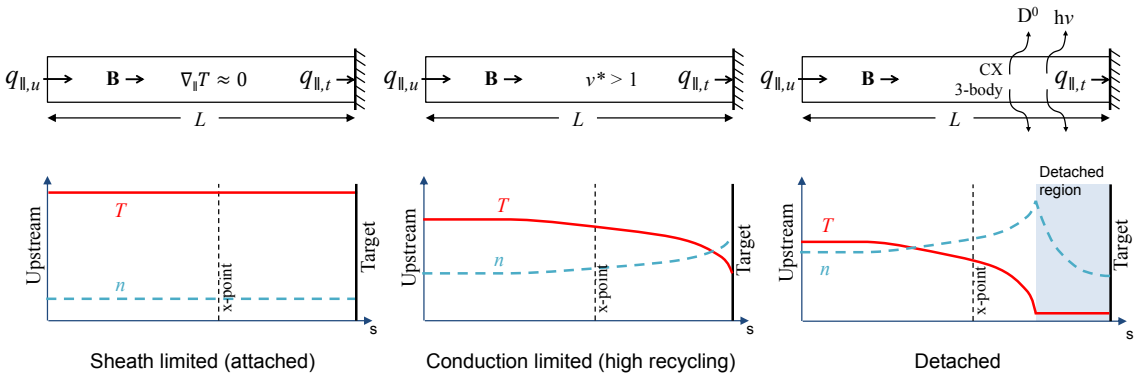

Figure 2.4: Main features of the sheath limited, conduction limited, and detached divertor operating regimes.

the formation of a parallel temperature gradient, necessitated by the more stagnant SOL, such that $\nabla_\parallel T \neq 0$. This is quantified with an increase in the SOL collisionality parameter, $\nu^* \sim n_u L/T_u^2$, for which high values ($\gtrsim 10$) signify strong temperature gradients (Stangeby, 2000a, p. 194). A SOL characterised by a significant parallel temperature gradient is said to be in the *conduction limited regime* (or high recycling regime), shown as the middle case in Figure 2.4. While the plasma pressure is conserved in this regime (i.e., a parallel density gradient opposes the temperature gradient such that $nk_BT_e + nk_BT_i + (1/2)nm_iv_i^2 \approx$ constant), the plasma temperature at the target can be significantly lower than upstream, leading to reduced sputtering and erosion.

By further increasing the upstream density through active fuelling the temperature at the target can fall below 5 eV at which point charge exchange collisions between hot ions and cold recycled neutrals start to predominate over ionisation in the vicinity of the target plate. This is evident in Figure 2.5 which shows the temperature dependence of the effective ionisation, charge-exchange and recombination rate coefficients for pure hydrogen plasmas using derived atomic data from the ADAS ADF11 class. The resulting hot neutrals, no longer magnetically confined, remove momentum and energy from the plasma thereby lowering the plasma pressure and reducing the temperature even further. This is highly beneficial as it results in a reduction in both $q_\parallel$ as well as the particle flux to the target, $\Gamma_\parallel$. At $T_e \lesssim 1.5$ eV another channel of plasma momentum and radiative energy loss becomes accessible as the three-body recombination rate becomes the dominant atomic process. This leads to significant volume recombination and a further increase in the neutral pressure and conversely a rapid decrease of the plasma density near the target. The ionisation front effectively 'detaches' from the solid target surface and

moves some distance upstream, hence this operating regime is referred to as the *detached* divertor, shown as the last case in Figure 2.4. Volumetric processes in the detached region can therefore dissipate a significant fraction of the exhaust power over a much larger area relative to the sheath limited and conduction limited regimes in which the heat flux is confined to the very narrow strip of wetted area characterised by λ_q. The experimentally observed signatures associated with detachment are typically: (i) an initial increase in the ion flux to the target, as measured by Langmuir probes, and a subsequent roll-over in the ion flux as the plasma detaches and the plasma sink moves away from the surface (see e.g. Loarte et al., 1998; Harrison et al., 2011); (ii) an increase in the D 3→2 emission in the divertor even after the ion flux roll-over; (iii) the presence of high-n hydrogenic series lines (Lyman, Balmer, Paschen) associated with the higher lying excited states being primarily populated by recombination. Spectroscopic measurements of the hydrogen isotope emission in the detached regime are therefore typically used to quantify the degree of volume recombination and the plasma properties in the cold and dense detached divertor plasma (e.g. Meigs et al., 1998). For instance, studies of recombination on Alcator C-Mod using spectroscopic techniques (Lumma et al., 1997) have shown the three-body recombination rate to account for ≈90% of the total recombinations, with the remainder mostly attributed to direct radiative recombination and some small fraction due to molecular-activated recombination (MAR). Consequently, the total recombination rate on Alcator C-Mod has been shown (Lipschultz et al., 1999) to account for up to 75% of the ion sink.

In describing the characteristics of plasma detachment, it is important to highlight the stability issues associated with this operating regime. The extent to which the plasma can be fueled to increase the upstream density in order to access detachment depends on the degree to which the cold and dense plasma and neutrals interact with the confined region and the resulting impact on the core plasma performance. Observations from detachment experiments on many devices, including JET (Monk et al., 1999; McCracken et al., 1998), Alcator C-Mod (Lipschultz et al., 1998) and DIII-D (Stacey et al., 1999) show that detachment can eventually lead to the formation of an unstable radiating region near the X-point, known as a MARFE (Multifaceted Asymmetric Radiation From the Edge) (Lipschultz et al., 1984). This is usually the precursor to an eventual density limit disruption which terminates the plasma. Figure 2.6 shows an example of the expansion of the cold radiating region during detachment from bolometry measurements of the radiated power spatial distribution in JET density ramp experiments (Huber et al., 2007). The concentration

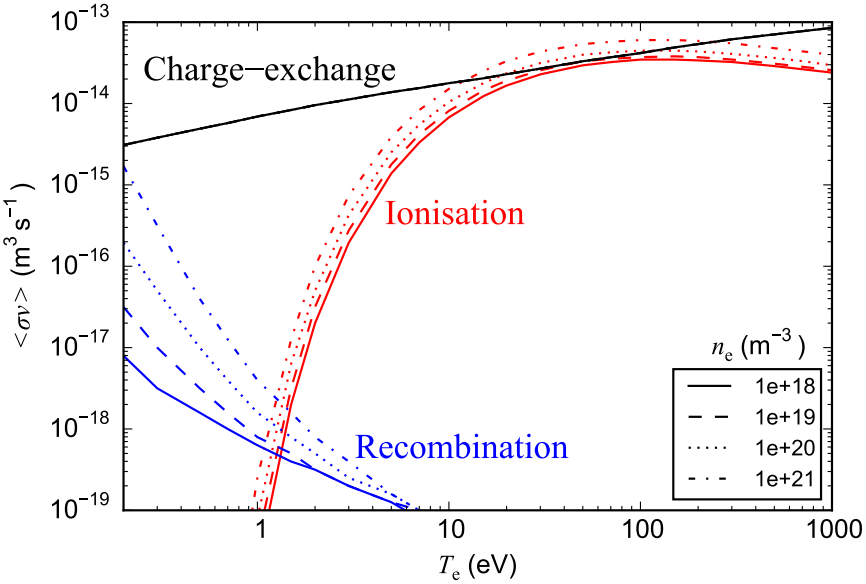

Figure 2.5: Effective ionisation, recombination and charge-exchange rate coefficients from the ADAS ADF11 class.

of radiation near the X-point and incursion into the confined core region at $t > 16.4$ s is in contrast to the radiation distribution in the earlier phase of the discharge at $t < 16.0$ s which is confined along the inner and outer divertor SOL, outside of the core plasma.

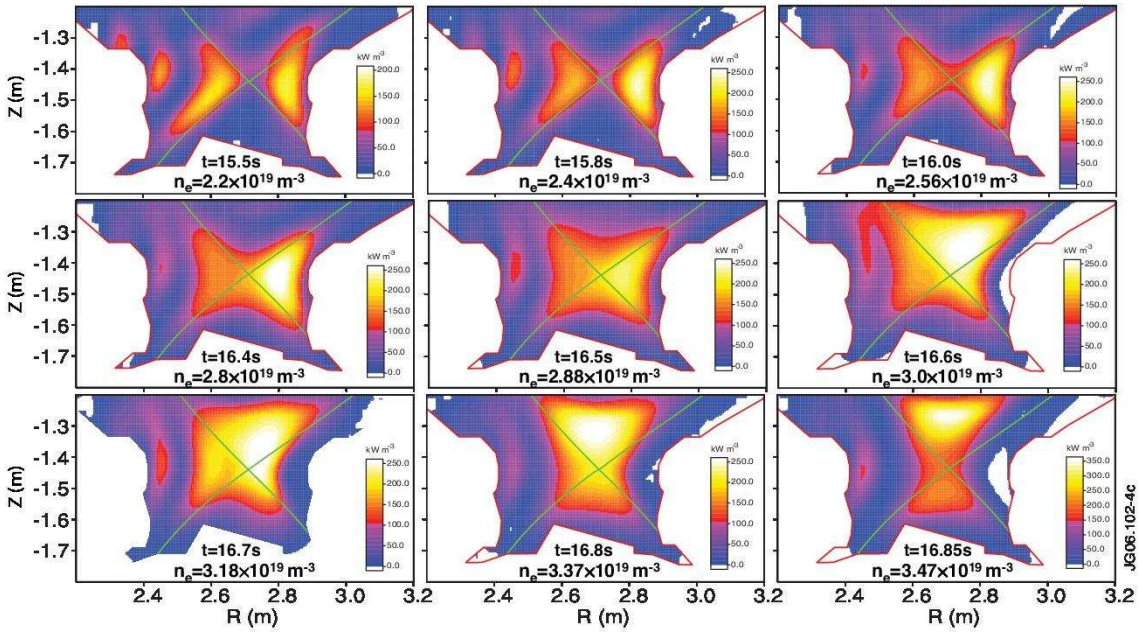

Figure 2.6: Tomographic reconstruction of JET divertor bolometry data from a density ramp discharge (Huber et al., 2007).

An active area of research is concerned with the exploration of more exotic divertor geometries for improved control and mitigation of exhaust power. One example is the Super-X configuration on the MAST-Upgrade (Fishpool et al., 2013; Katramados et al., 2011), being built at the time of writing, which is designed to increase the wetted area and connection length of the outer divertor by relocating the outer target radially outward. In combination with mangetic flux expansion and improved divertor baffling, this should facilitate improved access to and stability of detachment. Another example is the TCV tokamak which has the unique capability of introducing additional field nulls to the divertor magnetic geometry with the aim of distributing the exhaust power to multiple target zones in a configuration known as the *snowflake* divertor (e.g Piras et al., 2009).

2.3 Divertor Plasma Radiation Sources

The spectral features of tokamak plasma radiation depend on the local plasma density and temperature as well as the density and transport of the dominant populations of atoms, ions and molecules in the ground and metastable states in the spatially and temporally inhomogeneous plasma. The radial temperature profile in the core usually peaks near the magnetic axis with typical values of electron temperature above 1 keV. A steep gradient in both temperature and density, called the pedestal, is usually observed in high confinement (H-mode) operating scenarios (e.g. Hubbard, 2000), such that temperature in the edge and SOL plasma are of the order of few tens to hundreds of eV. Plasma densities in the core are typically $\geq 10^{19}$ m^{-3}. Downstream of the SOL in the divertor, atomic processes (e.g., in the detached divertor regime) can lower the plasma temperatures below 5 eV or even 1 eV and conversely raise the plasma density above 10^{20} m^{-3}. Light impurity ions, such as Be, C, O, N, and Ne are predominantly fully ionised in the core, with partially ionised concentrations at the edge, SOL, and divertor. Medium-Z ions, such as Fe or Ar, will exist in H-like and He-like states in the core while high-Z ions, such as W, retain a significant number of electrons in the core and thus radiate strongly. The working plasma hydrogenic species are fully ionised in the core, with the exception of neutral beam particles which, owing to their high injection energies ($\sim$ 100 keV), can penetrate into the core before losing their electrons through charge-exchange collisions with hydrogenic and impurity ions. Likewise, excursions of the cold radiating region to the X-point and beyond the LCFS to the confined plasma region during MARFE formation can lower the screening of impurities and hydrogenic neutrals which have

a deleterious cooling effect on the core plasma.

Strongly localised plasma-wall interaction at the divertor targets in combination with relatively cool and dense plasma conditions in the divertor results in an emission spectrum with many of the low-Z neutral and partially ionised electronic transition photon energies in the UV, VIS and NIR part of the spectrum. The low concentrations or complete absence of these radiating species in the core plasma is convenient for line-of-sight integrated observations of the divertor plasma. The recycling of hydrogenic neutrals is typically dominated by the high ion fluxes at the divertor targets. The re-ionisation depth of these neutrals depends on the electron and ion density and temperature and the ionisation rate can be related to the measured intensity of a particular electronic transition using the derived ADAS SXB coefficients. Higher energy neutrals from charge-exchange processes as well as Frank-Condon processes due to molecular breakup can also contribute to the line intensities and spectral line profiles of hydrogenic species. Volume recombination in detached plasmas provides an additional mechanism in producing significant fractions of neutrals via three-body recombination into high-n excited levels.

Bremmstrahlung radiation occurs across the entire plasma volume due to Coulomb interactions as free electrons decelerate in the electric field of an ion. The bremmstrahlung intensity is $\propto n_e^2 T_e^{-1/2}$ according to eqn. 2.5, with the main contribution attributed to the cool and dense divertor plasma region. Likewise, the contribution from free-bound recombination radiation is also localised to colder and denser plasma regions. Heat loads on divertor target plates can heat up the solid surface locally to temperatures in excess of 1000 K depending on machine size, divertor geometry and the power entering the SOL from the core plasma. Heat loads can be exacerbated by transient edge-localised modes (ELMs), during which a significant amount ($\sim 0.1 - 10\%$) of the plasma stored energy is rapidly expelled from the confined region, with typical time scales of < 1 ms (e.g. Clement et al., 1999). Thermal emission can thus contaminate the observed emission from the plasma volume. The problem is compounded in all-metal divertors, such as the JET-ILW tungsten divertor, where reflections from both surface thermal emission and volume plasma emission can introduce spurious signals to spectroscopic measurements. Thermal emission is given by the Planck black-body distribution, modified by an appropriate surface emissivity. Taking eqn. 2.14 and rewriting in terms of wavelength λ, the spectral radiance attributed to thermal emission is

$$I_\lambda d\lambda = \epsilon_{\lambda,sur} \frac{2hc^2}{\lambda^5} \frac{1}{exp(h\nu/k_B T) - 1} d\lambda \ [\mathrm{W\ m^{-2}\ sr^{-1}}] \tag{2.38}$$

where $\epsilon_{\lambda,sur}$ is the total hemispherical spectral emissivity of the surface.

2.3.1 Illustrative Example of VIS-NIR Spectra

To illustrate the main spectral features associated with radiation from hydrogenic divertor plasmas, synthetic spectra including continuum contributions as well as the Balmer and Paschen series lines were calculated for the visible (VIS) and near-infrared (NIR) wavelength range (300-2000 nm).

Figure 2.7 shows the relative contributions of the continuum free-free (eqn. 2.5), free-bound (eqn. 2.4) and thermal spectral radiance (eqn. 2.38) given a 100 mm thick homogenous pure hydrogen plasma observed perpendicular to a tungsten surface at temperature T_{sur}, with the Gaunt and Biberman factors taken to be unity, and using the empirically derived tungsten emissivity from the ITER Materials Properties Database (ITER Doc. G 74 LS 102-03-22 W0.1). In the high density (5×10^{20} $\mathrm{m^{-3}}$), low electron temperature case ($T_e = 1$ eV), representative of detached plasma conditions, the steady-state heat flow to the divertor strike point can be dissipated via atomic processes thus reducing the tile surface temperature. In this regime the dominant contribution is from the plasma free-free and free-bound radiation. Conversely, in the lower density (5×10^{19} $\mathrm{m^{-3}}$), higher electron temperature ($T_e = 10$ eV) case, the dissipation of exhaust power is less effective and thus higher target temperatures are expected, depending on upstream parameters such as the magnitude of P_{SOL}, $q_\parallel$ and λ_q. For temperatures in excess of 1000 K the thermal emission will dominate in the NIR spectral range for viewing chords intersecting the target surface hot spots.

Spectra of the Balmer and Paschen hydrogen series lines are shown in Figure 2.8 for the low density, high temperature case. Their intensities were estimated using the inverse photon efficiencies ($SXBs$) from ADAS with a hydrogen ion flux at the divertor surface of $\Gamma = 10^{23}$ $\mathrm{m^{-2}\ s^{-1}}$ and assuming that all of the impinging particles are recycled back into the plasma with a characteristic re-ionisation depth of the order of the divertor plasma size. The lines are doppler broadened assuming a Maxwellian energy distribution of the neutrals with $T_n = T_i = T_e$ and Stark broadened according to the quasi-static approximation (eqn. 2.28). The discrete to continuum transition that occurs at the series limit is not fully resolved as SXB

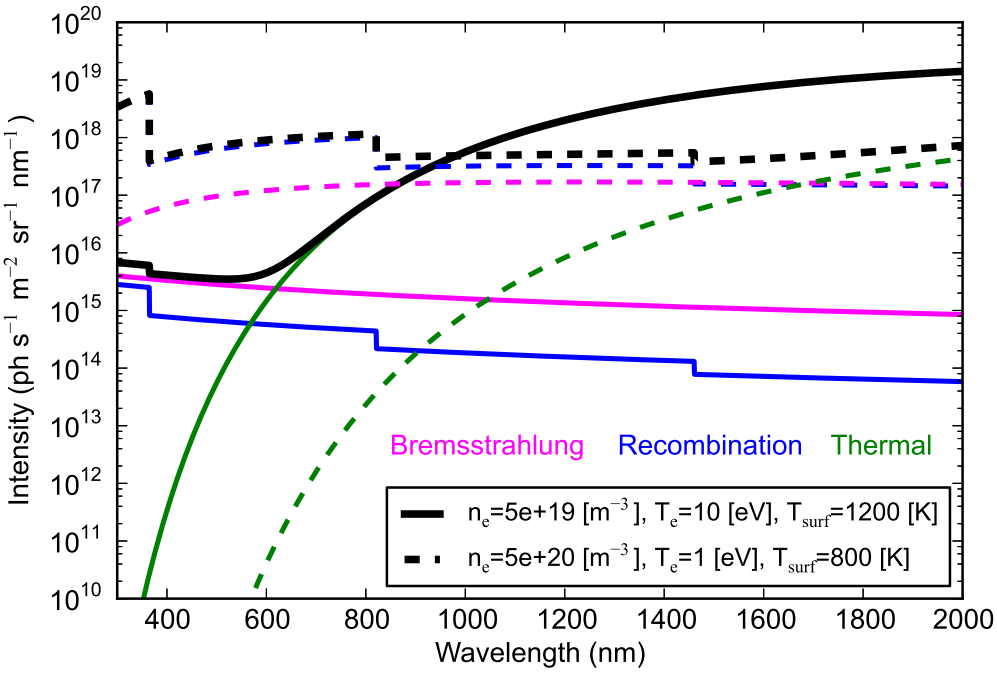

Figure 2.7: Calculated continuum emission spectrum contributions from Bremsstrahlung, radiative recombination and thermal emission for a 100 mm thick isotropic hydrogen plasma with the line-of-sight direction normal to an isothermal tungsten surface.

coefficients for transitions with upper state $n > 12$ are not available. The synthesised spectrum suggests that the thermal contribution can be quite significant for $T_{sur} \gtrsim$ 1000 K and starts competing with the Paschen series line intensities depending on the magnitude of the recycled particle flux. The extent of the thermal contamination on the Pa-α (H 4→3) line intensity measurements in the JET-ILW divertor is examined in more detail in Section 4.5.

The high density and low temperature hydrogen series spectrum (Figure 2.9) was synthesised using the Saha relation (eqn. 2.15) in accordance with the assumption of LTE conditions. According to eqn. 2.16, the thermal limit with $n_e = 5 \times 10^{20}$ m^{-3} and $T_e = 1$ eV is $n_{th} \approx 2.5$, validating the LTE assumption for all transitions with upper level $n \geq 3$. The discrete to continuum transition is again incomplete as only lines with upper level $n \leq 24$ are shown. At high densities the three-body recombination process becomes appreciable since the reaction rate is $\propto n_e^2$. As illustrated in Figure 2.5, for $T_e < 1$ eV, the effective recombination rate dominates over ionisation.

It is evident that the intensities of the higher-n transitions in Figure 2.9 decrease

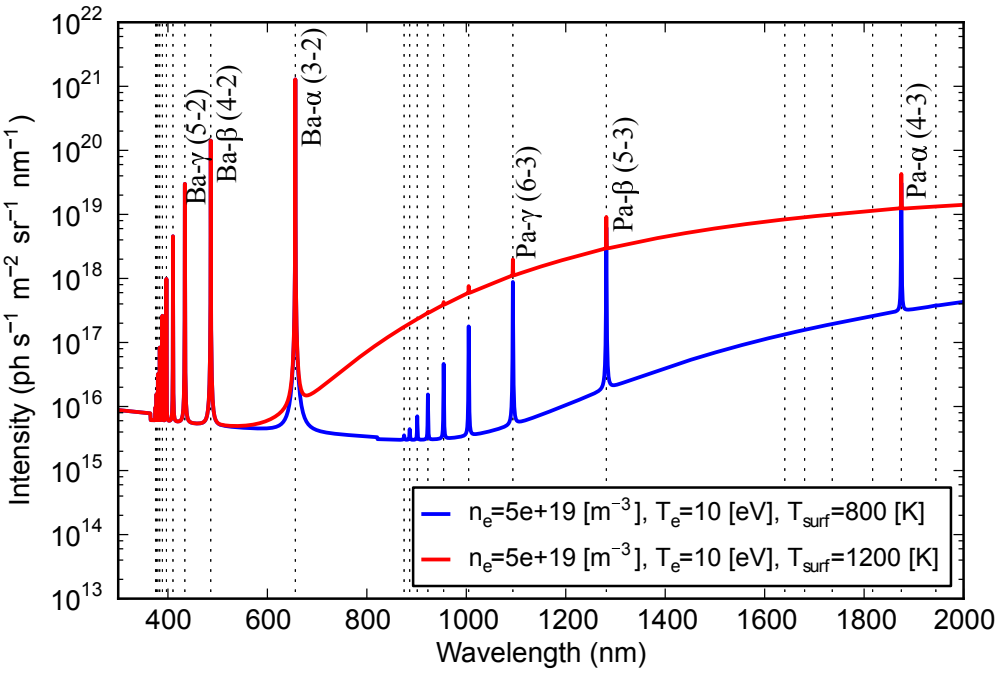

Figure 2.8: Calculated VIS-NIR emission spectrum for an ionising hydrogen plasma.

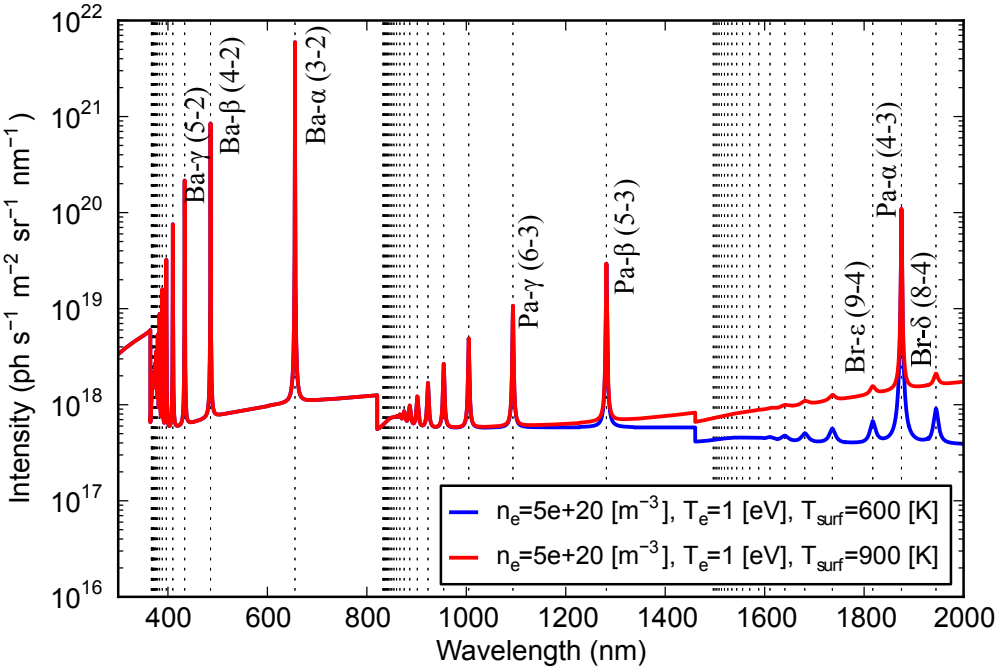

Figure 2.9: Calculated VIS-NIR emission spectrum for a recombining hydrogen plasma.

at a slower rate than in the ionising plasma of Figure 2.8. This is the signature of volume recombination and is a consequence of the recombination flux populating

mainly the higher levels. The broad high-n Brackett series lines are now visible on either side of the Pa-α line.

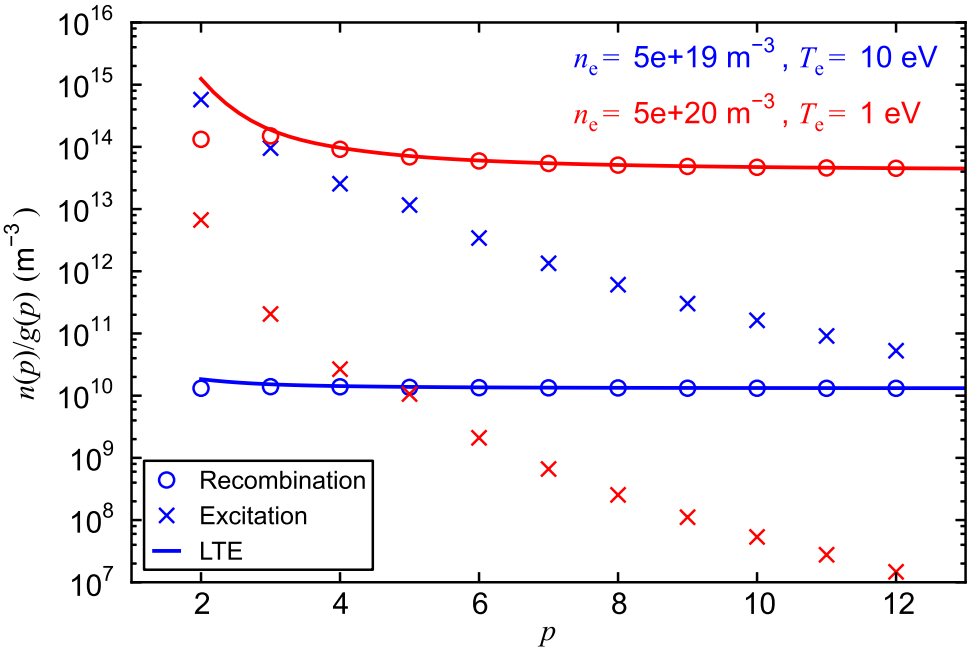

Figure 2.10: Hydrogen excitation and recombination contributions to the excited state population densities obtained using PEC coefficients from the ADAS ADF15 class. Also shown are the population densities assuming LTE conditions. $g(p)$ is the statistical weight for each excited level p.

The role of excitation and recombination fluxes is further illustrated in Figure 2.10 which shows the excited state populations for the high temperature, low density and low temperature, high density cases. These populations were obtained using the PEC coefficients from the ADAS ADF15 data set, eqn. 2.2 and eqn. 2.22, assuming a neutral fraction $n_0/n_i = 0.1$, and are normalised by the statistical weight $g(p) = 2p^2$ for each excited level p. The population distributions demonstrate the negligible impact of the excitation flux in the high density, low temperature plasma, and, conversely, the predominance of excitation in the low density, high temperature plasma. Also shown are the LTE populations for each case using the Saha-Boltzmann distribution which are in good agreement with the collisional-radiative model derived PEC coefficients for $n > 3$. Thus in the recombining plasma the PEC derived populations are shown to be statistical except for the low lying levels $n \leq 3$, whereas in the ionising plasma the total populations only converge to the LTE distribution at very high levels $n > 12$, which are thus in the PLTE regime.

This is an important result as it facilitates a straightforward spectroscopic technique for estimating the electron temperature based on measured line intensities of the higher-n transitions. The procedure is based on taking the logarithm of the Saha eqn. 2.15:

$$\log\left(\frac{n_z(p)}{g_z(p)}\right) = \left(\frac{1}{T_e}\right)\frac{13.6}{p^2} + \log\left(\frac{n_{z+1}(g)n_e h^3}{g_{z+1}(g)\left(m_e k_B T_e\right)^{3/2}}\right), \tag{2.39}$$

where the ionisation energy $E_{z,p}$ has been replaced with $13.6/p^2$ in eV units for hydrogen isotopes, $n_{z+1}(g)$ is the hydrogen isotope ion density and $n_z(p)$ is the population density of the excited level p. A straight line is therefore obtained relating the excited state population densities determined from spectroscopic measurements and the electron temperature. In practice, uncertainties in determining the line intensities of the high-n transitions can arise not only from the measurement apparatus and detector noise, but also from the smooth discrete-to-continuum (D-C) transition where the Stark broadened hydrogen lines are merged with the radiative recombination edge. The Inglis and Teller (1939) model, for instance, estimates the wavelength of the observed discrete series limit beyond which the Stark broadened lines are no longer distinguishable by combining the overlapping lines with the sharp step attributed to the radiative recombination edge. However, in more recent work by Pigarov et al. (1998) the recombination edge is considered as a smooth transition and a collisional-radiative model is proposed for calculating the D-C spectrum. An example of the calculated spectrum is shown in Figure 2.11 for the Balmer series in a pure hydrogen plasma at $T_e = 1$ eV and $n_e = 10^{21}$ m^{-3}. The Balmer photo-recombination continuum (BPRC) is thus shown to have a significant influence for transitions with $n \geq 10$. Although it is not possible to separate the measurement of the continuum and discrete lines in laboratory plasma observations, it is nevertheless advisable to consider the lower lying levels for inferring electron temperature using the Saha-Boltzmann procedure. This is valid as long as the excitation contribution to the population densities of those levels is not significant.

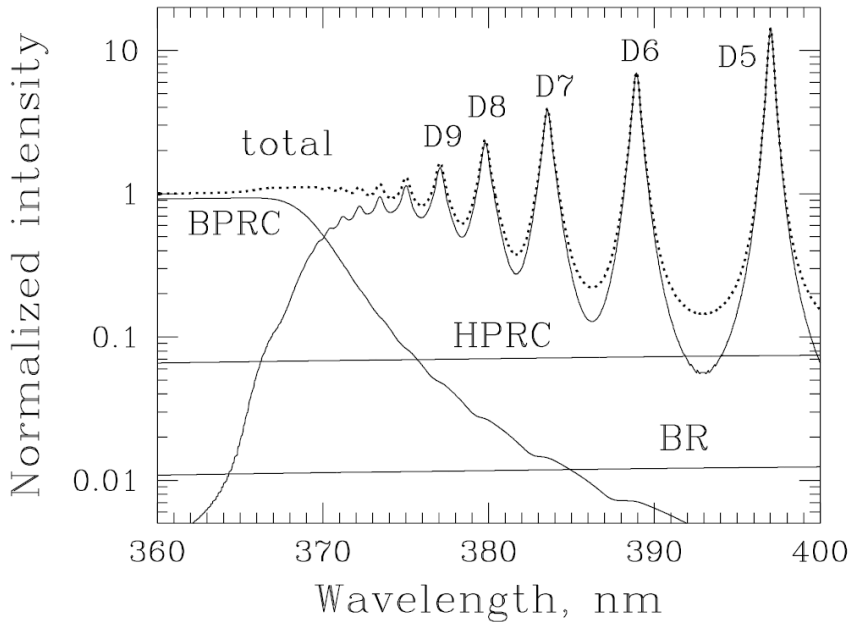

Figure 2.11: Calculated emission spectrum components of the Balmer series discrete-to-continuum transition, including the Balmer photo-recombination continuum (BPRC), photo-recombination continuum from higher sereis transitions (HPRC) and bremsstrahlung (BR). Reproduced with permission from (Pigarov et al., 1998).

Chapter 3

Spectroscopic Survey on MAST

In this chapter a spectral survey is presented from measurements on MAST using a purpose built spectroscopy diagnostic covering the VIS and NIR spectral range on the same line-of-sight in the lower divertor. The measurement aims and instrumentation design are discussed, followed by an analysis of spectral data from select plasma discharges during the M9 MAST experimental campaign in 2013. In particular, emphasis is given to identifying prominent spectral features in the NIR region including the deuterium Paschen series lines, low charge states lines from intrinsic impurities and extrinsic impurities introduced by vessel conditioning. A comparison of the deuterium Balmer and Paschen series lines is then made to highlight the potential application of NIR spectroscopy as a complementary technique for inferring the plasma electron temperature. This pilot programme leads naturally to a more integrated study of VIS-NIR divertor spectroscopy on the JET tokamak presented in Chapters 4 and 5.

3.1 Instrumentation Overview

During the M9 campaign, a 50 mm diameter quartz window on the lower HL01 port of the MAST vessel was made available for the VIS-NIR spectroscopy diagnostic and provided access to views of the inner and outer divertor. The orientation of the collection lens was then considered based on the typical magnetic geometry of MAST divertor plasmas and regions of strong deuterium plasma emission. Figure 3.1 shows an example of a single-null lower divertor plasma magnetic geometry with regions of the primary plasma-wall interaction highlighted at the inner and outer divertor target plates. The high concentration of recycled neutrals near the inner and outer strike points are of primary interest for observing deuterium plasma emission;

however, differences in the performance of the inner and outer divertor targets and implications on the divertor radiation must be considered. The vertical orientation of the MAST inner divertor target plate is likely to promote a horizontal trajectory of recycled neutrals away from the target surface towards the separatrix such that the ionisation front in the vicinity of the separatrix will have a cooling and fuelling effect on the divertor plasma, thus increasing density and lowering temperature (Harrison, 2010). In addition, an asymmetry in the SOL power flow to the inner and outer divertor targets is typically observed on MAST (e.g Temmerman et al., 2010), with most of the power going to the outer divertor for both single (SND) and double-null (DND) divertor discharges. The combination of divertor plate geometry and heat load distribution thus leads to plasma conditions at the inner divertor more conducive to the formation of a volume recombining region and divertor detachment. In fact, observations from experiments on many tokamaks have shown a similar basic trend in accessing the detached regime more readily on the inner divertor (e.g. Pitcher and Stangeby, 1997; Loarte et al., 1998).

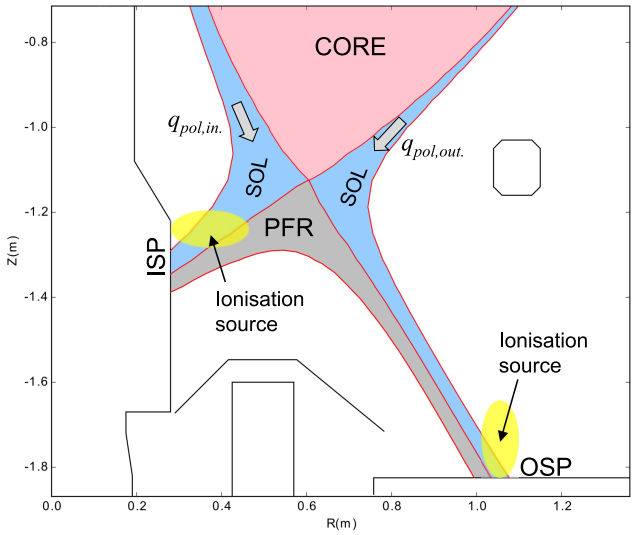

Figure 3.1: Typical magnetic geometry of a MAST lower single-null (LSN) divertor plasma.

Since detachment is typically associated with the presence of volume recombination at low (< 1.5 eV) electron temperatures, and from which the electron temperature can be inferred as described in Section 2.3.1, a view of the inner divertor is therefore of primary interest for obtaining VIS-NIR spectroscopic measurements. To increase the spectral radiance at the collection lens, the line-of-sight (LOS) path was selected tangent to the central column such that the plasma volume intersected by the line-of-sight is maximised. This is demonstrated in Figure 3.2 using sam-

ple D 3→2 tomographically reconstructed emissivity distribution from pulse 25028 (Harrison, 2010).

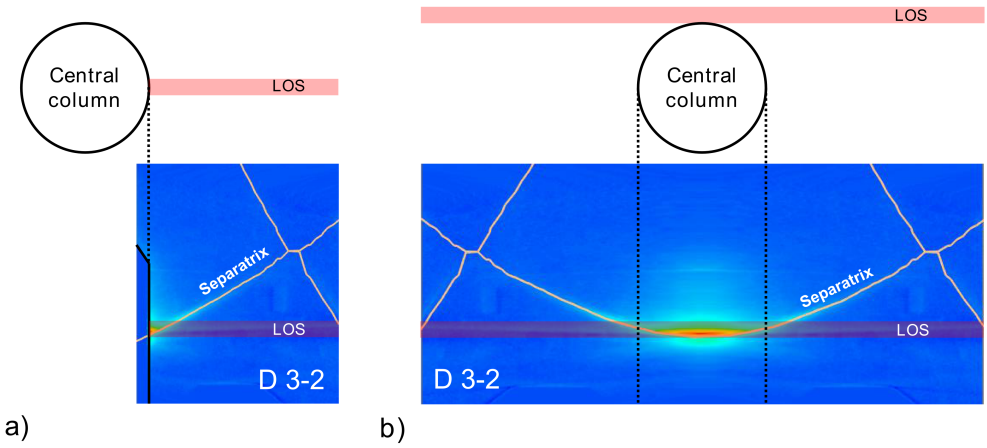

Figure 3.2: Example D 3→2 poloidal emissivity distribution (pulse 25028) in the MAST lower divertor with a) spectroscopic line-of-sight terminating at the central column and b) spectroscopic line-of-sight tangent to the central column.

The layout of the VIS-NIR spectroscopy diagnostic is shown in Figure 3.3. Light collected by the main lens at the port window is relayed via a 600 µm core diameter multimode fibre (NA=0.22) optic cable to the diagnostic hall (a distance of ∼35 m). The light from the fibre is then fed into a VIS and NIR spectrometer via a dichroic beam splitter optical arrangement. A novel feature of the diagnostic is an image slicer designed to maximise the light coupling efficiency at the entrance slit of the NIR spectrometer to increase the throughput. The VIS spectrometer (OceanOptics HR2000+) utilises a 2048 pixel linear CCD array with 14 × 200 µm pixel size and a spectral resolution of ≈ 1 nm FWHM, a usable range of 380-780 nm and f/4 optics. The NIR spectrometer (BaySpec SuperGamut) features a high efficiency transmissive volume phase grating, f/1.8 optics and an indium gallium arsenide (InGaAs) linear photodiode array consisting of 256 pixels with 25 × 500 µm pixel size and a spectral resolution of ≈ 10 nm FWHM. The InGaAs detector is thermoelectrically cooled to -5°C to reduce the dark shot noise while the CCD detector operates at ambient temperature.

3.1.1 Optical Design

An important criteria of the optical design is to maximise the light coupling efficiency from the fibre to the NIR spectrometer since the intensity of the Paschen series lines is relatively lower than the Balmer series lines in the VIS. For example, under ionising

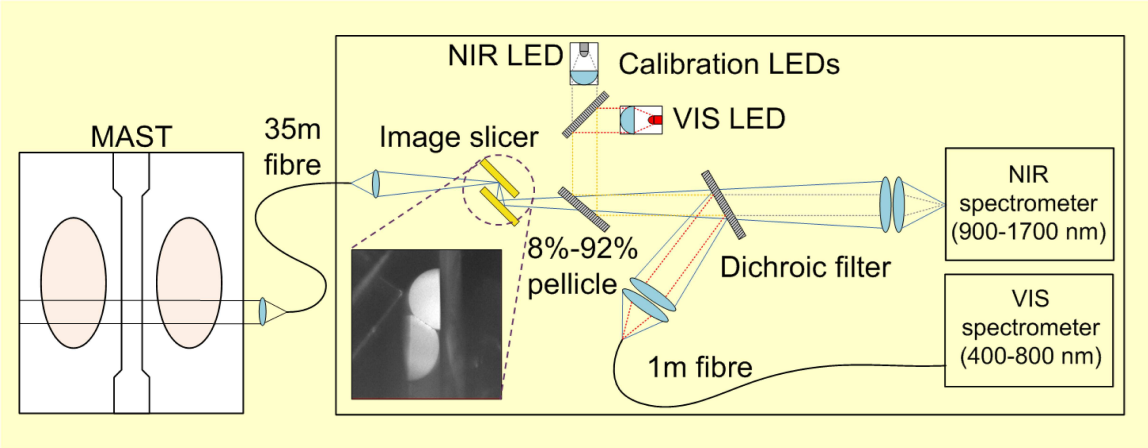

Figure 3.3: Schematic of the MAST VIS-NIR spectroscopy diagnostic.

plasma conditions at $T_e = 5$ eV the emissivity ratio in ph s^{-1} m^{-3} of the H 4→2 (486 nm) line to the H 5→3 (1282 nm) line is ≈ 6.5 according to ADAS excitation $PECs$ at typical divertor plasma densities $\sim 10^{19} m^{-3}$. In units of W m^{-3} the ratio is ≈ 17 due to the difference in the transition energies.

To maximise the light coupling efficiency of the fibre to the spectrometer, the input light cone should be matched to the spectrometer optics (f/1.8) while optimally filling the input slit taking into account the vertical dimension of the detector. With a spectrometer magnification factor of 1 from input slit to detector plane, the usable slit height of the NIR spectrometer is restricted to 500 µm. Figure 3.4.(a) shows the main elements of the optical design for the NIR arm of the beamsplitter configuration. The fibre launch lens forms an intermediate image of the fibre spot at the image slicer where the spot is then divided into two stacked hemispheres using a two-mirror arrangement based on the design detailed in Avila et al. (2012). The focusing achromatic doublet lenses at the NIR spectrometer entrance slit forms an image of the sliced fibre spot with a height of ≈600 µm and an input cone of f/1.7, which is closely matched to the spectrometer optics thus minimising potential for stray light from overfilling the input slit. This arrangement results in a factor of ≈1.5 increase in coupling efficiency compared to a design without the image slicer. A dichroic filter with a cutoff at ≈800 nm reflects the light in the VIS, as shown in the optical breadboard layout in Figure 3.4.(b). A short 1000 µm diameter fibre (NA=0.22) is then used to couple the light to the VIS spectrometer 25 µm wide input slit.

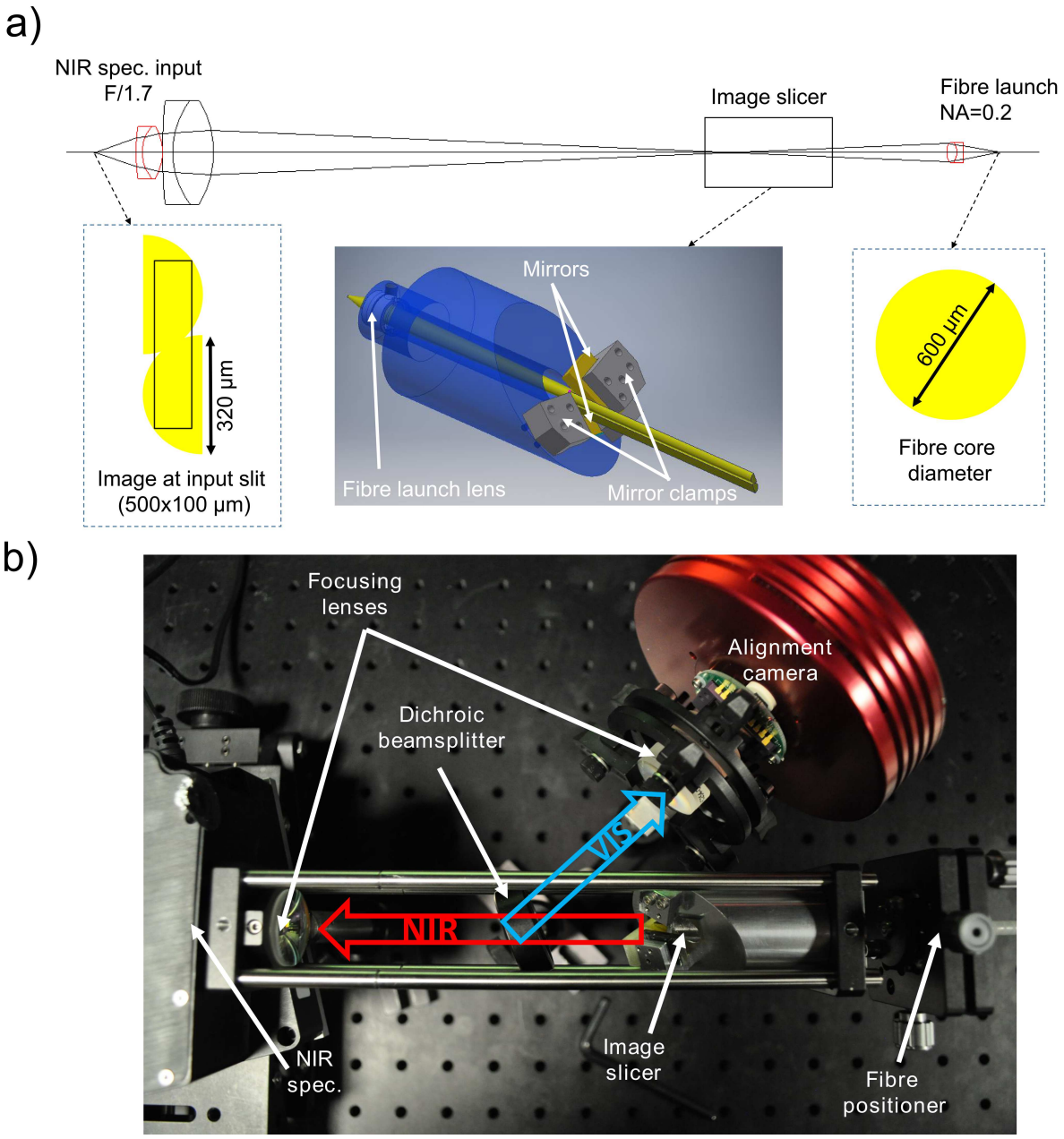

Figure 3.4: a) Optical design of the fibre launch, image slicer and NIR spectrometer input slit coupling; b) breadboard assembly showing the NIR and VIS arms of the dichroic beamsplitter configuration.

3.1.2 Absolute Calibration

The capability for measuring the absolute intensity of spectral lines relies on a radiometric calibration of the spectroscopic diagnostic using a uniform radiance source placed in the line-of-sight. For diagnostics operating in the VIS range this is usually accomplished by placing an integrating sphere illuminated by a calibration standard lamp in front of the collection lens, ideally from inside the vessel in order

to account for the entire optical train including the port window.

For the MAST VIS-NIR diagnostics, the available integrating sphere and calibrated light source (OL-455 series with 150 W EKE halogen lamp) provided a calibration standard spectral radiance data in the range 385-780 nm, suitable for absolute calibration of the VIS spectrometer. A separate irradiance source was required to cover the NIR 900-1700 nm range. For this purpose a cavity blackbody source with a temperature controller was utilised to provide the known spectral radiance according to the Planck blackbody distribution (eqn 2.38). Since the aperture of the blackbody source was smaller than the diameter of the collimated spectroscopic line-of-sight afforded by the 50 mm diameter collection lens, a lambertian diffuser placed in front of the blackbody cavity aperture was used to provide a suitably uniform spectral radiance source for the NIR spectrometer. The calibration methodology using the blackbody irradiance standard and lambertian diffuser is described in more detail in Appendix A. As access to the MAST vessel was not possible during the commissioning phase of the VIS-NIR diagnostic, the quartz window transmission could not be directly measured. The integrating sphere (VIS calibration) and the lambertian diffuser illuminated by the blackbody source (NIR calibration) were thus placed in front of the collection lens with the lens removed from the port window goniometer.

Figures 3.5 and 3.6 show the spectral radiance of the integrating sphere and blackbody source, the raw DN spectrum from a sample single exposure during the calibration, and the resultant calibrated spectrum and uncertainty ($\pm 1\sigma$). For the VIS calibration, the uncertainty in the source radiance has been estimated to be $< 5\%$ based on a previously produced spectral radiance calibration sheet. For the NIR calibration, the uncertainty in the spectral radiance (reflection of the spectral irradiance on the lambertian diffuser, as described in Appendix A) takes into account the propagation of independent measurement errors, including: the size of the blackbody cavity aperture (25 ± 1 mm); the distance to the lambertian diffuser (500 ± 5 mm); the viewing angle of the lens with respect to the diffuser ($30^\circ \pm 5^\circ$); and the reflectance of the diffuser plate (97 ± 2 %). The uncertainty associated with the temperature controller was neglected as it is assumed to be relatively small compared with the distance and angle measurements. The absolutely calibrated spectrum is then given by

$$L_\lambda = L_{\lambda,cal} \left(\frac{DN_\lambda}{DN_{\lambda,cal}} \right) \left(\frac{t_{int,cal}}{t_{int}} \right) \frac{1}{T_{pw}} \tag{3.1}$$

where L_λ is the measurement spectral radiance, DN_λ is the background corrected measurement raw DN in counts, $L_{\lambda,cal}$ and and $DN_{\lambda,cal}$ are the spectral radiance and averaged background corrected raw DN of the calibration standard source, t_{int} and $t_{int,cal}$ the measurement and calibration exposure time and T_{pw} is the port window transmittance. The uncertainty in the calibrated spectrum (conversion of the measurement raw DN counts to spectral radiance units) for a single exposure with subtracted dark frame includes:

- Estimated transmittance and vignetting of the quartz port window (0.85 ± 0.1).
- The standard deviation in the calibration and measurement dark frames which accounts for the electronic noise and dark current shot noise.
- The signal shot noise which is estimated by converting the raw DN to electrons using the camera's gain setting.

The dominant term in the total measurement error estimate is associated with the port window transmittance, except for spectral regions of low detector quantum efficiency. Figure 3.7 demonstrates the sensitivity of the absolute measurements in the VIS and NIR by converting the raw digital counts of a single dark exposure (VIS: 5 ms, NIR: 10 ms) to spectral radiance units. The estimated noise equivalent power (NEP), defined as the optical power which yields a signal-to-noise (SNR) ratio of 1 independent of exposure time, is therefore: NEP(475-675 nm)$\approx$ 0.75 mW m^{-2} sr^{-1} Hz$^{-1/2}$ and NEP(1000-1650 nm)$\approx$ 0.02 mW m^{-2} sr^{-1} Hz$^{-1/2}$. The throughput of the NIR spectrometer in this range is therefore greater than the VIS spectrometer by a factor of $\approx$38, and is mainly associated with the reduced optical coupling efficiency from the input fibre to the VIS spectrometer entrance slit. Since the total intensity of the low-n Paschen lines is lower than the Balmer lines by roughly the same amount, the VIS and NIR spectral radiance sensitivity is therefore well matched for plasma measurements at similar exposure times.

In post-processing the VIS spectrometer data from the absolute calibration, a drift in the measured spectral radiance of the lamp source was observed over the course of the measurements, yielding a systematic offset. This was not immediately obvious during the calibration as the spectra were recorded at difference luminance values and exposure times. Since it was not possible to repeat the procedure due to MAST scheduling constraints, the systematic offset of the calibration curve was instead corrected for by examining the D 5$\rightarrow$3 (1281.5 nm) and D 5$\rightarrow$2 (433.9 nm)

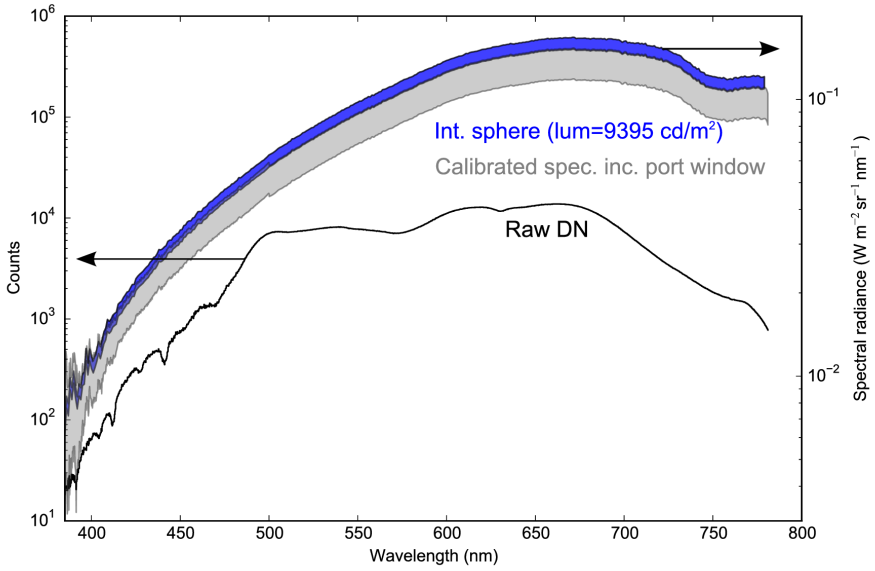

Figure 3.5: Sample VIS absolute calibration spectrum including the raw DN signal (black), integrating sphere spectral radiance (blue) and calibrated spectral radiance accounting for the port window (grey). Colour bands represent estimated calibration uncertainty of $\pm 1\sigma$.

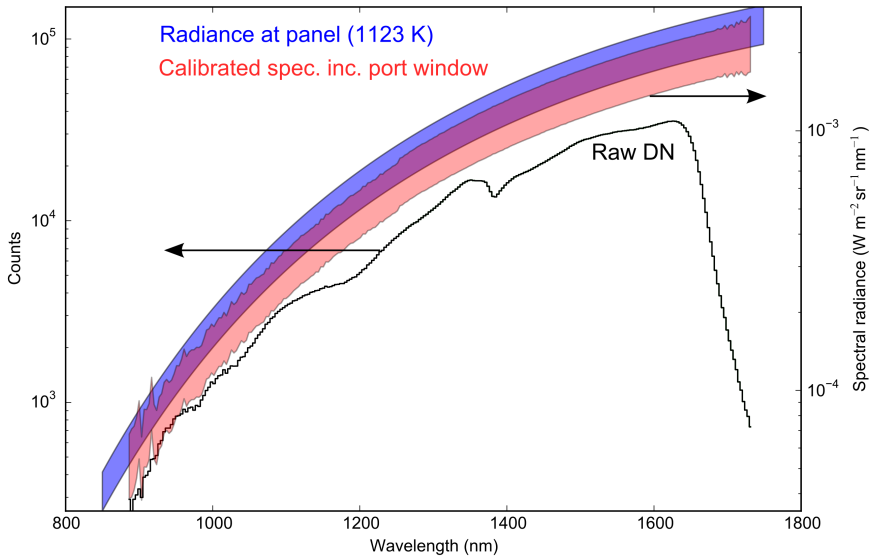

Figure 3.6: Sample NIR absolute calibration spectrum including the raw DN signal (black), spectral radiance at the lambertian diffuser panel (blue) and calibrated spectral radiance accounting for the port window (red). Colour bands represent estimated calibration uncertainty of $\pm 1\sigma$.

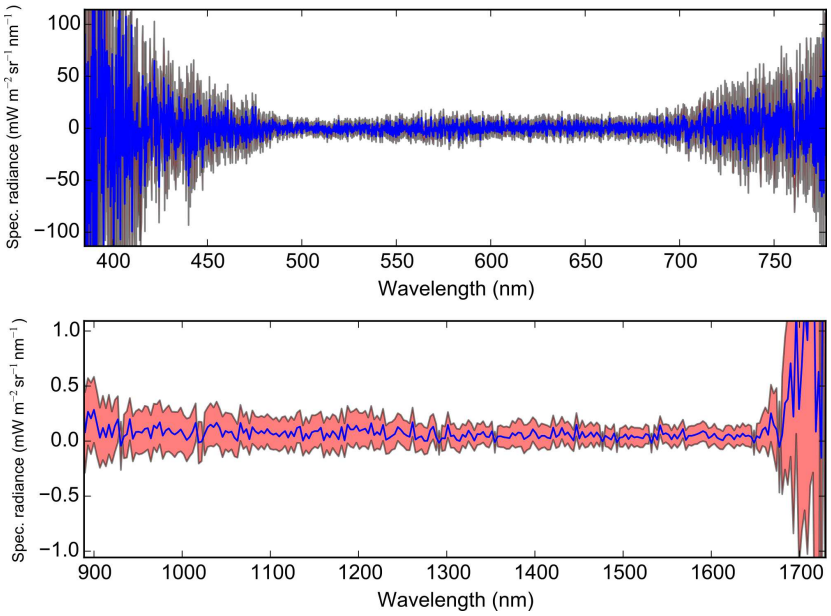

Figure 3.7: Absolute spectral radiance sensitivity of the VIS (top) and NIR (bottom) spectroscopic channels from a single dark 5 ms (VIS) and 10 ms (NIR) exposure. Colour bands represent estimated calibration uncertainty of $\pm 1\sigma$.

line ratio. Since these lines share the same principal quantum number of the upper excited state, their intensity ratio is determined simply by the ratio of the Einstein A spontaneous emission coefficients. Taking into account the photon energy of each transition, the D 5→2 / D 5→3 ratio in units of mW m^{-2} sr^{-1} is 3.4. Figure 3.8.(a) shows the time evolution of the D 5→3 and D 5→2 line intensities from pulse 29964 during a volume recombining phase of the discharge which facilitated high SNR of the two lines for comparison. In Figure 3.8.(b) the resulting line ratios are plotted yielding an average line ratio of 3.1 ± 0.2. The VIS absolute calibration was subsequently adjusted for all recorded spectra based on these results.

3.2 Spectral Survey Results

3.2.1 Identification of Spectral Features

Hydrogen isotope spectral lines, low charge state impurity spectral lines and molecular bands from emission in the VIS range (350-800 nm) of tokamak edge and divertor plasmas have been well characterised due to the ubiquitous use of CCDs and relatively straightforward signal extraction techniques associated with detection of photons with energies in the VIS range. As such, the identification of the typical

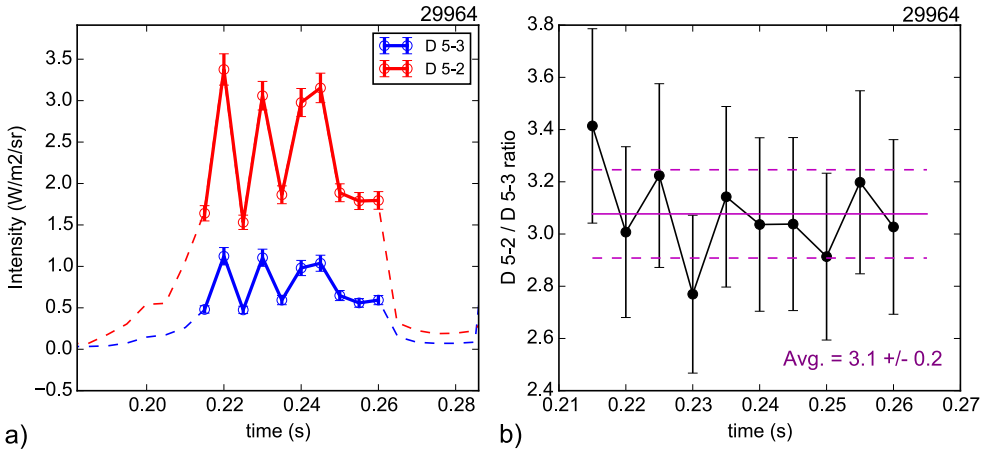

Figure 3.8: a) Time evolution of the D 5→3 and D 5→2 line intensities; b) time evolution of the D 5→2 / D 5→3 line ratio.

spectral features recorded with the VIS spectrometer relied mostly on previous spectroscopic studies (e.g. Stratton et al., 2008; Biewer et al., 2004; Meigs et al., 1998; Whyte et al., 2001; Brooks et al., 1997; Maggi, 1997). Figure 3.9 shows a typical spectrum measured using the VIS spectrometer accompanied by higher resolution spectra from the MAST SPEX spectrometer (Princeton Instruments SpectraPro 2500i) near 465 nm and 434 nm. Strong emission lines include C II, C III, deuterium Balmer series, O II and He II, as well as the C_2 and CD molecular bands. Also shown is the instrumental line shape and FWHM which exhibits an asymmetrical profile, most likely as a result of aberrations (coma, astigmatism) introduced by the spectrometer optics in imaging the entrance slit onto the linear CCD array.

The identification of the spectral features in the measured NIR spectra is made more difficult due to the coarse resolution of the NIR spectrometer which results in many blended spectral line features. This is compounded with a relatively poor characterisation of the NIR spectral region with few spectroscopic studies (see Section 1.2) in the fusion plasma context. The approach used in characterising the typical NIR spectral features thus relied on first identifying the strong lines from low charge intrinsic impurity species (C I, C II, He I, He II) and the deuterium Paschen series lines using the NIST Atomic Database (Kramida et al., 2014) and the ADAS atomic *PEC* data from the ADF15 derived class (Summers, 2004). A useful NIST Atomic Database feature is the Saha-LTE spectrum for a given species and charge state which provides an indication of the relative line strengths, although it must be used with caution as the typical excited populations in the tokamak divertor plasmas are in the collisional-radiative regime. To isolate spectral lines from

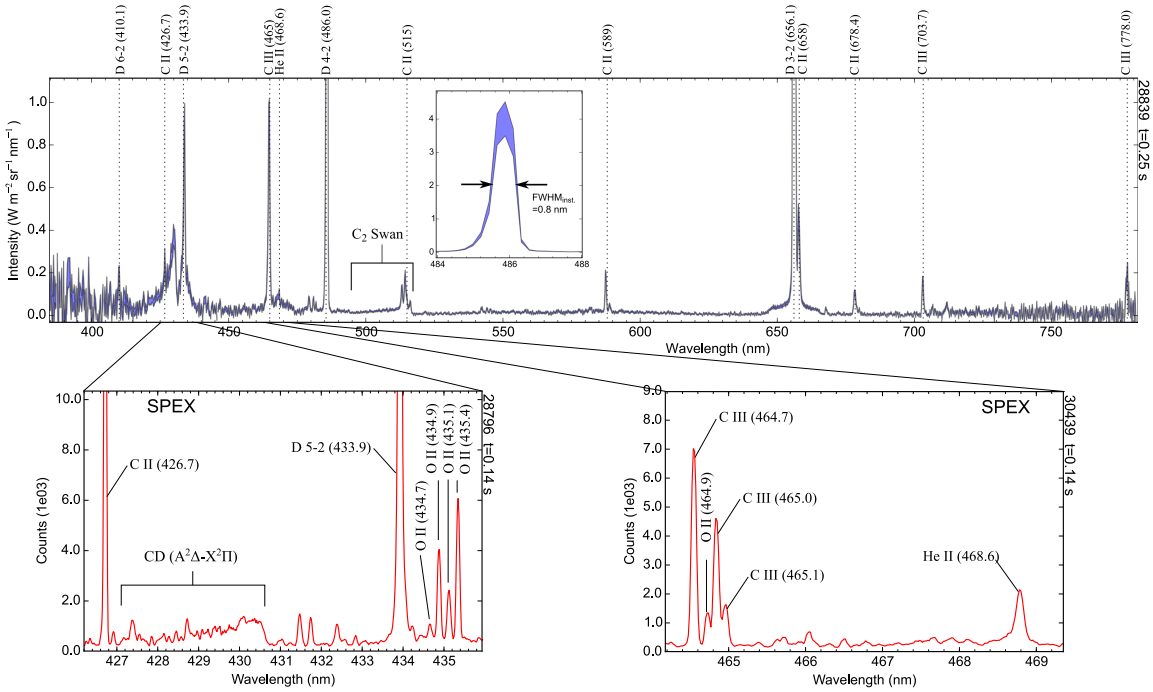

Figure 3.9: Spectrum from the VIS spectrometer (top) and higher resolution spectra from the SPEX spectrometer (bottom).

the blended features in the recorded spectra, a multi-Gaussian model (i.e., each candidate spectral line approximated by one Gaussian component) was then applied to fit the experimental data in a least-squares manner using the Levenberg-Marquardt algorithm (Press et al., 1986) for minimisation of the χ^2 statistic, with constraints on the center wavelength ($\pm$0.5 nm) and the spectral width of the candidate lines. To account for the spectral variation of the instrumental line width, known isolated spectral lines from Ar and Xe discharge tubes were measured and fitted using a Gaussian model. Figure 3.10 shows the FWHM spectral distribution from the discharge tube measurements and the best fit second order polynomial which yielded normalised residuals within two standard deviations of the estimated line widths. The polynomial coefficients obtained from this fit were then used to constrain the FWHM of the candidate spectral lines as a function of their central wavelengths.

Figure 3.11 shows an example of the multi-Gaussian fit (top two plots) to experimental data obtained with the NIR spectrometer from MAST pulse 28839 at t =0.25 s. A bremsstrahlung model (eqn. 2.5) was used to account for the continuum baseline with a λ^{-2} dependence parametrised by n_e and T_e, an estimated effective charge of Z_{eff} = 1.5 and an estimated length of the region of emission along the spectrometer LOS of ΔL =20 cm. The normalised residuals across the spectrum suggest a reasonable fit to the data in the vicinity of the candidate lines,

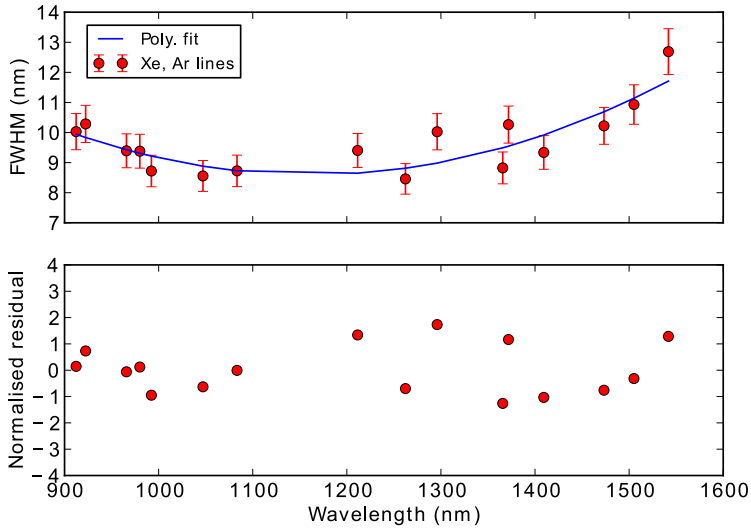

Figure 3.10: NIR spectrometer instrumental line FWHM measurements using Xe and Ar discharge tubes and polynomial fit to the spectral variation of line widths.

although the model proved to be relatively insensitive to the continuum baseline with very large fit uncertainties for n_e and T_e. This is manifested as a positive offset in the residual values in regions free of spectral lines (e.g., 1030-1070 nm) suggesting an underestimate in the background intensity. Also evident from the residual structure in the 1330-1400 nm region is the presence of additional weak spectral lines that were not accounted for by the model. The uncertainty estimates in line intensity obtained from fitting the candidate lines with a Gaussian model ranged from around 10% for the strong lines to 30% for the weak lines. Since the spectrum contains a large number of neutral carbon lines, comparison of the measured relative intensities to atomic data is useful for verifying the selected candidate lines and identifying possible overlapping lines of different species. The two bottom plots in Figure 3.11 compare the reconstructed spectrum obtained from the multi-Gaussian fit results (shown line widths are narrower for clarity) to a synthetic spectrum composed of relative C I intensities obtained using ADAS excitation $PECs$. Qualitative agreement is observed for a wide range of n_e and T_e values, but good quantitative agreement was obtained for $n_e = 10^{18}$ m^{-3} and $T_e = 4$ eV, except for two C I lines (1166.0 nm and 1167.0 nm) which exhibit significantly lower intensity compared to the experimental results. The neutral boron doublet at 1166 nm overlaps the two C I lines and may account for the discrepancy. It should be noted that the use of excitation PEC coefficients to derive the C I relative line intensities is valid only for ionising plasma conditions. This is an appropriate assumption for $T_e \gtrsim 1$ eV according to the fractional abundance of neutral carbon shown in Figure 3.12. Un-

der such conditions the ionisation front of the neutral carbon influx is located in close proximity to the divertor target. The presence of multiple C I lines in the NIR spectrum could potentially be used to infer the electron temperature and density if the measured relative intensity pattern can be reproduced with a unique set of atomic data excitation $PECs$ in the n_e and T_e parameter space. A more detailed investigation is needed to determine the sensitivity of such a technique, including the influence of C I metastable levels on the excited state population structure.

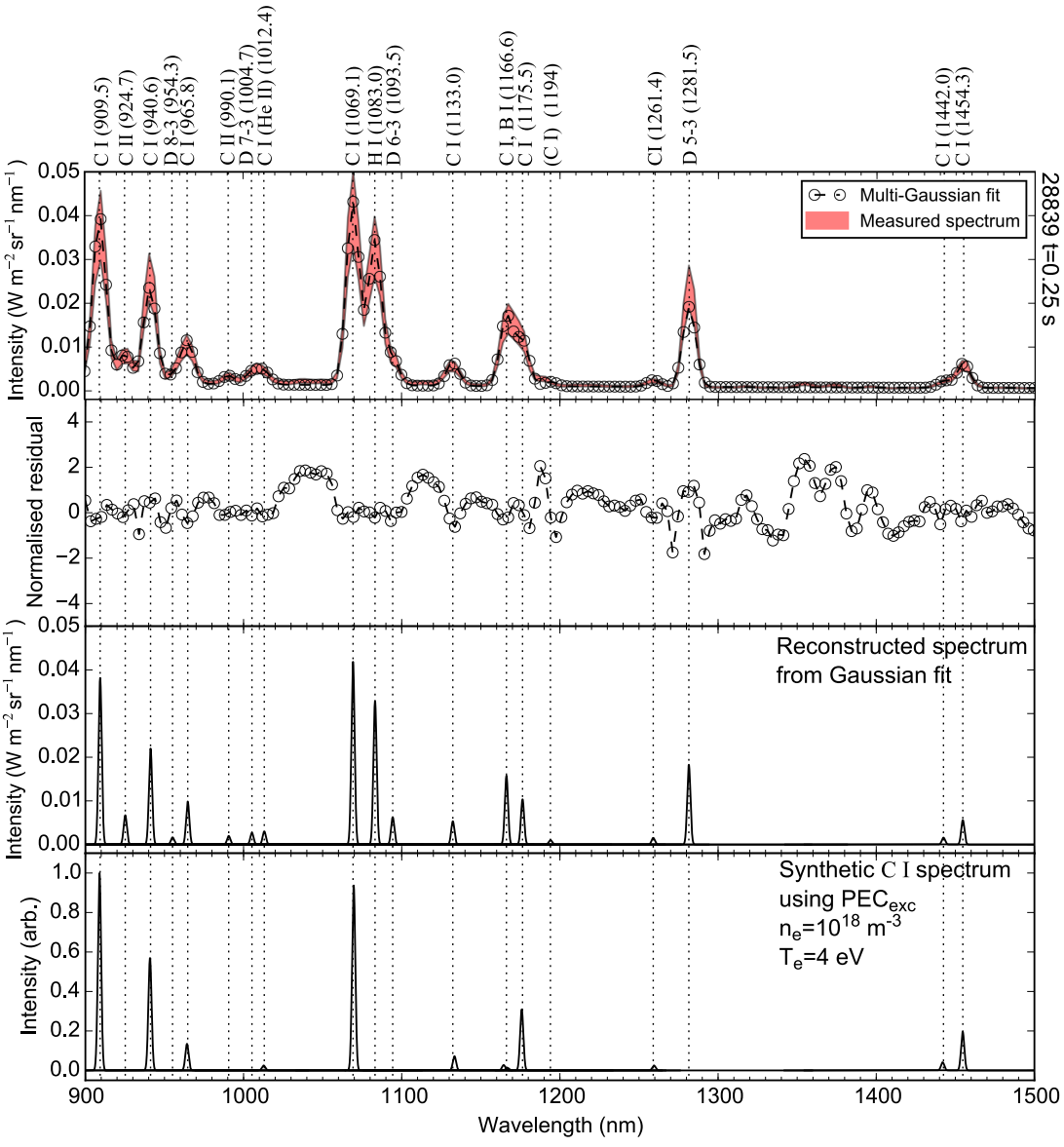

Figure 3.11: Multi-Gaussian fit to measured NIR spectrum and normalised residuals (top two plots); reconstructed spectrum from multi-Gaussian fit with narrow line widths for clarity; and C I synthetic spectrum using ADAS excitation PEC coefficients (bottom two plots).

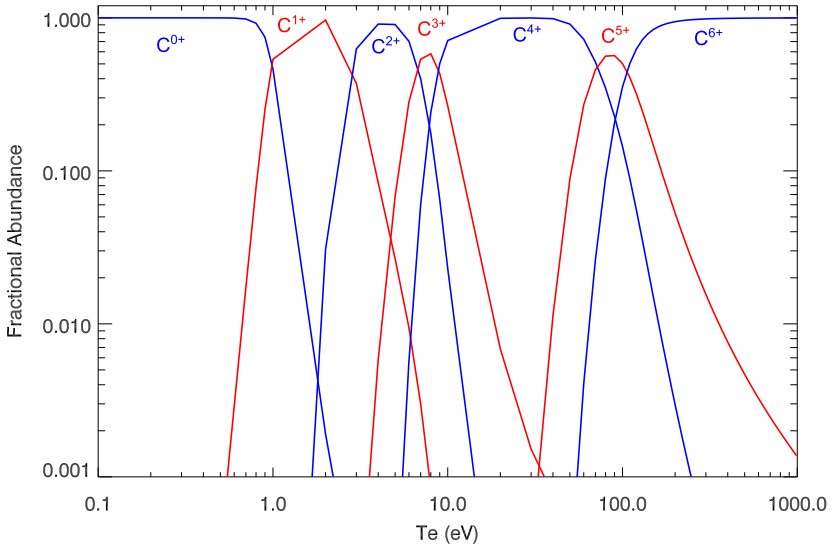

Figure 3.12: Fractional abundances of carbon ionisation stages as a function of plasma electron temperature derived using ADAS data (Summers, 2004). Reproduced with permission from Harrison (2010).

3.2.2 Neutral Boron Line

The possible presence of a neutral boron line (B I $2s^2 3p \rightarrow 2s^2 3s$ doublet, 1166.3 nm, 1166.6 nm) is of interest for monitoring the impact of vessel conditioning on plasma performance. In tokamaks with a carbon first wall, the process of boronisation is typically used to condition the vessel by vapour deposition of a thin boron layer (on MAST using trimethylborane and helium glow discharge) onto plasma facing components. This process has been widely reported (e.g Higashijima et al., 1995; Nishimura et al., 2003) to be effective in reducing the oxygen concentration through gettering and reducing plasma recycling by trapping hydrogen (wall pumping). The reduced impurity content and reduction of plasma fuelling from the wall have been shown to be highly beneficial for access to high performance operating regimes (e.g Kugel et al., 2003). On MAST the influence of boronisation on plasma performance is typically monitored by measuring the D 5→2 / O II ratio (see lines near 435 nm in Figure 3.9); however, a direct measurement of the influx of boron via wall erosion is not available due to insufficient brightness of boron spectral lines in the VIS spectrometer range 380-750 nm (e.g., B III 424 nm $1s^2 5d \rightarrow 1s^2 4p$, B III 463 nm $1s^2 5p \rightarrow 1s^2 4d$, B II 412 nm and 494 nm $1s^2 2s4f \rightarrow 1s^2 2s3d$). According to the NIST Atomic Database, the B I doublet ($2s^2 3p \rightarrow 1s^2 2s3d$) at 1166.3 nm and 1166.6 nm is the brightest neutral boron line in the range 300-2000 nm assuming LTE conditions. Due to the close proximity of the B I doublet to the two C I

lines ($2s^2 2p3d \rightarrow 2s^2 2p3p$ at 1166.96 nm and 1165.97) direct intensity measurement with the coarse resolution NIR spectrometer is not possible. As a result only the combined total line intensity of the C I and B I doublets can be inferred using the multi-Gaussian fitting technique.

To verify the presence of the B I doublet in the NIR spectra, a line ratio comparison was carried out covering a large number of pulses throughout the M9 campaign. Figure 3.13 shows the pulse averaged line ratios for the following line combinations:

- (D 5→2) / (O II 435 nm) measured with the SPEX spectrometer.
- (D 5→3) / (C I + B I 1166 nm), measured with the NIR spectrometer.
- (CI 1176 nm) / (C I + B I 1166 nm), measured with the NIR spectrometer.

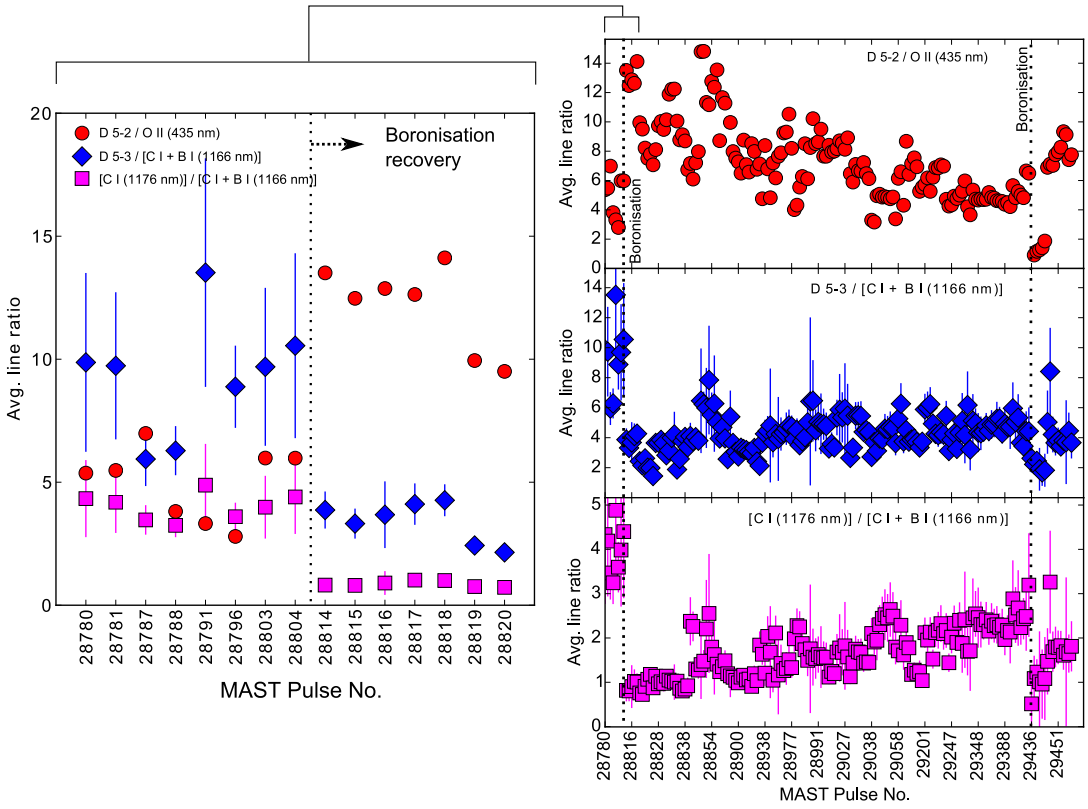

Figure 3.13: Pulse scan of select line ratios measured by the NIR spectrometer and the SPEX visible spectrometer spanning two boronisation cycles during the M9 campaign. Error bars represent the estimated uncertainty, $\pm 1\sigma$, in the spectral line intensity ratios.

The average ratio for each pulse was calculated over the time window corresponding to the flat-top phase of the plasma current. A clear increase in the (D 5→2)/(O II 435 nm) ratio and conversely a decrease in the (D 5→3)/(C I + B I 1166 nm) and

(C I 1176 nm)/(C I + B I 1166 nm) ratios is observed right after boronisation (left plot in Figure 3.13). This is consistent with a reduction in the oxygen concentration via gettering and, assuming the total line intensity at 1166 nm contains the B I doublet, an increase in the boron emission as a result of PSI with the boron coated tiles. The overall gradual decrease in the (D 5→2)/(O II 435 nm) ratio with pulse number is also evident (Figure 3.13 right plot) and is most likely associated with a reduction in the ability of the wall surface to getter oxygen as the boron coating material is slowly removed in areas of net erosion and deposited elsewhere in the vessel. Consistent with this behaviour is the gradual increase in the (C I 1176 nm)/(C I + B I 1166 nm) ratio signalling a reduction in boron influx. This same trend is less pronounced, however, in the time evolution of the (D 5→3)/(C I + B I 1166 nm) ratio and may be influenced to some extent by an increase in the intensity of the C I lines at 1166 nm which would, in effect, counteract the decreasing boron line intensity. Further evidence in support of the presence of the B I doublet is shown in Figure 3.14 in which the measured intensity of the C I + B I 1166 nm lines and the C I 1442 nm line is compared to the intensity of the C I 909 nm line for two pulses before (28791, 28796) and shortly after boronisation (28817, 28820). Also shown in this figure is the region of expected values of the line ratios (CI 909 nm)/(C I 1166 nm) and (C I 909 nm)/(C I 1442 nm) obtained using ADAS excitation $PECs$ for $T_e > 3$ eV and $10^{18} \leq n_e \leq 10^{19}$ m^{-3}. This is an appropriate temperature and density range if ionising plasma conditions can be assumed along the VIS-NIR LOS. Given the absence of high-n Balmer and Paschen lines in the VIS-NIR spectra which are typically associated with high density and low temperature volume recombining plasma, such an assumption is reasonable. The measured (C I 909 nm)/(C I 1442 nm) line ratio for both pre and post-boronisation pulses remains relatively constant and lies within the expected region, whereas there is a clear departure in the (C I + B I 1166 nm)/(C I 909 nm) line ratio values which lie beyond the expected range of values for the two post-boronisation pules. This cannot be accounted for by the presence of the two C I lines at 1166 nm alone. Thus the most likely cause of the increase in the total line intensity at 1166 nm is attributed to the presence of the B I doublet, as there are no other lines in this region of the NIR spectrum associated with impurities typically present (e.g., O, He) in MAST discharges.

In addition to the commonly used (D 5→2)/(O II 435 nm) line ratio to monitor the impact of boronisation on plasma performance, spectroscopic measurement of boron influx using the B I 1666 nm doublet intensity offers a means to directly monitor the degradation of the boron coating in different vessel locations. The

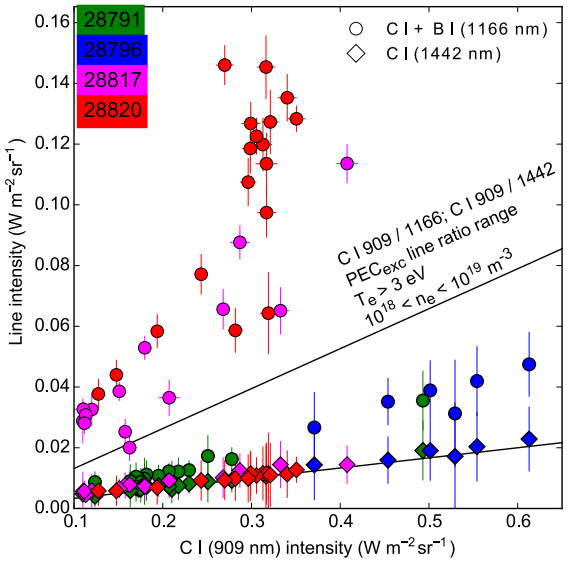

Figure 3.14: C I + B I (1166 nm) and C I (1442 nm) line intensity vs. C I (909 nm) line intensity for two pulses before boronisation (28791, 28796) and two pulses after boronisation (28817, 28820).

supporting evidence for the presence of the B I doublet in the NIR spectrum can therefore be considered in future for the selection of an appropriate spectrometer with sufficient resolution and sensitivity for more accurate measurements in the 1166 nm region.

3.2.3 Evaluation of Electron Temperature

Passive divertor spectroscopy plays a key role in characterising plasma emission associated with the detached operating regime and facilitates measurement estimates of T_e and n_e at and away from the strike points. The spectral resolution of the VIS-NIR diagnostic ($\approx$ 1 and 10 nm, respectively) is insufficient for a quantitative analysis of spectral line broadening as the instrumental function width is much larger than the line profile widths associated with the broadening and splitting mechanisms described in Section 2.1.4. However, given sufficient SNR, it is possible to estimate the total line intensities of the Balmer and Paschen series lines for determination of the excited state population densities and line ratios. This is of particular interest for T_e estimation in detached plasmas using the technique described in Section 2.3.1 if the excited state populations are primarily driven by recombination processes.

MAST pulse 29964 from experiment M9-IPS-010 (benchmarking of JINTRAC

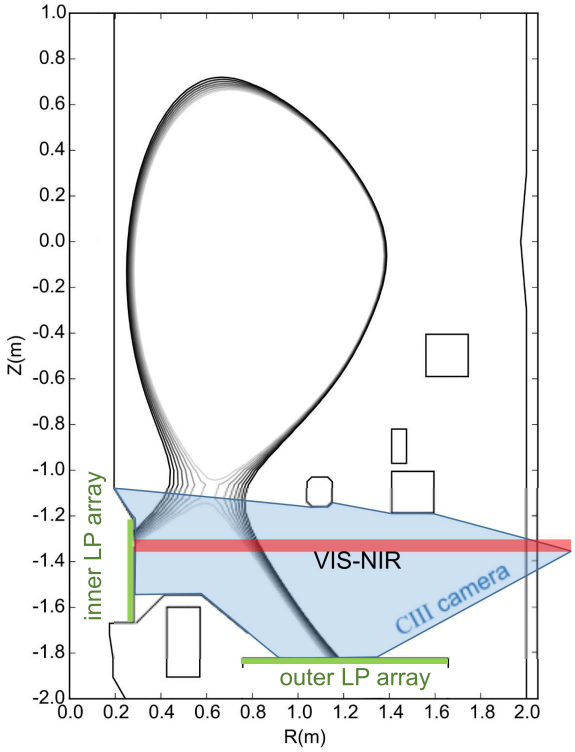

Figure 3.15: MAST lower divertor diagnostics locations, viewing geometry and edge magnetic equilibrium reconstruction for pulse 29964. Note: the C III camera is the Coherence Imaging diagnostic (Silburn et al., 2014).

/ EDGE2D modelling with high-field side (HFS) gas puffing) provided a good data set for analysis of Balmer-Paschen spectra in volume recombining conditions. The plasma density was ramped by puffing D_2 gas using a controllable HFS gas valve (cHFS) located at the midplane of the central column. The main plasma parameters for the discharge are: maximum ohmic heating power, $P_{ohm} = 1.4$ MW; total neutral beam heating power $P_{NBI} = 2$ MW; average plasma current $I_p = 550$ kA; maximum toroidal magnetic field magnitude, $B_\phi = 0.43$ T; lower single null (LSN) divertor configuration with the ion ∇B drift directed downwards. Figure 3.15 shows the poloidal viewing geometry of the VIS-NIR spectroscopy diagnostic and C III filtered imaging camera, as well as the inner and outer Langmuir probe arrays (data from the outer probe arrays was not used in the analysis). Figure 3.16 shows the time evolution of the line averaged plasma density; plasma current; total ion saturation current at the inner divertor strike point; fast D 3→2 filtered photo-multiplier tube (PMT) viewing the outer mid-plane; and the cHFS fuelling time window at a constant valve pressure of 400 mbar. Also shown is the time evolution of selected spectral line in-

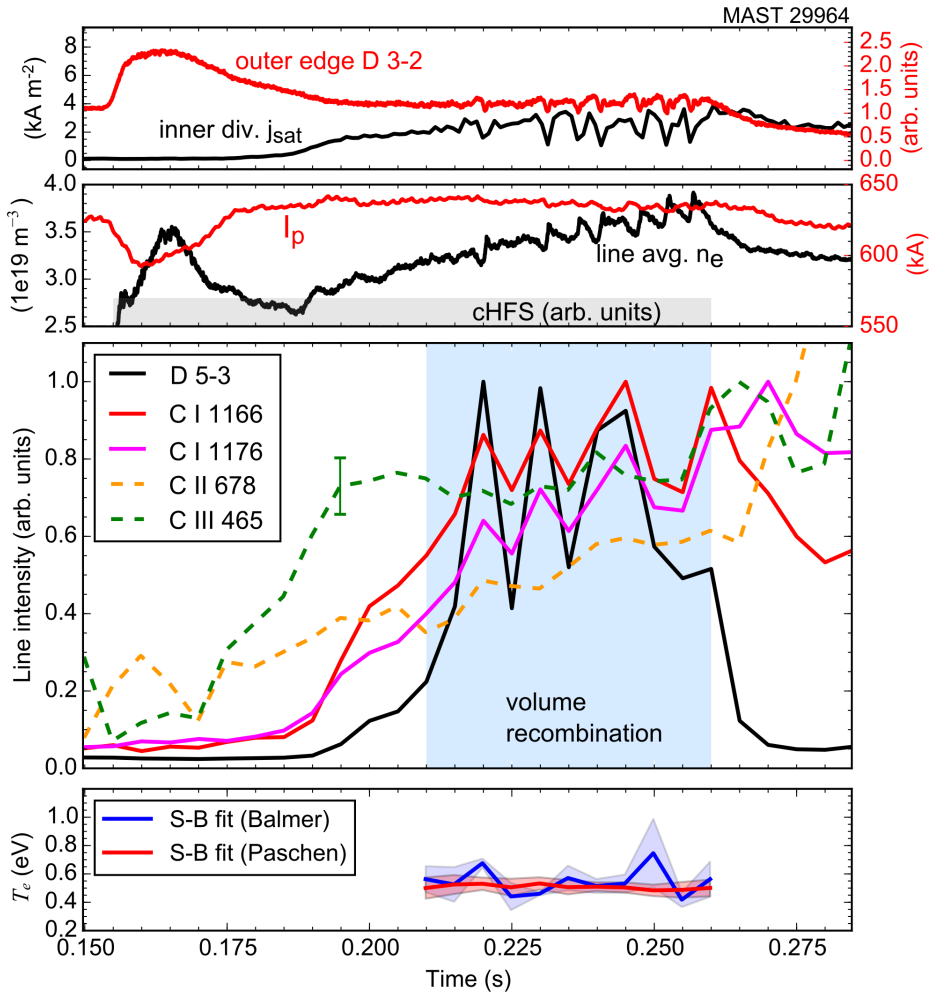

Figure 3.16: Time traces of signals from pulse 29964: outer edge D 3→2 intensity; inner divertor saturation current j_{sat} measured by Langmuir probes; plasma current I_p; line averaged density; cHFS fuelling window; D 5→3 intensity; C I, C II, C III line intensities. Also shown are T_e estimates from the Saha-Boltzmann population distribution applied to the Balmer and Paschen series line intensities.

tensities from the VIS-NIR diagnostic, including the D 5→3 line and neutral, singly and doubly ionised carbon lines. Shortly after the onset of cHFS fuelling, the plasma line averaged density and edge D 3→2 intensity rise while a decrease in the plasma current is observed, likely due to an increase in the plasma resistivity as a result of the cold gas puffing. Fluctuations in the line averaged density, inner divertor ion flux and outer edge D 3→2 intensity are observed at $t = 0.21 - 0.26$ s and are attributed to short-lived transitions from the low confinement to high confinement mode (L-H transitions). These fluctuations are particularly pronounced in the neutral carbon and D 5→3 line intensities along the VIS-NIR divertor LOS. Figure 3.17 shows two frames from a mid-plane port filtered D 3→2 camera (DIVCAM) which exhibit the

typical plasma emission signatures associated with L and H modes. At $t = 0.252$ s the plasma edge is characterised by a well defined region of emission consistent with good confinement due to the formation of an edge pedestal defined by steep temperature and density gradients at the edge which suppresses radial transport. In contrast to this sharp boundary, at $t = 0.255$ s the emission at the edge and SOL exhibits wispy filamentary structures along magnetic field lines which channel expelled heat and particles from the plasma core and are characteristic of the low confinement mode. This is further supported by the anti-correlated line averaged density and edge D 3→2 signals such that a sudden increase in density during the L-H transition due to increased confinement corresponds to a sudden decrease in the wall recycling flux and thus a decrease in the light emitted by edge neutrals. The decrease in particle flux to the divertor during the brief transitions to H-mode is also consistent with the above phenomenology. The location of cHFS fuelling is indicated by the bright region of emission at the central column mid-plane valve position.

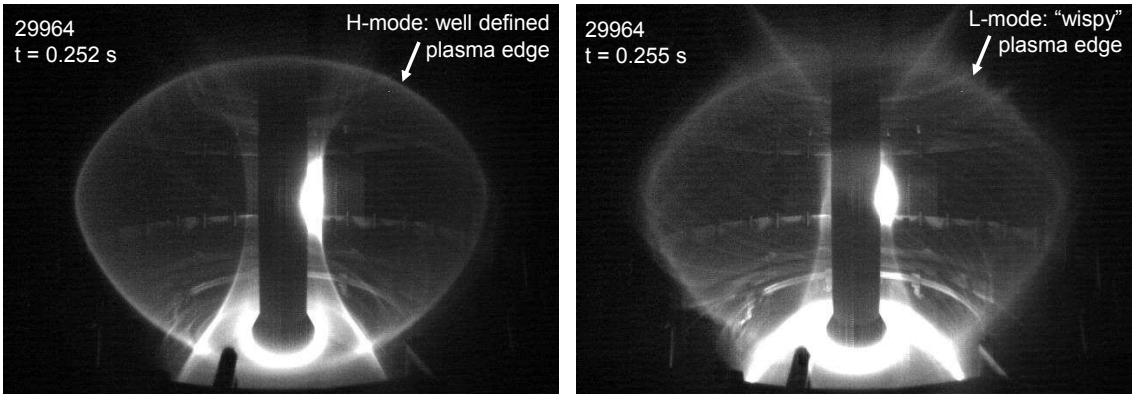

Figure 3.17: D 3→2 emission measurements from a mid-plane filtered camera for pulse 29964 at $t = 0.252$ s and $t = 0.255$ s.

The time window of volume recombination ($t = 0.21 - 0.26$ s) is inferred from the presence of high-n lines, the SNR of which is typically below the measurement noise floor of the VIS-NIR spectrometers, except for the D 5→3 line. For example, Figure 3.18 shows the high-n Balmer and Paschen lines during the volume recombination phase. The line intensities on the VIS spectrometer are calculated by summation over the appropriate pixel range of the Balmer lines from which the background is then subtracted by taking an average of near-by pixels in a region free of impurity lines. The SNR of the D 8→2 line is low due to the poor sensitivity below 395 nm. Estimating the Paschen and impurity line intensities from the NIR spectra is

achieved by the multi-Gaussian least-squares fitting procedure. Whereas the uncertainty on the Balmer lines is estimated from summation by propagating the error on each pixel value in quadrature, the uncertainty on the NIR line intensities is estimated from the standard error on the best-fit parameter values.

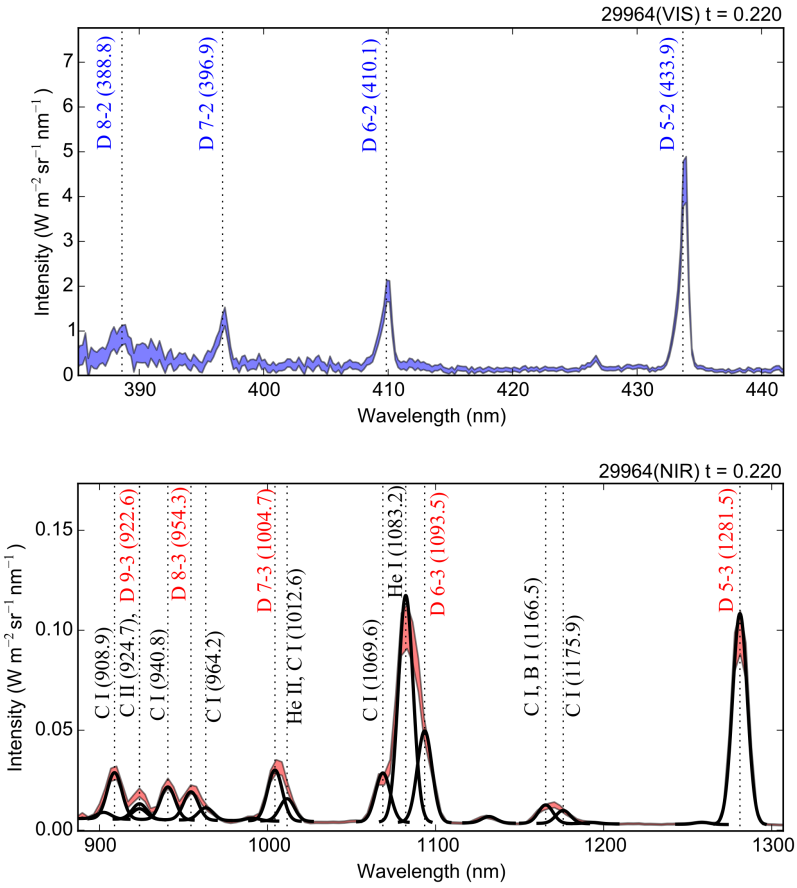

Figure 3.18: Balmer (top) and Paschen (bottom) series recombination spectra for pulse 29964 at $t = 0.220$ s. The Paschen lines have been isolated from the blended line spectrum using the multi-Gaussian fitting technique.

To investigate the degree to which the excited state population densities are influenced by recombination fluxes, the ratios of Balmer and Paschen lines are compared to atomic data using ADAS $PECs$ and eqn. 2.22, where both excitation and recombination contributions are considered, metastable levels have been ignored and $n_e = n_i$ is assumed. The time evolution of selected Balmer and Paschen line ratios from the VIS-NIR measurements during the volume recombination window is shown in Figure 3.19. The observed line ratios exhibit relatively constant values throughout this period, within the measurement uncertainty. To estimate the electron temperature, the measured line ratios are plotted against PEC derived line ratios as a

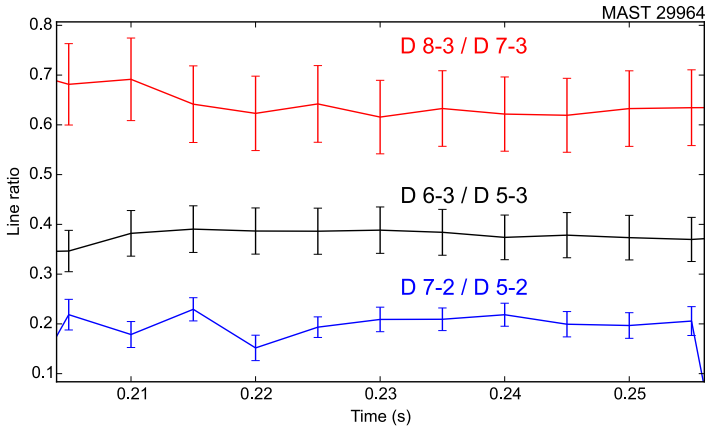

Figure 3.19: Deuterium line intensity ratios from the VIS-NIR spectroscopic measurements during the volume recombination phase in pulse 29964.

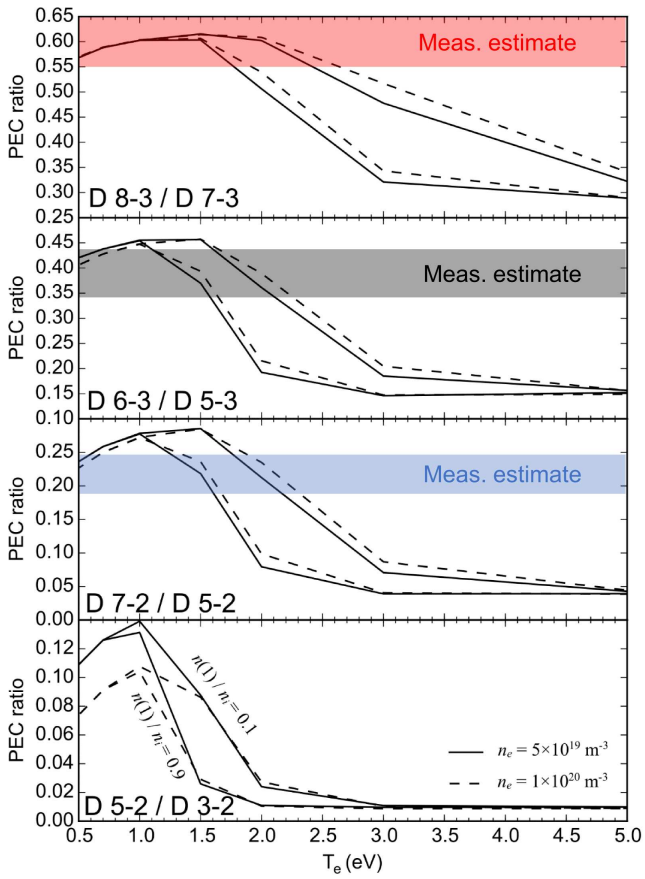

Figure 3.20: Calculated deuterium line ratios using ADAS *PEC* coefficients for two density values and two neutral fraction values. Also shown are measurement estimates of the line ratios from pulse 29964 (see Figure 3.19)

.

function of T_e in Figure 3.20 for two representative divertor density values and high and low values of the neutral fraction ($n(1)/n_i = 0.1$ and $n(1)/n_i = 0.9$). The neutral density can influence the line ratios significantly depending on the particular lines examined and the threshold value of T_e below which recombination begins to predominate. Since this temperature threshold varies for different line combinations, it can be used as a diagnostic tool to determine which side of the line ratio curve in Figure 3.20 corresponds to the measured line ratio. For example, the range of possible T_e values corresponding to the measured D 8→3 / D 7→3 ratio is about 0.5-2.5 eV depending on the neutral fraction. However, the D 6→3 / D 5→3 and D 7→2 / D 5→2 measured ratios constrain the possible values to $T_e \approx 0.5$ eV or 1.3-2 eV. The D 5→2 / D 3→2 line ratio is quite useful as it exhibits the highest sensitivity to recombination at very low temperatures and could therefore be used to further constrain the possible temperature range. For instance, if this line ratio is above ≈ 0.1 a temperatures above 1.5 eV can be ruled out for any reasonable value of the neutral fraction. Due to detector saturation this measurement was not available in the time window of interest. Therefore, without diagnostic access to the D 5→2 / D 3→2 line ratio, one cannot definitively rule out the higher end of the temperature range as indicated by the obtained line ratio measurements.

Ignoring the possible influence of excitation fluxes (i.e., assuming that the line ratios are consistent with $T_e < 1$ eV in Figure 3.20), the populations of the upper levels from the measured Balmer and Paschen lines with $n \geq 5$ are in the LTE regime. A more precise value of the line averaged T_e can then be estimated using the logarithmic form of the Saha equation 2.39. Figure 3.21 shows the measured line intensities of the Balmer and Paschen lines at $t = 0.22$ s and the corresponding T_e values obtained from a linear fit to the relative excited state populations using least-squares χ^2 minimisation. Good agreement is observed between the T_e fit estimates obtained using the Balmer ($T_e = 0.65 \pm 0.04$ eV) and Paschen ($T_e = 0.53 \pm 0.04$ eV) series lines, although the low value of χ^2/DoF for the Balmer fit is indicative of overestimated error variances as a result of the large uncertainty in the D 8→2 line measurement. The line intensity values can be reconstructed using recombination $PECs$ with good agreement at $T_e = 0.6$ eV over a density range $10^{20} \leq n_e \leq 10^{21}$ m^{-3}, as shown in Figure 3.21 (also shown are the D 3→2 and D 4→3 lines which could not be measured). It is also instructive to note that with additional information on the line averaged n_e from Stark broadening measurements, and assuming $n_e = n_i$, an estimate of the extent of the emitting region ΔL (see eqn. 2.1) along the spectroscopic LOS could be obtained. The time evolution of the T_e estimates from the Balmer

and Paschen line intensity measurements is shown in the bottom plot of Figure 3.16, with relatively constant values throughout the volume recombination phase of the discharge.

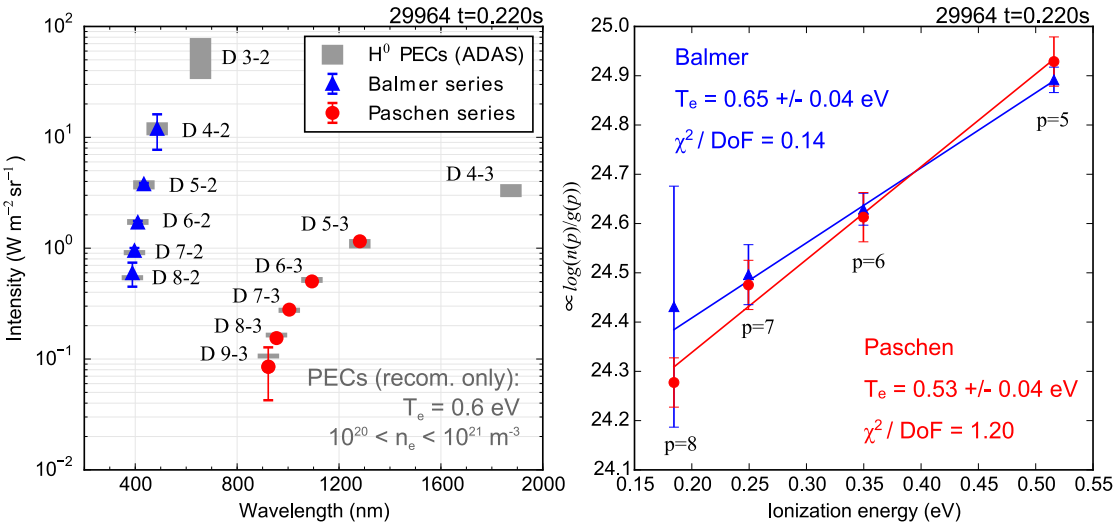

Figure 3.21: Balmer and Paschen measured line intensities using the VIS-NIR spectroscopy diagnostic relative to calculated intensities using recombination $PECs$ at $T_e = 0.6$ eV (left); excited state populations (normalised by their statistical weights) calculated from Balmer and Paschen line intensities and estimated T_e values from a linear least-squares fit and eqn. 2.39 (right).

In a typical MAST LSN divertor discharge, the VIS-NIR spectroscopic LOS intersects the outer divertor leg, private plasma region and the inner divertor strike point (see magnetic geometry in Figure 3.15). The line averaged intensity and T_e measurements are therefore insufficient for localising the region of emission which contributes most strongly to the observed line intensities. To interpret the spatial temperature distribution along the VIS-NIR LOS, the 2D reconstructed poloidal emissivity distribution of the C III 464.9 nm multiplet ($1s^2 2s3p \rightarrow 1s^2 2s3s$) is examined from absolute intensity measurements obtained using the Coherence Imaging diagnostic (Silburn et al., 2014), primarily used on MAST during the M9 campaign to study SOL and divertor flows. By taking the zeroth order moment of the recorded fringe pattern the LOS integrated emissivity is obtained with spatial resolution better than 1 cm and a time resolution of 2 ms with 1 ms exposures. The 2D emissivity distribution is then reconstructed by inverting the line averaged emissivity camera data using an iterative procedure based on the simultaneous algebraic reconstruction technique (SART) and assuming toroidal symmetry (see Silburn et al., 2014, and references therein). The 2D reconstructed emissivity matrix is then revolved

toroidally in order to obtain the emissivity distribution along the vertical plane which intersects the VIS-NIR LOS (see Figure 3.2). The resulting C III emissivity distributions are shown in Figure 3.22 for two times slices during and after the volume recombining window. At $t = 0.222$ s during the volume recombination phase the C III emission along the inner diveror leg is notably absent and peaks at the upstream inner separatrix near the X-point, whereas C III emission along the outer divertor leg is relatively evenly distributed. At $t = 0.282$, after the cHFS fuelling is turned off, strong C III emission is observed along the inner divertor leg and near the inner strike point as well as more modest emission at the outer leg and outer divertor strike point. Since the line emission of a particular carbon charge state is sensitive to T_e depending on its fractional abundance (see Figure 3.12), the observed C III emission regions in Figure 3.22 corresponds roughly to a temperature in the range $3 \leq T_e \leq 10$ eV. Given the upper bound of $T_e \lesssim 2.3$ eV obtained from the D 7→2 / D 5→2 line ratio in Figure 3.20 during the volume recombination phase, the absence of C III emission at the inner divertor leg indicates that the volume recombining region lies in the vicinity of the inner strike point. The contribution to the measured line intensities for Balmer-Paschen $n > 5$ lines from the outer leg can therefore be neglected as the presence of C III emission places a lower temperature bound of $T_e > 3$ eV. At such temperatures the effective recombination rate coefficient is much lower than the effective ionisation rate coefficient (see Figure 2.5) therefore the excited state population densities of the high-n lines in the ionising plasma of the outer divertor are relatively small. For example, the D 5→2 intensity is reduced by an order of magnitude relative to the D 3→2 line for $T_e > 3$ eV (Figure 3.20).

The fluctuations in the D 5→3 line intensity in Figure 3.16 due to the L-H transitions are also observed in the LOS integrated CI (1166 nm and 1176 nm) lines but less so for the C II (678 nm) and C III (465 nm) lines. Since the time resolution of the two spectrometers is similar (10 ms for NIR lines, 5 ms for VIS lines), averaging out of the fluctuations in the VIS line measurements can be ruled out. It is therefore reasonable to deduce that, taking into account the lack of C III emission along the inner leg during the volume recombination phase, the region of strongest C I emission is located at the inner divertor while the C II emission is attributed to the region where the spectroscopic LOS intersects the outer divertor leg. The inferred absence of C II emission at the inner leg is also consistent with $T_e < 1$ eV which further supports the spectroscopically derived temperature at the inner divertor. The question then remains as to the source of the C I emission in the cold

inner divertor plasma since such low temperatures are below the physical sputtering energy threshold from bombarding ions in the vicinity of the inner strike point. A previous investigation by Whyte et al. (2001) on the influence of detachment on carbon erosion-deposition in the DIII-D divertor concluded that the presence of C I emission in the cold detached plasma is most likely due to material migration from the main wall through SOL transport. The influence of chemical erosion on the C I source in the detached plasma was also considered to be weak based on molecular spectroscopy measurements. On the basis of these conclusions, the most likely scenario accounting for the presence of C I emission in the cold plasma region is the inflow and recombination of hotter upstream carbon ions.

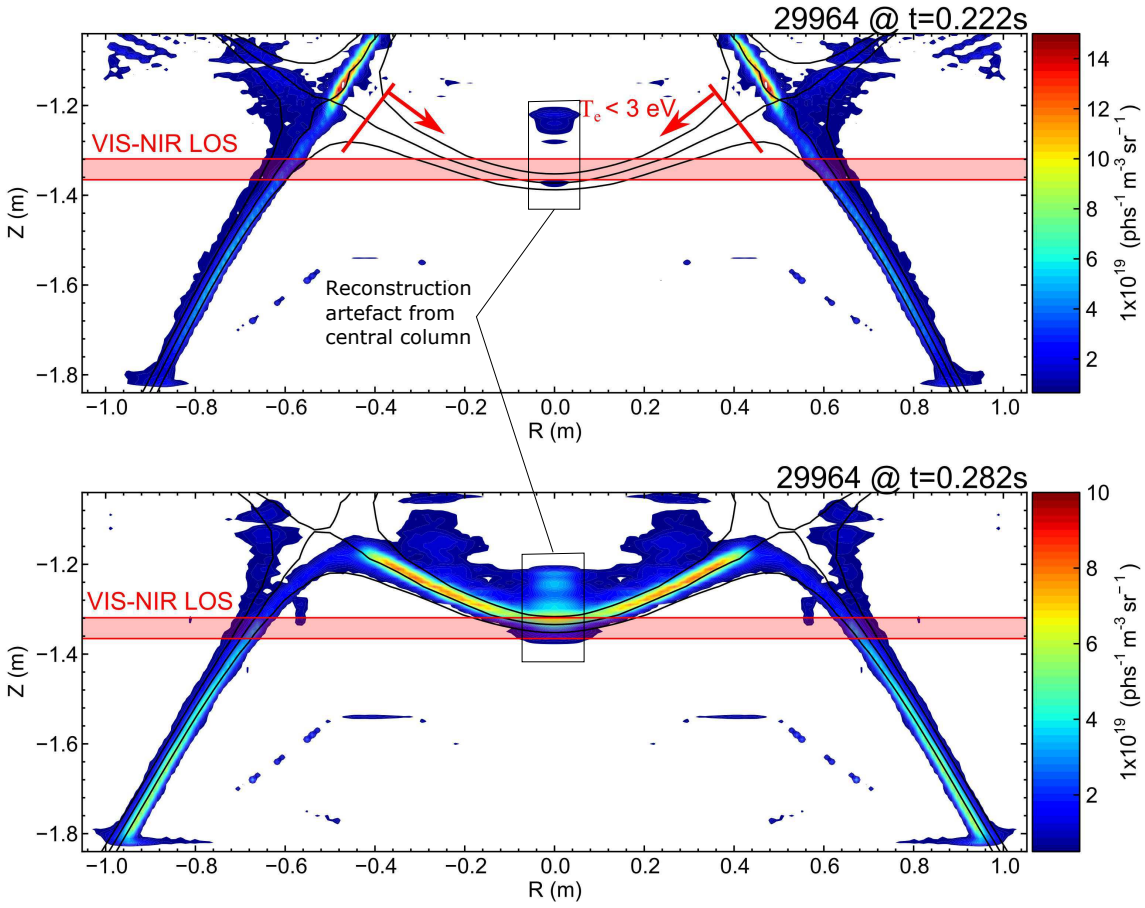

Figure 3.22: C III poloidal emissivity reconstructions and magnetic equilibrium reconstructions (black lines), revolved toroidally and sectioned along a vertical plane which intersects the VIS-NIR spectroscopy diagnostic line-of-sight.

Chapter 4

Enhanced Capabilities of the JET-ILW Mirror-Linked Divertor Spectroscopy System

The mirror-linked divertor spectroscopy system on JET (diagnostic designation KT3) provides spatially resolved passive spectroscopy measurements of plasma emission from the outer divertor. The system covers a spectral range of 350-1000 nm between three spectrometers (KT3A/KT3B/KT3C) with a range of grating options providing flexibility in the selection of wavelength window vs. spectral resolution. In preparation for the JET ITER-like wall (ILW) campaigns the system was upgraded in 2008 with an extended field of view (FOV, from 150 mm to 360 mm) and 2x optical throughput (Meigs et al., 2010). After the 2013 JET-ILW campaign further opportunities were identified for improving the system, namely:

- Extending the near-infrared spectral coverage to 1875 nm
- Increasing the time resolution of Balmer series and Be line intensity spatially resolved measurements up to 500 µs
- Improving the spectral coverage for dedicated Balmer series measurements

These improvements facilitate: measurements of the hydrogen Paschen series up to Pa-α (H 4→3); increased capabilities for supporting exhaust physics studies with a dedicated Balmer series survey spectrometer; and resolving the influence of ELMs, which deposit a significant portion of the stored plasma energy onto the divertor tiles on timescales of 100 µs, on divertor performance with an emphasis on plasma detachment.

4.1 Diagnostic Overview

The new visible system consists of an additional imaging spectrometer (KT3E) and two imaging filter-scope cameras (KT3-E8TA/B) for spatially resolved Balmer series and impurity line emission measurements in the 390-700 nm range. A notable feature of the KT3E 0.32 m focal length grating spectrograph is the Schmidt Czerny-Turner (SCT) optical configuration designed to reduce astigmatism and coma across the focal plane while providing an f/4.6 aperture ratio for increased throughput.

The near-infrared system extends the diagnostic spectral range to 1875 nm. This is achieved with: a single chord, low resolution (instrumental FWHM$\approx$ 7 nm) volume phase grating compact spectrometer (KT3D) providing surveying capability from 900-1700 nm; a filter-scope photodiode system (KT3D-PD) which provides access to the Pa-α (D 4$\rightarrow$3) line at 1874.6 nm and a second channel for measuring the relative contribution of the thermal background emission; and a medium resolution imaging SCT spectrometer (KT3D-MR, instrumental FWHM=0.25-0.5 nm) with a cooled InGaAs camera (640$\times$512 pixel detector), commissioned for a two-week period in order to obtain a higher spectral resolution, spatially resolved survey in the range 900-1650 nm and line profile measurements of the Paschen series lines. Table 4.1 summarises the specifications of the new visible and near-infrared systems.

4.2 Optical Design

The KT3 optical configuration consists of a series of mirrors that relay light emitted in the outer JET-ILW divertor through the top port of the torus and up to the roof lab situated on top of the shielded torus hall. Figure 4.1 shows the recently expanded FOV (blue pre 2008, orange post 2008), mirrors A-G, the objective lens A, roof apertures through the penetration tube, as well as the roof lab layout including the dichroic filters, newtonian telescopes, and base spectrometers. By unfolding the optical path and removing all flat mirror elements, the optical train can be visualised more simply, as illustrated in Figure 4.2.

The remaining optical components consist of the objective lens A, which forms an intermediate image on the field mirror D. Mirror D subsequently converges the ray bundles of the field points given by angle θ_o through the penetration tube with diameter $\phi_r \approx$ 130mm. The FOV is limited by the vessel port geometry such that the total radial extent is $h_o \approx$ 360 mm. The curvature of Mirror D is selected such that an image of lens A is formed inside the biological penetration tube. Thus, in

Table 4.1: Description of the enhanced mirror-linked divertor spectroscopy system.

Designation	Description	Specifications
KT3D	NIR survey spectrometer	Model: BaySpec SuperGamut Detector: 256 linear InGaAs array, 25 × 500 µm pixels Measurement spectral range: 900-1700 nm Spectral resolution: inst. fn. FWHM≈ 7 nm Time resolution: 50-250 ms (typ.) Spatial resolution: single chord, full FOV
KT3D-PD	Pa-α photodiodes	Model: Hamamatsu G12182-210K Detector: Extended-InGaAs, 1 mm diameter Time resolution: ≈ 50 ms Spatial resolution: single chord, full FOV Filters: 2-cavity, 4.5 nm FWHM bandpass, 1874.6 nm, 1886.0 nm
KT3D-MR	NIR imaging spectrometer	Model: Princeton Instruments IsoPlane SCT 320 Detector: Princeton Instruments NIRvana, 640x512 InGaAs sensor, 20 µm pixels Measurement spectral range: 900-1650 nm Focal length: 0.32 m Gratings: 300, 600 l/mm Spectral resolution: inst. fn. FWHM=0.25-0.5 nm Time resolution: 50-250 ms (typ.) Spatial resolution (post-process binned): 15 mm
KT3E	VIS imaging spectrometer	Model: Princeton Instruments IsoPlane SCT 320 Detector: Princeton Instruments ProEM:1024B, 1024x1024 frame transfer CCD, 13 µm pixels Measurement spectral range: 390-700 nm Focal length: 0.32 m Gratings: 200, 1200, 1800 l/mm Spectral resolution: inst. fn. FWHM=0.08-0.8 nm Time resolution: 15-40 ms (typ.) Spatial resolution (on-chip binned): 15 mm
KT3-E8TA/B	Filtered imaging spectroscopy	Model: AVT Pike F-032 Detector: 640x480 interline CCD, 7 µm pixels Time resolution: $\geq$ 500 µs Spatial resolution: 1.2 mm max. Filters: 2-cavity, 1.5 nm FWHM bandpass, Ba-α,β,γ, Be II 436.0 nm, 467.3 nm

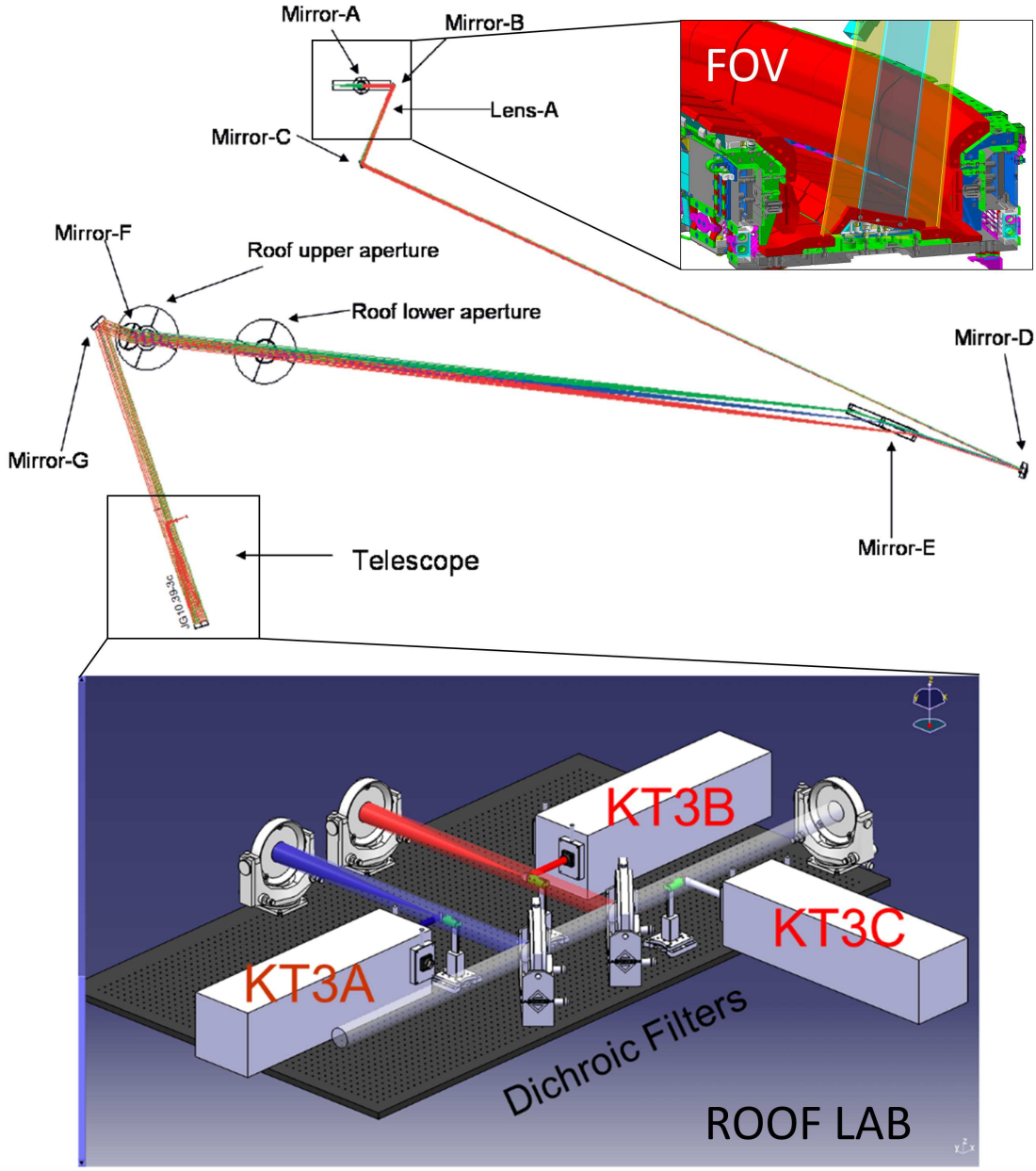

Figure 4.1: Schematic of the KT3 optical configuarion.

the absence of a physical aperture stop placed at lens A, the biological penetration tube is the limiting element in determining the light collection area upstream and is therefore the aperture stop of the system. Upstream of the penetration tube in the roof lab, a pseudo-collimated on-axis beam emerges and intercepts the primary mirror of three Newtonian telescopes which focus the intermediate divertor image onto the entrance slits of the three base spectrometers, KT3A, KT3B and KT3C (details on the optical design and base spectrometer specifications are in Meigs et al., 2010). Off-axis field points are mechanically vignetted as a function of the

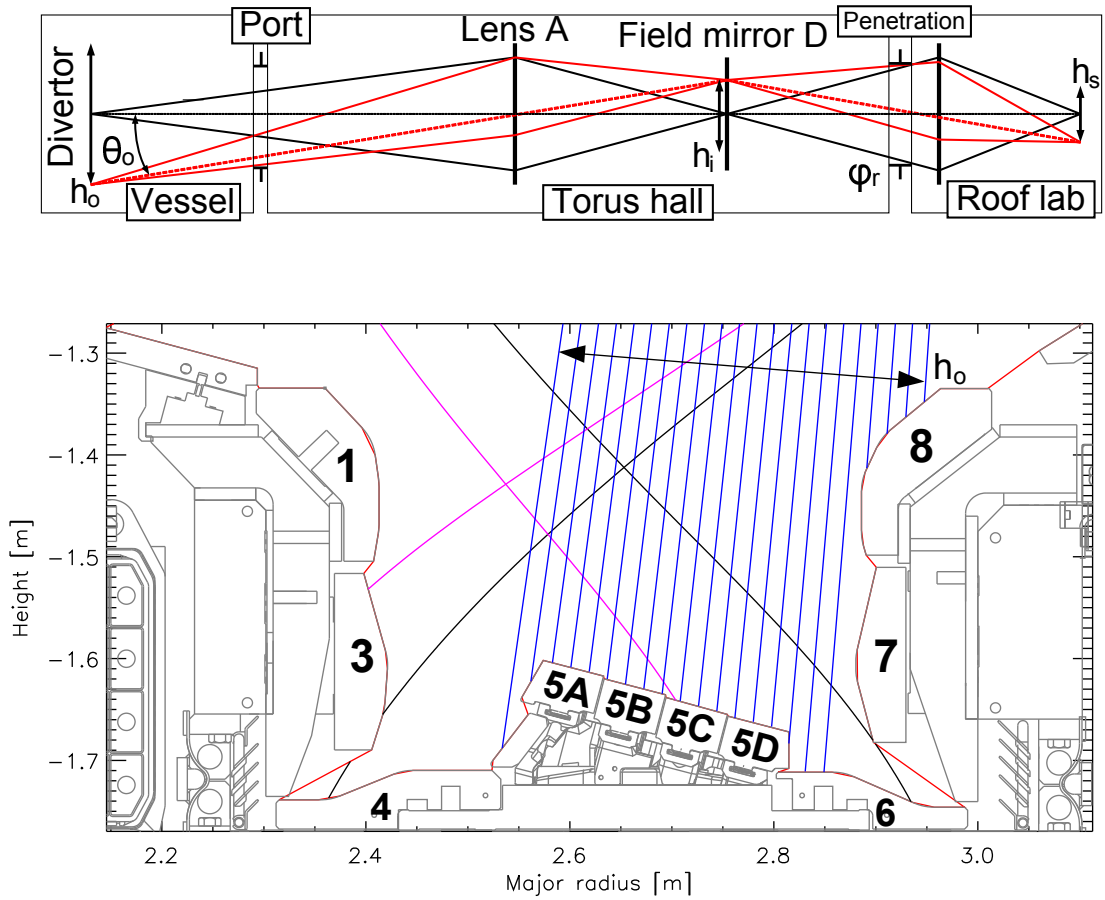

Figure 4.2: Top: simplified optical schematic of KT3. Bottom: JET-ILW divertor tile schematic (numbered), KT3 FOV (blue rays) and typical divertor plasma configurations (black and purple lines represent the separatrix).

field angle θ_o by the penetration tube. Additional vignetting of the high-field side (HFS) (R=2.5-2.6 m) also occurs at the port window due to the geometry of the vessel port tube. Treating the intermediate image as the object-space with $h_i = 310$ mm, the final image height on the spectrometer entrance slit is

$$h_s = \frac{h_i f}{x_i - f} \tag{4.1}$$

where f is the Newtonian telescope focal length and $x_i \approx 20000$ mm is the distance from mirror D to the final focusing element. With a primary mirror focal length of $f = 750$ mm, $h_s = 12$ mm and the lateral demagnification $M = h_o/h_s \approx 30$. With this conjugate ratio the divertor is imaged onto the entire vertical extent of the CCD cameras providing good spatial resolution and an f-number close to the acceptance cone of the spectrometers.

The basis of the optical design for the new system is the utilisation of the portion

of the main optical beam area that is otherwise obstructed by the base spectrometer Newtonian telescope secondary mirror cell. A turning fold mirror placed in front of the secondary mirror cell gives access to both the VIS and NIR arms of the dichroic beamspliter configuration, as shown diagrammatically in Figure 4.3. Figure 4.4 shows the compact optical table layout of the new systems utilising 50 mm optics and standard catalogue flat mirrors and achromatic doublet lenses.

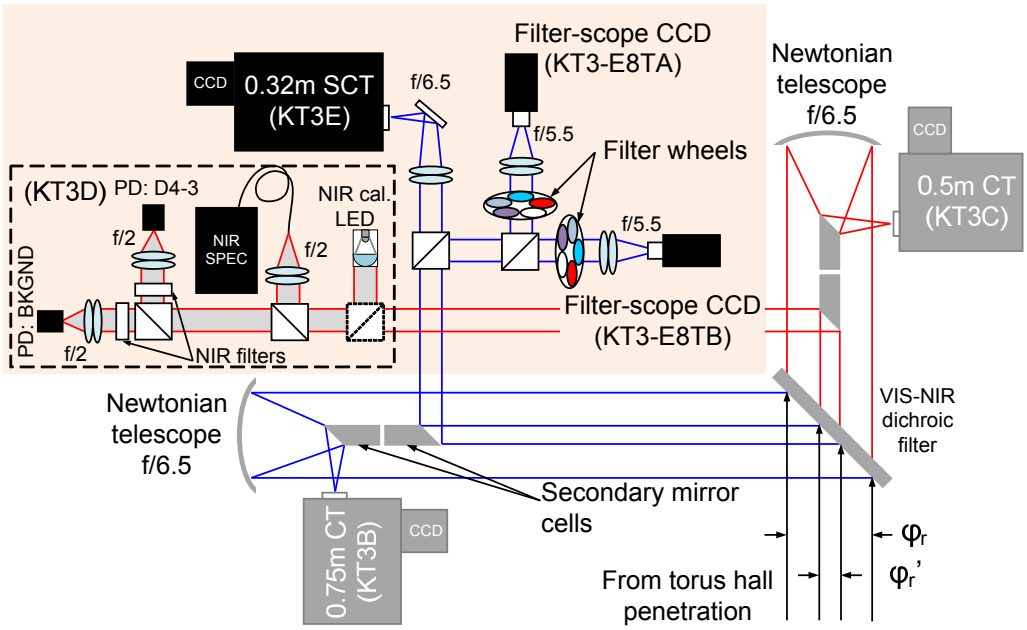

Figure 4.3: Schematic of new KT3 system and secondary mirror pick-ups from the VIS and NIR arms of the existing KT3 system.

The turning mirror of diameter $\phi'_r = 27$ mm placed behind the Newtonian secondary mirror cell is now the aperture stop in the optical train of the new system. Vignetting by the penetration tube is diminished, but the throughput is reduced by the ratio

$$\frac{G(\theta_o)}{G'} \approx \frac{[\phi_r V(\theta_o)]^2 - (\phi'_r)^2}{(\phi'_r)^2} \tag{4.2}$$

where G and G' are the etendue of the existing and new systems, respectively, and $V(\theta_o)$ is the vignetting factor of the existing system. The ratio has a range $10 \lesssim G/G' \lesssim 22$ depending on the field angle, with the highest value on-axis. Although this geometric effect reduces the amount of available light for the new system, it also allows for the use of small diameter 50 mm optics facilitating a flexible and easily adjustable optical layout.

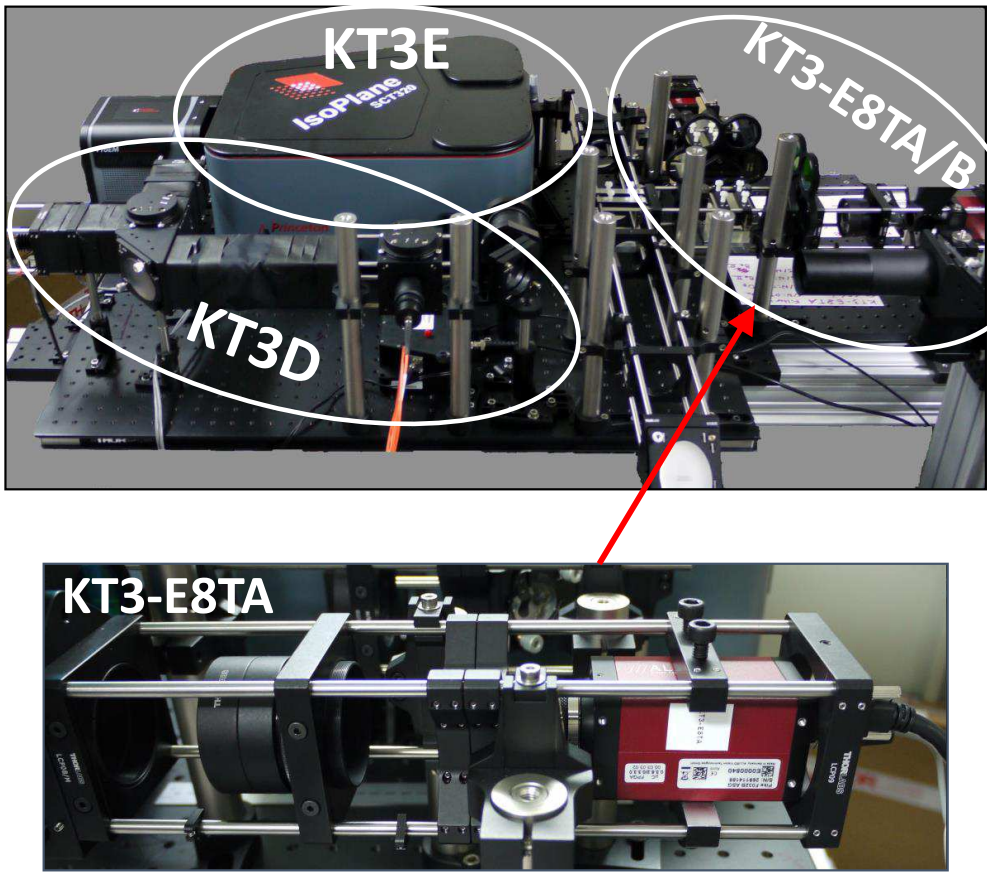

Figure 4.4: Optical table layout of the new KT3 systems.

To compensate for the reduction in throughput, an f/6.5 input cone was selected for the new visible spectrometer (KT3E, f/4.6 SCT) to ensure adequate utilisation of the grating area and to maximise the toroidal extent of the divertor FOV that is imaged on the 50 µm × 12 mm entrance slit. Similarly, the resulting demagnification (M≈ 130) at f/6.5 allows for significant reduction in the detector region of interest (ROI) on the filtered imaging cameras, thus increasing the maximum achievable frame rate. Figure 4.5 shows imaging characteristics of the base spectrometer (KT3B, h_s = 12mm; ≈ 920 pixels), the new visible system spectrometer (KT3E, h_s = 2.7 mm; ≈ 210 pixels) and filtered imaging cameras (KT3-E8TA/B, h_s = 2.4 mm; ≈ 320 pixels). The images of mirror E were obtained by fully opening the entrance slits to the spectrometers and setting the grating position to zero order. Even with the reduced image size on the new visible system, equivalent base system spatial resolution at the divertor object plane (KT3A/B/C, ≈15 mm per binning track) was easily achieved by ×10 vertical binning. The achieved spatial resolution of the filtered imaging system is sufficiently high to resolve individual

tungsten lamellae on tile 5 stacks B, C and D (see tile identification in Figure 4.2) as further demonstrated in Section 4.5.

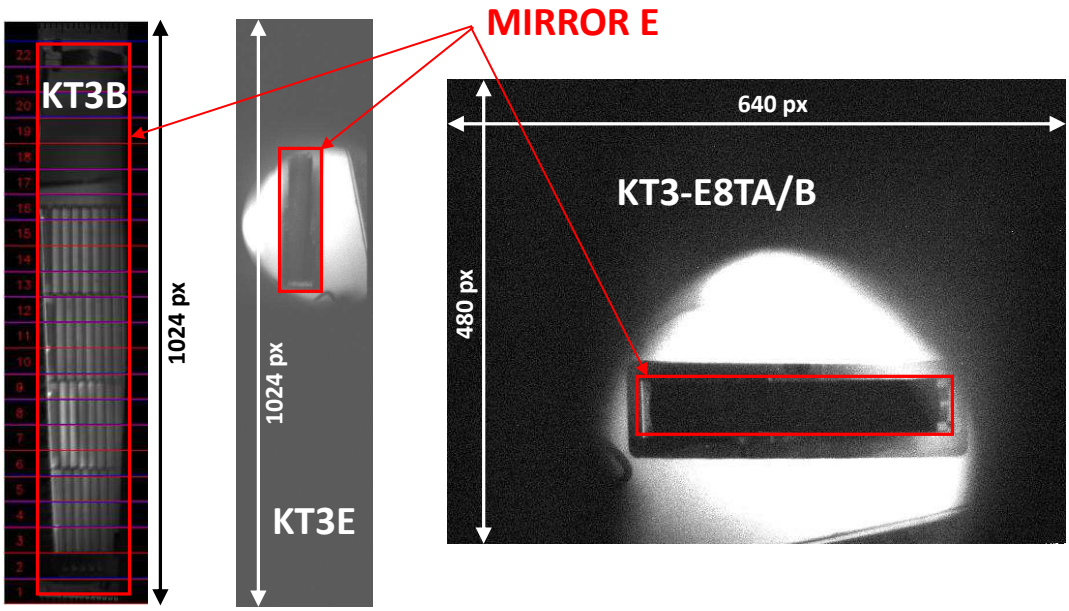

Figure 4.5: Imaging characteristics of the new VIS systems compared to the base KT3B system.

The measured vignetting functions of the base and new KT3 systems were obtained from in-vessel calibrations during the shut-down period after the summer 2014 JET-ILW campaign. An integrating sphere equipped with a calibration lamp was placed inside the vessel using remote handling equipment such that the aperture of the sphere intersected the KT3 LOS. Since the aperture diameter is smaller than the radial extent of the KT3 FOV, the lamp was placed in three radial positions such that full coverage could be obtained. The resulting full radial profiles across the CCD binning tracks for KT3A/B/C and the new KT3E systems are shown in Figure 4.6, in the standard spatial binning scheme, normalised to the profile peaks. The base systems exhibit a similar degree of vignetting towards the high-field side as a result of the port tube geometry which increasingly restricts the view at larger field angles towards the inner divertor. The increasingly peaked profiles of KT3B and KT3C indicate additional vignetting caused by transmission through the dichroic filters, relative to KT3A for which the light path is reflected from the first dichroic filter. The vignetting profile for the new KT3E system exhibits sharp edges and reduced vignetting compared to the base systems. The sloped and relatively flat KT3E vignetting profile may indicate some misalignment in the vertical position of the secondary pick-up mirror placed behind the Newtonian telescope secondary

mirror cell.

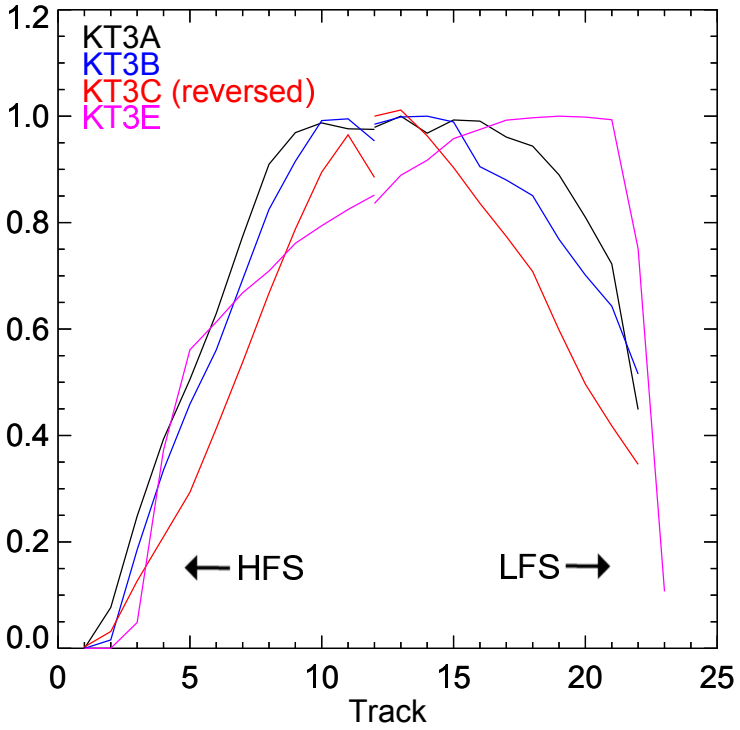

Figure 4.6: Measured vignetting profiles obtained during an in-vessel calibration.

4.2.1 Narrowband Interference Filters

The VIS and NIR filter-scopes employ 50 mm diameter Fabry-Perot interference filters for transmitting a well-defined band of light centered on the emission line of interest. A 2-cavity design provides a narrowband transmission profile with a width of $\approx 3.5 \times$ FWHM at 1% of the peak transmission. Filters for the Balmer series lines (Ba-α, β, γ) and Be lines (Be II 436.0 nm, Be II 467.3 nm) limit the bandpass to 1.5 nm FWHM while the Pa-α (1874.6 nm) and background correction (1886 nm) filters provide a 4.5 nm FHWM bandpass. A narrower bandpass in the NIR can technically be achieved but at substantial additional cost relative to the VIS filters. The small ($< 0.5°$) incidence and field angles of the pseudo-collimated light result in a negligible center wavelength shift (< 0.03 nm) for all rays intersecting the filters.

4.2.2 Schmidt Czerny-Turner Spectrograph Characteristics

The Czerny-Turner (CT) spectrograph is a widely used configuration for mounting plane reflective ruled or holographic gratings and typically consists of an entrance slit, collimating mirror, grating mount or turret, focusing mirror and exit slit or

detector plane, as shown in Figure 4.7 (left). In applications employing 2D detectors, attaining good imaging quality along the dispersion (horizontal) and spatial (vertical) axis is of primary concern for achieving optimal spatial resolution (e.g., to maximise the number of fibres placed along the slit) and spectral resolution to minimise the instrumental FWHM. Just as important is minimising off-axis aberrations in order to avoid excessive blurring towards the edges of the camera sensor as well as retaining a symmetric instrumental line profile.

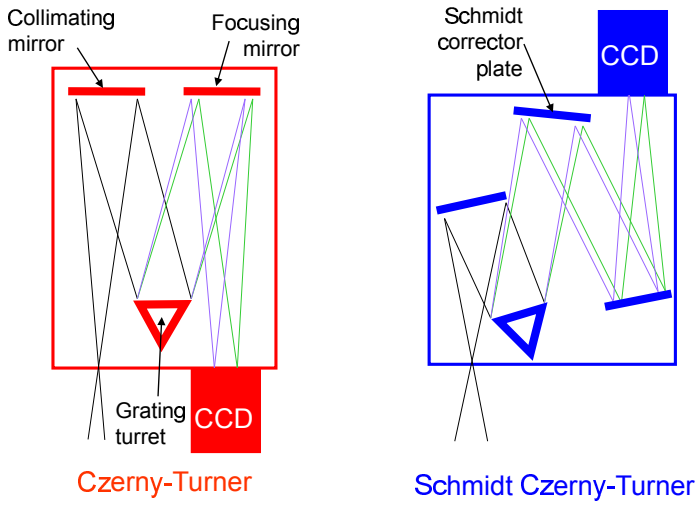

Figure 4.7: Schematic of the Czerny-Turner (left) and Schmidt Czerny-Turner (right) spectrograph configurations.

CT designs employing spherical mirrors typically suffer from astigmatism whereby the tangential and sagittal foci are well separated. This gives rise to elongation of the imaged point source either in the horizontal or vertical direction, with the optimal visual focus found between the two focal planes. An improvement on this design employs toroidal mirrors characterised by different horizontal and vertical radii of curvature. This effectively brings the tangential and sagittal focal planes closer together and significantly reduces astigmatism over the entire focal plane, with virtually no astigmatism on the optical axis. However, toroidal mirror CT designs still exhibit significant coma, or the blurring of off-axis point sources, the degree of which increases as a function of aperture size. Retaining good quality off-axis imaging characteristics and symmetrical line shapes thus requires operating at a larger f-number and/or limiting the analysis of the spectral/spatial information to point sources imaged near the optical axis.

An improvement in imaging quality and uniformity across the focal plane can be achieved by correcting for astigmatism and coma with an additional optical ele-

ment. One such design, the Schmidt Czerny-Turner (SCT) configuration, is shown in Figure 4.7 (right) and incorporates a reflective Schmidt corrector placed between the toroidal collimating and focusing mirrors. This is the basis of the IsoPlane SCT-320 (Princeton Instruments Inc., 2013) instrument, used for both the KT3E system and KT3D-MR near-infrared demonstration system. This spectrograph incorporates f/4.6 optics, resulting in a factor of 2 increase in maximum throughput compared to the Acton SpectraPro-500i conventional CT toroidal mirror imaging spectrograph (f/6.5) used in KT3C. A performance assessment of the KT3E SCT spectrograph was carried out by comparing its imaging quality and instrumental FWHM uniformity across the focal plane to the conventional CT (KT3C) under identical illumination conditions and using the same model of CCD camera (ProEM:1024B). The test set-up consisted of mounting Hg-Ar and Ne pencil style calibration lamps on a fixture attached directly onto the entrance slit housing. This combination provided sufficient isolated spectral line density in the range 600-700 nm to cover the entire focal plane area (1024×1024 pixels, 13 µm pixel size). The lamp placement at the entrance slits ensured sufficient illumination along the entire vertical (spatial) axis. A 300 l/mm ruled grating was selected on both spectrometers, yielding a spectral range of 129 nm for the 0.33 m focal length SCT and 85 nm for the 0.5 m focal length CT. Since both spectrometers are designed with 1:1 magnification of the entrance slit (set to 50 µm) on the detector focal plane, the spectral line FWHM in pixels provides a measure of the imaging quality as a function of the design aperture ratio and degree to which the optics correct for off-axis aberrations, independent of the grating groove spacing.

Figure 4.8 shows contour plots from measurements of the same two spectral lines imaged with the CT and SCT spectrometers near the detector center in the dispersion direction and across the entire sensor in the spatial direction, binned into 23 tracks consistent with the standard KT3C binning scheme. Since Doppler broadening of the spectral lines emitted from the pencil lamps is assumed to be negligible, the line FWHM and line shape is considered to be entirely attributed to the instrumental broadening. The dispersed slit images on the CT instrument exhibit some curvature and broadening away from the center. The slit images on the SCT instrument exhibit more consistent widths across the sensor but an asymmetric bump in the tails of the spectral line is also evident at the sensor edges. A 1-2 pixel shift in the line centre is also observed in the spatial direction across sensor and is attributed to a slight misalignment on the detector rotational axis. It was found that the line shape at the sensor edges of the SCT spectrometer was particularly

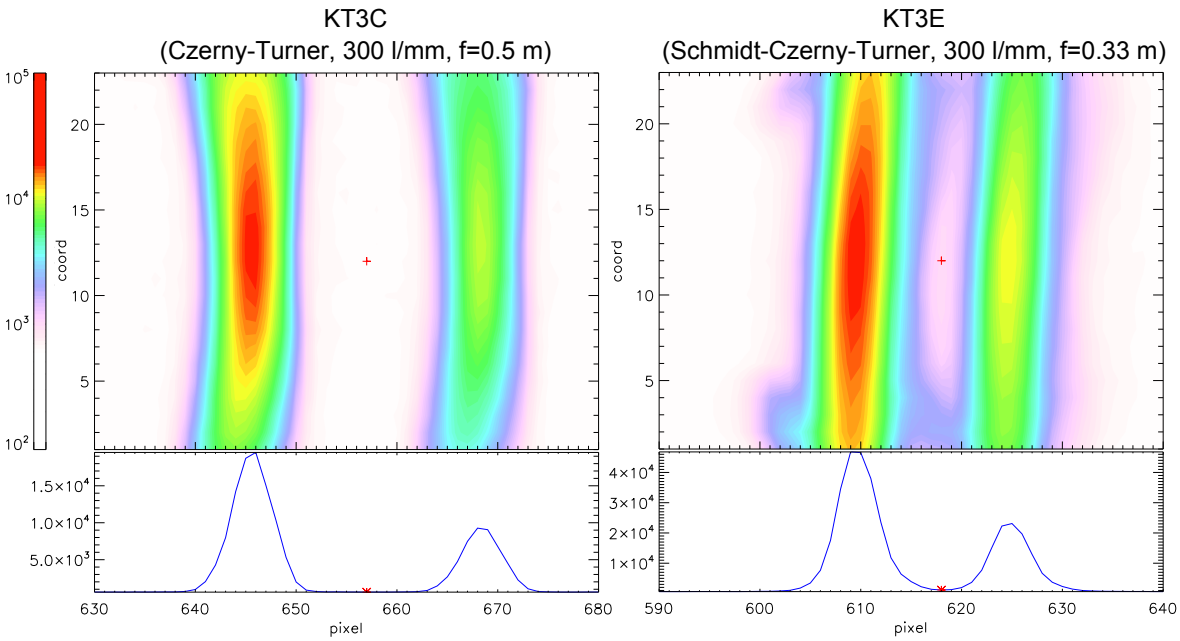

Figure 4.8: Comparison of the CT and SCT spectrometer instrumental line width over the spatial dimension of the CCD sensor from measurements of two spectral lines positioned near the center of the sensor in the dispersion direction. The bottom spectra correspond to track 12.

sensitive to small changes in the illumination position as the pencil lamp fixture was slightly rotated. This effect was much less noticeable with the CT spectrometer. It is unclear whether the presence of the SCT line shape asymmetry is a consequence of overfilling the design input light cone at f/4.6, inadequate alignment of the spectrometer optical elements and grating, or whether this is an inherent feature. Further testing is recommended using a fibre bundle and entrance slit adapter in order to more accurately map the imaging characteristics towards the sensor edges. Such a set-up was not available during the characterisation. Since the reduced image size of mirror E on KT3E only spans 220 pixels across the spatial axis (see Figure 4.5), the observed line asymmetries at the sensor edges were not of particular concern for plasma measurements.

It is also of interest to compare the line FWHM distribution over the entire sensor, disregarding the bump on tail asymmetric line feature at the sensor edges. This was carried out by fitting a Gaussian model in the least-squares manner to the measured Hg-Ar and Ne spectral lines spanning the entire width and height of the detector. The resulting change in the FWHM relative to the on-axis value as a function of binned track (vertical axis) and spectral line number (dispersion axis) is shown in Figure 4.9. Only a small variation in the ΔFWHM is evident along the

dispersion axis for both spectrographs. A significant increase in the spectral line FWHM is observed away from the optical axis for the CT instrument, whereas a more uniform FWHM profile across the slit is observed for the SCT instrument.

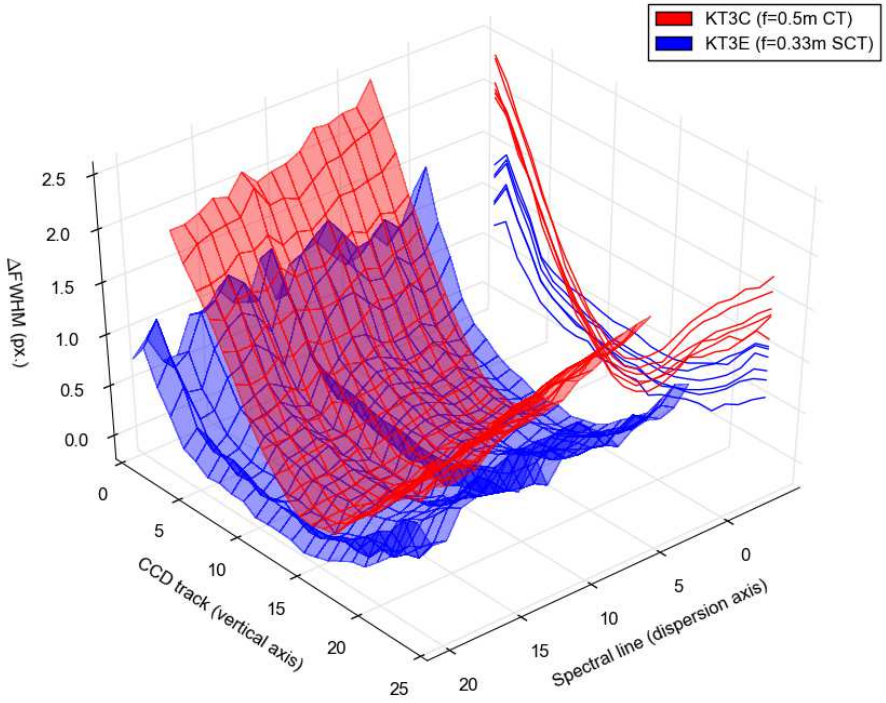

Figure 4.9: Variation of the change in instrumental FWHM over the spatial and dispersion extents of the CCD sensor for the CT and SCT spectrometers.

While the SCT spectrograph offers increased uniformity in the spectral line FWHM along the vertical axis, additional performance testing is required to draw definitive conclusions on the relative imaging performance compared to the conventional CT spectrograph. It was also found that the asymmetric bump on tail can be reduced somewhat by defocusing the slit image on the detector plane, at the cost of increasing the instrumental line width. A further recommendation for future testing is to incrementally decrease the slit width in order to ascertain the impact of the corrective optics on the minimum attainable instrumental width and its spatial distribution along the dispersion and spatial directions. Lastly, it should be noted that using spectral line measurements from tokamak plasma emission for the purpose of mapping the FWHM variations across the sensor is not recommended due to the influence of line broadening and splitting mechanisms (e.g., Doppler broadening, Stark broadening, Zeeman splitting) which tend to obfuscate the instrumental broadening contribution.

4.3 Visible System (KT3E and KT3-E8TA/B)

Selection of CCDs for the visible system was largely based on the application requirements for sensitivity vs. speed. For the new grating spectrometer (KT3E) a 1024×1024 pixel frame transfer cooled CCD (ProEM 1024B) offers excellent quantum efficiency (QE) with a peak of ≈95% at 650 nm due to a pixel fill factor of 100% . Cooling the sensor to -50°C reduces the dark current down to 0.04-0.002 e-/pixel/s, rendering the read noise as the dominant noise mechanism at low light levels. Frame rates are limited by the vertical shift rate in the readout cycle during which the charge from the entire exposed sensor region of interest (ROI) is transferred to the masked region. Since the active area is exposed to light during the transfer process, the frame transfer CCD is more prone to image smear at high light levels.

The main requirement of the visible imaging spectroscopy system (KT3-E8TA/B) is a fast frame rate up to ≈2 kHz. Machine vision interline progressive scan CCDs provide sufficient speed to meet this criterion while preserving sensitivity and sensor uniformity characteristic of CCDs. Although the QE for interline CCDs suffers due to relatively lower fill factors, the use of microlenses can recover much of the QE with a peak of ≈54% at 500 nm for the KAI-0340 640×480 pixel sensors used. The real advantage of interline CCDs is very quick charge transfer from exposed pixel columns to adjacent masked pixel columns. Smear is minimised in this arrangement and a dual shift register provides fast frame rates up to 2 kHz for a ROI of 320×10 pixels. The two cameras (AVT Pike F-032B) in the filtered imaging system operate at room temperature with typical dark currents of < 1000 e-/pixel/s. One limitation of interline-CCD cameras is a lack of an electronic rolling shutter feature, which could facilitate higher time resolution taking advantage of the delayed exposure timing at each row of pixels. CMOS cameras typically provide such functionality and should be explored for this application provided that the photon statistics and camera noise at sub-500 µs exposures results in adequate SNR.

The available light at the pick-up turning mirrors (located behind the secondary mirrors of the Newtonian telescopes) of the new VIS and NIR systems is estimated from

$$P_\lambda = L_\lambda \, G \, T_\lambda \tag{4.3}$$

where P_λ is the total photon flux [ph s^{-1} nm^{-1}] incident on the pick-up mirror, L_λ is the averaged spectral radiance [ph s^{-1} m^{-2} sr^{-1} nm^{-1}] across the divertor FOV, G

is the averaged etendue [m^2 sr] across the divertor FOV and T_λ is the total spectral optical transmission which takes into account all optical elements from the vessel port to the secondary turning mirror in the roof lab. Estimated values are $G \approx 1.1 \times 10^{-8}$ m^2 sr and $T_\lambda = 0.15$ in the range 300-2000 nm.

Based on observations of the outer divertor ion fluxes in JET-ILW discharges (e.g. Huber et al., 2013; Romanelli, 2013) and using ADAS SXB coefficients as a function of electron density and temperature, the range of expected H 3→2 radiance values averaged across the outer JET divertor is shown in Figure 4.10.(a). Taking into account the beamsplitter transmission (0.5), slit width (50 µm), image height (2.7 mm), grating efficiency (200 l/mm, 0.7@650nm), an instrumental line width of ≈ 3 pixels FWHM, the estimated SNR for D 3→2 intensity measurements on KT3E is $150 \leq SNR \leq 5500$ assuming a total CCD noise figure of 6 e^- RMS and 25 fps frame rate. Similarly, the SNR for the Pike cameras with a 1.5 nm FWHM narrowband filter and a 2.4 mm image height on the sensor yields values of $10 \leq SNR \leq 350$ assuming 1 kHz fps and 16 e^- RMS camera noise. On-chip binning on the frame transfer ProEM CCD (23 tracks) and post-process binning on the Pike cameras (23 spatial tracks and 30 pixels toroidally) will improve the SNR by a factor 3-5 for lower intensity impurity Be lines, D 4→2 , D 5→2 as well as hign-n Balmer recombination lines. A spatial resolution of 15 mm in the radial direction, consistent with the existing system, is preserved using this binning scheme.

Figure 4.10.(a) also shows the estimated bremsstrahlung and thermal contributions from the outer divertor plasma and tungsten tiles. Bremsstrahlung emission was modelled assuming a LOS integration of uniform emissivity through 100 mm of an isothermal divertor plasma, ignoring the high temperature core contribution. Thermal emission was calculated using the empirically derived tungsten emissivity from the ITER Material Properties Database (ITER Doc. G 74 LS 102-03-22 W0.1). The continuous spectral emission was then multiplied by the 1.5 nm bandpass 2-cavity filter transmission function centered at the H 3→2 wavelength.

4.4 Near-infrared System (KT3D)

4.4.1 Grating Spectroscopy

After the completion of the MAST M9 experimental campaign, the low resolution NIR spectrometer (BaySpec SuperGamut) was installed on the JET-ILW mirror-linked system and given the designation KT3D. The 100 µm input slit was replaced

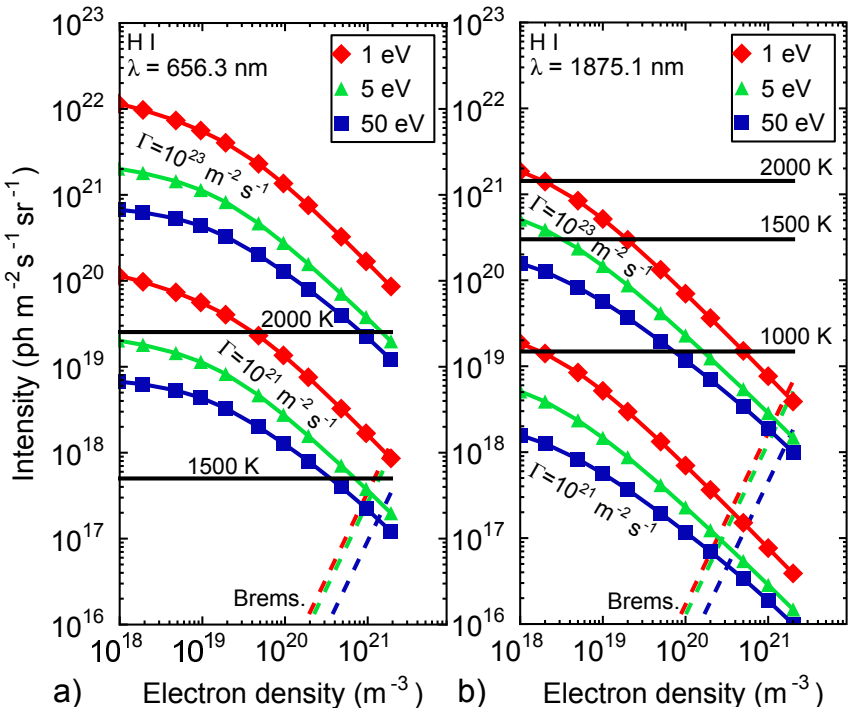

Figure 4.10: Estimates of the H 3→2 (656.3 nm) and H 4→3 (1875.1 nm) line intensity, bremsstrahlung and thermal emission.

with a 50 µm slit in order to improve the spectral resolution. The instrumental FWHM was thus reduced from ≈ 10 nm to ≈ 7 nm. The slit replacement required a wavelength re-calibration which was carried out using a combination of a fibre-fed Hg-Ar light source and later using the deuterium Paschen series lines from plasma measurements. Although the KT3D spectrometer is useful for surveying the NIR spectrum in the JET-ILW environment, the coarse resolution, even after the slit replacement, limits the interpretation of the spectral features and precludes both spatially resolved measurements and line shape measurements. The medium-resolution KT3D-MR imaging spectrometer was thus commissioned for a two week period on a loan basis from Princeton Instruments. The challenge in installing the KT3D-MR IsoPlane SCT-320 instrument was the limited space in the new optical table layout. To accommodate KT3D-MR, the remaining new NIR systems (KT3D and KT3D-PD) had to be disassembled for the duration of the loan. To ensure accurate realignment of KT3D and KT3D-PD, current-stabilised calibration LEDs (both VIS and NIR) were placed in-line with the optical path using a slit, collimator and beam-splitter arrangement (see Figure 4.3). Figure 4.11 shows images captured using a CCD camera during the initial KT3D alignment illustrating the view of mirror E, the LED reference source aligned with the position of mirror E, as well as an

inverted image showing tile 5 in the divertor illuminated by the in-vessel inspection lights (IVIS). With this system in place, the KT3D and KT3D-PD systems could be removed, reinstalled and realigned correcting for any measured spectral radiance offset using the current-stabilised LED light source.

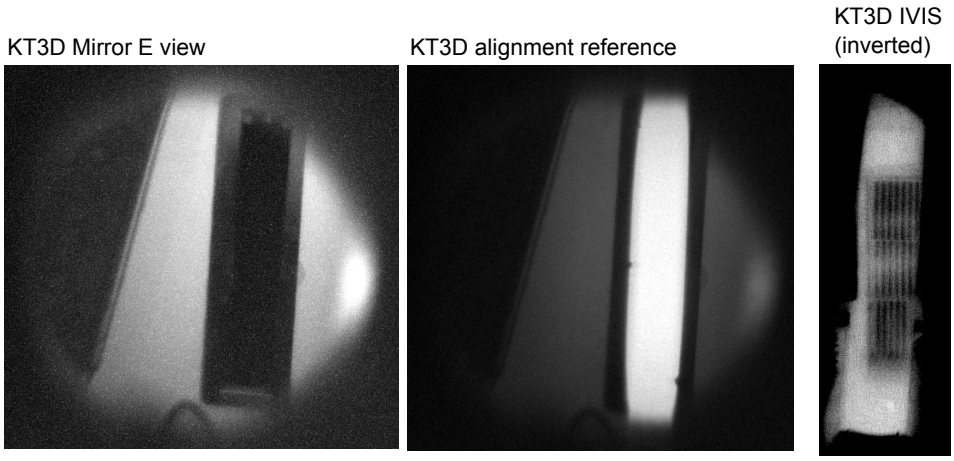

Figure 4.11: CCD alignment camera images of the NIR system including: a view of mirror E (left), overlapping alignment reference illumination (middle), and an enhanced image of tile 5 (using an inverse look up table) in the JET-ILW divertor (right).

To demonstrate the measurement capabilities of the KT3D-MR system, Figure 4.12 compares the Hg-Ar spectrum obtained with the low-resolution KT3D spectrometer and the composite spectrum obtained with the KT3D-MR imaging spectrometer with a 300 l/mm grating over several grating positions. A factor of 14 increase in the spectral resolution was thus achieved with the 300 l/mm grating (instrumental FWHM=0.5 nm), and a factor of 28 with the 600 l/mm grating (instrumental FWHM=0.25 nm). The trade-off for obtaining the higher spectral resolution is a reduction in the spectral range at each grating position. Figure 4.13 compares the spectral reciprocal linear dispersion (nm/mm) of both instruments thus illustrating the spectral range of the KT3D-MR 300 l/mm grating position settings. The imaging characteristics of KT3D-MR equipped with the 2D cooled InGaAs camera (PI NIRvana640) provided spatial resolution equivalent to the base and KT3E systems, depending on the post-process binning scheme.

4.4.2 InGaAs Photodiode Characteristics

The InGaAs photodiode is the most common detector for NIR applications in the range 900-2500 nm. Band gap energies of InGaAs photodiodes are smaller then Si photodiodes for operation at reduced photon energies, and can be tuned by changing

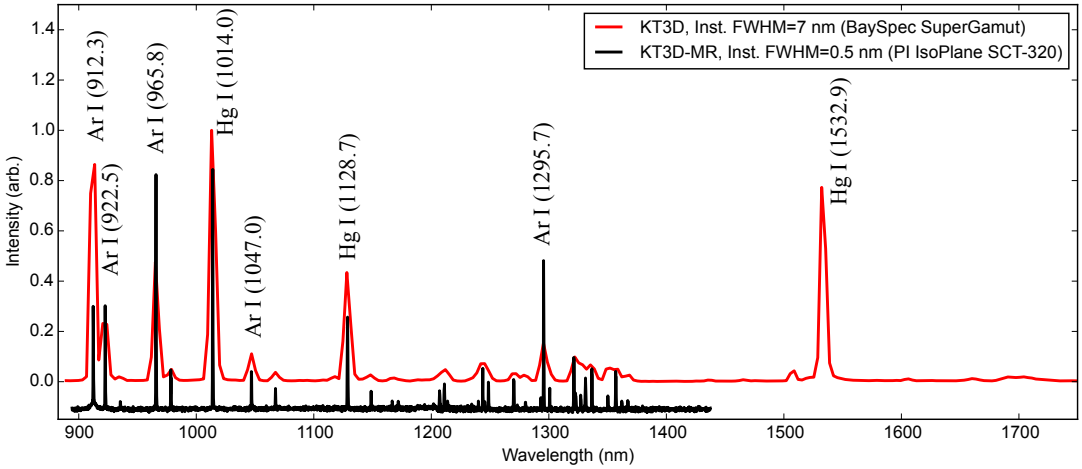

Figure 4.12: Comparison of the Hg-Ar calibration lamp spectrum obtained with the KT3D and KT3D-MR spectrometers.

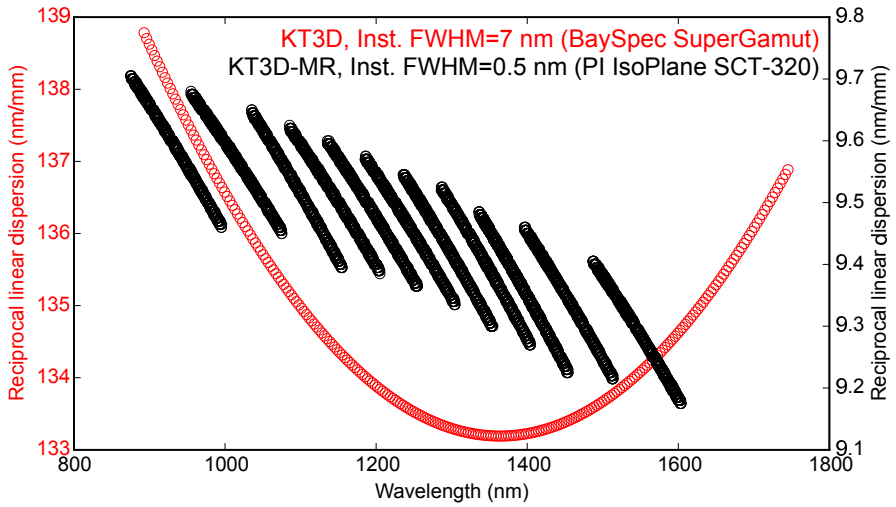

Figure 4.13: Comparison of the reciprocal linear dispersion for the KT3D and KT3D-MR spectrometers.

the composition ratio of indium and gallium. The standard type offers good spectral response in the 900-1700 nm range while extended-InGaAs photodiodes have cut-offs up to 2600 nm (Rogalski, 2010, p. 309) (see Figure 1.6).

The detectivity, or sensitivity per unit active area, given by

$$D^*_\lambda = \frac{\sqrt{A}}{NEP_\lambda} \tag{4.4}$$

is a commonly used figure of merit for comparing photodiode performance, where A is the active area [cm^2], and

$$NEP_\lambda = \frac{PA}{SNR\sqrt{\Delta f}} = \frac{PA}{\sqrt{\Delta f}} \tag{4.5}$$

is the noise equivalent power [W $Hz^{-1/2}$] corresponding to the rate of incident photon energy P [W cm^{-2}] which yields a SNR of 1 at a measurement bandwidth $\Delta f = 1$ Hz.

Ignoring any internal and operating circuit noise sources, the theoretical detection limit of infrared detectors is determined by the photon noise due to background fluctuation, given by

$$D_B^* = \frac{\lambda}{hc}\sqrt{\frac{\eta}{2Q_B}} \tag{4.6}$$

where η is the quantum efficiency and Q_B is the total background photon flux density reaching the detector. For a blackbody background flux at 300 K the theoretical detectivity, which is inversely proportional to the Planckian distribution, falls off with increasing wavelength. In the 1000-2000 nm region, the dominant noise mechanism at or near room temperature operation is not the background fluctuation but rather internal processes associated with thermal generation. The narrower band gap results in transition energies that become comparable to the thermal energy of charge carriers, k_BT, enabling thermal transitions (Rogalski, 2010, p. 59).

The total noise current of the InGaAs photodiode is given by

$$i_N = \sqrt{i_J^2 + i_{SD}^2 + i_{SP}^2}, \tag{4.7}$$

where i_J is the thermal (or Johnson) noise,

$$i_J = \sqrt{\frac{4k_BT\Delta f}{R_{Sh}}}, \tag{4.8}$$

i_{SD} is the dark current shot noise,

$$i_{SD} = \sqrt{2qi_D\Delta f} \tag{4.9}$$

and, similarly, i_{SP} is the photocurrent shot noise. q is the electron charge, i_D the dark current and R_{Sh} the shunt resistance of the photodiode. Both the dark current shot noise and thermal noise can be significantly reduced by cooling the detector.

Table 4.2 lists the performance characteristics of Si and InGaAs photodiodes with similar photosensitive areas. Si diodes offer very high detectivity at room temperature due to low noise current, whereas the infrared InGaAs photodiodes require a low temperature operating point to minimise the dark and Johnson noise currents. Extended InGaAs photodiodes with sensitivity up to 2100 nm exhibit the lowest performance due to a narrower band gap, hence even at -20°C the detectivity is an order of magnitude lower in comparison to the Si photodiode operated at room temperature.

Table 4.2: Performance characteristics of Si and InGaAs photodiodes.

Type	Element Temperature (°C)	Photosensitive Area (mm)	Spectral response range (nm)	Peak sensitivity (nm)	Photosensitivity at peak (A/W)	Detectivity at peak (cm $Hz^{1/2}$ W^{-1})
Si Hamamatsu S1336-18BK	25	1.1×1.1	320-1100	960	0.5	1.75×10^{13}
InGaAs Hamamatsu G12180-010A	25	⌀1	900-1700	1550	1.1	6.3×10^{12}
InGaAs Hamamatsu G12180-210A	-20	⌀1	900-1650	1550	1.1	6.7×10^{13}
InGaAs Hamamatsu G12182-010A	25	⌀1	900-2100	1950	1.2	3.5×10^{11}
InGaAs Hamamatsu G12182-210A	-20	⌀1	900-2050	1950	1.2	2.0×10^{12}

Photodiodes can be operated either in photoconductive (biased) mode by applying a reverse bias voltage, or photovoltaic (unbiased) mode, depending on the application requirements. To illustrate the working principle and trade-offs of photodiode operating modes, a typical current-voltage (I-V) characteristic curve of a photodiode is shown in Figure 4.14 with the shifted curves resulting from increasing photon flux incident on the detector area. The load lines (red) represent the load resistance R_L which converts the generated photocurrent to a measurable voltage. In the photoconductive mode, the reverse bias voltage V_R increases the depletion region width and decreases the junction capacitance C_j. Since the measurement cut-off frequency f_c or rise time τ_r (10% to 90%) is approximately

$$f_c \approx \frac{0.35}{\tau_r} \approx \frac{1}{2\pi R_L C_j}, \tag{4.10}$$

the main advantage of reverse biased operation is the increase in speed and detector linearity at the cost of increased noise due to additional dark current. Conversely

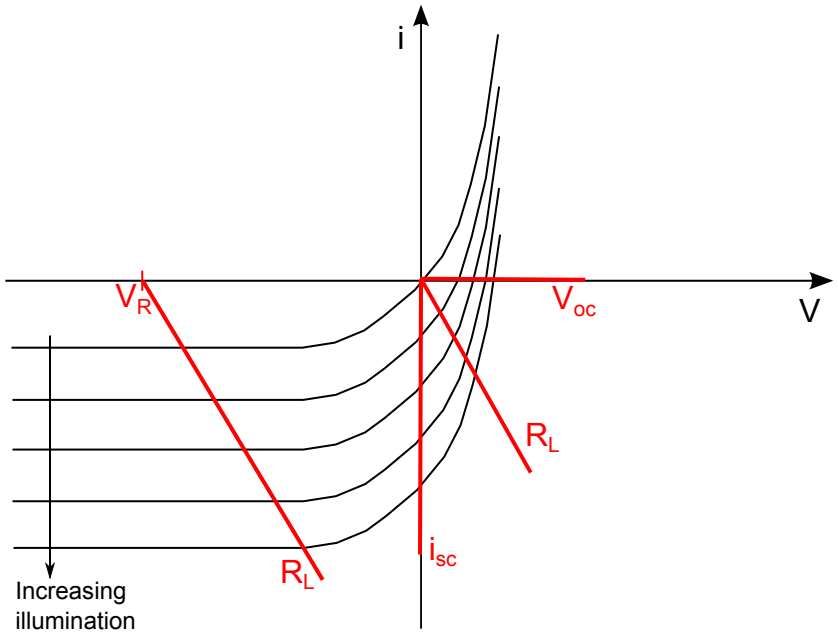

Figure 4.14: Current-voltage photodiode charactersitics and load lines (red) for different operating modes.

the photovoltaic mode ($V_R = 0$) offers reduced noise due to the absence of dark current and is particularly well suited to very low light level measurements at the cost of reduced bandwidth (speed) due to relatively larger value of C_j. In this case the detector linearity depends on the relative size of the internal photodiode shunt resistance R_{Sh}, and R_L. In the limit when $R_L \to 0$ (short circuit) the photodiode behaves as an extremely linear current generator and is typically connected to a transimpedance amplifier circuit to convert the generated photocurrent (i_{SC}) to a measurable voltage, the gain of which is determined by the value of the amplifier feedback resistance. In the limit when $R_L \to \infty$ (open circuit) the voltage across the photodiode (V_{oc}) is determined entirely by R_{sh}. In this case the forward bias voltage opposes the band gap potential of the photodiode junction, which results in an exponentially decreasing output voltage with increasing illumination. This non-linearity is the main disadvantage of the photovoltaic mode of operation, but at very low light levels it offers the highest detectivity due to elimination of the dark shot noise, relatively high output voltage level and an entirely passive circuit configuration. Addition of active operational amplifier elements (e.g., transimpedance amplifier) reduces the effective detectivity of the photodiode due to $1/f$, or flicker noise, especially at lower frequencies. This can be mitigated by selecting the measurement bandwidth at higher frequencies by modulating the input signal by means of a chopper wheel and lock-in amplifier, but at significant additional cost and com-

plexity.

To maximise the detection limit of the KT3D-PD D 4→3 and background filtered photodiode measurements, the photovoltaic mode of operation was chosen. This ensured timely commissioning of the diagnostic for the 2014 JET-ILW scientific campaign by reducing additional complexities associated with amplifier optimisation and/or additional costs associated with a lock-in amplifier and chopper wheel configuration. A dual stage cooled PIN photodiode (Hamamatsu G12182-210A) was selected based on its relatively high detectivity (D^*) compared to packaged detector and transimpedance amplifier configurations. The D 4→3 and thermal background photodiodes were connected directly to a digitiser (National Instruments 6221) with 10 GΩ input impedance using 5 m twisted pair shielded cables and were cooled using two temperature controllers (ILX Lightwave LDT-5525). Figure 4.15 shows the optical table configuration of the KT3D-PD system. The optimum photodiode operating temperature was determined to be -15°C as a compromise between the reduction in Johnson noise and the presence of a low frequency ripple in the thermoelectric cooler circuit. The observed ripple increased with lower temperature operating points due to the higher thermoelectric current demand, and eventually offset the SNR gains from Johnson noise reductions.

The two critical performance measures of the photodiode system are the SNR and detector linearity at the expected incident photon fluxes. An assessment of the detector linearity in the open circuit photovoltaic mode depends on the photodiode's I-V characteristics, which can be approximated with the ideal diode equation,

$$i_T = i_0 \left[\exp\left(\frac{qV}{Nk_BT} \right) - 1 \right] + i_P \tag{4.11}$$

where i_T is the total current flowing through the diode, i_P is the photocurrent, i_0 is the saturation or dark leakage current, V is the applied voltage across the diode and T is the absolute operating temperature. N is the ideality factor, which is typically in the range 1-2 for actual diodes. In the absence of photocurrent, the saturation current can be estimated using the photodiode's dark current characteristic (obtained from the manufacturer's datasheet) since the dark current is composed of contributions from the photocurrent generated by background fluctuation and the saturation current at the diode junction. The open circuit voltage V_{oc} can then be estimated from

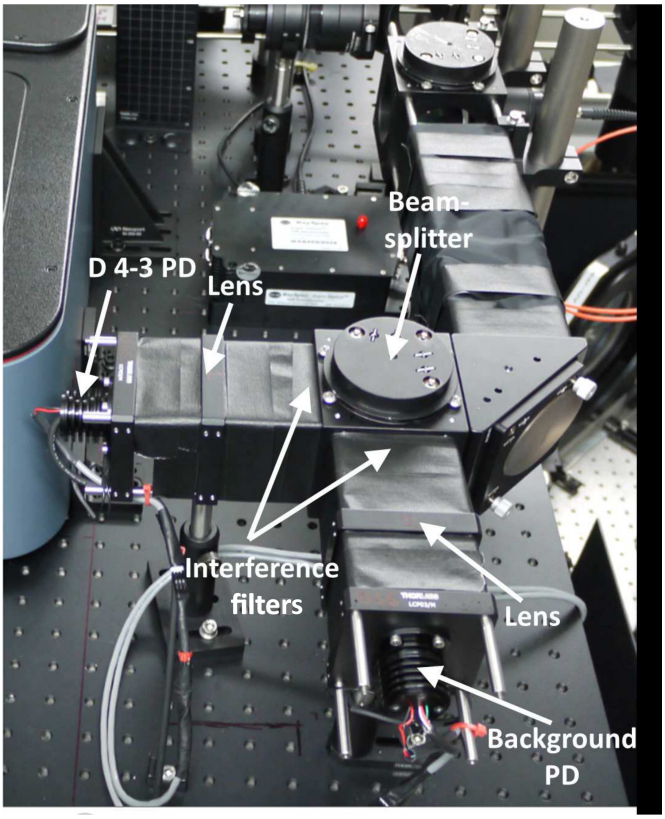

Figure 4.15: Optical table layout of the KT3D-PD filtered photodiode system.

$$V_{oc} = \frac{N k_B T}{q} \ln\left(1 - \frac{i_P}{i_0}\right). \tag{4.12}$$

The expected photocurrent i_P can be estimated using eqn. 4.3 and Figure 4.10.(b) which shows the estimated H 4→3 intensity calculated using ADAS SXB data for electron temperatures $1 \leq T_e \leq 50$ eV and electron densities $10^{19} \leq n_e \leq 10^{21}$ m^{-3}, as well as the tungsten thermal emission intensity. With the entire divertor FOV demagnified and focused onto the monolithic detector area with ⌀1 mm, the estimated photocurrent is in the range $0.1 \leq i_P \leq 10$ nA. Figure 4.16 shows the photodiode response in the open circuit configuration at -20°C according to eqn. 4.12 as a function of the expected photocurrent for three values of the ideality factor N. The response is close to linear for all ideality factors with $< 10\%$ drop from the purely linear response at an output voltage of 4-5 mV.

The photodiode linearity in the open circuit configuration was further scrutinised by comparing time evolved signals of the D 5→2 line intensity, obtained with KT3B and summed across all tracks, against the D 4→3 filtered photodiode output voltage from a divertor detachment experiment, JET pulse 86959 (Figure 4.17). The contri-

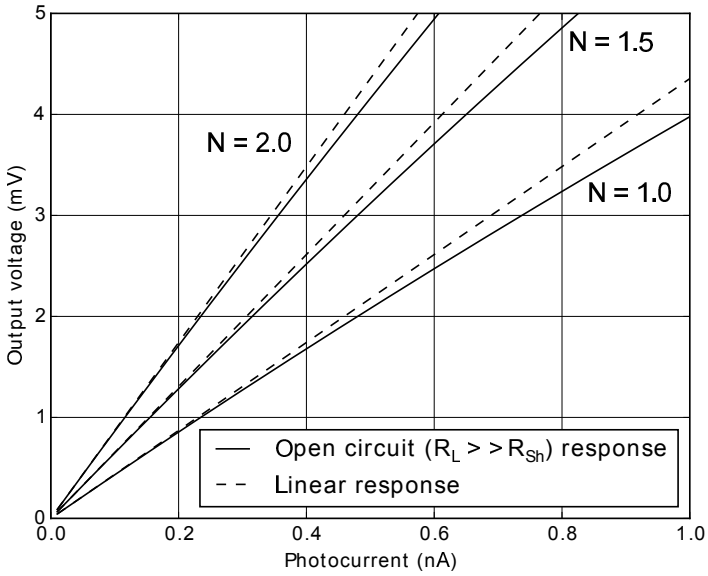

Figure 4.16: Ideal photodiode response for different ideality factors N.

bution of the background emission was negligible for this pulse. The measurement serves as a convenient ramp function for comparison of the relative changes in the slope of both signals and is also one of the strongest D 4→3 signals recorded during the 2014 JET-ILW scientific campaign. The D 5→2 peak-to-peak signal is scaled to the D 4→3 signal in order to isolate any differences in the slope. The very good agreement in the signal rate of increase up to 3 mV output voltage is consistent with near-linear photodiode response. This result confirms the suitability of the open circuit photodiode operating mode for D 4→3 line intensity and thermal background contribution measurements.

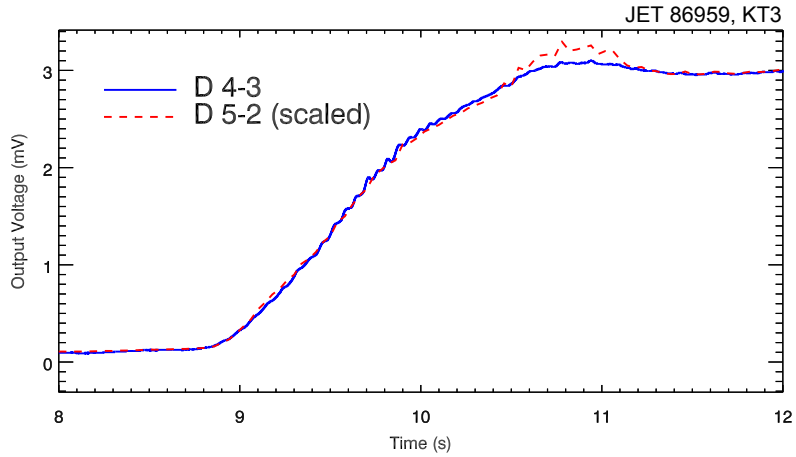

Figure 4.17: D 4→3 (KT3D-PD) photodiode output voltage vs. D 5→2 (KT3B) total line intensity (scaled) from JET pulse 86959.

The SNR at illumination levels representative of expected D 4→3 and thermal emission intensities was characterised using the current stabilised NIR LED (center wavelength 1450 nm, spectral FWHM 100 nm) calibration source. The time domain step response of the photodiode to the LED illumination is shown in Figure 4.18, as well as the frequency spectrum obtained using a fast Fourier transform (FFT) of the signal at $4.45 \leq t \leq 4.65$ s for three signal conditioning cases: (1) the raw signal sampled at 10000 samples/s; (2) the raw signal with the 50 Hz electromagnetic interference (EMI) component subtracted using a Butterworth filter with a bandpass of 10 Hz, and (3) raw signal smoothed using a Hann window with a width of 250 samples and subsequent subtraction of the 50 Hz interference component using the Butterworth filter. The SNR for the three signal conditions, shown in the bottom left plot, is calculated by dividing the peak-to-peak signal voltage by the standard deviation of a 1000 sample window. Clearly, the smoothing and removal of the 50 Hz EMI component significantly improves the SNR from ≈ 30 to ≈ 2000 at a peak-to-peak voltage of 4.6 mV. The rise time of all three signals, largely dictated by the photodiode R_{Sh} and C_j values according to eqn. 4.10, is $\tau_r \approx 40$ ms which yields a -3 dB cut-off frequency $f_c \approx 9$ Hz.

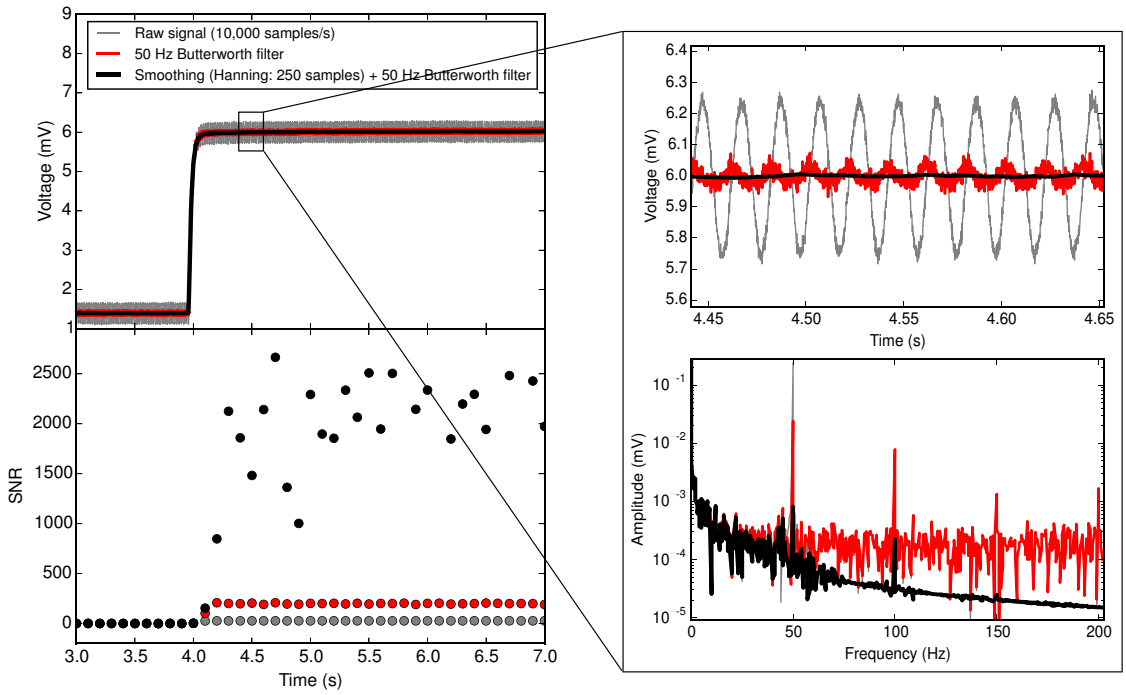

Figure 4.18: Time and frequency response and estimated SNR of the KT3D-PD filtered photodiode system for three different signal conditioning cases using illumination provided by the NIR calibration LED.

The 16 bit analog-to-digital conversion (ADC) resolution at the lowest available input range of ±0.2 V yields an effective digitiser resolution at the full scale plasma signal (≈ 5 mV) of 10 bits, or 1024 levels. Improving the digitiser resolution would require signal amplification and consequently a reduction in the SNR.

In summary, the filtered photodiode system in the photovoltaic open circuit configuration provides linearity at $< 10\%$ deviation at peak expected illumination levels (effective full scale), a maximum SNR≈ 2000 with appropriate signal conditioning in post-process and time resolution of ≈ 50 ms. Although there is significant room for improvement in increasing the detector speed, the current configuration performed sufficiently well within the main measurement criteria; mainly quantifying the extent of the thermal contribution to the D 4→3 line intensity.

4.4.3 Isolating the Thermal Emission Contribution

Contamination from thermal emission is of particular concern for quantitative measurements of the D 4→3 line intensity at 1874.6 nm, which coincides with the peak of a blackbody radiation spectral distribution at a temperature of 1547 K according to Wien's law. Maximum surface temperatures of the JET-ILW solid tungsten divertor target lamellae (tile 5) have been observed to exceed 1500 K due to steady-state and transient heat loading (Balboa et al., 2012). Figure 4.10.(b) includes estimates of the thermal emission contribution for different tungsten tile temperatures by applying the KT3D-PD filter function to the thermal emission continuum. The bremsstrahlung contribution admitted through the filter is also shown. Similar to the VIS range, signal contamination from bremsstrahlung only becomes appreciable for high electron density and low electron temperatures, typically associated with the detached divertor regime.

Removing the background contribution from the D 4→3 signal is achieved in the KT3D-PD system by a dedicated background channel with a 4.5 nm FWHM bandpass filter, with the center wavelength (1886 nm) shifted 11.4 nm away from the D 4→3 line centre (Figure 4.19.(a)). At this wavelength separation crosstalk between the two measurements is reduced to $\lesssim 5\%$. Due to the non-linear wavelength dependence of the black body spectrum, the corrected D 4→3 signal includes a non-linear component that varies with the tile temperature such that

$$I_{\alpha,corr} = I_{\alpha,Th} - \zeta I_{Th} \tag{4.13}$$

where $I_{\alpha,corr}$, $I_{\alpha,Th}$, and I_{Th} are the corrected D 4→3 intensity, combined D 4→3 and thermal intensity, and the stand-alone thermal intensity, respectively, as a function of the tungsten tile surface temperature and the given D 4→3 radiance I_α. Figure 4.19.(b) shows the corrected D 4→3 intensity according to eqn. 4.13, normalised to the actual value I_α, as a function of tungsten tile temperature. Three closely spaced values of the correction factor ζ result in quite different corrected signal functions, with ζ modifying the correction significantly at low values of I_α. The significance of this result is that, in practice, the uncertainty in the D 4→3 intensity measurement will become larger with increasing tile temperature. A narrower bandpass filter, at significant additional expense, would reduce the admitted thermal background component and thus decrease the measurement uncertainty at high tile temperatures. Finally, it should be noted that, in the absence of budgetary constraints, the optimal solution for obtaining D 4→3 line intensity measurements is by means of a grating spectrometer with a linear extended-InGaAs sensor. Removing the background thermal continuum could then be carried out in the usual manner by fitting and subtracting the continuum baseline from the spectral line measurement.

4.5 Results From Plasma Measurements

The increased spatial resolution afforded by the new filtered imaging system (KT3E8TA / B) allows for precise monitoring of any radial and toroidal view shifts during plasma pulses, since the features of the divertor target plates are well resolved, as shown in Figure 4.20,(a). An example of the dynamic FOV shift in the radial direction during JET pulse 86087 is shown in Figure 4.20,(b)-(c) from filtered D 3→2 and Be II emission during a strike point sweep on tile 5. A 10 pixel ($\approx$ 12 mm) shift is evident and is most likely caused by movement of the mirror box housing mirror D and E which is mounted to one of the transformer limbs. The highest recorded shift during the 2014 summer campaign was 40 pixels ($\approx$ 48 mm) during JET pulse 87075. The gaps between the lamellae stacks (5D, 5C, 5B) thus serve as a reference point for spatial calibration correction for the rest of the KT3 instruments. A possible method for automating such a correction is to track the position of the tile gap using, for instance, cross-correlation or a selection algorithm using the radial pixel array in the vicinity of the gap for each camera frame. Such a method relies on sufficient plasma emission or corner reflections to illuminate the tiles.

Operation of the imaging cameras at 1 kHz frame rate gives diagnostic access to ELM cycle resolution, the duration and frequency of which is usually determined

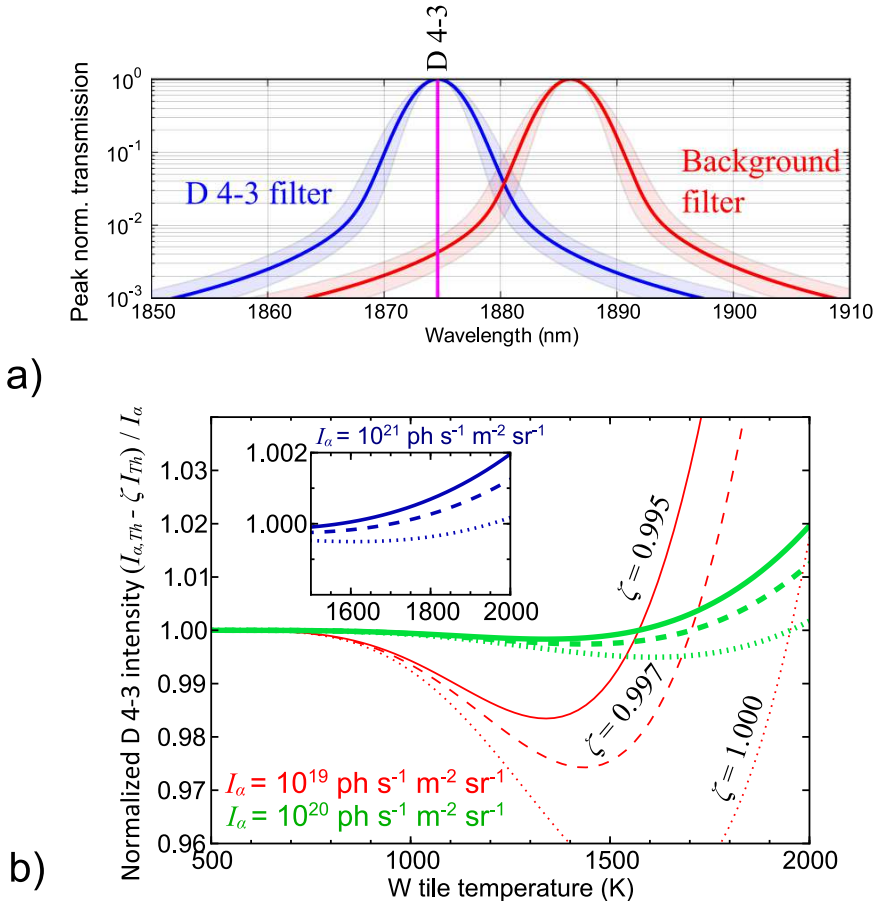

Figure 4.19: Thermal background corrected D 4→3 intensity as a function of tungsten tile temperature.

from fast measurements of the upstream edge pedestal temperature $T_{e,ped}$, the total radiated power P_{rad}, and peaks in the total Be II (527 nm) line emission from a sudden increase in impurity influx to the divertor during the ELM. Figure 4.21 shows first of its kind ELM-resolved divertor D 3→2 emission measurements at 1 ms time resolution and better than 1.5 mm radial spatial resolution using KT3E8TA during two H-mode JET-ILW pulses. The collapse in pedestal temperature, Be II intensity spikes and subsequent peaks in radiated power (Figure 4.21 (a) and (c)) are consistent with ELM cycles in both pulses (JET 86421 and 86255). The D 3→2 radial emission profiles, however, exhibit different features. In pulse 86421 the onset of each ELM causes first an increase in D 3→2 intensity near the strike point followed by a $\sim$ 30% decrease relative to the inter-ELM intensity. This is likely an indication of the ELM "burning" through the cool and dense region in the outer divertor caused by a sudden influx of hotter plasma from the upstream ELM event through parallel SOL transport. Conversely, the radial D 3→2 emission

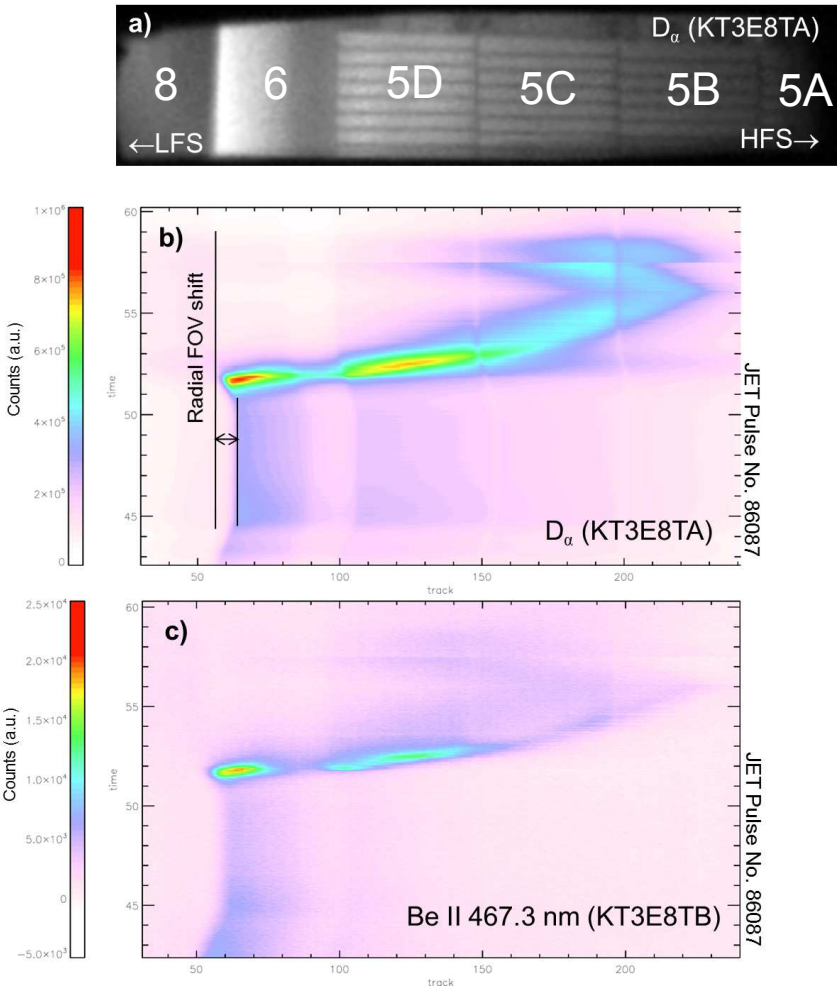

Figure 4.20: a) KT3E8TA raw camera frame from JET pulse 86087 with tile identifications; b)KT3E8TA time evolution of the D 3→2 radial intensity profile during a tile 5 strike point sweep; c) KT3E8TB time evolution of the Be II radial intensity profile for the same pulse.

profile in pulse 86255 exhibits transient ELM peaks, similar to the Be II signal, and is associated with increased recycling in ionising plasma conditions due to a sudden influx of particles during the ELM. The spatially resolved emission profiles thus provide valuable diagnostic information of the influence of the transient ELM events on the plasma state as well as any perturbations to the magnetic geometry which may cause an intra-ELM strike point shift. Further investigation, for example by comparing the D 5→2/3→2 line ratio, is needed to gain insight into the plasma radiation characteristics as well as the possible impact of deuterium out-gassing from the solid tungsten tiles during ELM cycles.

The low resolution KT3D NIR survey spectrometer allows for identification of the strong lines in the 900-1700 nm spectrum. As a proof of concept diagnostic,

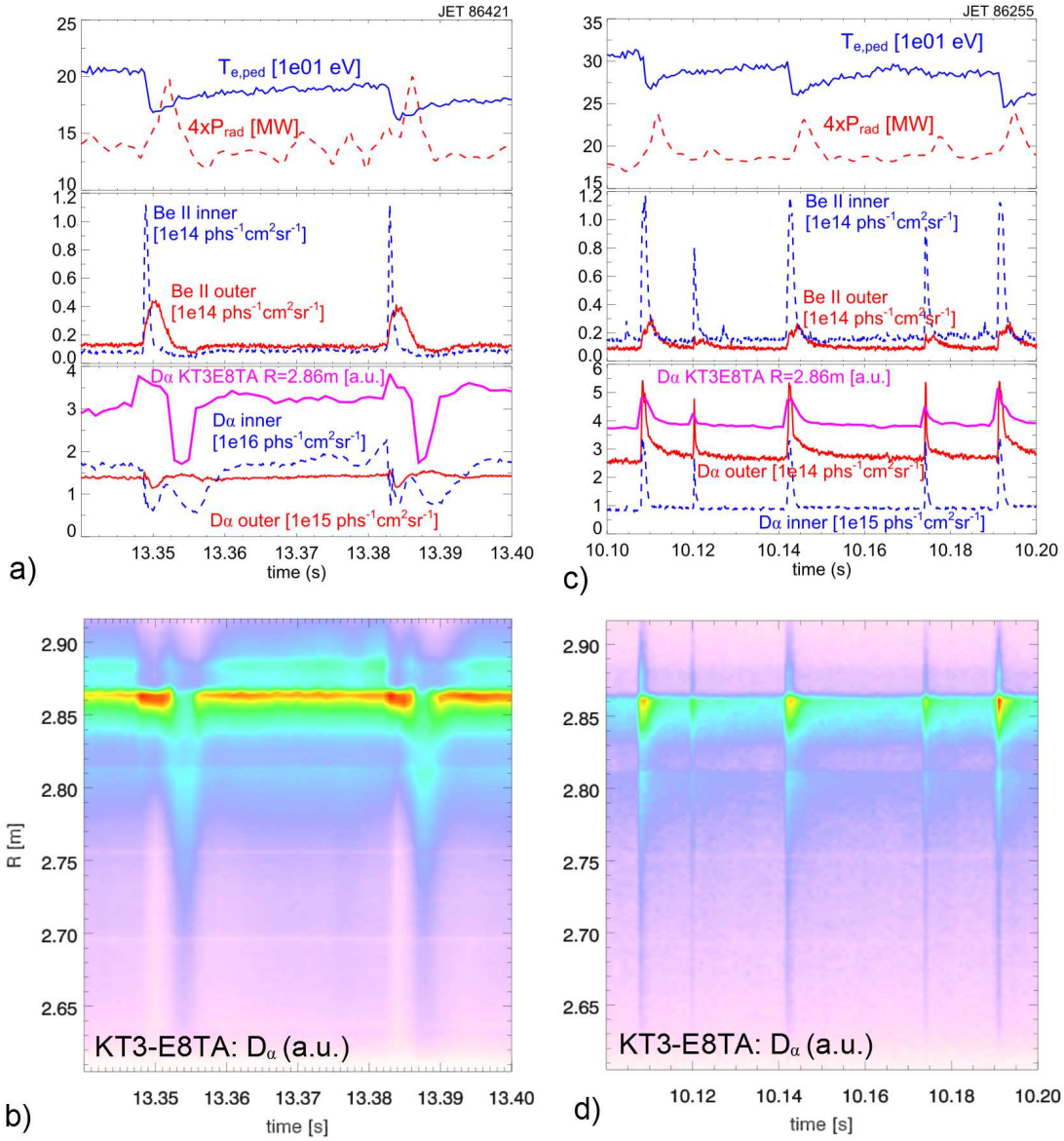

Figure 4.21: a) Time evolution of select signals and D 3→2 radial intensity profiles from JET pulse 86421 and 86255. Ordinate units are given in square brackets for each signal. R is the plasma major radius and extends from $2.60 \leq R \leq 2.92$ m over the outer divertor tiles.

the survey is useful for identifying the regions of interest for further study at higher resolution. Two KT3D spectra are shown in Figure 4.22 with the strong lines from intrinsic impurities (Be I, Be II, C I) and the D 5→3 and D 6→3 lines identified. Thermal emission from tile 5 contributes a significant broadband component in the spectrum of pulse 85829. A region of poor transmission around 1380 nm is also evident in the raw DN data, likely due to the KT3 main system dichroic filters. The presence of the thermal spectrum reduces the dynamic range and increases shot noise

for line intensity measurements, but also provides spectrally resolved temperature data of possible use for IR thermography. Quantitative measurements of spectral line emission intensities and line profiles are possible given a suitable background subtraction technique, provided the sum of spectral emission contributions does not saturate the detector.

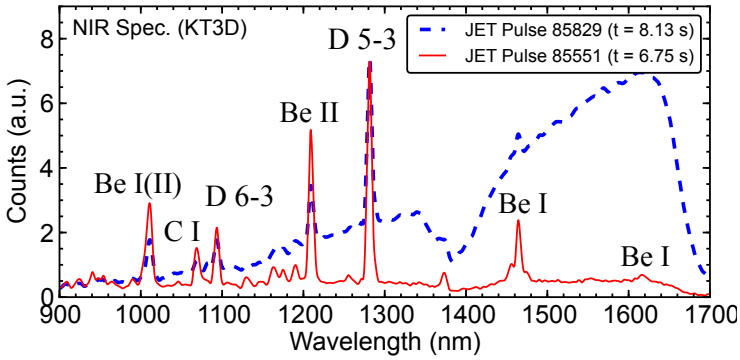

Figure 4.22: KT3D spectra from JET pulse 85829 and 85551.

The extent of the thermal contribution relative to the D 4→3 line intensity was examined using the KT3D-PD photodiode pair by scanning the range of plasma pulses throughout the 2014 campaign. Horizontal target plasma configurations, in which the outer strike point position on tile 5 is directly in the LOS of the photodiodes, is of particular interest. It was found that the thermal contribution was significant for high input power discharges ($P_{NBI} > 20$ MW) and attached divertor plasma conditions. In such scenarios the bulk of the power entering the SOL upstream is deposited onto the target plates in a narrow strip characterised by the power width λ_q (see Section 2.2.2), typically of the order of a few to several mm on JET (e.g. Fundamenski et al., 2002). The highest thermal contribution to the D 4→3 line intensity was observed in pulse 86718 ($P_{NBI} = 22.7$ MW, $I_P = 2$ MA), shown in Figure 4.23.(a), where at the thermal peak with a maximum surface temperature of 1463 K the D 4→3 / background intensity ratio is ≈ 1.6. The outer divertor D 3→2 smoothed and scaled intensity trace (JET signal EDG8/DAO) is in good agreement with the thermal background corrected D 4→3 signal. This indicates very low cross-talk between the D 4→3 and background KT3D-PD photodiode narrowband filters thus confirming reliable background correction.

To gain insight into the spatial extent of D 4→3 emission in Figure 4.23.(a), the D 3→2 radial emission profile obtained using KT3-E8TA is shown in Figure 4.23.(b) at a time window near the thermal peak (t =7.60-7.65 s). The radial profile is localised to the strike point (the location of the outer strike point (OSP) from the magnetic

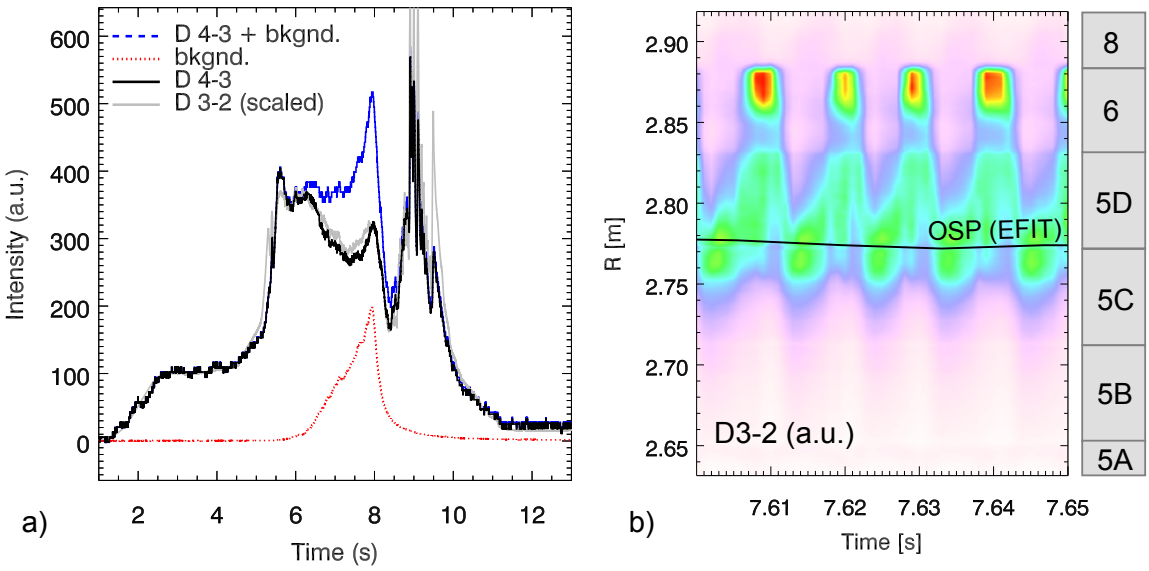

Figure 4.23: JET pulse 86718: a) Outer divertor total D 4→3 intensity and thermal background contribution (KT3D-PD), and total D 3→2 intensity (EDG8/DAO); b) D 3→2 radial intensity profiles (KT3E8TA).

reconstruction EFIT [1] signal is indicated), shifting outward towards the tile 6 corner during each ELM cycle. This indicates that the measured volume integrated D 4→3 / background ratio is representative of the local conditions near the OSP. As such, the above comparison supports the utility of D 4→3 line intensity measurements on the JET-ILW divertor, even at high input power and high tile temperatures, albeit with increased shot noise ($\leq \sqrt{2}$) and decreased dynamic range. It is also worth pointing out that KT3D-PD thermal background measurements did not exceed the photodiode noise level in detached plasma scenarios in which the power deposition on divertor targets is reduced due to atomic processes upstream of the target. Lastly, the time resolution of the D 4→3 and background photodiode signals ($\approx$ 50 ms) is not sufficient for examining the intra and inter-ELM thermal contribution, thus the photodiode measurements represent the average over one or more ELM cycles.

Interpretation of hydrogenic Balmer and Paschen series lines relies on sufficient spectral resolution for resolving line profile features and identifying contributions from nearby impurity lines that may obfuscate the measurements. The base KT3 system (KT3A/B) provides an instrumental FWHM of 0.08 nm using the 1200 l/mm grating. This is sufficient for resolving Stark broadening of the Balmer lines with $n \geq$

[1] EFIT (Equilibrium Fitting) is a computer code which translates measurements from magnetic probe diagnostics into useful outputs such as plasma geometry, stored energy and current profiles.

5 and identifying impurity lines with high precision. To gain insight into the spectral character of the NIR region in more detail, the KT3D-MR spectrometer was used to survey the region from 900-1350 nm under different plasma conditions. Figure 4.24 shows composite spectra spanning the VIS and NIR range using KT3A/B, KT3D-MR (solid line) and KT3D (dotted line) instruments in unseeded, Ne seeded and N_2 seeded plasmas. Impurity seeding on JET-ILW is frequently used in experiments with the aim of promoting a high radiative fraction in the SOL and divertor in order to dissipate the exhaust power upstream of divertor targets. A consequence of such extrinsic impurity puffing is the presence of many low charge state (e.g., N I-IV, Ne I-IV) spectral lines across the VIS and NIR spectrum, the intensity of which may be comparable to the Balmer and Paschen series lines depending on the seed gas injection rate and divertor plasma conditions. This is most evident for the high-n Balmer lines near the discrete to continuum transition (370-380 nm) as well as for the high-n Paschen lines (900-1100 nm). Lines which are relatively free from contamination due to seeded impurity lines are D 4→2, 5→2, 7→2, 8→2, 5→3 and 6→3. These lines are therefore good candidates for estimating plasma parameters such as T_e and n_e for both unseeded and seeded plasmas. It is also interesting to note that, although the low resolution KT3D spectrometer is not suitable for Paschen line intensity measurements under Ne and N_2 seeded conditions due to contamination from unresolved blended lines, the Paschen spectrum is sufficiently free of intrinsic impurity lines (e.g., Be I-II, C I-II) in unseeded plasmas. This is especially relevant in detached plasmas in which the volume recombining conditions give rise to relatively strong Balmer and Paschen series line emission. Therefore, as already demonstrated in Section 3.2.3, useful information for T_e estimation can be extracted from even a low resolution spectrometer, with the benefit of facilitating a wider spectral range relative to measurements with longer focal length instruments.

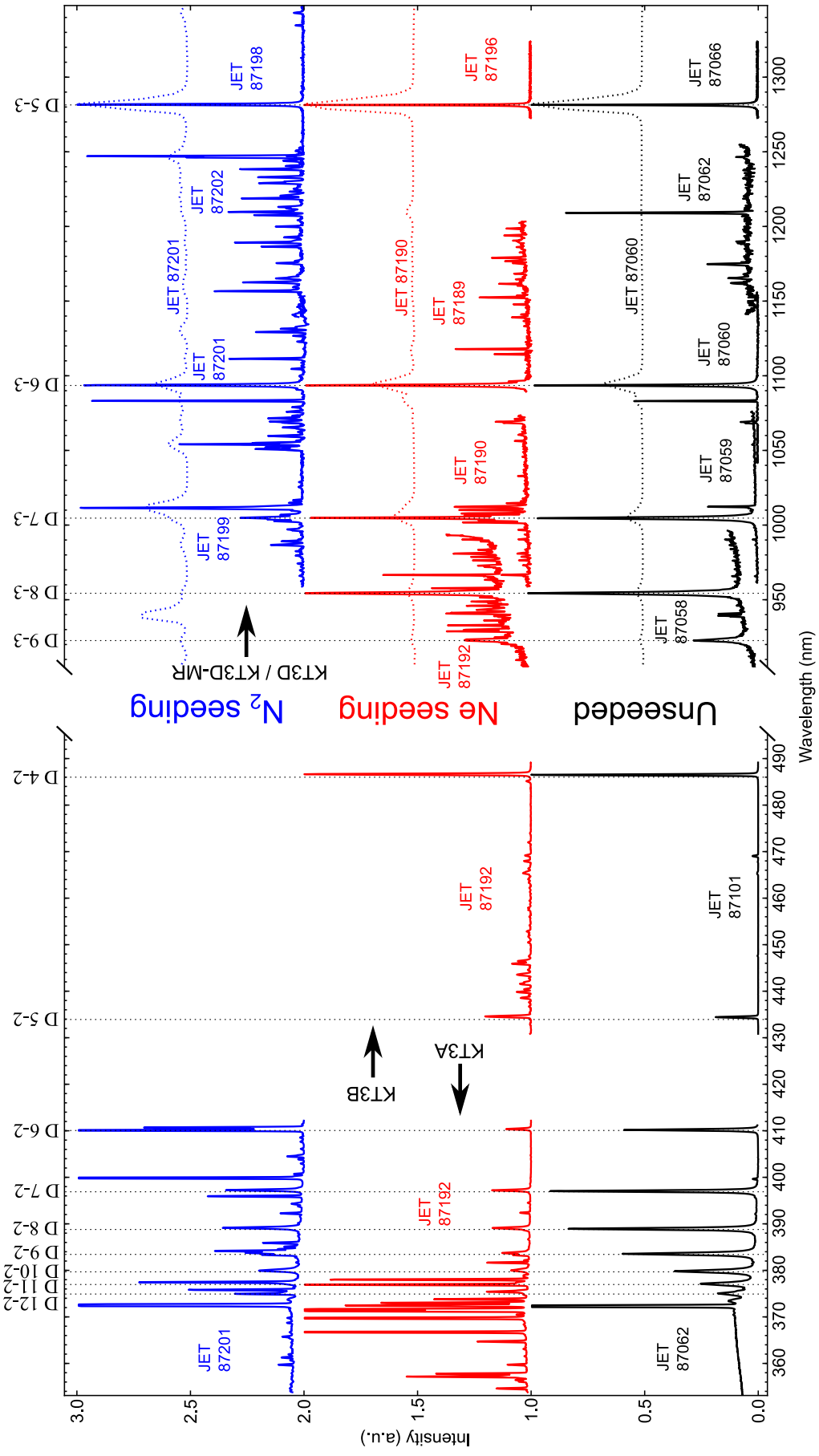

Figure 4.24: Composite spectra from KT3 grating spectrometers.

Chapter 5

Parameter Estimation From Balmer-Paschen Spectroscopy

The interpretation of hydrogen isotope line emission spectra in tokamak divertors is of great interest in advancing the understanding of plasma exhaust and divertor physics. This is especially relevant for detachment experiments in preparation for the ITER baseline scenario (Ikeda, 2007) for which operation at high density and partial detachment is mandatory for reducing heat loads on plasma facing components to tolerable levels. Likewise, operation in the detached regime is necessary for reducing the tungsten sputtering yields to prevent impurity accumulation and its deleterious effects on energy confinement and fuel dilution in the core plasma. Reliable measurements of plasma parameters such as density and electron temperature at and away from the divertor targets are needed for characterising the conditions under which volumetric dissipative processes act to reduce the particle and heat fluxes incident on the divertor targets. Application of divertor spectroscopic measurements for providing real-time spatially resolved information on the state of the detached plasma is also of interest due to increased opportunity for feedback control (e.g. Huber et al., 2013; Brezinsek et al., 2009) of the detached regime in the all metal JET-ILW machine (Matthews et al., 2011). Exploitation of the high-n hydrogen Paschen series lines (in the CCD sensitivity range up to the cut-off at around 1000 nm) as a spectroscopic diagnostic tool for estimating density has thus far been limited (e.g. Soukhanovskii et al., 2006; Brezinsek et al., 2009). The line profile features of the Paschen lines above 1000 nm and their applicability as divertor spectroscopy diagnostic have not, to date, been explored.

In this chapter the scope for plasma parameter recovery from analysis of hydrogenic Balmer and Paschen series spectral line profiles is investigated. The diagnostic

capabilities are examined through the formulation of a simplified and computationally efficient line profile model suitable for application to batch analysis of spectroscopic data and multi-parametric fitting techniques.

5.1 Methodology

The total spectral line profile for a given electronic transition of a neutral hydrogenic species is characterised by multiple influences in the plasma environment. In the simplest case of a pure hydrogen isotropic plasma at thermal equilibrium, described by electron and ion density $n = n_e = n_i$ and temperature $T = T_e = T_i = T_n$, the spectral line is Doppler broadened with a Gaussian profile due to a Maxwellian velocity distribution describing the motion of the emitter atoms. Stark broadening of the spectral line occurs due to the presence of charged particles which impose an electric field experienced by the emitter. The broadening effect is proportional to the surrounding particle densities and can be approximated in the parameter range of tokamak plasmas using the impact approximation for electrons and the quasi-static approximation for the ions, as described in Section 2.1.4. The total line profile for this simple case is given by the convolution of the Doppler and Stark broadened profiles assuming that the two processes are statistically independent (i.e., ignoring any correlations between Stark and Doppler broadening, (see Griem, 1997, Chap. 4.6). The wings of the combined line shape are influenced by the Stark broadened profile, typically approximated by a Lorentzian function, which decays weakly compared to the Gaussian function arising from Doppler broadening.

The presence of a static magnetic field causes Zeeman splitting of degenerate energy levels according to the magnetic quantum number M with partial polarisation of the resulting multiplet components. Each of the split components can then be Doppler and Stark broadened, with the sum of the components yielding an approximation of the total profile. However, the magnetic field also influences the Stark broadening process by imposing a quantisation axis on the space averaged electric microfield. Thus a more accurate treatment must consider separately the parallel and perpendicular microfield components, relative to the magnetic field direction (Ferri et al., 2011). Furthermore, consideration of ion dynamics can result in significant deviation of the line shape and total width from the quasi-static approximation, particularly for low-n transitions (e.g., Ba-α, Ba-β, Pa-α, Pa-β) for which the ion microfield broadening predominates over the electron impact broadening contribution (Potzel et al., 2014; Ferri et al., 2011). The hydrogenic isotope mixture of H,

D, and T species also influences the spectral line shape through the isotopic energy (wavelength) shift resulting in overlapping line profiles, the intensities of which are given by the ratio of isotope concentrations.

In tokamak edge and divertor plasmas asymmetries in the Doppler broadened line profile are observed (see Kukushkin et al., 2014a, and references therein). The local neutral velocity distribution function (VDF) at some distance away from the wall is influenced by multiple kinetic processes occurring due to the interaction of neutral, molecular and ion fluxes into and out of the wall. Charge exchange of relatively hot background plasma ions with cold recycled neutrals near the wall results in a broad Gaussian contribution, while reflection of fast atoms can add an asymmetric component to the line-of-sight averaged Doppler profile. Formation of $\lesssim 5$ eV energy neutrals from Franck-Condon dissociation of recycled H_2 molecules can be significant, even when the local plasma temperature is $\leq$1 eV in the detached plasma regime.

With a suitably narrow instrumental function, the spectral line profiles of the hydrogen Balmer and Paschen series lines offer a range of diagnostic possibilities for the recovery of line-of-sight averaged plasma parameters. Typically, high resolution Ba-α spectroscopy has been employed for diagnosing the neutral VDF in the scrape-off layer (SOL) (e.g. Kukushkin et al., 2014b), while the broad profiles of the high-n ($n \geq 9$) lines dominated by Stark broadening offer a robust measure of electron density in detached or partially-detached plasmas (e.g. Meigs et al., 1998, 2013; Potzel et al., 2014; Soukhanovskii et al., 2006). In the context of JET-ILW SOL and divertor plasma conditions ($B < 3.0$ T, $n_e > 5 \times 10^{19}$ m^{-3} and $T_n < 10$ eV), Zeeman splitting and Doppler broadening can generally be neglected for high-n Balmer lines, while Stark broadening of the Ba-α line is small relative to Doppler broadening in the SOL plasma. The use of high-n Balmer lines as a density diagnostic is limited by the population distribution of excited upper states, which only become significant when driven by three-body recombination in low temperature, high density volume recombining plasmas ($T_e \leq 1.5$ eV, $n_e \geq 10^{20}$ m^{-3}). In divertor plasma conditions, where density is typically higher and temperature lower than in the SOL, the Ba-α profile can generally include a significant contribution from Zeeman splitting and even Stark broadening at high densities. For profiles of intermediate lines, such as Ba-β, Ba-γ, a general treatment of Stark, Zeeman and Doppler broadening mechanisms is also required for recovery of plasma parameters.

5.1.1 Line Profile Model

The present analysis of the Balmer and Paschen series transitions is underpinned by a parameterised forward model of the spectral line profile in which the Zeeman, Stark and Doppler effects are treated individually and the convolution of the Doppler and Stark contributions is assumed to be valid in the range of JET-ILW SOL and divertor plasmas.

The magnetic effects are calculated using the `ADAS603` code (Summers, 2004) which generates the Zeeman / Paschen-Back multiplet feature for hydrogenic species spectral lines, separated into the π and σ polarisation components, as a function of magnetic field magnitude B and observation angle θ. For a given B field value, the Zeeman/Paschen-Back multiplet component wavelength and intensity values are linearly interpolated from a set of `ADAS603` results across a 10 point grid of B values in the range $0.5 \leq B \leq 5.0$ T.

A semi-analytic neutral VDF model (Kukushkin et al., 2014a) is used for determining the Doppler broadening function $S_{VDF}(\lambda)$ for the i-th Zeeman / Paschen-Back component, with allowance for multiple Maxwellian ($M1$) and non-Maxwelian ($M2$) contributions, such that

$$\begin{aligned} S_{VDF,i}(\lambda) = &\sum_{m=1}^{M1} S_M^m F_{Gauss}(\lambda - \lambda_i, T_M^m) \\ &+ \sum_{n=1}^{M2} S_N^n F_{Gauss}(\lambda - \lambda_i, T_N^n) D_\lambda(\lambda - \lambda_i, \Lambda^n) \eta(\lambda - \lambda_i, \mathbf{k}, \mathbf{l}) \end{aligned} \tag{5.1}$$

where F_{Gauss} is the normalised Gaussian line shape according to eqn. 2.25; S_M^m and S_N^n are statistical weights of the m-th Maxwellian and n-th non-Maxwellian contribution to the VDF, respectively. The damping factor D_λ is given by

$$D_\lambda(\Delta\lambda, \Lambda) = \exp\left(-\frac{\Lambda}{|\Delta\lambda|}\right), \tag{5.2}$$

where Λ is derived from the characteristic damping velocity which describes the attenuation of the inward neutral flux due to ionisation by electron impact and charge exchange. η is the Heaviside step function whose argument, defined by the line-of-sight unit vector $\mathbf{l}$ and the direction unit vector of the inward neutral flux $\mathbf{k}$, modifies the sign and magnitude of the step.

The Zeeman-Doppler profile is then convolved with a pure Stark broadened profile using a parameterisation of the Model Microfield Method (MMM) (Brissaud

and Frisch, 1971) tabulations generated by Stehlé and Hutcheon (1999) for a pure hydrogen isotropic plasma. A power law of the form

$$\Delta\lambda_{1/2}(p \to q) = C(p \to q)\frac{[n_e]^{a(p\to q)}}{[T_e]^{b(p\to q)}} \tag{5.3}$$

is adopted for recovery of the Stark FWHM, $\Delta\lambda_{1/2}$ (nm), with n_e given in m^{-3} and T_e in eV, with a set of coefficients C, a, and b for each transition $p \to q$. The coefficients were determined by first interpolating the tabulated MMM profiles for a given n_e and T_e. Due to the coarsely discretised wavelength detunings in the tables, the interpolated profile was fitted in the least-squares manner to a modified Lorentzian fitting function of the form

$$S(\gamma, \Delta\lambda) \propto \frac{1}{\Delta\lambda^{5/2} + \gamma^{5/2}} \tag{5.4}$$

in order to more accurately estimate the Stark FWHM, where $\gamma = \Delta\lambda_{1/2}/2$.

The Stark profile wing shape is attributed to the relative influence of electron and ion broadening. Progressing through the Balmer or Paschen series to higher principal quantum number n, the electron broadening contribution increases relative to the ion microfield contribution. Electron broadening in the impact approximation results in a pure Lorentzian wing decay, assuming random collisions, whereas a somewhat faster decay is typically observed due to the influence of the ion microfields (see Griem, 1997; Kunze, 2009, for details). For the Holtsmark microfield distribution function (Holtsmark, 1919) (see Section 2.1.4) the wing decay is $\propto \Delta\lambda^{-5/2}$. Figure 5.1 demonstrates the impact of the choice of wing decay functions with $\propto \Delta\lambda^{-2}$ decay (pure Lorentzian) and $\propto \Delta\lambda^{-5/2}$ decay (eqn. 5.4) on fitting to the H 9→2 MMM line profile, where magnetic effects have been ignored. The $\propto \Delta\lambda^{-5/2}$ decay is shown to be the more suitable functional form, even for this high-n transition.

To obtain the FWHM for transitions with a shift in the central component (e.g., Ba-β (4→2), Pa-β (5→3)) the line fitting model consisted of one central and two shifted modified Lorentzian components (eqn. 5.4) in order to resolve the central dip, as shown in Figure 5.2.(a). This procedure was repeated over the density and temperature range of $10^{19} \leq n_e \leq 10^{21}\,\mathrm{m}^{-3}$ and $1 \leq T_e \leq 10\,\mathrm{eV}$, respectively, with 200 samples. The coefficients of eqn. 5.3 were then determined in the least-squares manner based on the set of 200 FWHM values. Using this method, the parameterised FWHM error in the specified n_e and T_e range is under 10% compared

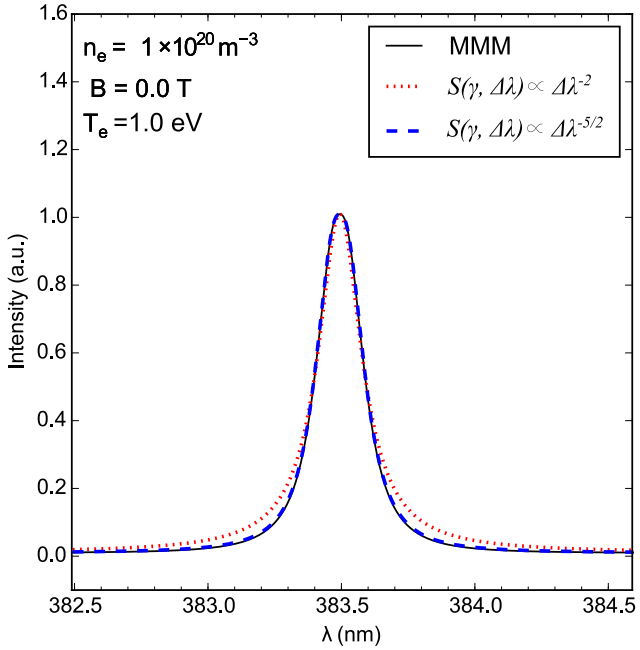

Figure 5.1: H 9→2 peak normalised line profiles with different wing decay functions relative to the MMM profile.

with the original MMM tabulations. Table 5.1 shows the recommended coefficient values for Balmer and Paschen transitions up to $n = 9$.

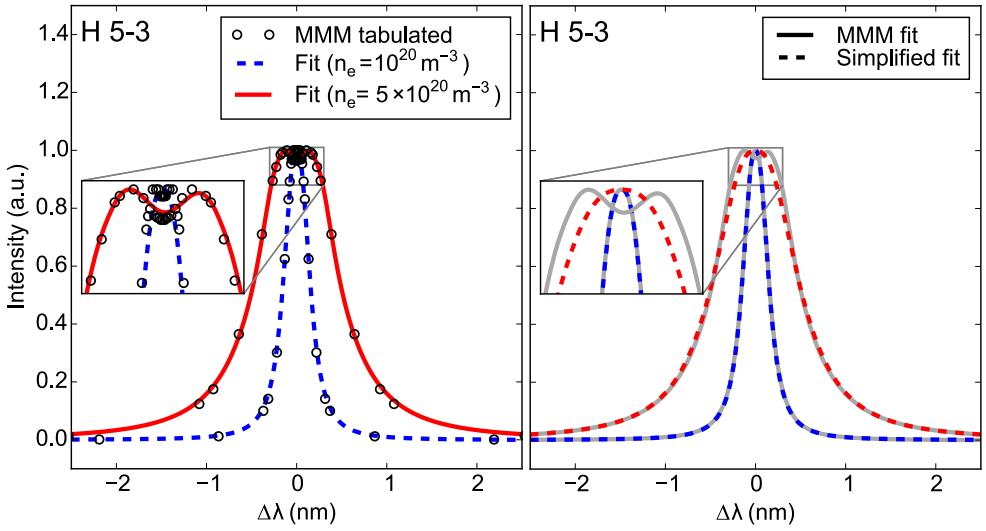

Figure 5.2: a) Three component fit to MMM tabulated H 5→3 line profiles; b) comparison to a simplified single component fit using coefficients in Table 5.1, equations 5.3 and 5.4.

To simplify the Stark profile parameterisation, profiles for all transitions, includ-

Table 5.1: Parameterised MMM Stark profile coefficients for use with equations 5.3 and 5.4. Fit errors above 5% shown in parantheses.

H transition ($p \rightarrow q$)	$C(p \rightarrow q)$	$a(p \rightarrow q)$	$b(p \rightarrow q)$
$3 \rightarrow 2$	3.710e-18 (17.49)	0.7665	0.064 (6.51)
$4 \rightarrow 2$	8.425e-18 (10.86)	0.7803	0.050
$5 \rightarrow 2$	1.310e-15	0.6796	0.030
$6 \rightarrow 2$	3.954e-16 (6.24)	0.7149	0.028
$7 \rightarrow 2$	6.258e-16	0.7120	0.029
$8 \rightarrow 2$	7.378e-16 (5.42)	0.7159	0.032
$9 \rightarrow 2$	8.947e-16 (6.88)	0.7177	0.033
$4 \rightarrow 3$	1.330e-16 (13.04)	0.7449	0.045
$5 \rightarrow 3$	6.640e-16 (7.28)	0.7356	0.044
$6 \rightarrow 3$	2.481e-15 (7.02)	0.7118	0.016
$7 \rightarrow 3$	3.270e-15	0.7137	0.029
$8 \rightarrow 3$	4.343e-15	0.7133	0.032
$9 \rightarrow 3$	5.588e-15 (6.81)	0.7165	0.033

ing ones with a shifted central component, are recovered using the single modified Lorentzian function (eqn. 5.4) for which $\gamma = \Delta\lambda_{1/2}/2$ is obtained with eqn. 5.3 and Table 5.1. The suitability of the parameterised MMM single broadening function and coefficients in Table 5.1 is illustrated in Figure 5.2.(b) in which the three component fit model is compared to the simplified single component broadening function for the H 5→3 line profile. Some loss in resolution of the central dip is evident, but an otherwise good fit away from the line centre is obtained with the single broadening function. Since instrumentation effects and Doppler broadening will tend to blur the details of the line center it is primarily the line wings and the FWHM that encode the Stark broadening information; hence the loss in resolution of the central dip is not expected to significantly influence the recovered n_e value. Moreover, the line center features of β transitions are particularly sensitive to ion dynamic effects and, as such, are the main source of discrepancy between established Stark broadening models and experiment (e.g. Wujec et al., 2002; Ferri et al., 2014).

The separate calculations and subsequent convolution of the Zeeman-Doppler and Stark profiles make the model suitable for efficient application to multi-parametric non-linear least squares minimisation, but any coupling of the magnetic and electric field perturbations on the emitter is ignored. To assess the applicability of the

proposed model for interpretation of diagnostic data, the PPP-B code (Ferri et al., 2011) was used as a benchmark. A reformulation of the original PPP code based on the frequency fluctuation model (FFM) (Talin et al., 1995; Calisti et al., 2010), the PPP-B code extends the calculations to magnetised plasmas and has been validated with full numerical simulations (see Ferri et al., 2011, and references therein). The line profile calculation in PPP-B is carried out by first establishing the static profile. In this step the electrons are treated in the impact approximation and ions in the quasi-static approximation, with the static electric field integrated over the microfield distribution function for the directions parallel and perpendicular to the magnetic field direction. The coupling in the π and σ components of the static Stark-Zeeman profile, as shown in the H 3→2 example in Figure 5.3 (left), is evident in the profile asymmetries between the central π and shifted σ components. In the H 5→3 example (Figure 5.3, right), the static Stark-Zeeman profile exhibits additional features in the line wings. Ion dynamics are introduced at a later stage in the calculation and have a significant smoothing effect. Doppler broadening has been ignored in Figure 5.3 for clarity.

In comparison to the PPP-B dynamic results, profiles generated with the proposed simplified line profile model (denoted as ADAS603-MMM in Figure 5.3) generally reproduce the line width and wing decay with sufficient accuracy especially at high densities, but a loss in resolution of the line-centre features is evident for the β transitions, as well as a modest discrepancy in the σ-component shift in the α transitions. Good agreement was obtained for the higher-n lines for which the strong Stark contribution tends to smooth any Stark-Zeeman coupling effects. With a negligible Zeeman splitting contribution for the higher-n lines, this is effectively a direct comparison of the pure Stark MMM model with the FFM model.

The above comparisons suggest that the proposed parameterised line profile model is suitable for application to diagnostic studies and JET-ILW divertor measurements, with acknowledgement of likely higher uncertainties associated with recovering n_e using the β transitions. Lastly, while the influence of higher effective charge on the Stark profile due to plasma impurities was ignored, a cursory investigation using the PPP-B code did not show this effect to be significant at divertor plasma densities. However, previously reported simulation results (Halenka et al., 2002) at high densities ($n_e > 10^{24}$ m^{-3}) in helium plasmas showed a 10% increase in the Stark FWHM for H 4→2. A more detailed investigation of this effect is therefore warranted.

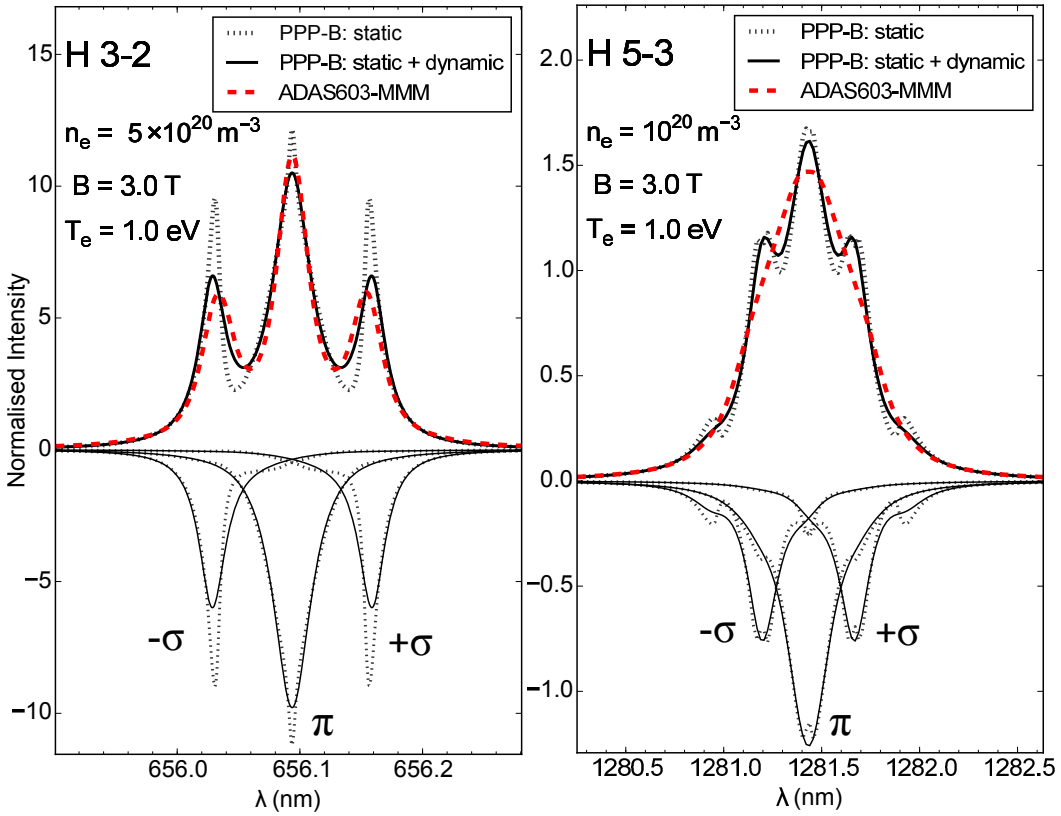

Figure 5.3: Comparison of H 3→2 and H 5→3 Stark-Zeeman line profiles generated with the PPP-B code (static and dynamic ions) and the simplified Stark-Zeeman model (ADAS603-MMM). Observation angle $\theta = 90°$. Separate π and σ polarisation components are shown below the abscissa.

5.1.2 Overview of Diagnostics

Plasma density and electron temperature spectroscopic measurements were carried out using the mirror-linked JET-ILW divertor spectroscopy system KT3 (see Chapter 4). This includes: spectral coverage of the Balmer series (KT3A/B, spatially resolved, instrumental FWHM=0.08 nm with the 1200 l/mm grating); Paschen series medium resolution spectra up to D 5→3 (KT3D-MR, spatially resolved, instrumental FWHM=0.24 nm with the 600 l/mm grating).

In addition to the mirror-linked system, a fibre-fed high resolution spectroscopy system (KSRB/KSRD, instrumental FWHM=0.024 nm) provided access to D 3→2 neutral VDF measurements in the outer divertor and density measurements from the D 6→2 line in the inner divertor. For these measurements the collecting optics are fitted with linear polarisers in order to isolate the π-polarisation component.

Fixed divertor Langmuir probes (KY4D) were used to corroborate the spectroscopic plasma density and electron temperature measurements with localised probe

measurements. Figure 5.4 shows the relevant spectroscopic views, Langmuir probe (LP) locations, divertor geometry with tile identification, as well as the plasma configurations for the two plasma discharges examined.

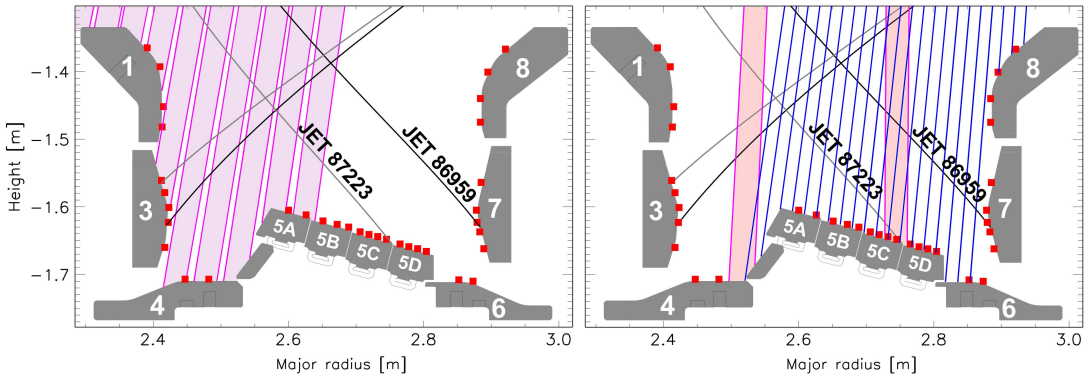

Figure 5.4: JET-ILW divertor geometry, tile identification and diagnostic views: Langmuir probes (KY4D) (red squares), high-resolution D 6→2 spectroscopy (KSRD) (left, shaded), selected chords from high-resolution D 3→2 spectroscopy (KSRB) (right, shaded), mirror-linked outer divertor imaging spectroscopy (KT3) (right, blue lines). Also shown are the horizontal (JET 87223, grey line) and vertical (JET 86959, black line) target plasma configurations as indicated by the separatrix geometry and location of the outer strike point on the horizontal or vertical divertor tiles, respectively.

5.1.3 Data Evaluation

Radial Density Profiles

Spatially resolved density profiles in the radial coordinate in the outer divertor were inferred from Stark broadened Balmer and Paschen lines, depending on the mirror-linked spectroscopy setup, and measurement SNR. Density profiles across the inner divertor were inferred from the D 6→2 line measured with the high-resolution fibre-fed spectroscopy system (KSRD). The simultaneous measurements of different transitions offered a basis for evaluating the robustness of the parameterised line profile model.

In the magnetic field magnitude range (typically $B < 3$ T) of large tokamaks such as JET or ASDEX-Upgrade (AUG) Zeeman splitting and Doppler broadening effects can be neglected for the high-n Balmer series lines employed for spectroscopic density measurements (Potzel et al., 2014; Meigs et al., 1998). For the lower-n Balmer and Paschen lines, the contributions from Zeeman and Doppler broadening

effects relative to Stark broadening must be examined based on the scaling with respect to the transition wavelength:

$$\Delta\lambda_{1/2}^{Dopp.} \propto \lambda_p \sqrt{\frac{k_B T_i}{m_i}}, \tag{5.5}$$

$$\Delta\lambda_{sep.}^{Zeeman} \propto \lambda_p^2 B, \tag{5.6}$$

from eqn. 2.25 and eqn. 2.32, and, using the Rydberg formula to calculate isotopic shift, the D-T separation is:

$$\Delta\lambda_{DT}^{Rydberg} \propto \lambda_p. \tag{5.7}$$

The wavelength scaling is examined in Figures 5.5-5.9 for the D 3→2, 4→2, 5→2, 4→3, 5→3 lines using the simplified line profile model based on the parameterised MMM model for Stark broadening, the `ADAS603` module for the Zeeman / Paschen-Back effect and a simple Gaussian component for Maxwellian neutral temperature Doppler broadening. The peak-normalised profiles demonstrate the influence of density variation in the range $5\times10^{19} \leq n_e \leq 5\times10^{20}$ m^{-3} and neutral temperatures in the range $1 \leq T_n \leq 10$ eV. Line profiles on the right hand side plots have been convolved with a Gaussian instrument function corresponding to the diagnostics used for the measurement of each line. Spectrally resolved measurements of the D 4→3 line profile were not possible hence the instrument function for this line is taken to be equivalent to the D 3→2 instrument function from the KSRB spectrometer.

It is clear that the D 3→2 and 4→3 line profiles are influenced by all three processes, although the density sensitivity is certainly less pronounced in the D 3→2 line. Spectral profile analysis of these two lines is therefore non-trivial, and is examined in more detail in Section 5.3. For the other low-n lines, the absolute differences in the line FWHM (including the convolved instrumental function) as a result of the neutral temperature variation are: D 4→2=20% D 5→2=18% and D 5→3=5% . Likewise, for variation of the magnetic field magnitude in the range $2\leq B \leq 3$ T (only $B = 3$ T is shown in the Figures), the absolute FWHM differences are: D 4→2=9% D 5→2=5.5% and D 5→3=17.5% . The influence of electron/ion temperature on the MMM Stark profiles in the range $1\leq T_{e,i} \leq 10$ eV was less than 5% for all cases examined. Therefore, it is reasonable to proceed with the assumption that the D 5→3 line is only weakly sensitive to Doppler broadening

while the D 5→2 line is only weakly sensitive to Zeeman splitting, in the parameter range representative of JET divertor conditions.

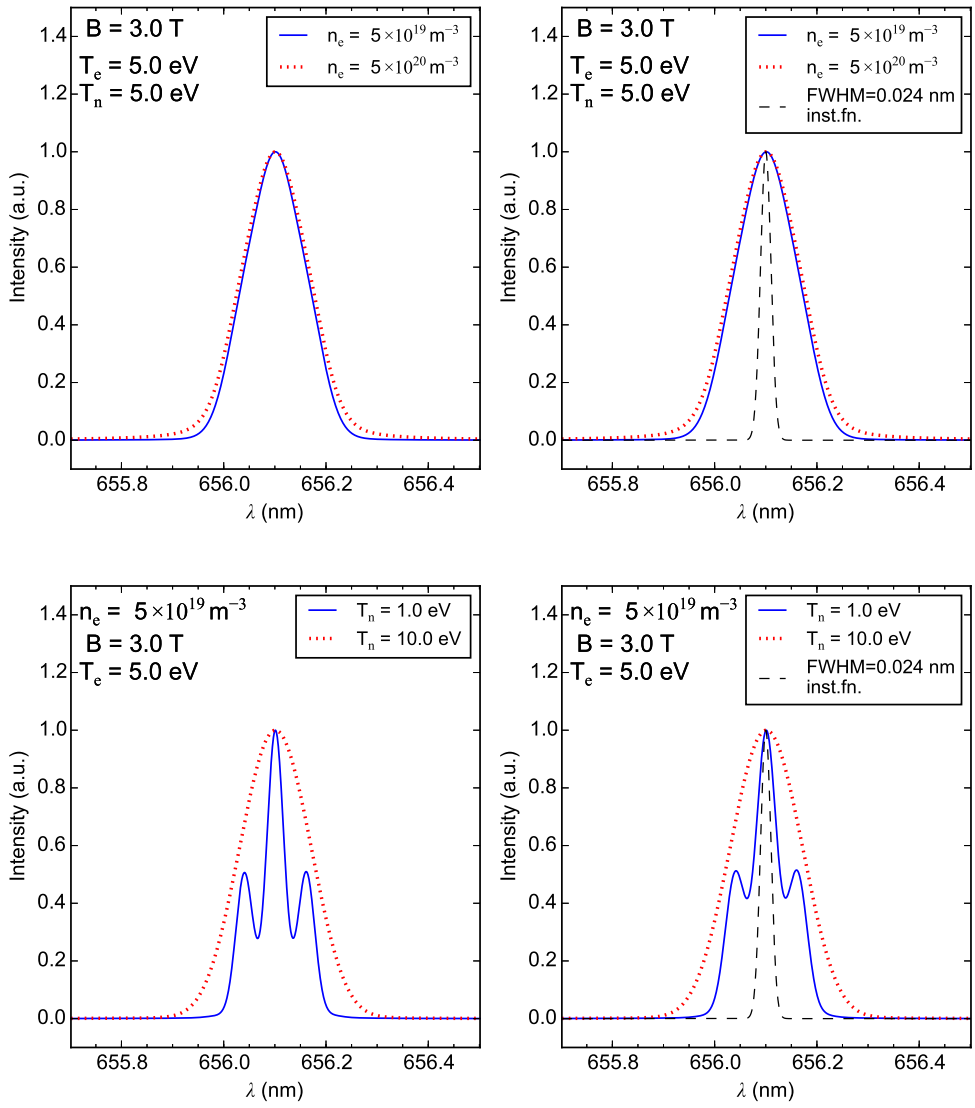

Figure 5.5: D 3→2 calculated line profile variation with density and neutral temperature. Plots on the right include the convolution of an instrument function with FWHM=0.024 nm.

The practical execution of Stark broadening analysis to spectral lines for which Zeeman effects must be captured relies on sufficient spectral resolution for resolving the π-σ polarisation components directly. Alternatively an *a priori* diagnostic calibration accounting for the transmission of each polarisation state through the optical train containing reflective, refractive and dichroic filter components would provide such information. For the D 5→3 line which exhibits significant sensitiv-

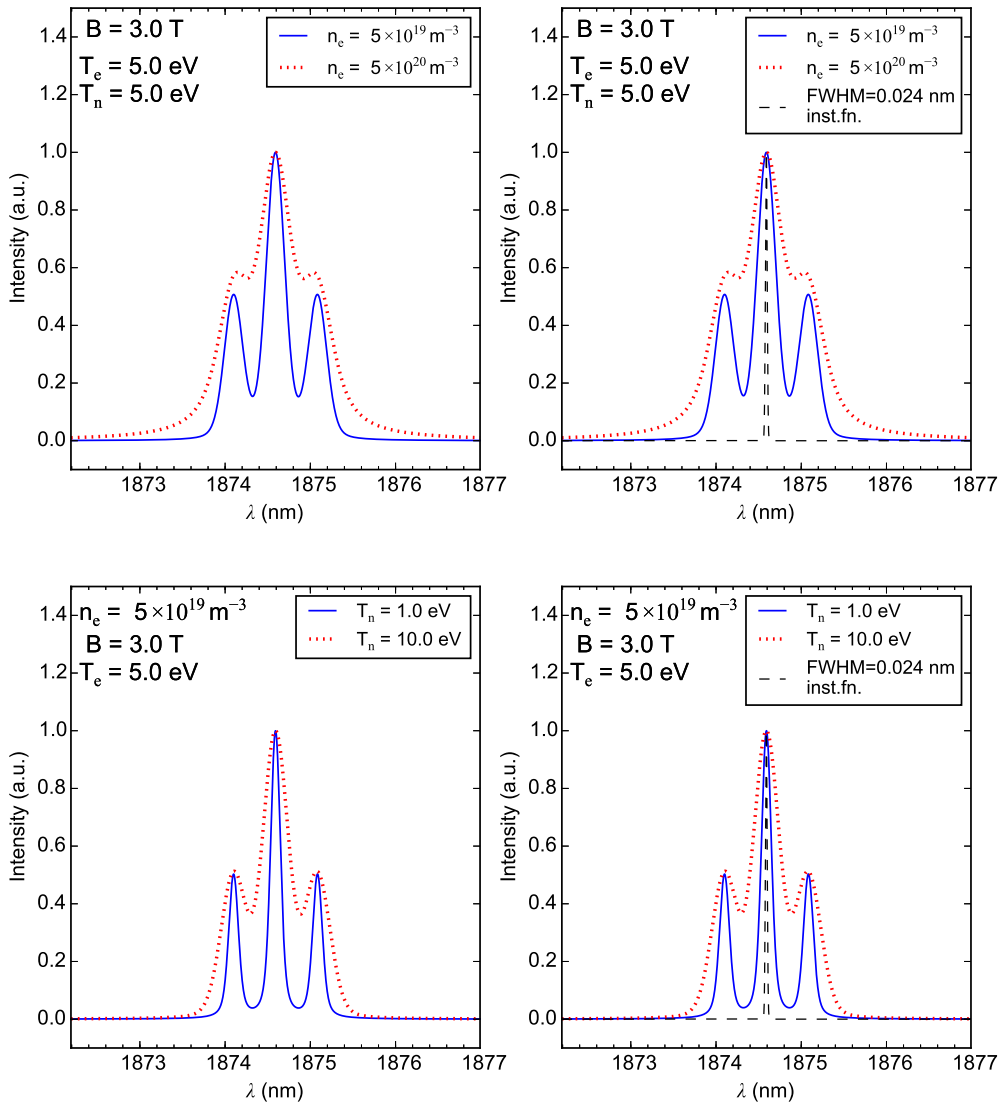

Figure 5.6: D 4→3 calculated line profile variation with density and neutral temperature. Plots on the right include the convolution of an instrument function with FWHM=0.024 nm.

ity to Zeeman splitting, the π-σ component transmission calibration could not be performed for the KT3 system. Likewise, the spectrometer did not offer enough resolution to measure the component intensities directly. Therefore the σ/π ratio was inferred by comparing derived density values from the D 5→3 line to the high-n Balmer lines, yielding an estimate of $\sigma/\pi \approx 0.3$.

The ADAS Feature Generator (`AFG`), coupled to the Framework for Features Synthesis (`FFS`) package (Nicholas, 2011), was employed for non-linear least-squares fitting of the spectral line profiles. This fitting package is already integrated within

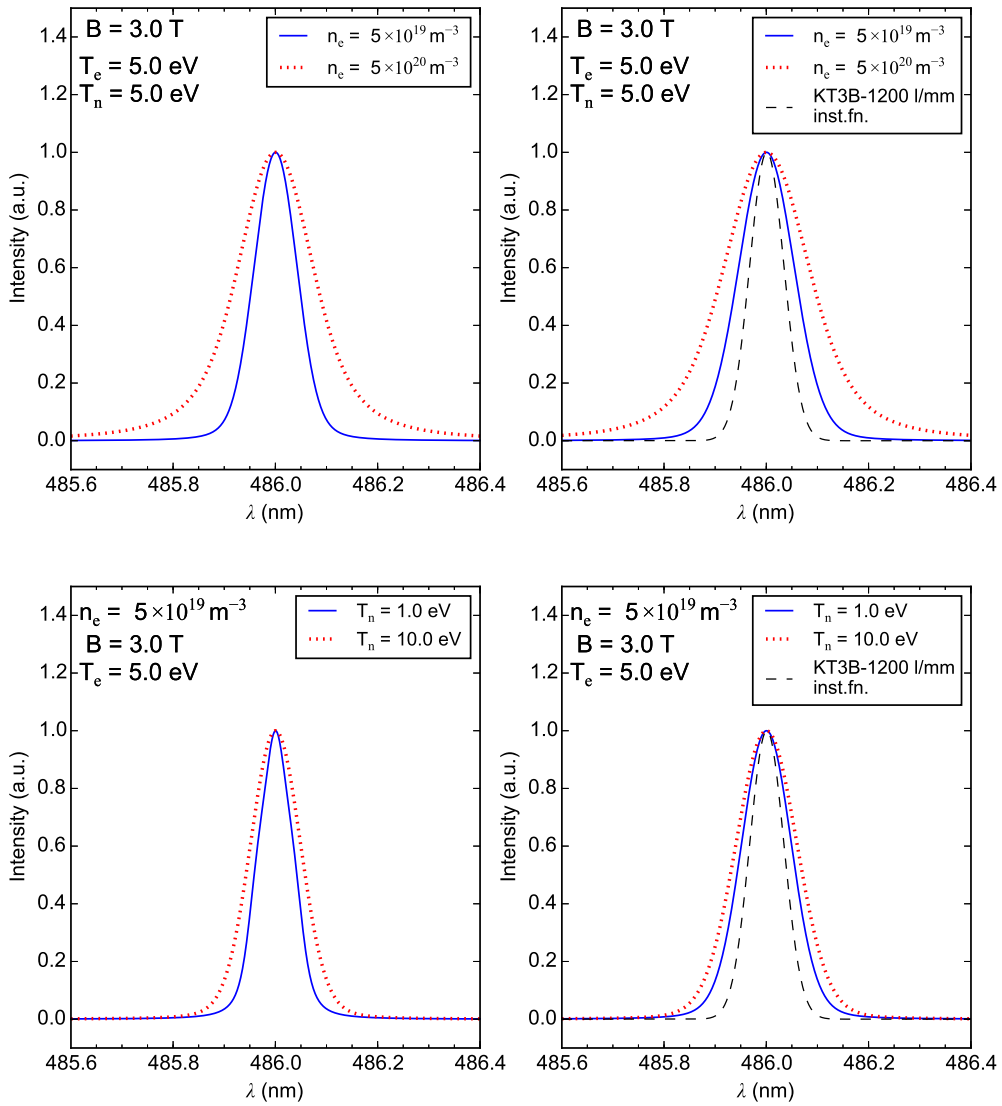

Figure 5.7: D 4→2 calculated line profile variation with density and neutral temperature. Plots on the right include the convolution of an instrument function with FWHM=0.08 nm.

JET spectroscopic analysis tools and provides an object oriented platform for parameterising line feature components such as Gaussian, Lorentzian, Voigt and customised functions, with provision for bounds and coupling. Moreover, Zeeman splitting is directly integrated into the fitting model via the `AFG`, which yields the Zeeman / Paschen-Back multiplet relative intensities and wavelength position using the `ADAS603` module. The modified Lorentzian broadening function (eqn. 5.4) was added to the `FFS` package to capture the parameterised MMM model.

In the analysis of the D 5→3 line, Doppler broadening has been neglected since

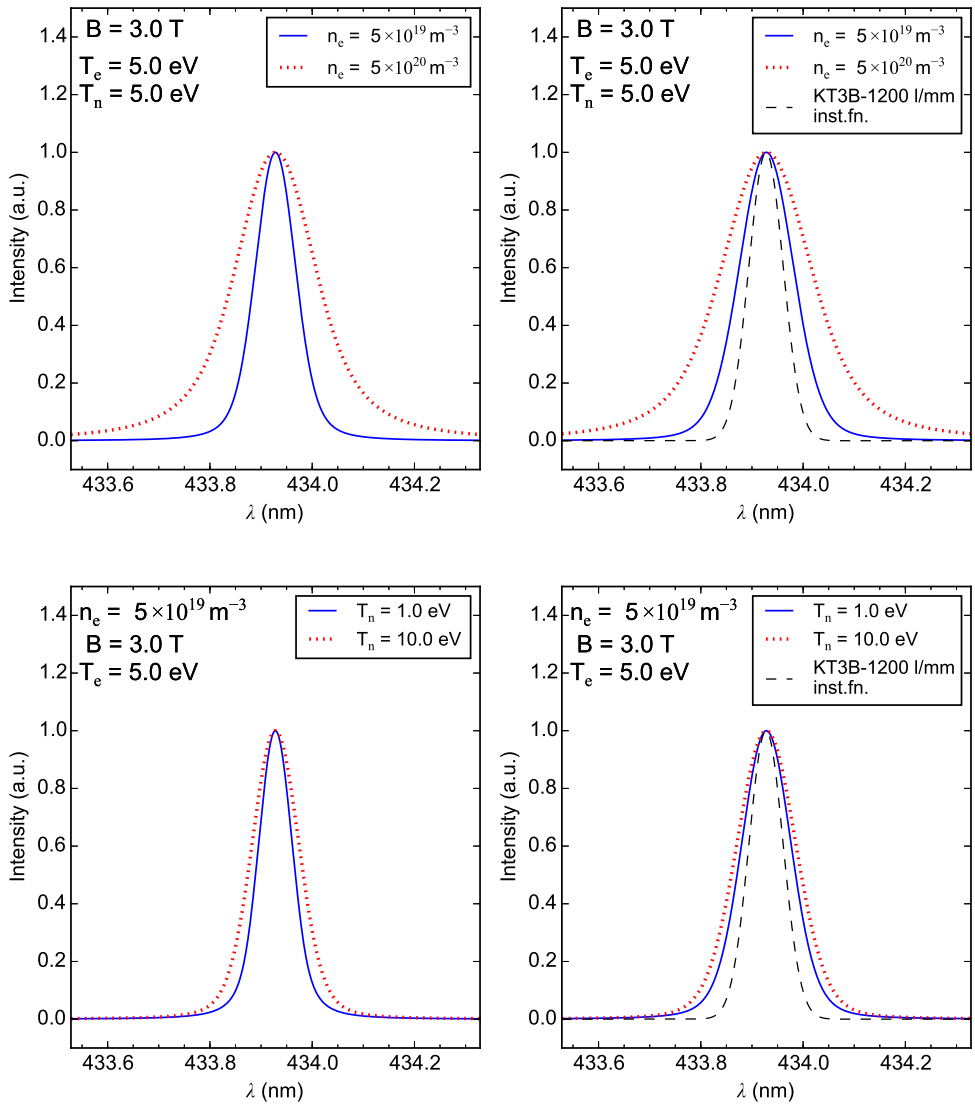

Figure 5.8: D 5→2 calculated line profile variation with density and neutral temperature. Plots on the right include the convolution of an instrument function with FWHM=0.08 nm.

the line width exhibits only weak sensitivity in the range $1 \leq T_n \leq 10$ eV relative to the KT3D-MR instrument FWHM and Stark broadening. The model is constrained with the total magnetic field magnitude, obtained using the `FLUSH` library for post-processing EFIT magnetic equilibrium reconstruction data (Pamela, 2013), at R and Z machine coordinates corresponding to each vertical spectral cord location in the divertor. Figure 5.10 shows an example of the total magnetic field magnitude contours and the magnetic equilibrium. The $1/R$ decay of the magnetic field magnitude from the inner to outer divertor vertical tiles is typically around 0.5 T. The

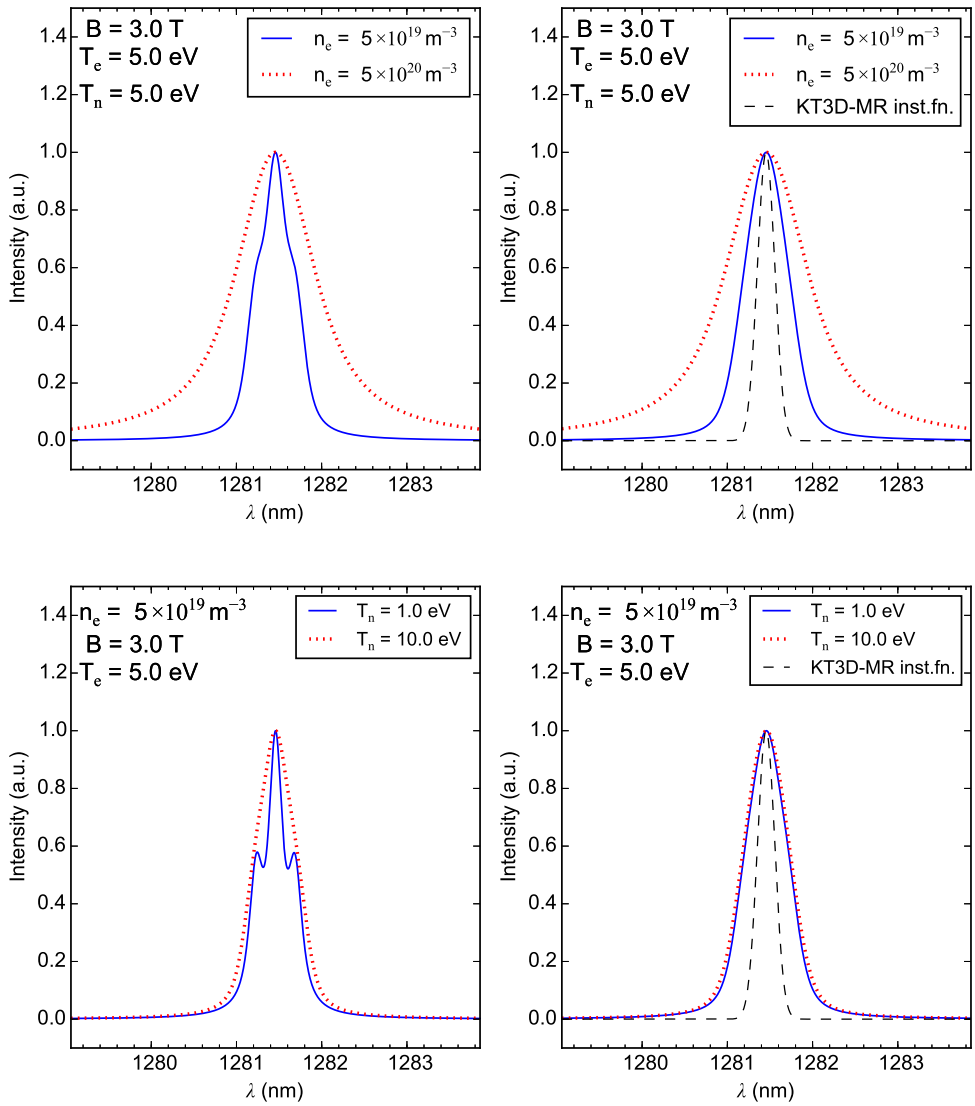

Figure 5.9: D 5→3 calculated line profile variation with density and neutral temperature. Plots on the right include the convolution of an instrument function with FWHM=0.24 nm.

uncertainty of inferred density values from the D 5→3 line is estimated to be $\lesssim 25\%$ due to insufficient knowledge of the σ/π polarisation component ratio, compounded with the loss in resolution of the central line shape features using the simplified line profile model.

To maintain consistency in the fitting technique, the same procedure was followed for the higher-n Balmer lines with principal quantum number $n \geq 5$. Zeeman splitting had no effect on the recovered density values for Balmer lines with n≥6 and typical magnetic field magnitude of B≈2.5 T. Given the sensivity of the D 5→2

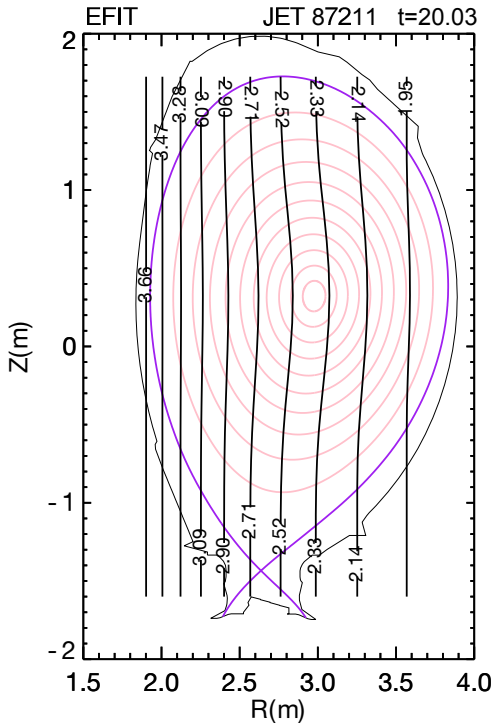

Figure 5.10: Example of EFIT outputs from the FLUSH library, including contours of the total magnetic field magnitude (vertical black lines) and magnetic equilibrium reconstruction (separatrix: purple, closed flux surface contours: red).

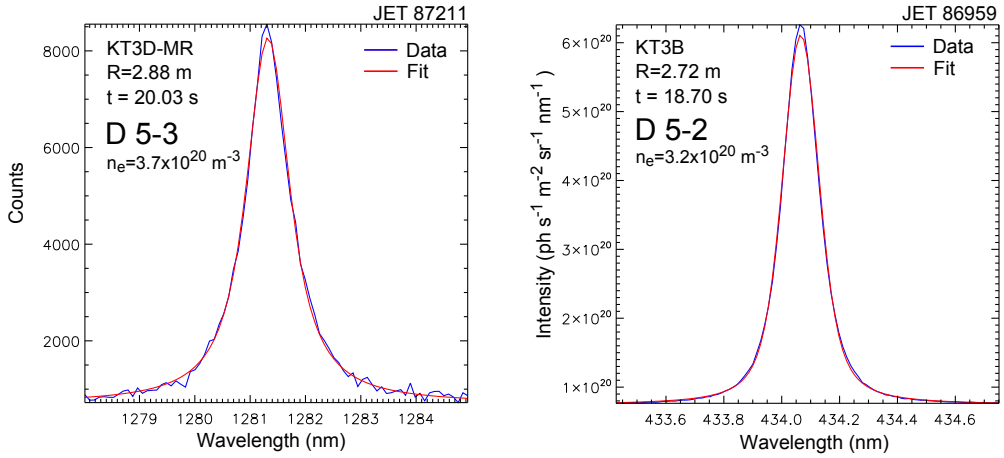

Figure 5.11: Example of fit results to the D 5→3 and D 5→2 line profiles using the FFS package.

line to Doppler broadening (see Figure 5.8), this line was only used in the analysis of high density, low temperature detached plasmas for which the Doppler contribution is small, although some broadening corresponding to a few eV from Frank-Condon dissociation energy of recycled D_2 molecules is likely present. Figure 5.11 shows an example of the least-squares fit results from the `FFS` package for the D 5→3 and D

5→2 lines. Example fits to the high-n Balmer lines near the discrete-to-continuum transition are shown in Figure 5.15.

Radial Profiles of Electron Temperature

As discussed in Section 2.3.1, at $T_e \lesssim 1.5$ eV the effective recombination rate for hydrogenic species begins to predominate over excitation and thus the excited state populations of high-n hydrogen series lines are largely driven by the three-body recombination process. The characteristic volume recombination spectroscopic signature has already been exploited in Section 3.2.3 for electron temperature estimates on MAST using the Saha-Boltzmann distribution (eqn. 2.15) for the higher excited levels which are assumed to be in LTE. Similarly, the ADAS PEC coefficients offer an alternative method of inferring the electron temperature by means of relating the line-integrated spectral line intensities to the dominant driving populations according to eqn. 2.22. In the general case in which both excitation and recombination $PECs$ are considered, the unknowns in eqn. 2.22 are T_e, n_e, n_i, and n_0. Assuming $n_e = n_i$, the inferred density values from the line profile measurements can be used as an additional constraint, thus leaving n_0 and T_e as the remaining unknowns. In JET-ILW, Penning gauges (KT5P/PEN1-PEN2) located in the sub-divertor below the plasma-facing tiles are used to monitor neutral pressure. However, information on the local neutral density in the divertor plasma volume is not available. Consequently, T_e estimates using atomic data rely on neglecting the excitation term in eqn. 2.22, which is only appropriate if recombination is the dominant populating mechanism. Hence T_e estimates using either the PEC approach restricted to the recombination contribution or the Saha-Boltzmann distribution are effectively equivalent. The most common approach for justifying this assumption is by monitoring the D 5→2/D 3→2 line ratio, the value of which rises sharply for $T_e \lesssim 1.5$ eV from about 0.02 to 0.1, depending on the plasma and neutral densities (see Figure 3.20).

An initial attempt at estimating the electron temperature using the high-n Balmer lines (including upper states n =9 through n =12 shown in Figure 5.15) in detached plasma conditions proved unsuccessful as the inferred temperatures using eqn. 2.15 to relate the populations to T_e yielded negative values. This is very likely attributed to the influence of the D-C merging at high densities as discussed in Section 2.3.1, which effectively leads to an overestimation of the line intensities close to the D-C transition. Estimates of radial T_e profiles were therefore obtained using

the D 9→2/5→2 line intensity ratio assuming the influence of excitation fluxes on $n \geq 5$ excited state populations to be negligible for typical plasma temperatures associated with detachment ($T_e \leq 1.5$ eV). This is a reasonable assumption for spectral measurements which exhibit strong volume recombination, as indicated by high-n Balmer line spectra extending up to n=14. Although more accuracy would certainly be gained by using multiple isolated lines away from the D-C transition (e.g., D 6→2, 7→2, 8→2), KT3 data for these lines was not available for the selected plasma discharges since KT3E, the new Balmer survey spectrometer, was not fully commissioned at the time.

Langmuir Probe Data Preparation

LP current-voltage (I-V) characteristics for the selected plasma pulses were interpreted using a 4-parameter model accounting for sheath expansion (see Gunn et al., 1995), or a 3-parameter model (e.g. Wesson, 2004)) in cases where the four parameter model yielded unphysical T_e vales (and the derived $n_e \propto T_e^{-1/2}$ vales) due to increased scatter in the data points. LP divertor data for the present analysis was obtained from the KY4D responsible officer at JET.

Neutral Velocity Distribution Function

The Kukushkin neutral VDF parametric model (see Section 5.1.1) was applied to the high-resolution outer divertor D 3→2 measurements obtained with the KSRD diagnostic. Previously this has been carried out in JET-ILW SOL measurements using the KSRD midplane views (chord 10 and 11) (Kukushkin et al., 2014b). The interpretation is more straightforward for the divertor chords compared to the midplane radial and tangential chords due to the absence of significant stray light. Since Stark broadening of the D 3→2 line profile becomes significant for $n_e > 10^{20}$ m^{-3}, the least-squares fit was constrained with the parameterised MMM Stark broadening model based on density values inferred from the D 9→2 line for the corresponding chord location and plasma discharge time-slice. Since the σ components are removed via polarisation filters on the KSRD divertor spectral chords, the fit was performed on the measured central π component. A fixed Gaussian component with $\Delta\lambda_{1/2}$=0.024 nm was also included to account for the instrumental width. The total spectral profile was then obtained by least-squares minimisation using the `FFS` fitting package.

5.2 Measurement Results and Discussion

5.2.1 Comparison to Langmuir Probe Measurements

The overestimation of T_e from LP measurements in high recycling and detached plasmas, and hence an underestimation of the derived n_e, is a well known observation (e.g. Horacek et al., 2003). A possible explanation of this effect is based on the influence of hot upstream electrons, which can penetrate into the divertor plasma, on the probe I-V characteristics (Stangeby, 1995). A meaningful comparison of spectroscopically derived density values to LP measurements should therefore be carried out under fully attached plasma conditions characterised by a lack of significant parallel temperature and density gradients along the SOL. Typical upstream edge-SOL conditions in this case are $T_e \gtrsim 100$ eV and $n_e \lesssim 10^{19}$ m^{-3} in JET-ILW (e.g. Duran et al., 2015), for which Stark broadening measurements in the divertor are prohibitive due to low SNR of the high-n lines and a significant Doppler contribution to the low-n line profiles. As such, a horizontal outer target configuration discharge was examined (JET 87223, $P_{\mathrm{NBI}} = 7$ MW, $P_{\mathrm{ICRH}} = 2.6$ MW and $I_{\mathrm{p}} = 1.9$ MA) with midplane separatrix density and electron temperature values of $n_e \approx 1-2\times10^{19}$ m^{-3} and $T_e \approx$100-200 eV obtained from the core LIDAR Thomson scattering system (Maslov et al., 2013). Divertor conditions in the time window of interest from $t = 10-11$ s determined from LPs near the outer strike point were $n_e \approx 0.3-1.4\times10^{20}$ m^{-3} and $T_e \approx$10 eV. Although at such SOL density and temperature gradients the divertor plasma is likely in the high recycling regime in which n_e underestimation from LPs is possible, the high recycling rate on the horizontal tungsten tile 5 provided sufficient SNR to measure the D 5→3, 6→2 and 7→2 lines which exhibited Stark broadening.

Figure 5.12.(a) shows the time evolution of outer divertor radial profiles of the D 7→2 line intensity and the ion saturation current, j_{sat}, from tile 5 LPs. The OSP position was swept along tile 5 at 4 Hz during this phase of the discharge. There is evidence of volume recombination at the outer divertor following a sawtooth crash at t =10.14 s, as indicated by the sudden rise in the D 7→2 intensity as well as a rise in higher-n Paschen line intensities observed on KT3D (not shown). This corresponds to a sudden drop in j_{sat} followed by its recovery and a corresponding collapse in the recombining plasma. Figure 5.12.(b) compares the spectroscopically derived density profiles from D 7→2 Stark broadening and LP derived local density values. During the recombination phase (t =10.38 s) the LP density values are significantly lower than the spectroscopically derived values. In the recovery phase (t =10.66 s) where

j_{sat} is high, there is better agreement particularly around the OSP. Inward of the OSP, the LP derived density decays to very low values and high fit uncertainties (not shown for clarity) indicative of insufficient particle fluxes in the private plasma region.

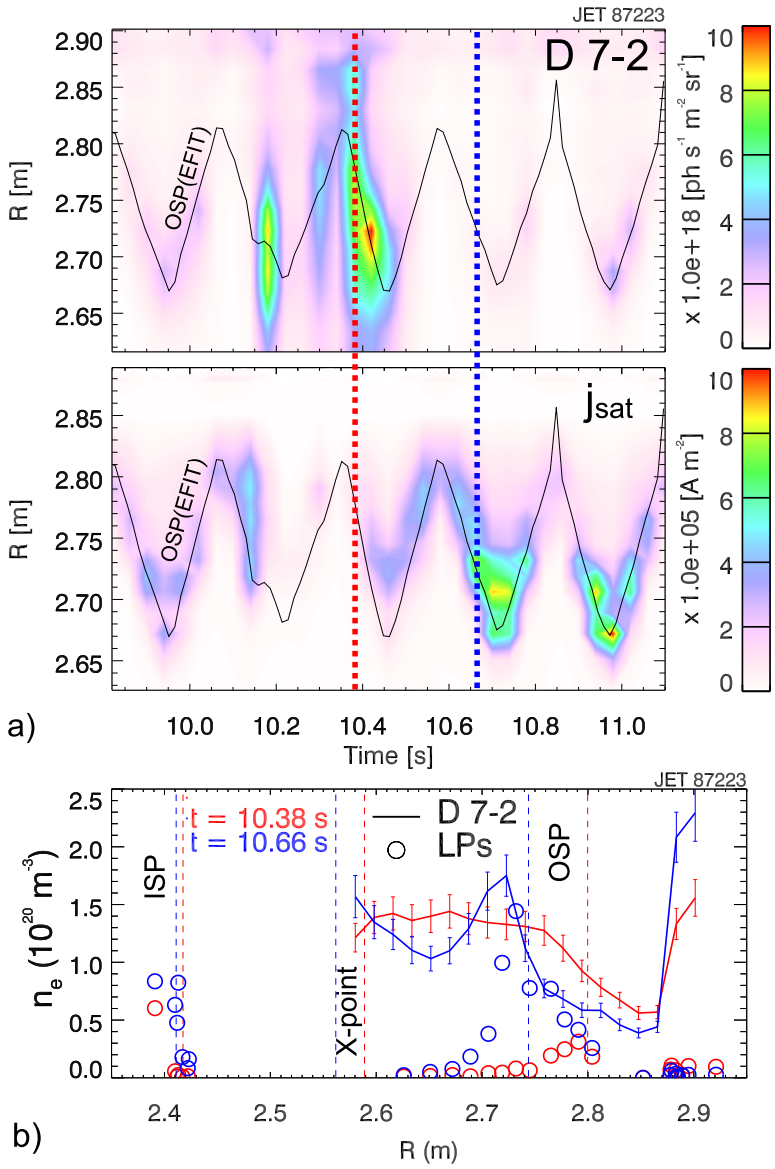

Figure 5.12: a) Time evolution of outer divertor radial D 7→2 intensity and j_{sat} profiles; b) radial density profiles from Stark broadening of D 7→2 line and LPs for JET pulse 87223.

The sudden rise in the spectroscopically derived density profile at R>2.88 m is consistent with reflections on the tungsten coated tile 8, the curvature of which facilitates specular reflections from the inner divertor and/or the X-point emission and possibly from tile 5, depending on the plasma configuration. A detailed reflection

analysis of the JET-ILW divertor is needed to predict the source of the reflected light (e.g. following initial work by Zastrow et al., 2008). This feature is observed in most discharges and, compounded with the obstructed view of tile 7 by the KT3 system, makes density measurements at the OSP of vertical configuration discharges unreliable.

In an earlier ohmic phase of the discharge, the fixed horizontal OSP position facilitated the comparison of spectroscopically derived density profiles from three different spectral line measurements: D 5→3 (time resolution of 150 ms), D 7→2 (time resolution of 40 ms) and D 6→2 (time resolution of 100 ms). Figure 5.13 shows the density profiles for which the three separate spectroscopic measurements and LPs were interpolated along the time axis to account for the different exposure times. Good agreement is observed between the D 5→3 and D 7→2 profiles except for near R =2.85 m where the D 5→3 density profile is markedly lower. This is likely due to increasing uncertainty in the line shape fitting procedure at low densities. Good agreement is also evident in the overlap region near the X-point between the outer and inner density profiles, whereas LP measurements at both the inner and outer divertor underestimate the local density by a factor of 2-3 at the OSP and more so at the ISP.

General consistency in the spectroscopically derived density profiles, in combination with the good agreement with LP results at t=10.66 (Figure 5.12.(b)) where j_{sat} is relatively high, reinforce the suitability of the parameterised Stark broadening model extending to lower-n lines.

5.2.2 Detachment Experiments

Divertor detachment experiments are typically conducted by steadily increasing the plasma density, at constant input heating power, by introducing additional deuterium fuelling (and possibly impurity seeding) to the edge and divertor. In L-mode experiments the discharge is usually terminated by a density limit disruption, the precursor of which is the MARFE cooling instability (Lipschultz et al., 1984) in the plasma edge. In H-mode detachment experiments, with higher input heating power, the high to low (H-L) confinement transition constitutes an effective undisruptive density limit, causing the collapse of the edge pedestal transport barrier and a back-transition to the low confinement mode.

The recent installation of the all-metal ITER-like wall (Matthews et al., 2011) on JET has allowed for direct comparisons of the influence of wall material on

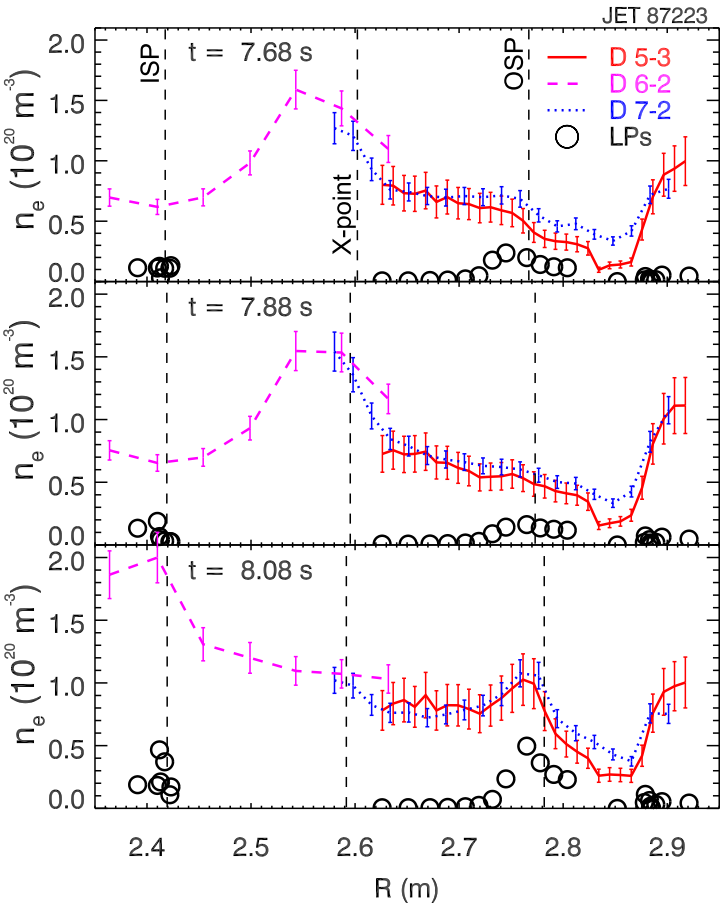

Figure 5.13: Radial density profiles from Stark broadening of D 5→3, 6→2 and 7→2 lines and localised density measurements from LPs for JET pulse 87223.

detachment behaviour. Main observations of the impact on detachment of the Be-W wall (JET-ILW) vs. the previous carbon wall (JET-C) are (Huber et al., 2013; Brezinsek, 2015): (1) a higher density limit in JET-ILW than in JET-C; (2) the radiation fraction is higher in JET-C due to the presence of carbon (an efficient radiator in the edge and SOL) leading to a reduction of power flow to the SOL and thus earlier detachment than in the JET-ILW; (3) due to a tenfold carbon concentration decrease in the JET-ILW, reaching the density limit requires larger deuterium puffing rates; and (4) in contrast to the C wall, JET-ILW L-mode density limit discharges demonstrate a stable fully detached outer divertor phase and a much longer lifetime of the X-point MARFE formation. The extended MARFE lifetime and increased detachment stability in JET-ILW presents an opportunity for feedback control to stabilise the detached operating regime by means of gas puffing (actuator) and appropriate diagnostic signal (e.g. using the edge density as feedback signal, Brezinsek et al. (cf. 2009)). In this regard, Balmer-Paschen series divertor

spectroscopy in the detached plasma regime is well suited for estimating divertor T_e, n_e, for monitoring volume recombination and the incursion of the high density low temperature recombining plasma region into the X-point region during MARFE formation.

L-mode density limit discharge

An L-mode density limit discharge has been examined (pulse 86959, Figure 5.14; B_{T}=2.5 T, I_{p}=2.5 MA, P_{NBI}=1.2 MW, P_{OHM}=2.3 MW, low-triangularity magnetic equilibrium and outer vertical target configuration) from a series of experiments aimed at investigating the impact of the outer strike point configuration (horizontal vs. vertical target) on divertor plasma conditions (Groth et al., 2015). Measurements of the the $n \geq 5$ Balmer lines were utilised for inferring plasma density and electron temperature. The density is ramped by puffing D_2 gas into the outer and inner divertor at constant input power starting at t =8.5 s up to a steady state value of 2×10^{23} e^- s^{-1} at t =10.5 s. The total ion flux to the outer target rises rapidly as the D_2 puffing rate increases, until at t =9.3 s the characteristic roll-over is observed. At the inner target, the roll-over occurs slightly earlier at t =9.0 s, shortly after the start of D_2 puffing. A sharp increase in the total radiated power P_{RAD}, as well as total D 3→2 intensity in the inner and outer divertor, is also observed after the start of puffing. The line-averaged mid-plane density rises steadily from 2.8×10^{19} m^{-3} to 8.9×10^{19} m^{-3} right before the density limit disruption terminates the pulse at t =20 s. The onset of the density limit disruption is consistent with Greenwald density limit (GDL) scaling, a well known operational limit where the Greenwald density $n_{\mathrm{GW}} \propto I_{\mathrm{P}}/a^2$, and a is the plasma minor radius (Greenwald, 2002). The neutral pressure, measured in the sub-divertor (not-shown), also follows the same trend, rising sharply followed by a more gradual increase towards the density-limit disruption.

The signature volume recombination Balmer and Paschen high-n spectrum, shown to be closely correlated on JET with the onset of detachment (McCracken et al., 1998), is observed to occur shortly after the onset of D_2 fueling consistent with the rise of the D 3→2 intensity in the divertor. Figure 5.15 shows the time evolution of the high-n Balmer spectra from the KT3A cord viewing the outer divertor leg at $R = 2.72$ m. Two frames are highlighted: the first coinciding with the start of fueling at $t = 8.54$ s, and the second at $t = 14.06$ s. In comparing the two spectra, the main observations are the significant rise in the intensity of the Balmer lines as well the

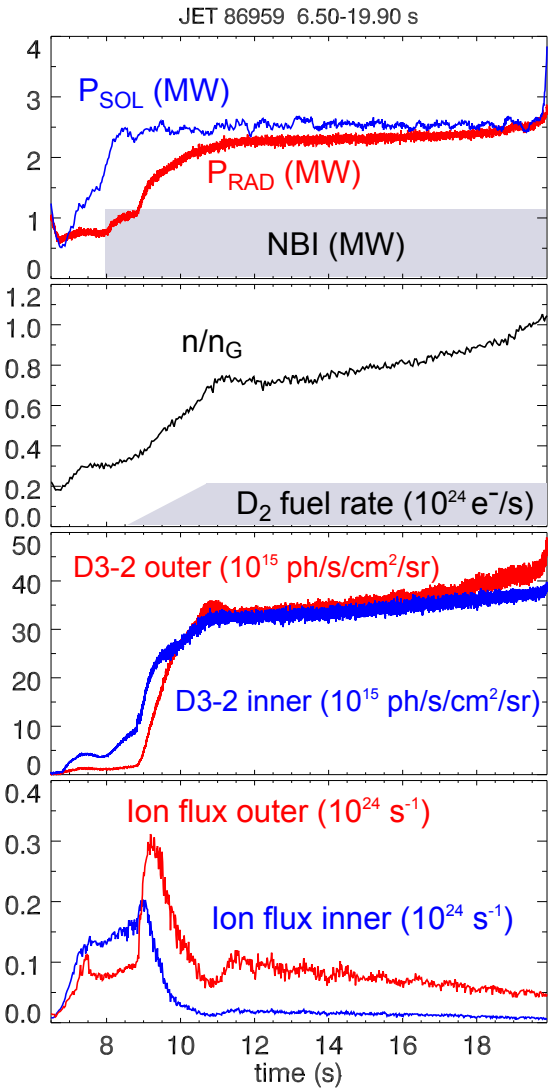

Figure 5.14: Time evolution of selected signals from JET pulse 86959: estimated power entering the SOL, P_{SOL}; estimated total radiated power from bolometry, P_{RAD}; neutral beam (NBI) heating; the Greenwald density fraction, n/n_G; D_2 fuelling rate; total inner and outer D $3 \rightarrow 2$ intensity; and total ion flux on the inner and outer divertor targets.

broadening of their profiles indicative of an increase in plasma density. The overlap in the line wings of the D 11→2, D 12→2 and D 13→2 lines, compounded with the D-C transition merging (see Figure 2.11), leads to increasing uncertainty in determining the total intensity of these lines. In the example shown, the selection of the functional form describing the continuum background is non-trivial, and although a good fit was obtained to the spectra using a constant offset background model, the $n \geq 10$ lines were subsequently excluded from evaluating electron temperature radial profiles.

To elucidate the spatial distribution of the deuterium radiation pattern in the

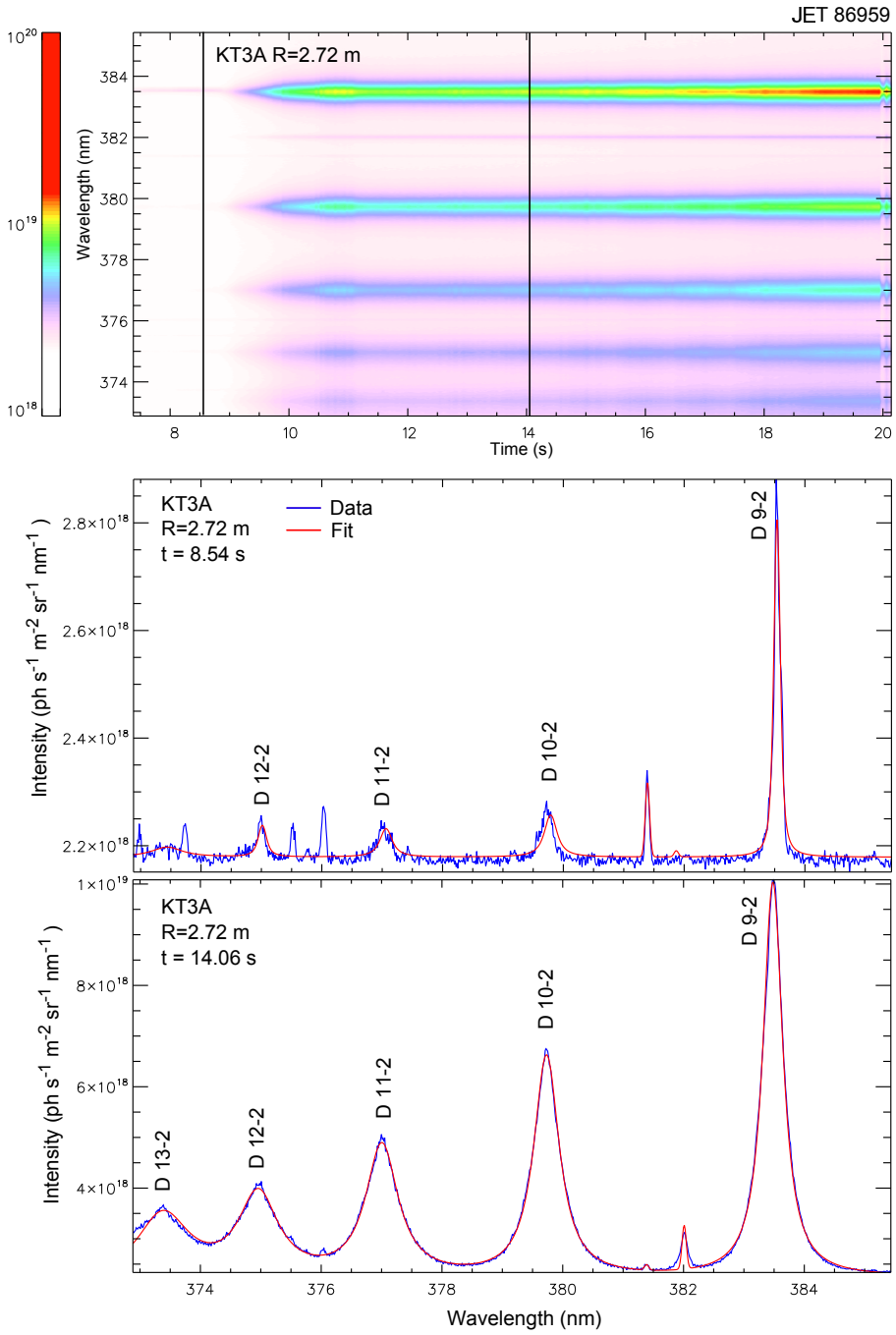

Figure 5.15: High-n Balmer spectra from KT3A measurements for pulse JET 86959, and the corresponding FFS fits.

divertor for pulse 86959 and thus provide context for the location of strong radiating regions along the line-integrated spectral cords, Figure 5.16 shows 2D poloidal tomographic reconstructions of the D 5→2 emissivity and the D 5→2/3→2 line ratio from a similar L-mode density ramp discharge, pulse 81548. These results were reported by Huber et al. (2013) in an investigation on the influence of the main

wall and divertor surface material upgrade to Be and W, respectively, in comparison to the previous all-carbon machine. Regions of high D 5→2 emissivity and D 5→2/3→2 line ratio values are associated with strong volume recombination. In the early phase of the discharge high D 5→2 emissivity is is observed near the strike points, with the inner divertor radiating more strongly. As the plasma density is increased further, the outer leg radiation increases rapidly. The strong radiating region then moves towards the X-point and eventually into the plasma core consistent with MARFE formation. Values of the D 5→2/3→2 line ratio $\gtrsim 0.1$ indicate low electron temperatures of around 1 eV (see Figure 3.20). This basic phenomenology has been observed in detachment experiments on other machines (e.g. Goetz et al., 1996; Potzel et al., 2015). For the present analysis of pule 86959, Figure 5.17 shows the time evolution of the line-integrated D 5→2 radial intensity profiles from KT3A, with select time slices before the onset of fueling and in the later part of the discharge. The basic features of increasing emission along the outer leg and incursion of the strong radiating region towards the X-point are qualitatively consistent with the poloidal reconstructions from pulse 81548.

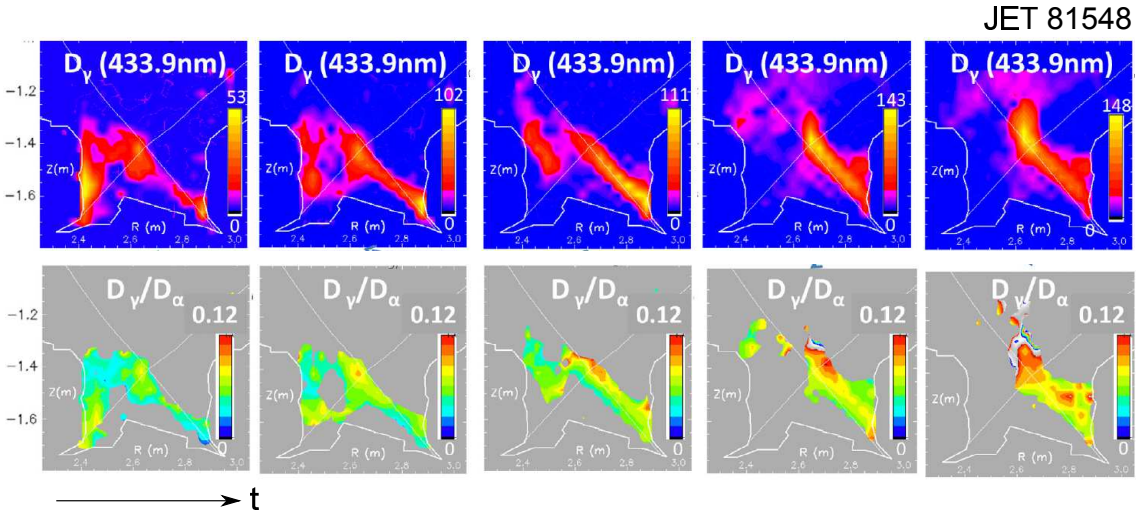

Figure 5.16: Poloidal D 5→2 emissivity and D 5→2/3→2 line ratio reconstructions from the KL11 filtered imaging diagnostic for JET pulse 81548 (Huber et al., 2013).

The presence of volume recombination as well as the roll-over in ion saturation current is evidence of partial or full detachment. Full detachment is characterised by the plasma detaching from the physical target across the entire width of the SOL, thereby forming a virtual target ion sink in the plasma volume upstream. In partially detached plasma the ion flux reduction occurs first at the strike point and, with increasing density, gradually propagates outward along the SOL width

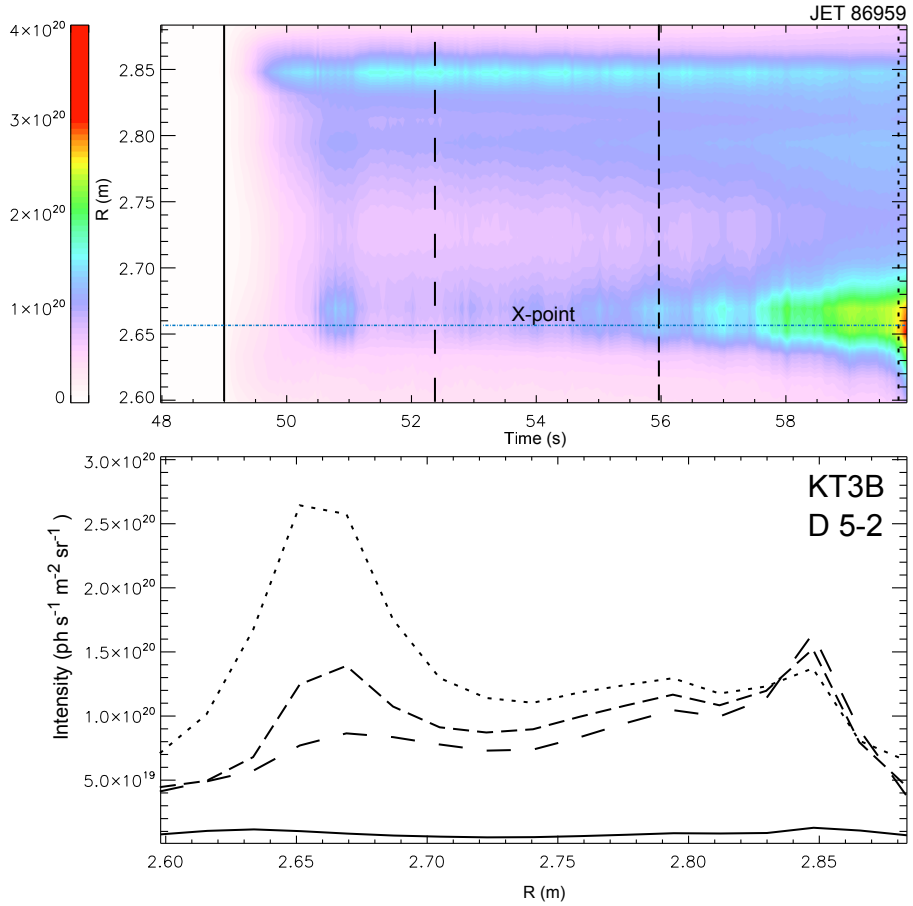

Figure 5.17: Time evolution of the D 5→2 radial intensity profile.

until transitioning to the fully detached regime. A convenient quantitative scaling of the 'degree of detachment' (DoD), first introduced by Loarte et al. (1998), uses the simple two point model of the edge and divertor (Stangeby, 2000a) to calculate the reference ion flux, which can then be compared to measurements to assess the degree of detachment achieved in the experiment. Within the two point model approximations, the divertor ion flux is given by

$$I_d \propto \frac{n_s^2}{T_s^{3/2}}, \tag{5.8}$$

where n_s and $T_s \propto P_{SOL}^{2/7}$ are the separatrix density and temperature values upstream, respectively. Selecting an early phase of the density ramp at constant input power, for which the divertor plasma is in the attached or high recycling regime, and assuming that the line-averaged midplane density $\langle \bar{n}_e \rangle$ is proportional to the density at the separatrix, the two point model scaling gives

$$I_d^{scal} = C\langle \bar{n}_e \rangle^2, \tag{5.9}$$

where I_d^{scal} is the extrapolated ion flux and C is the proportionality constant which is obtained from measured values of I_d. The DoD is then given by

$$DoD = \frac{I_d^{scal}}{I_d^{meas}} \tag{5.10}$$

where I_d^{meas} is the measured ion flux in the high density phase of the discharge. Given sufficient spatial distribution of LPs along the target plate, the DoD can be determined locally at the separatrix as well as for the total, or integral, ion flux (DoD^{int}). A convenient criteria for classifying the detachment state based on integral values of DoD has been proposed by Loarte et al. (1998) as: partial detachment for $DoD^{int} < 10$ and full detachment for $DoD^{int} > 10$. The high-recycling, constant input power window in pulse 86959 prior to detachment is small due to the large D_2 puffing rate commencing shortly after NBI heating begins at t=8 s. Therefore the C coefficients for the inner and outer divertor are determined during the time $t = 8.2 - 8.8$ s, where the ion flux ramp is steady and P_{SOL} is relatively constant.

Figure 5.18 shows spectroscopically derived plasma radial density and electron temperature profiles and local LP derived values for pulse 86959. The neutral temperature contribution to the D 5→2 line profile was ignored which could account for the modest discrepancy observed between the D 9→2 and 5→2 density profiles. The overlap region between the inner and outer profiles is again in good agreement. The radial profile values right near the OSP at $R > 2.85$ m are considered unreliable due to shadowing and reflections on tile 8 (see Figure 5.4).

At t =8.9 s, corresponding to the start of the fuelling ramp and before the ion flux roll-over, there is a gradual density increase from the X-point towards the ISP and OSP, indicating high recycling conditions consistent with DoD_{inner} and $DoD_{outer} \leq 1$. LP density values in this regime are in relatively good agreement with the spectroscopically derived density values near the strike points. LP T_e values are between 10-15 eV. The spectroscopically derived T_e profile is not available since application of the Saha-Boltzmann distribution to the D 9→2/5→2 ratio is not valid in this temperature range due to the influence of excitation fluxes on the upper state populations.

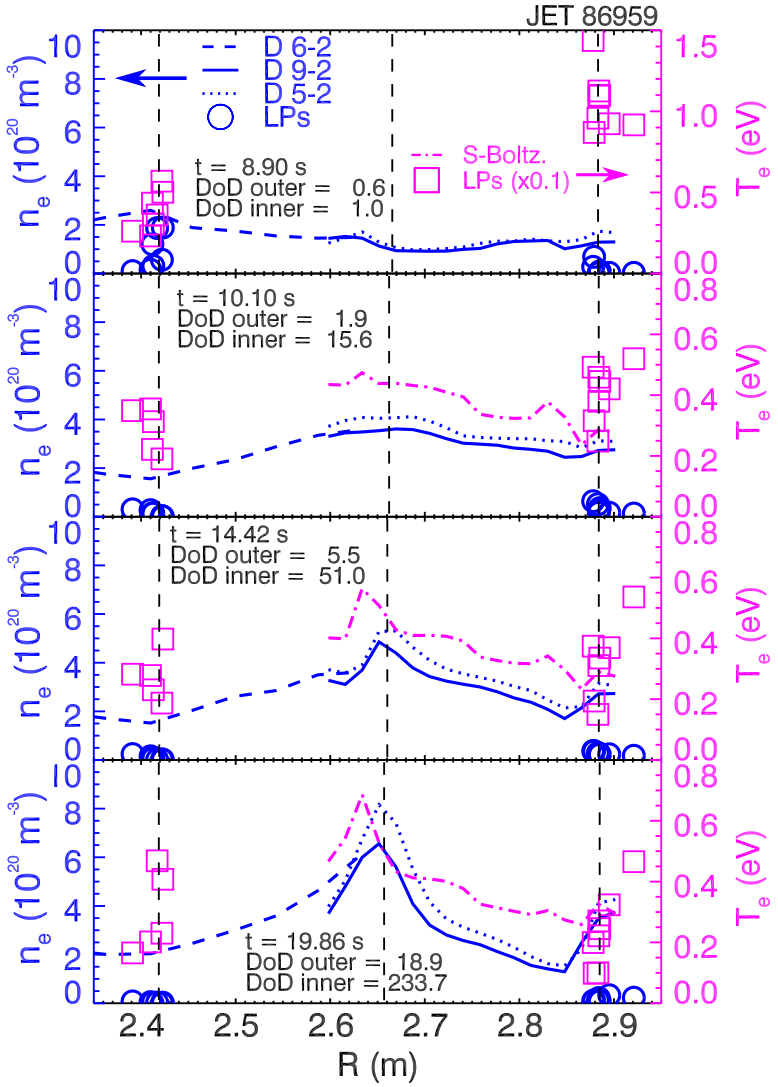

Figure 5.18: Radial density profiles from Stark broadening of D 5→2, 6→2, 9→2 lines and LPs, and electron temperature profile from D 9→2/5→2 line ratio for JET pulse 86959. Electron temperature LP values scaled by 10^{-1} for clarity.

At t =10.10 s (Figure 5.18) after the ion flux roll-over, $DoD_{inner} > 10$ indicating full detachment, while the outer divertor is partially detached ($DoD_{outer} = 1.9$). The density decreases gradually away from the X-point towards the ISP and OSP and the LP density measurements at the strike points are significantly underestimated. Spectroscopic T_e estimates are between 04-0.6 eV, much lower than LP values at the OSP, indicating significant overestimation of LP T_e results. It is important to reiterate the assumption of LTE conditions for the $n = 5$ excited level in obtaining such low values for the spectroscopically derived T_e estimates. In future work it is thus recommended to obtain intensity measurements of the D 6→2, D 7→2 and D 8→2 lines which exhibit reduced sensitivity to excitation fluxes for $T_e \lesssim 2.0$ eV

relative to the D 5→2 line and are sufficiently far away from the D-C transition for continuum merging to be significant. This is illustrated in Figure 5.19, which shows the recombination and excitation contributions and the total excited state population densities derived using ADAS $PECs$ for $T_e = 2.0$, $T_e = 1.5$ and $T_e = 1.0$ eV assuming a neutral fraction of 0.5. The selected density, $n_e = 2 \times 10^{20}$ m^{-3}, is consistent with conditions in the outer divertor.

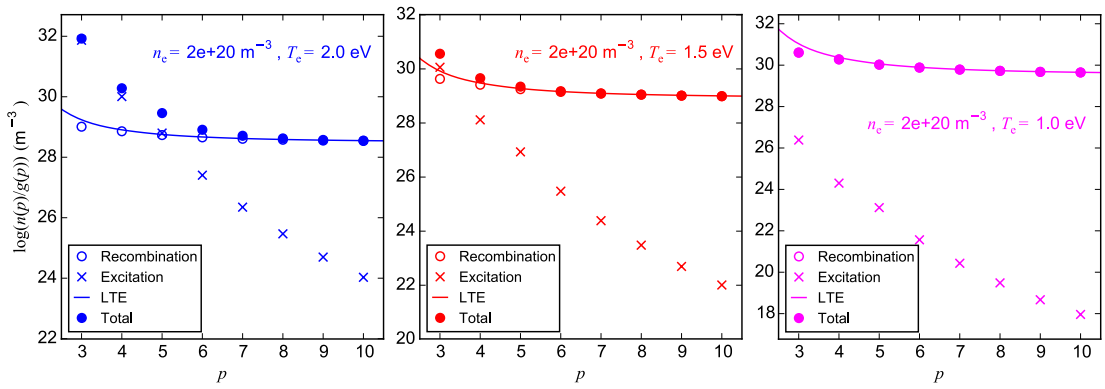

Figure 5.19: Excitation, recombination contributions and the total excited state populations for Hydrogen using ADAS $PECs$ assuming a neutral fraction of 0.5. Calculation of LTE populations as a function of excited level p using eqn. 2.15.

At t =14.42 s (Figure 5.18) the density near the X-point rises and the profile begins to exhibit a well defined peak, while the density continues to decrease towards the OSP. This is consistent with the incursion of the dense plasma away from the strike point and towards the X-point. A peak in the temperature profile is also evident.

At t =19.86 s (Figure 5.18), shortly before the density limit disruption, both the outer and inner divertor are completely detached and the density peak increases further, consistent with the radiation pattern during MARFE formation in Figure 5.16. Density along the outer leg continues to fall.

Changes in the T_e profile are less pronounced compared to relatively strong shaping of the density profile. This feature offers a good measure of density gradients associated with the MARFE formation near the X-point. By replacing the least-squares fitting technique with computationally efficient look-up tables based on a 2-point FWHM estimate of the Stark broadened line (using Table 5.1), estimates of n_e profiles for feedback control should be feasible within the KT3 real-time interface. Currently this interface can be used for real-time monitoring of total line intensities (e.g., seeded impurity lines) for a particular set of viewing chords, depending on the aims of the control scenario.

5.3 Multi-parametric Fitting of Low-n Line Profiles

Whereas the $n \geq 5$ Balmer lines are used routinely for n_e, T_e determination and as indicator of the extent of volume recombination in detached plasmas, the low-n Balmer and Paschen lines offer additional diagnostic capabilities. Given sufficient instrument resolutions, their spectral profiles contain information on the B-field magnitude, hydrogen isotope ratio, the neutral VDF as well as plasma density. In this section the scope for parameter recovery from the low-n Balmer and Paschen lines is examined using a survey of synthetic diagnostic data generated with the parameterised line profile model. A localised divertor emission source is assumed, consistent with JET-ILW vertical view observations.

5.3.1 Simulation Setup

Synthetic diagnostic data was generated for the D 3→2, 4→2, 5→2, 4→3, 5→3 lines using instrument characteristics which correspond to a high resolution spectroscopy configuration with a linear dispersion of 0.0075 nm/pixel and an instrumental function FWHM=0.02 nm. Zeeman component filtering is not applied to the synthetic data in order to asses the entire line profile including the magnetic field effects. Since no capabilities exist for measuring the D 4→3 line profile on JET-ILW at present, one of the aims of the analysis is to evaluate its properties.

Photon shot noise and camera electronic noise, σ_e, are added to the synthetic data such that the SNR=$I_{max}/\sqrt{(I_{max}+\sigma_e^2)}$ corresponds to good photon statistics with a chosen value of 150. The synthetic data is generated by randomly sampling the line profile at each pixel position according to a normal distribution with the standard deviation corresponding to the total noise term. The input parameters that define the line profile are recovered via a non-linear least squares fitting routine which minimises χ^2 using the Levenberg-Marquardt algorithm (Press et al., 1986), weighted by the variances of the pixel intensity values.

The spectroscopic and LP measurement results in the previous section are used as a guide for establishing an appropriate range of values for n_e. Since the Stark broadening contribution is only weakly dependent on T_e, and, treating electron and ion temperatures as equal in the model, a value of T_e=1 eV was used for high density detached plasmas cases and T_e=5 eV for high-recycling and attached plasma cases.

To elucidate the appropriate selection of Maxwellian and non-Maxwellian neu-

tral temperatures and their relative contributions to the total VDF, D 3→2 divertor spectra from KSRB were examined for JET discharges 87223 (high recycling) and 86959 (detached). Since absolutely calibrated measurements of the D 3→2 spectra were not available, the total camera noise σ_c was estimated by calculating the standard deviation of the raw DN counts away from the spectral line, thus isolating the combined read noise and dark current shot noise contributions. The signal shot noise σ_{sn} was estimated by converting the DN counts to electrons using the camera gain setting $G[\mathrm{e}^-/\mathrm{ADU}]$ such that the total estimated variance on each on-chip binned pixel is

$$\sigma_t^2 = \sigma_c^2 + \sigma_{sn}^2 = \sigma_c^2 + DN \times G \ . \tag{5.11}$$

The neutral VDF model was defined with the following contributions: (i) a single non-Maxwellian component with statistical weight S_{NM}, temperature T_{NM} and the damping parameter Λ; (ii) two Maxwellian components parameterised together with the statistical weights S_{M1}, S_{M2} and corresponding temperatures T_{M1} and T_{M2}.

Figure 5.20 shows an example of the weighted fit for pulse 86959 at t =9.65 s and R =2.52 m with parameter estimates and standard errors. The majority of residuals are within $\pm 2\sigma$ except for a statistically significant peak in the red wing which is not accounted for by the model. Similar fit quality was obtained for pulse 87223 (not shown), t =8.45s, R =2.74 m, but with a negligible non-Maxwellian contribution, and higher Maxwellian temperatures ($T_{M1} = 18$ eV, $T_{M2} = 2.5$ eV and $S_{M2} = 0.5$). These results suggest that the model is a reasonably good representation of the LOS integrated neutral VDF in the JET-ILW divertor for the selected pulses. Selection of the neutral VDF parameters in the multi-parameteric fitting analysis was therefore based on these measurements. Table 5.2 summarises the input parameters that describe the total line profile and their range of values considered for the analysis.

5.3.2 Simulation Results and Discussion

In the first iteration, multi-parametric fits were carried out for each line by varying the input parameters n_e, B and $T/(T+D)$ (tritium fraction) in the range according to Table 5.2 and using a simplified neutral VDF described by a single Gaussian with a temperature range $1 \leq T_n \leq 10$ eV. The fit precision and accuracy results for each line are presented in Figure 5.21, where each marker corresponds to a simulation case and its position to the relative difference between the model input value and the free

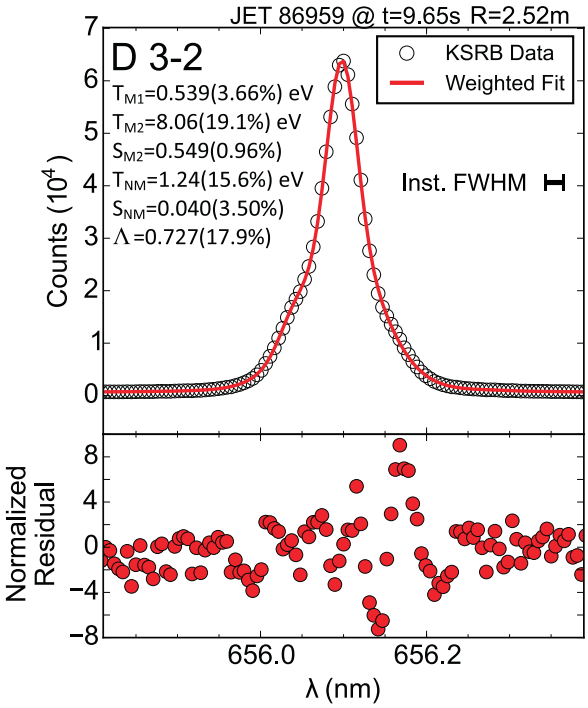

Figure 5.20: Example of neutral VDF parametric fit to divertor the D 3→2 measured line profile from KSRB.

parameter estimate and associated standard error. The best results were obtained for the D 4→3 line with parameter estimates for all cases recovered within 10% of their input values. The D 3→2 results show poor sensitivity to Stark broadening, especially for cases with $n_e < 10^{20}$ m^{-3}. Conversely, the D 4→2, 5→2 and 5→3 line results show decreased sensitivity to T_n and increased sensitivity to n_e. Parameter recovery from D 3→2 and 4→3 is generally more sensitive to B and $T/(T+D)$.

Overall, the synthetic diagnostic fitting results indicate that in the absence of additional information to constrain the fit, the D 4→3 line offers increased scope for recovery of plasma parameters from spectroscopic observations. This is consistent with the wavelength scaling of the broadening and splitting mechanisms (eqn. 5.5, eqn. 5.6 and eqn. 5.7). For example, relative to the D 3→2 line at 656 nm, Doppler broadening for the D 4→3 line (1874.6 nm) is ×2.9 wider for the same neutral temperature, as is the D-T separation. The quadratic wavelength dependence on the Zeeman splitting leads to a $\pi-\sigma$ separation that is ×8.4 greater, whereas the pure Stark broadening FWHM is wider by a factor of ≈13.5. The initial results therefore suggest that measurements of the D 4→3 profile can benefit from reduced demands on spectral resolution and/or enhanced profile feature resolution. However, the shift in emphasis in wavelength space towards the Stark broadening contribution may also

Table 5.2: Input parameters and range of values for multi-parametric fitting of synthetic diagnostic spectral line profiles.

Fit parameter	Range	Units
n_e	5.0 - 50.0	$10^{19}\mathrm{m}^{-3}$
T_{M1}	0.5 - 5.0	eV
T_{M2}	5.0 - 20.0	eV
T_{NM}	1.5 - 5.0	eV
S_{M2}	0.4 - 0.6	-
S_{NM}	0.00 - 0.05	-
Λ	0.656 (fixed)	nm
B	2.5 - 4.5	Tesla
$T/(T+D)$	0.2 - 0.5	-

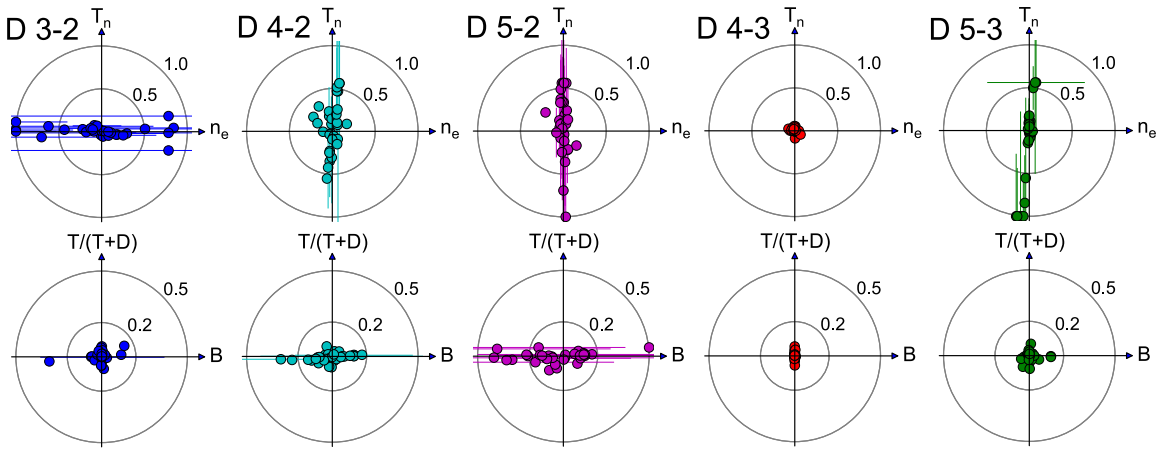

Figure 5.21: Simulation results for 4-parameter fits for the D 3→2, 4→2, 5→2, 4→3, and 5→3 lines. Each marker corresponds to a simulation case and its position to the relative difference between the fit estimate and input value. Fit error bars <25% are not shown for clarity.

reduce the scope for recovery of more complex neutral VDFs at high densities.

To further examine the diagnostic capabilities of the D 3→2 and 4→3 lines, the more representative neutral VDF was considered according to Table 5.2. The second iteration of the multi-parametric fitting analysis thus included 9 free parameters: B, $T/(T+D)$, n_e, S_{M2}, T_{M1}, T_{M2}, S_{NM}, T_{NM}, Λ, where the first Maxwellian statistical weight is then derived from $S_{M1} = 1 - S_{M2} - S_{NM}$. Figure 5.22 shows an example of the synthetic diagnostic data and the line of best fit for the D 3→2 and 4→3 lines.

Plasma parameter sets corresponding to attached, high-recycling and detached

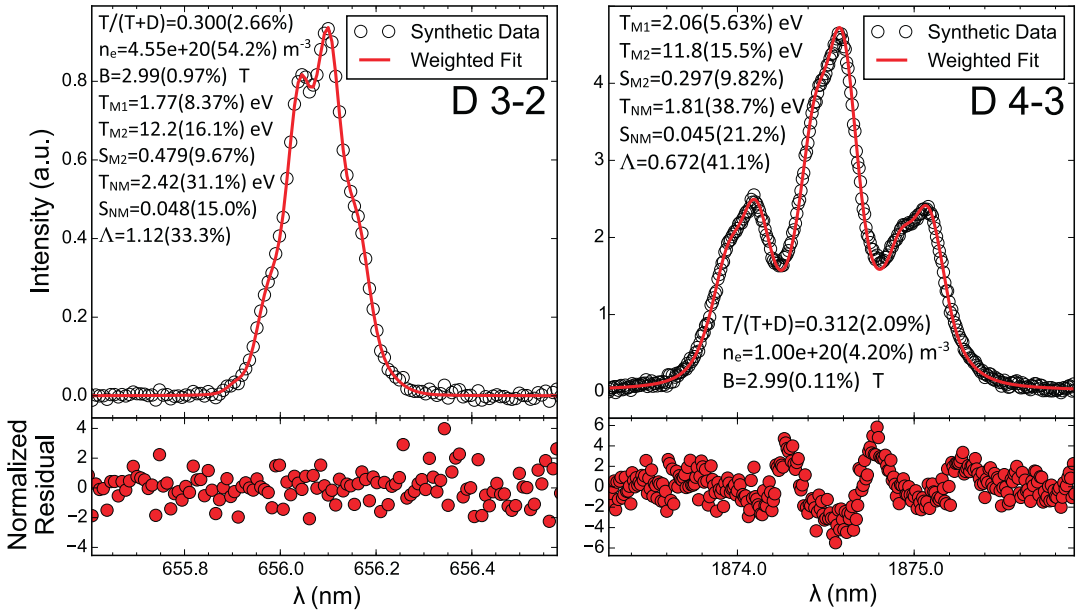

Figure 5.22: Example of 9-parameter fits to synthetic D 3→2 and D 4→3 line profile data. Input values: $T/(T+D) = 0.30$, $n_e = 10^{20}$ m^{-3}, $B = 3.00$ T, $T_{M1} = 2.00$ eV, $T_{M2} = 10.0$ eV, $S_{M2} = 0.50$, $T_{NM} = 2.00$ eV, $S_{NM} = 0.05$ eV, $\Lambda = 0.656$.

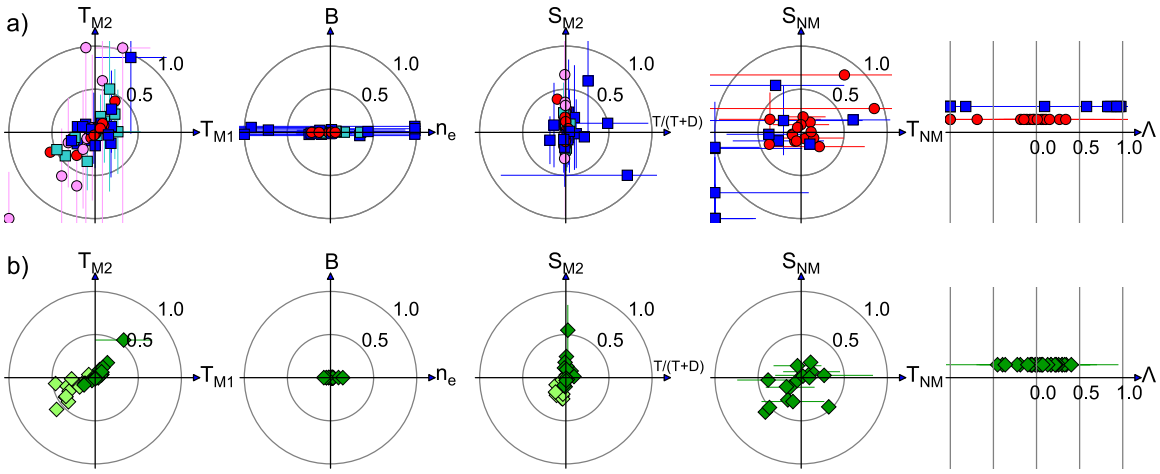

Figure 5.23: Simulation results for 9-parameter fits for a) isolated D 3→2 (squares, high-density light blue, low-density dark blue) and D 4→3 (circles, high-density purple, low-density red) lines; b) combined D 3→2, 4→3 line profiles (high-density light green, low-density dark green). Each marker corresponds to a simulation case and its position to the relative difference between the fit estimate and input value. Fit error bars <25% are not shown for clarity.

divertor plasma conditions were selected comprising 27 simulation cases. The relative differences between the free parameter fit estimates and their input values for low density ($n_e \leq 10^{20}$ m^{-3}) and high density ($n_e > 10^{20}$ m^{-3}) cases are presented

in Figure 5.23.(a). Since the non-Maxwellian contribution in the given range has only a small contribution to the total line profile, it is the most difficult feature to recover, especially for the D 4→3 line. This contribution was removed from the set of input parameters in the high density cases due to poor sensitivity, large fit uncertainties ($> 100\%$) for S_{NM}, T_{NM}, and Λ and to ensure faster solution convergence. Comparing the D 4→3 results to the first iteration (Figure 5.21), the increased number of parameters has clearly degraded the parameter recovery, especially for the neutral temperature components at high density and conversely low temperature ($T_{M1} < 1.5$ eV, $T_{M2} < 7.5$ eV). At low densities the D 4→3 parameter recovery is generally more accurate, whereas the D 3→2 results show more scatter and larger fit uncertainties, especially in n_e, S_{NM} and T_{NM}. The quality of the fits shift in favour of the D 3→2 line at high densities due to improved sensitivity to Stark broadening. The sensitivity of the D 3→2 line profile to low neutral temperatures remains sufficient for the T_{M1}, T_{M2} fit estimates to fall within 50% of the input values, and S_{M2} within 20% of the input values.

Given the inverse relationship between fit quality in high vs. low density conditions (and conversely, low vs. high neutral temperatures), coupling the D 3→2 and 4→3 lines takes advantage of the sensitivity range of each line in isolation. Such coupling improves the overall recovery of parameters, as shown in Figure 5.23.(b), for the same set of simulation cases and input parameters. The results show a marked improvement in the fit accuracy and estimated parameter uncertainty for all 9 input parameters. Some degree of systematic error and parameter estimate correlation is evident in the recovered values of T_{M1} and T_{M2} at high densities and low temperatures.

The results of the above analysis demonstrate the difficulties associated with recovering information from an isolated low-n hydrogen spectral line characterised by a large set of input parameters, and highlight the potential for substantial improvement in parameter recovery through simultaneous multi-parametric fitting of the D 3→2 and 4→3 line profiles. The findings can be generalised to other lines which show similar characteristics in terms of complementary sensitivity to broadening and splitting mechanisms over different parameter ranges.

Chapter 6

Conclusions

In this thesis the principles of passive spectroscopy diagnostics in the VIS and NIR spectral range and their application to observations of plasma emission in tokamak divertors have been investigated. The utility of spectroscopic data interpretation methods for estimating divertor plasma properties and the complementary characteristics of signal extraction techniques in the VIS and NIR make passive spectroscopy diagnostics essential for divertor physics studies and the development of exhaust power mitigation strategies.

6.1 Summary of Thesis

Diagnostic applications of VIS-NIR passive divertor spectroscopy have been investigated through a combination of:

i. Instrument development on MAST and JET-ILW: this work demonstrated the complementary characteristics of signal extraction techniques in both the VIS and NIR spectral range

ii. Measurement and data analysis: the properties of the Balmer and Paschen series and their application to plasma parameter estimation were ascertained using measurements from MAST and JET-ILW plasma experiments, underpinned by plasma spectroscopy theory and atomic data.

iii. Spectral line profile modelling: development of a parametrised Stark-Zeeman-Doppler line model facilitated both interpretive capability in fitting measured data, and forward modelling capapability as a tool for quantifying the scope for parameter recovery from complex spectral line shapes.

The implementation of the VIS-NIR spectroscopy diagnostic on MAST provided valuable insight into the operational performance of light detection in the VIS and NIR as well as an initial survey of the NIR spectral region. The measurement sensitivity of both VIS and NIR spectrometers facilitated operation at similar time resolution, while providing good SNR in both the 390-750 nm and 900-1700 nm regions. The low resolution of the NIR spectrometer necessitated the use of a multi-Gaussian fitting technique for identification of some of the blended spectral features. Besides the Paschen series lines, a large number of neutral and singly ionised carbon lines were identified with the aid of atomic data. Evidence for the presence of a blended neutral boron doublet was also given, and may be of interest for directly measuring the boron influx as a vessel conditioning diagnostic. The use of both the Balmer and Paschen series lines for electron temperature estimation in volume recombining plasma was successfully demonstrated.

The diagnostic upgrade of the JET-ILW mirror-linked divertor spectroscopy system provided a unique opportunity for extending spectral coverage to the NIR range and increasing the VIS range measurement capabilities. Key results from the development work include:

- Successful time-resolved measurement of the Pa-α line intensity using a pair of filtered extended-InGaAs photodiodes.

- Filtered photodiode background thermal emission and Pa-α line intensity measurements showed a sufficiently high Pa-α/background ratio across a wide range of plasma conditions and input powers, thus demonstrating the limited impact of signal contamination from thermal emission on Pa-α line intensity measurements in the JET-ILW environment.

- Successful survey of the NIR spectral range with a medium resolution imaging spectrometer providing first of its kind spectral line profile measurements of the Pa-β line, as well as a detailed survey of the NIR spectrum in the JET-ILW divertor plasma environment.

- Successful measurement of ELM-resolved Balmer line radial emission profiles in H-mode scenarios demonstrating the spatial and temporal dynamics associated with inter and intra-ELM divertor plasma emission.

- An assessment of the Schmidt Czerny-Turner spectrograph performance relative to the conventional Czerny-Turner design, which showed an improvement

in the instrument function width uniformity over the spatial and dispersion direction of the sensor, but proved inconclusive due to uncertainty in the impact of the test conditions on the line shape asymmetries observed at the sensor edges.

The Stark-Zeeman-Doppler parametrised line profile model was formulated with emphasis on computational efficiency, thus neglecting the effect of magnetic and electric field coupling effects which require more detailed calculation. Compared to the coupled Stark-Zeeman `PPP-B` code, the proposed model reproduced the spectral profile features, including the line FWHM and wing decay, with good accuracy especially at high densities and for high-n transitions. For the low-n lines, and particularly the β transitions, some loss of resolution near the line center was evident. Likewise, the σ-component shifts and asymmetries in the D 3→2 and 4→3 lines arising from Stark-Zeeman coupling could not be fully reproduced with the simplified model. However, the computational efficiency of the proposed model makes it more suitable for inter-shot analysis and possibly for real-time measurements of divertor density gradients as observed from strong shaping of the density profiles near the X-point during L-mode detachment.

The parametrised line profile model was applied for estimation of divertor plasma density from spatially resolved measurements of the Balmer and Paschen series lines on JET-ILW. Good agreement was obtained using different lines, including D 7→2, 6→2, 5→2, lines and the first of its kind application of the D 5→3 line. Due to the low neutral temperature sensitivity and broader Stark contribution, the D 5→3 line profile characteristics offer potential for fast density measurements at relatively low spectral resolution, but must be constrained with the magnetic field magnitude due to sensitivity to Zeeman splitting.

Multi-parametric fitting simulations to synthetic diagnostic spectral data for isolated low-n Balmer and Paschen lines across a range of divertor plasma conditions showed particularly good parameter recovery (within 10%) for the D 4→3 line for cases with a simplified single Maxwellian neutral VDF, while the D 4→2 and 5→2 exhibited poor sensitivity to recovery of the neutral temperature and magnetic field. The accuracy and precision of the recovered parameters for D 3→2 and 4→3 lines was markedly degraded once a more representative multi-component neutral VDF was considered. Simultaneous fitting of both D 3→2 and 4→3 profiles yielded significant improvement in fit quality for all 9 free parameters, but at high densities the fits were largely insensitive to the small non-Maxwellian neutral temperature contribution. The results of the synthetic data fitting analysis highlight the benefits

of complementary measurements of low-n line spectra, from which significant plasma parameter information can be extracted.

6.2 Implications for Tokamak Divertor Spectroscopy

As has been intimated throughout the thesis, the advantage gained in combining VIS and NIR spectroscopy diagnostics is the added versatility of measurements and increased scope for evaluation of plasma parameters. This is best exemplified by the utility of the enhanced JET mirror-linked divertor spectroscopy system (KT3) in providing simultaneous access to the Balmer and Paschen series lines. Such flexibility is conducive to obtaining improved coverage of the hydrogen isotope high-n and low-n excited state populations in future exploitation of the system. Diagnostic access to both line series provides additional capability with respect to the range of measured excited population densities, which not only increases the scope for data interpretation using collisional-radiative population models, but allows for direct comparison of the results for improved data validation. In addition, the different sensitivity range of Balmer and Paschen series transitions to spectral profile broadening and splitting mechanisms expands the capabilities for plasma parameter recovery through least-squares fitting techniques which utilise multiple spectral lines to improve the fit quality.

6.3 Future Work

Although the properties of the Balmer and Paschen series lines have been examined in this work in significant detail, recommendations for refining and advancing the complementary VIS-NIR passive divertor spectroscopy diagnsotic techniques include:

- An evaluation of the impact of the discreet-to-continuum transition on both the Balmer and Paschen high-n lines, in order to identify to what extent the D-C merging is expected to influence the line measurements, and thus whether any advantage can be gained by using the high-n Paschen lines for evaluation of electron temperature.

- Based on the simulation results which showed improved scope for parameter recovery through simultaneous D $3\rightarrow2$ and $4\rightarrow3$ spectral profile fitting, capability for spectrally resolved D $4\rightarrow3$ measurements should be explored. This

would not only facilitate diagnostic exploitation of the fitting technique, but it would also serve as a test-bed for line profile comparisons to codes such as PPP-B owing to the enhanced profile feature resolution of the D 4→3 line.

- Although 1D profiles of density and electron temperature in the divertor are quite informative, a need exists for obtaining 2D spatially resolved information for benchmarking edge and divertor fluid and transport codes, particularly for detachment studies. In this regard, consolidation of the JET-ILW divertor grating spectroscopy and filtered imaging diagnostics offers significant benefits from combined measurements of the Balmer series and intrinsic/extrinsic impurity lines. Integration of the spectrally resolved line-of-sight integrated measurements with 2D spatially resolved line ratio and emissivity poloidal reconstructions provides opportunities not only for tomography validation, but also for exploration of data reduction techniques with the aim of obtaining localised plasma parameter estimates.

- Further investigation is needed to explore the potential benefits of NIR spectroscopy measurements in the burning plasma environment of ITER. This would involve extrapolating the scope for parameter recovery from Paschen line profiles to the parameter range representative of ITER divertor plasmas. A reassessment of the potential advantages of NIR measurements from the perspective of optics degradation is also needed in light of recent advances in mirror cleaning techniques for recovering optical performance in the UV-VIS range.

Bibliography

C. Angioni, P. Mantica, T. Ptterich, M. Valisa, et al. Tungsten transport in jet h-mode plasmas in hybrid scenario, experimental observations and modelling. *Nuclear Fusion*, 54(8):083028, 2014.

G. Avila, C. Guirao, and T. Baader. High efficiency inexpensive 2-slices image slicers. In *Society of Photo-Optical Instrumentation Engineers (SPIE) Conference Series*, volume 8446 of *Society of Photo-Optical Instrumentation Engineers (SPIE) Conference Series*, page 9, September 2012.

I Balboa, G Arnoux, T Eich, B Sieglin, et al. Upgrade of the infrared camera diagnostics for the JET ITER-like wall divertora). *Rev. Sci. Instrum.*, 83(10):–, 2012.

D. R. Bates, A. E. Kingston, and R. W. P. McWhirter. Recombination between electrons and atomic ions. i. optically thin plasmas. 267(1330):297–312, 1962.

K. Behringer, H.P. Summers, B. Denne, M. Forrest, and M. Stamp. Spectroscopic determination of impurity influx from localized surfaces. *Plasma Physics and Controlled Fusion*, 31(14):2059, 1989.

T. M. Biewer, R. E. Bell, R. Feder, D. W. Johnson, and R. W. Palladino. Edge rotation and temperature diagnostic on the national spherical torus experiment. *Review of Scientific Instruments*, 75(3):650–654, 2004.

D. Bohm. *The characteristics of electrical discharges in magnetic fields*. New York: McGraw-Hill, 1949.

S. Brezinsek. Plasma-surface interaction in the Be/W environment: Conclusions drawn from the JET-ILW for ITER. *Journal of Nuclear Materials*, 463:11 – 21, 2015. Proceedings of the 21st International Conference on Plasma-Surface Interactions in Controlled Fusion Devices Kanazawa, Japan May 26-30, 2014.

S. Brezinsek, A.G. Meigs, S. Jachmich, M.F. Stamp, et al. The impact of divertor detachment on carbon sources in JET L-mode discharges. *J. Nucl. Mater.*, 390-391:267–273, June 2009.

S. Brezinsek, M.F. Stamp, D. Nishijima, D. Borodin, et al. Study of physical and chemical assisted physical sputtering of beryllium in the jet iter-like wall. *Nuclear Fusion*, 54(10):103001, 2014.

B. Brichard, A. Fernandez, H. Ooms, F. Berghmans, et al. Radiation-hardening techniques of dedicated optical fibres used in plasma diagnostic systems in {ITER}. *Journal of Nuclear Materials*, 329333, Part B:1456 – 1460, 2004. Proceedings of the 11th International Conference on Fusion Reactor Materials (ICFRM-11).

A. Brissaud and U. Frisch. Theory of stark broadeningii exact line profile with model microfield. *Journal of Quantitative Spectroscopy and Radiative Transfer*, 11(12): 1767 – 1783, 1971.

N. H. Brooks, D. Fehling, D. L. Hillis, C. C. Klepper, N. N. Naumenko, S. N. Tugarinov, and D. G. Whyte. Visible spectroscopy in the diiid divertor. *Review of Scientific Instruments*, 68(1):978–981, 1997.

A Calisti, C Mossé, S Ferri, B Talin, et al. Dynamic Stark broadening as the Dicke narrowing effect. *Phys. Rev. E*, 81(1):16406, January 2010.

S. Clement, A. Chankin, D. Ciric, J.P. Coad, et al. Power deposition in the {JET} divertor during {ELMs}. *Journal of Nuclear Materials*, 266269:285 – 290, 1999.

J W Conner and H R Wilson. Survey of theories of anomalous transport. *Plasma Physics and Controlled Fusion*, 36(5):719, 1994.

J. Cooper. Plasma spectroscopy. *Reports on Progress in Physics*, 29(1):35, 1966.

M. Cox. The Mega Amp Spherical Tokamak. 46(2–4):397–404, 1999.

I. Duran, K. Ješko, V. Fuchs, M. Groth, et al. Assessment of the effect of parallel temperature gradients in the JET SOL on Te measured by divertor target Langmuir probes. *Journal of Nuclear Materials*, January 2015.

C. Durell, D. Wilks, and J. Kinkaid. Preliminary Data for Space Grade Spectralon BRDF Targets and Standards. In *23rd Conference on Characterisation and Radiometric Calibration for Remote Sensing*, 2014.

EFDA. Fusion electricity: A roadmap to the realisation of fusion energy, 2012.

T. Eich, A.W. Leonard, R.A. Pitts, W. Fundamenski, et al. Scaling of the tokamak near the scrape-off layer h-mode power width and implications for iter. *Nuclear Fusion*, 53(9):093031, 2013.

U Fantz. Basics of plasma spectroscopy. *Plasma Sources Science and Technology*, 15(4):S137–S147, November 2006.

S. Ferri, A. Calisti, C. Mossé, L. Mouret, et al. Frequency-fluctuation model applied to Stark-Zeeman spectral line shapes in plasmas. *Phys. Rev. E*, 84(2):026407, August 2011.

S. Ferri, A. Calisti, C. Mossé, J. Rosato, et al. Ion Dynamics Effect on Stark-Broadened Line Shapes: A Cross-Comparison of Various Models. *Atoms*, 2(3): 299–318, July 2014.

G. Fishpool, J. Canik, G. Cunningham, J. Harrison, et al. Mast-upgrade divertor facility and assessing performance of long-legged divertors. *Journal of Nuclear Materials*, 438, Supplement:S356 – S359, 2013. Proceedings of the 20th International Conference on Plasma-Surface Interactions in Controlled Fusion Devices.

P.J. Friedberg. *Plasma Physics and Fusion Energy*. Cambridge University Press, Cambridge, 1st ed. edition, 2007.

T. Fujimoto. *Plasma Spectroscopy*. Clarendon Press, 2004.

T. Fujimoto and R. W. P. McWhirter. Validity criteria for local thermodynamic equilibrium in plasma spectroscopy. *Phys. Rev. A*, 42:6588–6601, 1990.

W. Fundamenski, S. Sipil, G.F. Matthews, V. Riccardo, et al. Interpretation of recent power width measurements in jet mkiigb elmy h-modes. *Plasma Physics and Controlled Fusion*, 44(6):761, 2002.

J. A. Goetz, C. Kurz, B. LaBombard, B. Lipschultz, et al. Comparison of detached and radiative divertor operation in alcator cmod. *Physics of Plasmas*, 3(5):1908–1915, 1996.

M. Greenwald. Density limits in toroidal plasmas. *Plasma Physics and Controlled Fusion*, 44(8):R27, 2002.

H.R. Griem. *Spectral Line Broadening by Plasmas*. Springer-Verlag Berlin Heidelberg, 1974.

H.R. Griem. *Principles of Plasma Spectroscopy*. Cambridge University Press, Cambridge, 1997.

M. Groth, S. Brezinsek, P. Belo, M. Brix, et al. Divertor plasma conditions and neutral dynamics in horizontal and vertical divertor configurations in JET-ILW low confinement mode plasmas. *J. Nucl. Mater.*, page Article in press, December 2015.

M. Gryaznevich, R. Akers, P. G. Carolan, N. J. Conway, et al. Achievement of record β in the start spherical tokamak. *Phys. Rev. Lett.*, 80:3972–3975, 1998.

J.P. Gunn, C. Boucher, B.L. Stansfield, and S. Savoie. Flush-mounted probes in the divertor plates of Tokamak de Varennes. *Rev. Sci. Instrum.*, 66(1), 1995.

J. Halenka, W. Olchawa, B. Grabowski, and F. Gajda. Perturber s charge e ect on Stark broadened hydrogen lines in helium plasmas. *J. Quant. Spectrosc. Radiat. Transfer*, 74:539–544, 2002.

T. Hamacher and A.M. Bradshaw. Fusion as a future power source: recent achievements and prospects. In *Proc. of the 18th Congress, World Energy Council*, 2001.

SD-12 Hamamatsu Technical Information. Characteristics and use of infrared detectors [online], 2011. URL `http://www.hamamatsu.com`. Accessed: 25-08-2015.

J.R. Harrison. Improved Understanding of Edge Plasma Dynamics Through Visible Imaging on MAST. 2014.

J.R. Harrison, S.W. Lisgo, K.J. Gibson, P. Tamain, J. Dowling, and The MAST Team. Characterisation of detached plasmas on the {MAST} tokamak. *Journal of Nuclear Materials*, 415(1, Supplement):S379 – S382, 2011. Proceedings of the 19th International Conference on Plasma-Surface Interactions in Controlled Fusion.

R.J. Harrison. *Characterisation of Detached Plasmas on the MAST Tokamak*. PhD thesis, University of York, 2010.

S. Higashijima, T. Sugie, H. Kubo, S. Tsuji, et al. Impurity and particle recycling reduction by boronization in jt-60u. *Journal of Nuclear Materials*, 220222:375 – 379, 1995. Plasma-Surface Interactions in Controlled Fusion Devices.

E M Hollmann, S Brezinsek, N H Brooks, M Groth, et al. Spectroscopic measurement of atomic and molecular deuterium fluxes in the diii-d plasma edge. *Plasma Physics and Controlled Fusion*, 48(8):1165, 2006.

J. Holtsmark. Über die Verbreiterung von Spektrallinien. *Annalen der Physik*, 363 (7):577–630, 1919.

C.F. Hooper. Low-frequency component electric microfield distributions in plasmas. *Phys. Rev.*, 165:215–222, 1968.

J. Horacek, R.A. Pitts, P.C. Stangeby, O. Batishchev, et al. Predicted effects of parallel temperature gradients on the overestimation of TCV divertor target Langmuir probe Te measurements. *J. Nucl. Mater.*, 313-316:931–935, March 2003.

A.E. Hubbard. Physics and scaling of the h-mode pedestal. *Plasma Physics and Controlled Fusion*, 42(5A):A15, 2000.

A. Huber, K. McCormick, P. Andrew, M.R. de Baar, et al. Improved radiation measurements on {JET} first results from an upgraded bolometer system. *Journal of Nuclear Materials*, 363365:365 – 370, 2007.

A. Huber, S. Brezinsek, M. Groth, P.C. de Vries, et al. Impact of the ITER-like wall on divertor detachment and on the density limit in the JET tokamak. *J. Nucl. Mater.*, 438:S139–S147, July 2013.

K. Ikeda. Progress in the ITER Physics Basis. *Nucl. Fusion*, 47(6), June 2007.

D. R. Inglis and E. Teller. Ionic depression of series limits in cne-electron spectra. *Astrophysical Journal*, 90:439, 1939.

R. C. Isler, R. W. Wood, C. C. Klepper, N. H. Brooks, et al. Spectroscopic characterization of the diii-d divertor. *Physics of Plasmas*, 4(2), 1997.

W. J. Karzas and R. Latter. Electron radiative transitions in a coulomb field. *Astrophysical Journal Supplement*, 6:167, 1961.

I. Katramados, G. Fishpool, M. Fursdon, G. Whitfield, G. Thompson, and H. Meyer. {MAST} upgrade closed pumped divertor design and analysis. *Fusion Engineering and Design*, 86(911):1595 – 1598, 2011. Proceedings of the 26th Symposium of Fusion Technology (SOFT-26).

H. A. Kramers. Xciii. on the theory of x-ray absorption and of the continuous x-ray spectrum. *Philosophical Magazine Series 6*, 46(275):836–871, 1923.

A. Kramida, Yu. Ralchenko, J. Reader, and NIST ASD Team. Nist atomic spectra database (version 5.2), [online]. `http://physics.nist.gov/asd` , 2014. National Institute of Standards and Technology, Gaithersburg, MD., Accessed: 20-07-2015.

S. I. Krasheninnikov, A. Yu. Pigarov, D. A. Knoll, et al. Plasma recombination and molecular effects in tokamak divertors and divertor simulators. *Physics of Plasmas*, 4(5):1638–1646, 1997.

K. Krieger, S. Brezinsek, M. Reinelt, S.W. Lisgo, et al. Beryllium migration and evolution of first wall surface composition in the {JET} {ILW} configuration. *Journal of Nuclear Materials*, 438, Supplement:S262 – S266, 2013. Proceedings of the 20th International Conference on Plasma-Surface Interactions in Controlled Fusion Devices.

H. Kubo, H. Takenaga, K. Sawada, T. Nakano, et al. Spectroscopic study of hydrogen particle behavior in attached and detached divertor plasmas of jt-60u. *Journal of Nuclear Materials*, 337339:161 – 165, 2005.

H.W. Kugel, V. Soukhanovskii, M. Bell, W. Blanchard, et al. Impact of the wall conditioning program on plasma performance in {NSTX}. *Journal of Nuclear Materials*, 313316:187 – 193, 2003. Plasma-Surface Interactions in Controlled Fusion Devices 15.

A B Kukushkin, V S Neverov, M B Kadomtsev, V Kotov, et al. Parameterization of Balmer-alpha asymmetric line shape in tokamak SOL plasmas. *Journal of Physics: Conference Series*, 548:012012, November 2014a.

A B Kukushkin, V S Neverov, M F Stamp, A G Alekseev, et al. Theoretical Model of ITER High Resolution H-alpha Spectroscopy for a Strong Divertor Stray Light and Validation Against JET-ILW Experiments. In *Proc. 25th Fusion Energy Conf.*, St. Petersburg, Russia, 2014b. IAEA.

H-J Kunze. *Introduction to Plasma Spectroscopy.* Springer, 2009. ISBN 9783642022326.

B. Lipschultz, B. LaBombard, E.S. Marmar, M.M. Pickrell, J.L. Terry, R. R. Watterson, and S.M. Wolfe. Marfe: an edge plasma phenomenon. *Nuclear Fusion*, 24 (8):977, 1984.

B. Lipschultz, J. L. Terry, C. Boswell, A. Hubbard, B. LaBombard, and D. A. Pappas. Ultrahigh densities and volume recombination inside the separatrix of the alcator c-mod tokamak. *Phys. Rev. Lett.*, 81:1007–1010, Aug 1998.

B. Lipschultz, J. L. Terry, C. Boswell, J. A. Goetz, et al. The role of particle sinks and sources in alcator c-mod detached divertor discharges. *Physics of Plasmas*, 6 (5):1907–1916, 1999.

A. Litnovsky, V.S. Voitsenya, A. Costley, A.J.H. Donn, and for the SWG on First Mirrors of the ITPA Topical Group on Diagnostics. First mirrors for diagnostic systems of iter. *Nuclear Fusion*, 47(8):833, 2007a.

A. Litnovsky, P. Wienhold, V. Philipps, G. Sergienko, et al. Diagnostic mirrors for iter: A material choice and the impact of erosion and deposition on their performance. *Journal of Nuclear Materials*, 363365:1395 – 1402, 2007b. Plasma-Surface Interactions-17.

A Loarte, R D Monk, J R Martín-Solís, D J Campbell, et al. Plasma detachment in JET Mark I divertor experiments. *Nuclear Fusion*, 38(3):331, 1998.

A. Loarte, B. Lipschultz, A.S. Kukushkin, G.F. Matthews, et al. Chapter 4: Power and particle control. *Nuclear Fusion*, 47(6):S203, 2007.

H.A. Lorentz. The theory of electrons and its applications to the phenomena of light and radiant heat; a course of lectures delivered in columbia university, new york. *March and April*, 2, 1906.

D Lumma, J L Terry, and B Lipschultz. Radiative and three-body recombination in the Alcator C-Mod divertor. *Phys. Plasmas*, 4(7):2555–2566, 1997.

C.F. Maggi. *Measurement and Interpretation of Spectral Emission from JET Divertor Plasmas*. PhD thesis, University of Strathclyde, 1997.

C.F Maggi, L.D Horton, G Corrigan, H.J Jckel, A Loarte, R.D Monk, R Simonini, M Stamp, and A Taroni. Modelling of deuterium emission in high density divertor plasmas in {JET}. *Journal of Nuclear Materials*, 266269:867 – 872, 1999.

M. Maslov, M.N.A. Beurskens, M. Kempenaars, and J. Flanagan. Status of the jet lidar thomson scattering diagnostic. *Journal of Instrumentation*, 8(11):C11009, 2013.

Benjamin Matek and Karl Gawell. The benefits of baseload renewables: A misunderstood energy technology. *The Electricity Journal*, 28(2):101 – 112, 2015.

G F Matthews, M Beurskens, S Brezinsek, M Groth, et al. JET ITER-like walloverview and experimental programme. *Physica Scripta*, T145:014001, December 2011.

G.M. McCracken, M.F. Stamp, R.D. Monk, A.G. Meigs, et al. Evidence for volume recombination in jet detached divertor plasmas. *Nuclear Fusion*, 38(4):619, 1998.

R.W.P. McWhirter. Spectral Intensities. In *Plasma Diagnostic Techniques*, page 201, 1965.

R.W.P. McWhirter and H.P. Summers. Atomic Radiation from Low Density Plasma. In C. F. Barnett and M. F. A. Harrison, editors, *Applied Atomic Collision Physics, Volume 2: Plasmas*, volume 2, page 52, 1984.

A. Meigs, M. Stamp, R Igreja, S. Sanders, and P. Heesterman. Enhancement of JETs mirror-link near-ultraviolet to near-infrared divertor spectroscopy system. *Rev. Sci. Instrum.*, 81(10):10E532, 2010.

A G Meigs, G M McCracken, C Maggi, R D Monk, et al. Spectroscopic Electron Density Measurements and Evidence of Recombination in High Density JET Divertor Discharges. In *Proc. 25th EPS Conf. on Plasma Physics*, number 98, pages P–1.017, Prague, Czech Republic, 1998. European Physical Society.

A.G. Meigs, S. Brezinsek, M. Clever, A. Huber, et al. Deuterium Balmer/Stark spectroscopy and impurity profiles: First results from mirror-link divertor spectroscopy system on the JET ITER-like wall. *J. Nucl. Mater.*, 438:S607–S611, July 2013.

D.A. Meneley. Nuclear Energy Challenges in this Century. In *Proc. of the 17th Pacific Basin Nuclear Conference*, 2010.

R.D. Monk, A. Meigs, L. Horton, L.C. Ingesson, et al. Volume recombination and detachment in {JET} divertor plasmas. *Journal of Nuclear Materials*, 266269:37 – 43, 1999.

L. Moser, R. Steiner, F. Leipold, R. Reichle, L Marot, and E. Meyer. Plasma cleaning of {ITER} first mirrors in magnetic field. *Journal of Nuclear Materials*, 463:940 – 943, 2015. PLASMA-SURFACE {INTERACTIONS} 21Proceedings of

the 21st International Conference on Plasma-Surface Interactions in Controlled Fusion Devices Kanazawa, Japan May 26-30, 2014.

C.H. Nicholas. *Special features and spectral analysis for fusion plasmas.* PhD thesis, University of Strathclyde, 2011.

K. Nishimura, N. Ashikawa, A. Sagara, N. Noda, et al. Effects of Boronization in LHD. *Journal of Plasma and Fusion Research*, 79:1216–1217, 2003.

M. G. O'Mullane, H. P. Summers, A. D. Whiteford, A. G. Meigs, et al. Atomic modeling and instrumentation for measurement and analysis of emission in preparation for the iter-like wall in jet. *Review of Scientific Instruments*, 77(10):10F520, 2006.

S. Pamela. Flush user's guide, 2013. CODAS, JET Document.

N.J. Peacock. Fusion spectroscopy. *Astrophysics and Space Science*, 237(1-2):341–399, 1996. ISSN 0004-640X.

A Yu Pigarov, J L Terry, and B Lipschultz. Study of the discrete-to-continuum transition in a Balmer spectrum from Alcator C-Mod divertor plasmas Study of the discrete-to-continuum transition in a Balmer spectrum from Alcator C-Mod divertor plasmas. *Plasma Phys. Control. Fusion*, 40:2055–2072, 1998.

F. Piras, S. Coda, I. Furno, J-M Moret, et al. Snowflake divertor plasmas on tcv. *Plasma Physics and Controlled Fusion*, 51(5):055009, 2009.

C.S. Pitcher and P.C. Stangeby. Experimental divertor physics. *Plasma Physics and Controlled Fusion*, 39(6):779, 1997.

D.E. Post. A review of recent developments in atomic processes for divertors and edge plasmas. *Journal of Nuclear Materials*, 220222:143 – 157, 1995.

S Potzel, R Dux, H W Müller, A Scarabosio, and M Wischmeier. Electron density determination in the divertor volume of ASDEX Upgrade via Stark broadening of the Balmer lines. *Plasma Phys. Controlled Fusion*, 56(2):025010, February 2014.

S. Potzel, M. Wischmeier, M. Bernert, R. Dux, et al. Formation of the high density front in the inner far {SOL} at {ASDEX} upgrade and {JET}. *Journal of Nuclear Materials*, 463:541 – 545, 2015. PLASMA-SURFACE {INTERACTIONS} 21Proceedings of the 21st International Conference on Plasma-Surface Interactions in Controlled Fusion Devices Kanazawa, Japan May 26-30, 2014.

W. H. Press, B. P. Flannery, S. A. Teukolsky, and W. T. Vetterlin. *Numerical Recipies*. Cambridge University Press, Cambridge, 1st ed. edition, 1986.

Princeton Instruments Inc. Improved spectra with a schmidt-czerny-turner spectrograph. Technical report, 2013.

D Reiter, S Wiesen, and M Born. Radiation transfer in dense edge plasmas and divertors: experimental and recent computational results. *Journal of Nuclear Materials*, 313316:845 – 851, 2003. Plasma-Surface Interactions in Controlled Fusion Devices 15.

Gustav Resch, Anne Held, Thomas Faber, Christian Panzer, Felipe Toro, and Reinhard Haas. Potentials and prospects for renewable energies at global scale. *Energy Policy*, 36(11):4048 – 4056, 2008.

A. Rogalski. *Infrared Detectors, 2nd Edition*. CRC Press, 2010.

F. Romanelli. Overview of the jet results with the iter-like wall. *Nuclear Fusion*, 53 (10):104002, 2013.

D. L. Rudakov, J. A. Boedo, R. A. Moyer, A. Litnovsky, et al. First tests of molybdenum mirrors for iter diagnostics in diii-d divertor. *Review of Scientific Instruments*, 77(10):10F126, 2006.

Arthru B. Shafer, Lawrence R. Megill, and Leann Droppleman. Optimization of the czerny-turner spectrometer. *J. Opt. Soc. Am.*, 54(7):879–886, Jul 1964.

S. A. Silburn, J. R. Harrison, J. Howard, K. J. Gibson, H. Meyer, C. A. Michael, and R. M. Sharples. Coherence imaging of scrape-off-layer and divertor impurity flows in the mega amp spherical tokamak (invited)a). *Review of Scientific Instruments*, 85(11), 2014.

I.I. Sobelman, L.A. Vainshtein, and E.A. Yukov. *Excitation of Atoms and Broadening of Spectral Lines*. Academic Press, Inc., 1981.

V. A. Soukhanovskii. Near-infrared spectroscopy for burning plasma diagnostic applicationsa). *Review of Scientific Instruments*, 79(10):10F539, 2008.

V A Soukhanovskii, D W Johnson, R Kaita, and L Roquemore. Electron Density Measurements in the National Spherical Torus Experiment Detached Divertor Region Using Stark Broadening of Deuterium Infrared Paschen Emission Lines. *Rev. Sci. Instrum.*, 77:10F127, 2006.

V. A. Soukhanovskii, A. G. McLean, and S. L. Allen. Near-infrared spectroscopy for divertor plasma diagnosis and control in diii-d tokamak). *Review of Scientific Instruments*, 85(11):11E418, 2014.

W. M. Stacey, M. A. Mahdavi, R. Maingi, and T. W. Petrie. Multi-faceted asymmetric radiation from the edge formation in diii-d high-confinement mode discharges with continuous gas puffing. *Physics of Plasmas*, 6(10):3941–3954, 1999.

M.F. Stamp, K.H. Behringer, M.J. Forrest, P.D. Morgan, and H.P. Summers. Impurity influx behaviour in {JET}. *Journal of Nuclear Materials*, 145147:236 – 240, 1987.

P.C. Stangeby. A problem in the interpretation of tokamak Langmuir probes when a fast electron component is present. *Plasma Phys. Controlled Fusion*, 37:1031–1037, 1995.

P.C. Stangeby. *The Plasma Boundary of Magnetic Fusion Devices*. IoP Publishing Ltd., 2000a.

P.C. Stangeby. A tutorial on some basic aspects of divertor physics. *Plasma Physics and Controlled Fusion*, 42(12B):B271, 2000b.

C. Stehlé and R. Hutcheon. Extensive tabulations of Stark broadened hydrogen line profiles. *Astron. Astrophys. Suppl. Ser.*, 140(1):93–97, 1999.

B. C. Stratton, M. Bitter, K. W. Hill, D. L. Hillis, and J. T. Hogan. Chapter 5: Passive spectroscopic diagnostics for magnetically confined fusion plasmas. *Fusion Science and Technology*, 53(2):431–486, 2008.

T. Sugie, H. Ogawa, T. Nishitani, S. Kasai, et al. Divertor impurity monitor for the international thermonuclear experimental reactor. *Review of Scientific Instruments*, 70(1):351–354, 1999.

H.P. Summers. The ADAS User Manual, version 2.6, 2004. URL `http://www.adas.ac.uk`.

H.P. Summers, N.R. Badnell, M.G. O'Mullane, A.D. Whiteford, et al. Atomic data for modelling fusion and astrophysical plasmas. *Plasma Physics and Controlled Fusion*, 44(12B):B323, 2002.

H.P. Summers, W.J. Dickson, M.G. O'Mullane, N.R. Badnell, et al. Ionization state, excited populations and emission of impurities in dynamic finite density plasmas: I. the generalized collisionalradiative model for light elements. *Plasma Physics and Controlled Fusion*, 48(2):263, 2006.

A. Sykes, the START Team, the NBI Team, the MAST Team, and the Theory Team. The spherical tokamak programme at Culham. 39(9Y):1271, 1999.

B Talin, A Calisti, L Godbert, R Stamm, et al. Frequency-fluctuation model for line-shape calculations in plasma spectroscopy. *Phys. Rev. A*, 51(3):1918–1928, March 1995.

G. De Temmerman, E. Delchambre, J. Dowling, A. Kirk, S. Lisgo, and P. Tamain. Thermographic study of heat load asymmetries during mast l-mode discharges. *Plasma Physics and Controlled Fusion*, 52(9):095005, 2010.

G.J. van Rooij, J.W. Coenen, L. Aho-Mantila, S. Brezinsek, et al. Tungsten divertor erosion in all metal devices: Lessons from the {ITER} like wall of {JET}. *Journal of Nuclear Materials*, 438, Supplement:S42 – S47, 2013. Proceedings of the 20th International Conference on Plasma-Surface Interactions in Controlled Fusion Devices.

ITER Doc. G 74 LS 102-03-22 W0.1. Iter materials properties database. Technical report.

J Wesson. *Tokamaks*. Clarendon Press, Oxford, 3rd ed. edition, 2004.

D.G. Whyte, W.P. West, C.P.C. Wong, R. Bastasz, et al. The effect of detachment on carbon divertor erosion/redeposition in the diii-d tokamak. *Nuclear Fusion*, 41 (9):1243, 2001.

A. Widdowson. Removal of beryllium-containing films deposited in {JET} from mirror surfaces by laser cleaning. *Journal of Nuclear Materials*, 415(1, Supplement):S1199 – S1202, 2011. Proceedings of the 19th International Conference on Plasma-Surface Interactions in Controlled Fusion.

T. Wujec, W. Olchawa, J. Halenka, and J. Musielok. Experimental and theoretical Stark broadening studies of the hydrogen Paschen β line. *Phys. Rev. E*, 66(6): 066403, December 2002.

K.-D. Zastrow, S. R. Keatings, L. Marot, M. G. O'Mullane, G. de Temmerman, and JET-EFDA Contributors. Modeling the effect of reflection from metallic walls on spectroscopic measurementsa). *Review of Scientific Instruments*, 79(10):10F527, 2008.

Appendix A

Calibration Methodology Using an Irradiance Standard and Lambertian Diffuser

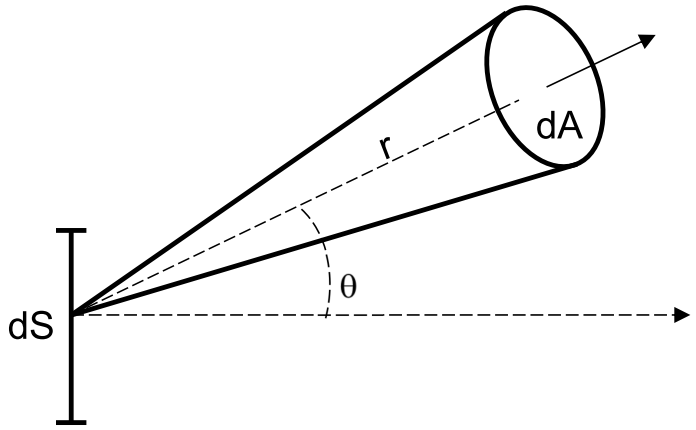

Figure A.1: Definition of radiance.

The radiant power $\mathrm{d}^2\phi$ [W] emitted by a small plane source of area $\mathrm{d}S$ into a small solid angle $\mathrm{d}\Omega = \mathrm{d}A/r^2$ (Figure A.1) is given by

$$\mathrm{d}^2\phi = L\ \mathrm{d}S\ \cos\theta\ \mathrm{d}\Omega \tag{A.0.1}$$

where L is the source radiance [W m^2 sr^{-1}]. For a Lambertian source, L is independent of the angle of observation (i.e., equally bright at all angles). The total power radiated by the small Lambertian source into a hemisphere can be calculated by considering the geometry in Figure A.2. The power radiated into a thin conical

shell is first derived by determining the solid angle $\mathrm{d}\Omega$ subtended by an annulus of width $\mathrm{d}r = r\ \mathrm{d}\theta$, and annulus area $\mathrm{d}A = 2\pi\ r\ \sin\theta\ r\ \mathrm{d}\theta$. The solid angle is then

$$\mathrm{d}\Omega = 2\pi\ \sin\theta\ \mathrm{d}\theta\ , \tag{A.0.2}$$

and the power radiated into the conical shell is

$$\mathrm{d}^2\phi = L\ \mathrm{d}S\ \cos\theta\ 2\pi\ \sin\theta\ \mathrm{d}\theta\ . \tag{A.0.3}$$

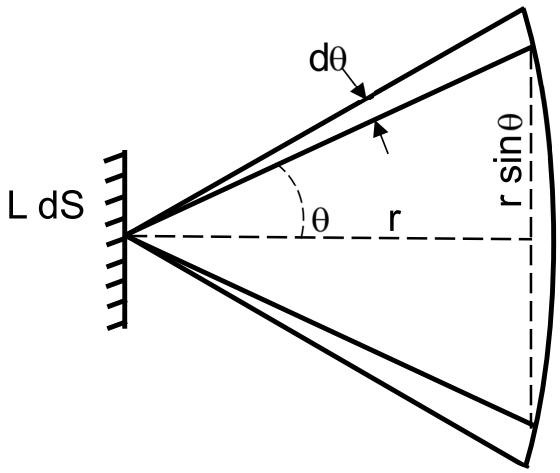

Figure A.2: Geometry of a thin conic shell.

The total power radiated into a cone of half angle θ_0 is then

$$\mathrm{d}\phi_{\theta_0} = 2\pi\ L\ \mathrm{d}S \int_0^{\theta_0} \sin\theta\ \cos\theta\ \mathrm{d}\theta = \pi L\ \mathrm{d}S\ \sin^2\theta_0\ . \tag{A.0.4}$$

The power radiated into a hemisphere with $\theta_0 = 90°$ is

$$\mathrm{d}\phi_L = \pi L\ \mathrm{d}S\ . \tag{A.0.5}$$

Figure A.3 shows the calibration layout of the source, diffuser and collection lens. The normal to the diffuser surface is aligned with the camera lens, whereas the diffuser normal is positioned at an angle θ with respect to the irradiance source.

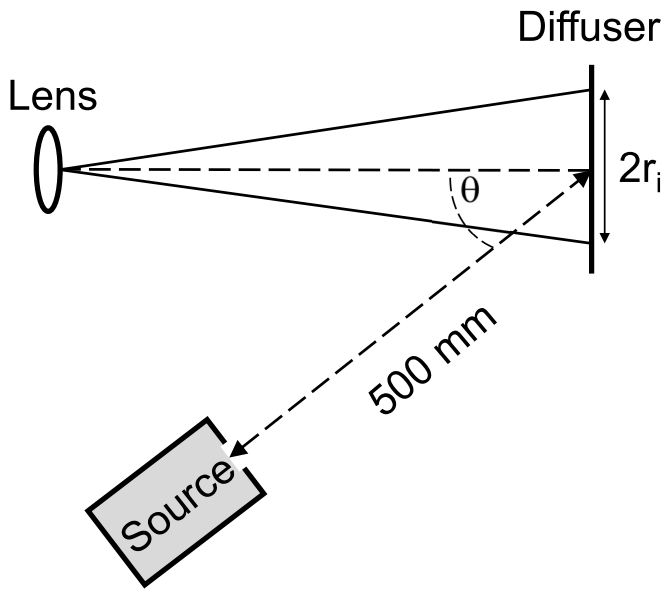

Figure A.3: Calibration layout.

The diffuser is positioned 500 mm away from the source. The power falling on the diffuser surface is reduced by a factor cosθ, neglecting any curvature associated with the irradiance front E_λ incident on the diffuser panel. Hence, the power falling on the diffuser surface is

$$\mathrm{d}\phi_i = E_\lambda \cos\theta \, \pi r_i^2 \, , \tag{A.0.6}$$

where $2r_i$ is the portion of the diffuser diameter that is imaged by the collection lens (i.e., the field of view of the lens).

The hemispherical reflectance of the diffuser is typically given for a particular illumination angle (typically 8°) viewed normal to the diffuser surface. More generally, the reflectance f_λ is a function of θ depending on the scattering properties of the coating. In the calibration of the NIR spectrometer, an illumination angle of $\theta = 30°$ was selected. For a Spectralon® diffuser, the reflectance has been shown to vary by about $\pm 3\%$ for illumination angles in the range 5-30° (Durell et al., 2014). Since the diffuser panel could not be characterised in detail, f_λ in the range 900-1700 nm was estimated at $97 \pm 2\%$ assuming the coating was not significantly degraded. The diffuser thus reflects a fraction f_λ of the incident power into the hemisphere (2π solid angle), hence

$$\mathrm{d}\phi_r = f_\lambda \, \mathrm{d}\phi_i = f_\lambda \, E_\lambda \cos\theta \, \pi r_i^2 \, . \tag{A.0.7}$$

Equating expressions A.0.5 and A.0.7, and replacing L with L_λ and dS with πr_i^2, the radiance of the diffuser is then

$$L_\lambda = f_\lambda \, E_\lambda \cos\theta \, / \, \pi \quad [\mathrm{W\ m^{-2}\ sr^{-1}\ nm^{-1}}]. \tag{A.0.8}$$